INFORMATION TO USERS

This manuscript has been reproduced from the microfilm master. UMI films the text directly from the original or copy submitted. Thus, some thesis and dissertation copies are in typewriter face, while others may be from any type of computer printer.

The quality of this reproduction is dependent upon the quality of the copy submitted. Broken or indistinct print, colored or poor quality illustrations and photographs, print bleedthrough, substandard margins, and improper alignment can adversely affect reproduction.

In the unlikely event that the author did not send UMI a complete manuscript and there are missing pages, these will be noted. Also, if unauthorized copyright material had to be removed, a note will indicate the deletion.

Oversize materials (e.g., maps, drawings, charts) are reproduced by sectioning the original, beginning at the upper left-hand corner and continuing from left to right in equal sections with small overlaps.

Photographs included in the original manuscript have been reproduced xerographically in this copy. Higher quality 6" x 9" black and white photographic prints are available for any photographs or illustrations appearing in this copy for an additional charge. Contact UMI directly to order.

ProQuest Information and Learning
300 North Zeeb Road, Ann Arbor, MI 48106-1346 USA
800-521-0600

UMI®

NOTE TO USERS

Page(s) not included in the original manuscript and are unavailable from the author or university. The manuscript was microfilmed as received.

222

This reproduction is the best copy available.

UMI

FORMATION AND CONTROL OF SOOT AND NO IN COUNTER-FLOW NON-PREMIXED AND PARTIALLY PREMIXED FLAMES

by

Hemant P. Mungekar

A dissertation submitted in partial fulfillment
of the requirements for the degree of
Doctor of Philosophy
(Mechanical Engineering)
in The University of Michigan
2001

Doctoral Committee:

Professor Arvind Atreya, Chairman
Professor Michael Chen
Professor James F. Driscoll
Assistant Professor Margaret S. Wooldridge

To my parents, Baba and Aai,
wife, Swati
sister, Jyoti
for their love and support.

ACKNOWLEDGMENTS

It would be unfair to start this section without acknowledging my teachers who have shaped my thinking. Profs. A.W. Date, S.P.Sukhatme and U.N. Gaitonde introduced me to the areas of heat transfer and thermodynamics at IIT, Mumbai. This interest was sustained at Rutgers University by Profs. C.Polymeropolous, Y. Jaluria, D. Knight and N. Glumac. Perhaps my most creative years were at Michigan with Prof. Atreya who gave me ample freedom to try things in the lab and who was more than an academic advisor in many ways. The valuable direction by Profs. V. Sick, J.F. Driscoll, M.M. Chen and M.S. Wooldridge at various stages of my research is gratefully acknowledged. I would also like to thank Profs. R. Akhavan and Hong Im for their feedback and caring concern of my academic progress. I deeply appreciate the help and company of Prof. Robert Keller during the design and assembly of some of the electronics used in data acquisition. My stay and study at Michigan would have been incomplete without Dr. David Everest who has been a friend and a mentor. Help from Harald Eberhart, Kent Pickett and John Mears in fabrication of equipment used in this work is acknowledged. I would like to acknowledge Cynthia Quann-White of the academic services offices for her help all through my graduate program.

My fellow graduate students, particularly Sean Berhan and Andy Praseteo, made the long working hours during the experiments seem less stressful. I learnt a lot from H.K. Kim, J. Suh, C.Zhang and T. Shamim during early stages of my thesis. Help and company of Geraldo Gaytan, Shawn Hunter, Melissa Chernovsky and Tershia Pinder while working in the lab is very much appreciated.

My stay in Ann Arbor was a period of great personal growth in the company of William and Cheri Albertson, Dr. Shashi Krishnan and her family and Dr. Hemant Pawar and his family. My roommates, Dr. Gyanesh Gupta and Jollin D'souza were a part of my support system at home away from home. The help of Sean Berhan, Gopal and Bhuvana Kota and Gyanesh and Sneha Gupta in the finishing stages of this thesis is greatly appreciated.

I would have been unable to sustain through the frustrating moments in research without the internal strength and insight that I gained in the company of Kishore and Kalyani Khairnar whose love and affection has shaped my thinking over years. The love and advice of Fr. Solomon Rodriguez, Fr. Joe Periera, Fr. Joe Rodricks, Swami Vishnupremananda, Rev. Anatole Rusanov and Sant Rajinder Singh changed my life in ways I could have never imagined. The letters from Dr. S.S. Mungekar and Dr. Dortothy Jones kept me going when the going got tough. My parents, Aai and Baba, and my sister, Jyoti, have been a source of encouragement all through my graduate study. My personal and academic progress is in a large part a result of their love and sacrifice over the years. My wife, Swati, and my in-laws have been a great source of support during the tail end of this thesis. I am indebted to my beloved wife, Swati, for her selfless help and understanding, even at the expense of delaying her own studies.

TABLE OF CONTENTS

LIST OF FIGURES

LIST OF TABLES

LIST OF APPENDICES

NOMENCLATURE

Greek Symbols

α	a free parameter in asymptotic analysis eqn 1.36, Shvab-Zel'dovich variable
β	Similarity variable defined by eqn 4.3
ε	emmisivity, Tp2/Ta
Φ	equivalence ratio
λ	a free parameter in asymptotic analysis eqn 1.37, Thermal conductivity, wavelength
μ	kinematic viscosity
η	dynamic viscosity, ground state population density, Non-dimensional distance
ρ	density
σ	Stefan Bolzmann constant, kg oxygen/kg fuel
θ	rotational temperature, angle, pseudo temperature in eqn 1.41
ν	coefficient in stoiciometric equation
χ	radiative fraction
ξ	nondimensional coordinate, defined by 1.20 for inner expansion

Roman Symbols

a_{ps}	Planck mean absorption coefficient for soot radiation
A	free parameter in asymptotic analysis, eq 1.27 in Appendix 4
C	specific heat, slip coefficient in particle viscous drag force eqn 3.5 Scattering cross section, calibration constant in eqn 3.8
Cm	thermal exchange coefficient in eqn 3.6
Cs	thermal slip coefficient in eqn 3.6
Ct	momentum exchange coefficient in eqn 3.6

D63	moment of soot aggregate diameter
D	diffusivity
Da	Dahmkohler number
Df	fractal dimension for soot mass fractal aggregate
dp	primary particle diameter
E(m)	soot refractive index function
Ea	activation energy
F	force, defined by eq 2.2
F(m)	soot refractive index function
Fv	soot volume fraction
G	defined by eq 2.2
g	degeneracy
H	eigenvalue constant defined by eqn 2.3
I	laser light intensity
J	rotational quantum number for OH line
K	number of species in reaction mechanism, strain rate
k	thermal conductivity
Kext	extinction coefficient for soot
Kn	Knudsen number
m	seed particle mass
	Complex refractive index for soot
M	Molecular mass
N	number density of soot particles
n	number of primary particles in soot aggregate
Nu	Nusselt Number
q	radiation flux, energy release per mole of fuel
	As defined by eqn 3.16

Qvv	scattering coefficient
r	radial coordinate
R	radius of seed particle, universal gas constant
Re	Reynolds number
Rg	radius of gyration
T	temperature
t	time
u	axial component of velocity
v	radial component of velocity
V	diffusion velocity
w	reaction rate
W	molecular mass for 1 mole
X	length of particle track in eqn 3.3
X	mole fraction
Y	mass fraction
Z	axial coordinate

Subscripts

A	region A of outer solution, Fig 4.2
B	region B of outer solution, Fig 4.2
C	region C of outer solution, Fig 4.2
F	fuel side inlet, fuel
f	fluid velocity
FO	fuel-oxidizer coupling
g	gas
k	kth species
mid	average of value at the two inlet ports
-∞	oxidizer side inlet

n	non-premixed reaction sheet
O	oxidizer side inlet, oxidizer
p	specific heat at constant pressure
p	primary particle, particle
$+\infty$	fuel side inlet
r	rotational
soot	soot
stoic	stoiciometric flame location
t	thermophoretic force in eqn. 3.4
v	viscous force in eqn. 3.4
w	vertical-vertical scattering polarization

CHAPTER 1

INTRODUCTION

1.1 Introduction

This dissertation pertains to formation and control of soot and NOx in radiating partially premixed flames. Soot particulate emission from combustion of hydrocarbon fuels is of concern due to health and environmental concerns. NOx refers to the oxides of nitrogen. NO and NO2. Combustion sources are major contributors to NOx emissions into atmosphere. NOx emissions are of concern due to their role in ozone layer depletion. acid rain and formation of photochemical smog. Emission of particulate matter and NOx from combustion sources is regulated by environmental protection agencies and is an important design constraint for the manufactures of combustion equipment today.

Flame radiation is of interest as an important mode of heat transfer. In atmospheric pressure flames about 10-30% of chemical energy release can be transferred as flame radiation. Flame radiation consists of radiation originating from gaseous species. mainly the products of combustion like water and carbon dioxide. and radiation from soot (often incorrectly referred to as 'carbon') particulates. Understanding of flame radiation can be used to enhance heat transfer in industrial furnaces and explore mechanisms of fire spread. Furthermore. accurate accounting of radiation heat transfer from flames. is necessary for accurate prediction of flame temperature which is an important parameter for temperature sensitive NO production rates in flames.

Partial premixing refers to the technique of adding small (less than the rich flammability limit) amount of oxygen into the fuel. Partial premixing is intentionally used in practical combustion equipment for the reasons of flame stabilization and

pollutant emission control. About 30% of natural gas use is accounted for by combustion in partially premixed mode. Dibble [1]. Unintentional partial premixing can result from insufficient mixing of the fuel and air due to geometric limitations in turbulent premixed burners while in turbulent non-premixed burners unintentional partial premixing can result from the flame extinction-reignition mechanisms. Unintentional partial premixing can be either fuel side partial premixing (small quantity of oxygen added to the fuel) or oxidizer side partial premixing (small quantities of fuel added into the oxidizer). Partial premixing differs from both the more common modes of combustion – premixed combustion in which the fuel and oxidizer are homogeneously mixed before entering the burner and non-premixed combustion where the fuel and the oxidizer are unmixed. Several studies have explored the flame structure [2-5]. extinction behavior [6-7]. soot [8-21] and NOx [22-32] formation in partially premixed flames. Relevant details of the previous work and the significance of the results of the present work to the previous studies are discussed in the subsequent chapters.

Two well-defined flame configurations are commonly used for laboratory studies of partially premixed flames: (1) steady laminar co-flow flames (2) laminar counter-flow flames. Figure 1.1 shows flame photographs of partially premixed co-flow flames of Kim et al. [25]. In the axisymmetric co-flow flame shown in the figure the fuel-air mixture ejected out of a central tube surrounded by an annular flow of air. It is noticed that with progressive partial premixing, as indicated by decreasing equivalence number,ϕ, the length of the flame decreases and the existence of two reaction zones becomes evident. The fuel reacts with the premixed oxygen in the inner premixed reaction zone and the leftover excess fuel then reacts with the outer airflow in the outer reaction zone. Figures 1.2 and 1.3 show photographs of non-premixed and partially premixed counter-flow flames. In axisymmetric counter-flow flames, which is the experimental configuration used in the present study, the fuel and the oxidizer eject from two opposing jets. We notice that, Fig. 1.3, with partial premixing the 'flame' consists of two reaction zones.

The oxygen added to the fuel stream reacts with fuel under fuel rich conditions in the premixed reaction zone while the unburnt excess fuel reacts with oxygen from the oxidizer side stream in the non-premixed reaction zone. This flame configuration is convenient for experimental studies since the distribution of species, temperature and axial velocity are approximately one-dimensional in the central 'core' of the flame. This flame configuration is convenient for theoretical studies due to one-dimensionality of mass, momentum, species and energy conservation equations along the stagnation streamline as adopted in Sandia opposed flow flame code, OPPDIF [33], used in this work. Furthermore, the counter-flow flame configuration is pertinent to turbulent combustion via flamelet approach, Fendell and Marble [34].

Motivated by health and environmental concerns of soot and NOx, industry relevance of partially premixed natural gas flames and the preceding arguments for the choice of counter-flow flame geometry, an experimental and theoretical study of radiating methane partially premixed counter-flow flames was undertaken.

1.2 Specific Objectives of Present Work

The specific objectives of this investigation are to:

1) Explain the effect of partial premixing on the premixed and non-premixed reaction zone locations.
2) Study the effect of fuel side partial premixing as well as oxidizer side partial premixing on formation and emission of soot from counter-flow flames.
3) Exploit the double flame structure of partially premixed flames to control soot particulate emission and flame radiation from counter-flames.
4) Study the effect of fuel side partial premixing as well as oxidizer side partial premixing on formation and emission of NOx from counter-flow flames.

5) Study transition to sooting for methane and ethylene non-premixed counter flow flames and to obtain experimental data that may be of value for future validation of computational models of soot nuclei formation in flames.

The studies conducted in this work are focused on methane though both methane and ethylene fuels are included in the study of transition to sooting. The choice of the fuel was motivated by methane as a major component of natural gas, a commercially important fuel. Furthermore, methane is the simplest hydrocarbon for which detailed chemical kinetic mechanisms are readily available. Although the experiments were conducted on laminar counter-flow flames, the results are pertinent to turbulent combustion via flamelet approach. Implications of results from this study for other fuels and flame configurations will be discussed when such extension or generalization is possible.

Chapter 2 describes computational modeling of counter-flow flames as pertinent to a modified version, Kim [35], of the OPPDIF code [33]. The description of the counter-flow flame burner and experimental methods is included in Chapter 3. A simplified analytical model for the locations of the premixed and the non-premixed reaction zones with respect to the stagnation plane is presented in Chapter 4. Experimental data and detailed computational modeling results of soot and NOx formation in counter-flow partially premixed flames are presented in Chapters 5 and 6 respectively. The changes in energy release distribution and flame radiation resulting from partial premixing are discussed and their implication for soot and NOx formation and control are emphasized in Chapters 5 and 6. Although the emphasis of this study was on fuel side partial premixing, a brief study of effect oxidizer side partial premixing on soot and NOx formation is included. Chapter 7 describes a study of transition from blue (soot free) flames to yellow (soot containing) flames. Key results from this study are summarized and recommendations for future work are presented in Chapter 8.

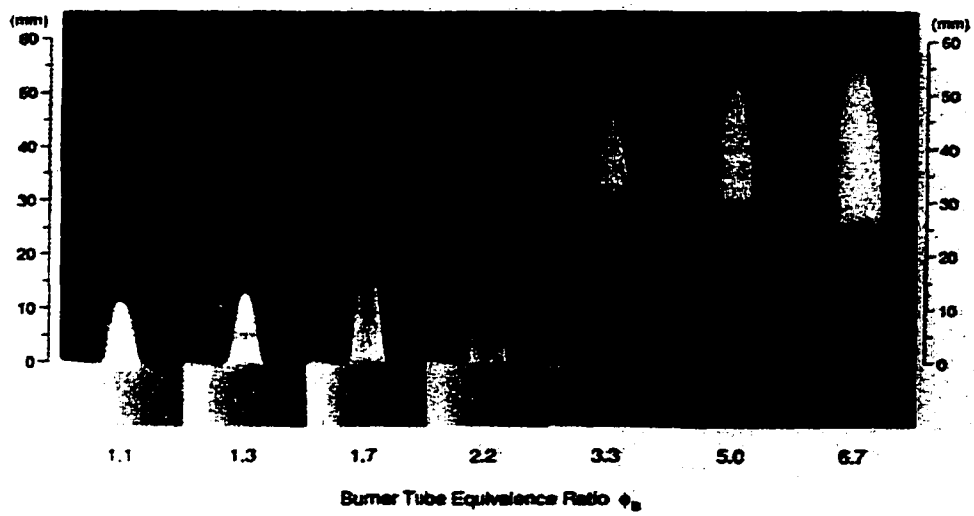

COMBUSTION SCIENCE AND TECHNOLOGY, Vols. 110-111, Color Plate II. See T. K. Kim *et al.*, Figure 3.

Fig 1.1 Co-flow laminar partially premixed flames [Kim et al., 1995]

Reproduced with Permission of Combustion Sci. and Technology

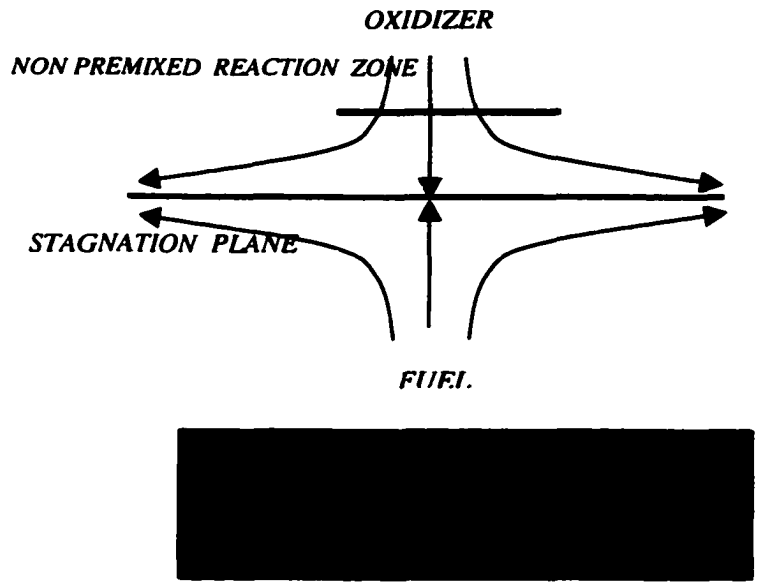

Fig 1.2 Counter-flow non-premixed flame

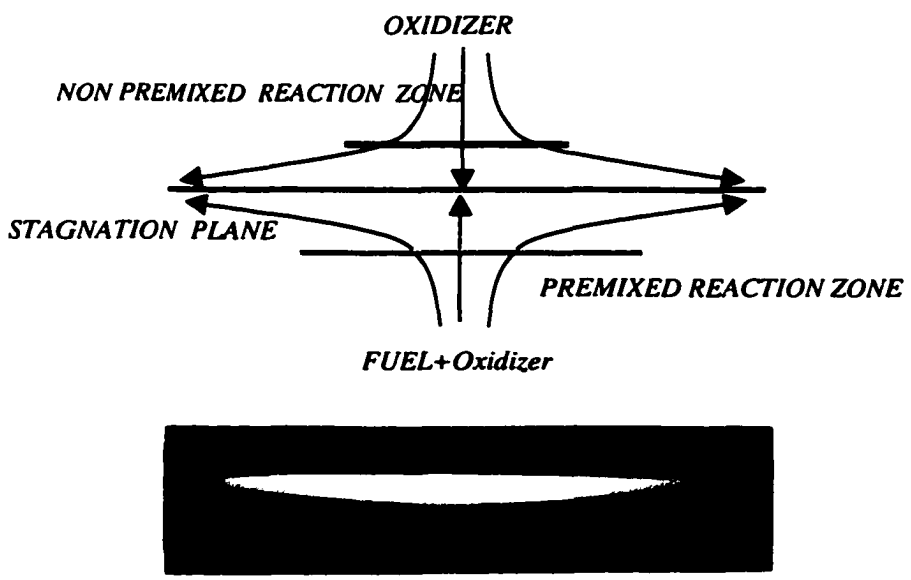

Fig 1.3 Counter-flow partially premixed flame

CHAPTER 2

COMPUTATIONAL METHODS

Sandia opposed flow flame code, OPPDIF, [33], modified by Kim, [35], to include an optically thin model for soot and gas radiation was used to gain understanding of chemical energy release, flame radiation and NO chemical kinetics in counter-flow flames. OPPDIF is a FORTRAN program that uses a similarity transformation to reduce the two-dimensional axisymmetric flow field into a one-dimensional problem. OPPDIF solves for temperature, species mass fractions, axial velocity component and radial pressure gradient, which is an eigenvalue problem for the steady state form of the discretized equations. In this chapter, the governing equations are described, with particular attention to the modification of energy equation for radiation term. Boundary conditions, initial grid selection and convergence parameters for meaningful comparison with low strain rate non-premixed and partially premixed flames are discussed.

2.1 Governing Equations

The governing equations for conservation of mass, momentum, energy and species along the axis of symmetry (z-axis) of the opposed-flow geometry, [33], are presented. The z-axis origin is located at the fuel side inlet with the positive z-direction oriented towards the oxidizer side inlet.

Conservation of Mass:

$$\frac{\partial}{\partial z}(\rho u)+\frac{1}{r}\frac{\partial}{\partial r}(\rho v r)=0 \qquad 2.1$$

where u and v are the axial and the radial velocity components and ρ is the mass density. Using the Von Karman similarity transformation, [36], (v/r and other variables are functions of z alone) we define:

$$G(z) \equiv -\frac{\rho v}{r} \quad \text{and} \quad F(z) = \frac{\rho v}{2}$$

for which the *continuity equation* reduces to:

$$G(z) = \frac{dF}{dz} \qquad 2.2$$

for the axial velocity u. Since F and G are function of z alone, so are ρ, u, T and Yk.

The *radial momentum* equation is satisfied by the eigenvalue:

$$H = \frac{1}{r}\frac{\partial p}{\partial r} = const \qquad 2.3$$

The *axial momentum* equation is:

$$H - 2\frac{d}{dz}\left(\frac{FG}{\rho}\right) + \frac{3G^2}{\rho} + \frac{d}{dz}\left[\mu\frac{d}{dz}\left(\frac{G}{\rho}\right)\right] = 0 \qquad 2.4$$

The *energy conservation* equation is written as:

$$\frac{d}{dz}\left(\lambda\frac{dT}{dz}\right) - \rho C_p u\frac{dT}{dz} - \sum_{k=1}^{K}\rho Y_k \dot{V}_k C_{pk}\frac{dT}{dz} - \sum w_k W_k h_k + \nabla\vec{q}_{gas} + \nabla\vec{q}_{soot} = 0 \qquad 2.5$$

Y_k, C_{pk}, h_k, w_k, W_k, V_k are the mass fraction, the heat capacity at constant pressure, the enthalpy, the volumetric molar reaction rate, molar mass and the diffusion velocity of the kth species. λ, ρ, C_p and u are the thermal conductivity, the density, the heat capacity at constant pressure and the convective velocity of the mixture. The last two terms in the energy equation correspond to the volumetric gas and soot radiation respectively.

The *species conservation* equation is written as:

$$\rho u\frac{dY_k}{dz} + \frac{d}{dx}(\rho Y_k V_k) - w_k W_k = 0 \qquad \text{k=1,K} \qquad 2.6$$

where the diffusion velocities are obtained using a multicomponent formulation described in [33].

2.2 Boundary Conditions

The two burner inlets for our study are 2.9 cm apart. The inlet boundary conditions included measured inlet velocity and temperature as well as species fluxes at the two inlets. The boundary conditions allow for gradients in temperature and species at the burner inlets, an important consideration for low strain rate flames.

The boundary conditions for the fuel (F) and the oxidizer (O) side inlets are:

$$z = 0.0cm: \quad F = \frac{\rho_F u_F}{2} \quad G = 0 \quad T = T_F, \quad \rho u Y_k + \rho Y_k V_k = (\rho u Y_k)_F \tag{2.7}$$

$$z = 2.9cm: \quad F = \frac{\rho_O u_O}{2} \quad G = 0 \quad T = T_O, \quad \rho u Y_k + \rho Y_k V_k = (\rho u Y_k)_O \tag{2.8}$$

The above boundary condition for energy equation may be *not* appropriate for low strain rate flames in some cases, especially when there is significant conduction heat loss from the flame to the burner. For this reason, energy equation was replaced by measured thermocouple temperature corrected for gas radiation in most of the computations reported in this work.

The differential Eqns. 2.2-2.6 and the boundary condition Eqns. 2.7-2.8 form a boundary value problem for the dependent variables F, G, H, T and Yk. The CHEMKIN library subroutines provide the reaction rates and the thermodynamic properties using a CHEMKIN based package, [33].

2.3 Gas and Soot Radiation Model

An optically thin gas radiation model as described by Kim, [35], which included contribution from CO, CO2 and H2O was used. The Planck mean absorption coefficient for gases was obtained from Abu-Romia and Tien [37] and the predictions from the model were checked with RADCAL predictions Grosshandler, [38].

An optically thin model for soot radiation was used following Atreya and Agrawal, [39]. Measured soot volume fraction distribution was specified as an input to the code for the computing the volumetric soot radiation term as:

$$\nabla \vec{q}_{soot} = 4\pi a_{ps} \sigma (T^4 - T_{mid}^4) \tag{2.9}$$

The value of Planck mean absorption coefficient for soot, a_{ps}, suggested by Atreya and Agrawal, [39], $a_{ps} = 11.86 f_v T \ cm^{-1}$ was used. f_v and σ are the soot volume fraction and the Stefan-Boltzmann constant. It was assumed that soot was at the gas temperature and exchanged heat by radiation with surrounding at a mean temperature, T_{mid}, considered to be the average of the two inlet port temperatures. This is a reasonable approximation as the temperature of the soot is considerably larger than the mean surrounding temperature. Although gas radiation is important in low strain rate flames, [33,40], in the flames typical of those in this study the contribution of gas radiation is less than 10% of the net chemical energy release and soot radiation contribution is typically smaller than that of gas radiation for the soot loading encountered in these flames. The treatment of gas and soot radiation outlined above is considered adequate for the present discussion of the effect of partial premixing on enhancement of soot and gas radiation in counter flow flames. Further details of treatment of radiation models are included elsewhere [35,39].

2.4 The choice of initial guess and convergence parameters

The solution was checked for dependence on the choice of the initial grid and convergence parameters. It was found that some knowledge of location of the flame is useful in obtaining convergence. In this regard, either an experimentally measured temperature or a converged temperature distribution solution for a previous similar flame makes for a good initial guess. The code has adaptive grid generation subroutines and adapts the initial grid to best suit the computational needs. In the case of partially premixed flames, it is beneficial to have an initial guess with at least 3-4 points around the place where the premixed reaction zone is observed in the experiment. When such experimental knowledge about the flame is not available, it was helpful to start with an initial guess of a previously computed solution of a non-premixed flame from which the partially premixed flame has been obtained.

CHAPTER 3

EXPERIMENTAL METHODS

The experimental methods are described in this chapter. While the counter-flow burner facility described here is identical to the one reported in previous work [35,41-44], the diagnostic techniques have been either thoroughly revised, in almost all the cases, or newly developed.

3.0 Counter-Flow Burner

Steady, laminar non-premixed as well as partially premixed flames were aerodynamically stabilized in the opposing flows of fuel and oxidizer in a unique low strain rate (5-15 sec^{-1}) axisymmetric counter-flow burner designed and constructed by previous workers [35,41-44]. A schematic diagram of the burner is shown in Fig. 3.1. Two circular inlet ports were located 2.9 cm apart. The areas of the two ports were 24.8cm^2 for the top port and 25.4 cm^2 for the bottom inlet port. The burner was equipped with several ports for inserting measurement probes and glass windows for optical diagnostics. The central 1 cm diameter 'core' cylindrical region of the burner has small radial variation of axial velocity, Mungekar and Atreya [45], species and temperature.

The gases used were of chemical purity grade (99.7% or better) and the gas flow rates were monitored using calibrated sonic orifices and rotameters (measurement error of ±1%). The inlet ports were made out of ceramic honeycombs, which insured straightening of the flow lines at the two burner inlet ports. The burner was equipped with flanges for the two inlet ports, designed on the basis of viscous streamline experiments of low strain rate opposed jet flows as described by Lee [44]. Due to these flanges a portion of the flame, approximately 7-8 mm distance in the axial direction from either inlet ports,

was not accessible by optical diagnostic techniques as discussed by Kim [35]. Several workers. [31.46]. have acknowledged difficulty in stabilizing low strain rate counter-flow flames. With careful selection of inlet flows and burner design. as outlined below. steady laminar low strain rate flames were established. The burner had the capability for an annular shroud gas flow. which was seldom used. as most flames were stable without the need for a shroud gas. A concentric screen around the burner protected the flame from disturbances in the room air. Appropriate use of diluents. for instance helium for the top inlet port and a heavy inert species for the bottom inlet port. insured buoyant stabilization. The exhaust gases flowed out in the annular space surrounding the burner to an exhaust hood equipped with an exhaust fan. Heating of the shroud surround this annular space using hot water facilitated the upward flow of exhaust gases.

A lighted cotton swab ignited flames. Previous work indicated that about two hours of time was sufficient to reach steady state conditions when starting with a cold burner at the room temperature. Soot deposits from the burner flanges were cleaned from time to time to ensure identical burner geometry for all the experiments. Occasional cleaning of the ceramic honeycombs was also performed to insure uniform inlet flow.

The burner was mounted on a precision vertical traverse. The vertical position of the burner was recorded with an electronic position-sensing device with a least count of .01mm although the accuracy of the burner position could be reported only within ±0.1mm due to accuracy of the vertical positioning mechanism. In this regard. the burner was traversed only in one direction when making axial distribution measurements, to avoid backlash error resulting from the burner traverse.

In a low strain rate burner, the gradients of temperature and species at the inlet ports can be significant. The modeling of boundary conditions for species and energy flux has been discussed earlier in Chapter 2.

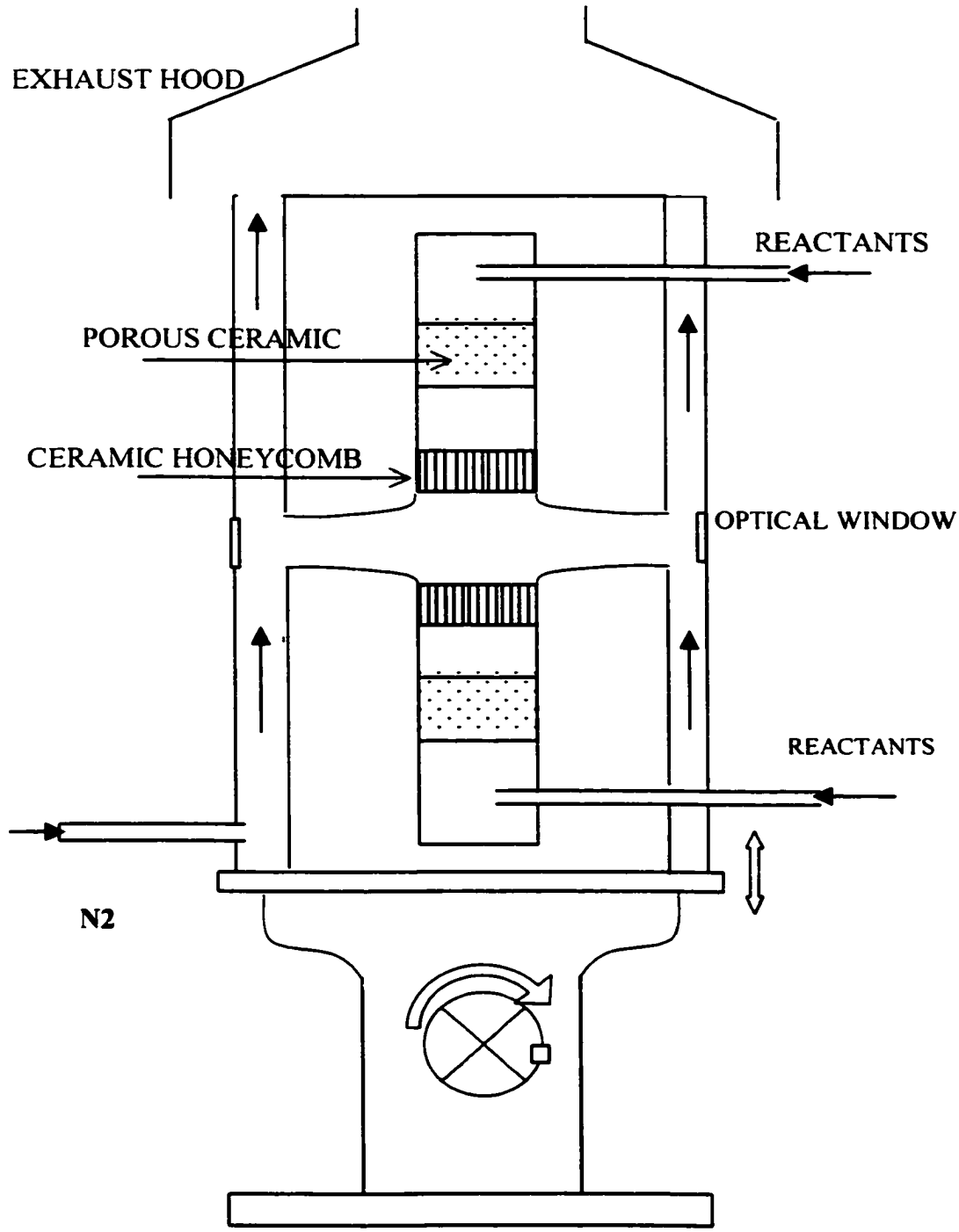

Fig 3.1 A schematic diagram of the counter-flow burner

3.1 Probe Sampling of flame gases and NO chemiluminescent Analysis

Introduction

Counter-flow flame configuration is an ideal geometry for computational modeling of NO kinetics since the problem is one-dimensional along the stagnation streamline. Until recently, when laser based diagnostic tools were not routinely used, limited experimental measurements, [35,41,47-48], of NO in counter-flow flames were available to validate the computations. While some of the recent in-situ laser based measurements of NO have shown error bars in excess of ± 10%, the previous ex-situ measurements had concerns regarding sampling errors.

Concerns regarding extractive NO sampling and analysis have been addressed in the past by several workers, [49-54]. These studies have highlighted the importance of probe design, sonic sampling and NO sample distortion resulting from reactions in the sampling system. Amongst the concerns raised before were NO→NO2 conversion via reactions with HO2 radicals, Hori [53], interaction of NO and hydrocarbon species in the sampling system, Jaasma and Borman [51], and NO to NO2 conversion on hot metal surfaces, Scire et al., [54].

In addition to the above concerns, concerns specific to the counter-flow flame configuration include identification of the central one-dimensional region of the flame and development of a technique for NO sample analysis on wet-basis using NO chemiluminescence analyzer. Previous studies have either encountered unrealistically broadened NO profiles, Drake and Blint [48], due to large sampling rate used to meet the sample size requirement of the NO analyzer or have performed analysis of NO on dry basis. The wet-analysis of NO sample from the flame is not routine due to condensation of water on cold surfaces of NO analyzer.

An investigation of sampling and ex-situ analysis of NO concentrations in counter-flow flames is reported. NO samples collected using a quartz microprobe were

analyzed on wet-basis using a novel sampling system and a chemiluminescene analyzer. Effects of the probe size and probe positioning on the measured NO concentration are discussed. NO→NO2 conversion in the sampling system was not detected within the measurement accuracy of the instrument. Problems pertinent to sampling and NO sample distortion in the sooty regions of flame are also discussed. Comparison of present ex-situ measurements with recently published in-situ measurements showed good agreement for peak NO concentration.

Experimental methods

Gas samples were collected from the flame using a quartz microprobe. Several quartz microprobes with different inlet diameters and tip shapes considered for selection of an appropriate probe for extractive sampling are shown in the Fig. 3.2. The samples were collected in an evacuated metal cylinder through stainless steel sampling lines with sampling pressure below –20"Hg (34kPa absolute) to ensure sonic conditions at the probe. Allen, [49], has emphasized the need for sonic sampling to quench the reactions in the sampling system. The probe, the sampling lines and the sample collection cylinder were heated to 70-100 °C to prevent condensation of water from the sample. The sample collected in the metal cylinder was pressurized and diluted about five to ten fold with nitrogen. The dilution of the sample with nitrogen was necessary to prevent condensation of water in the sample on cold surfaces of the NO analyzer for subsequent measurement of NO concentration. The diluted and pressurized sample was analyzed using a NOx chemiluminsecene analyzer (Model 42H from Thermo-Environmental Inc.). The NOx analyzer was calibrated using known samples of NO and its linearity was checked for the range of NO levels encountered in this work. The NO analyzer had a least count of 0.01ppm for detection of NO and NO2. Typical systematic uncertainty in measurement of a 50ppm NO sample at a five-fold dilution (with N2) was about ± 2 ppm, though the repeatability of measurement was much better. This error estimate does not include uncertainties due to probe distortion or sample distortion effects. Calibration of the NOx

analyzer was performed before and after every experiment to ensure the validity of the calibration during the experiment. Further details of the sampling system are described by Herding. [42].

The specifications of the two flames used in this study are given in Table 3.1. Flame 4. Atreya et al. [41], was a sooty methane flame with the peak flame temperature on the fuel side of the stagnation plane while the second flame was a blue methane flame with global strain rate and inlet composition identical to the "5 sec^{-1} methane flame" used by Ravikrishna and Laurandeau. [46]. While the previous authors were unable to stabilize our low-strain rate flames without difficulty. the flames selected in this work could be stabilized without any shroud gas flow.

Results and Discussion

Probe Positioning

The central 'core' of a counter-flow flame is the region where the distribution of species and scalar variables is approximately one-dimensional with a small variation in the radial direction. Measurements were confined to this one-dimensional region for comparison with computational modeling of flames.

The central one-dimensional core of the flame was identified as the 1cm diameter cylinder centered around the burner axis on the basis of radial distribution of flame temperature. Fig. 3.3. and previous experimental confirmation, Mungekar and Atreya [45], of one-dimensionality of the axial component of velocity in this region. Typical temperature difference between the centerline temperature and that measured at radius of .5 cm was less than 15 K as shown in Fig. 3.3. Measurement of NO concentrations of gas samples extracted from different radial locations for the same axial distance from the fuel side inlet showed a small change (within the repeatability of the experiment). To minimize the disturbance to the flame flow-field the probe was aligned along the radial direction in the plane perpendicular to the burner axis with the probe tip located between 3-5mm from the burner axis.

Probe Size

One of the primary concerns in probe sampling of flame species is the limitation on the spatial resolution due to finite size of the probe. This is critical for NO concentration distribution measurement in hydrocarbon fuel counter-flow flames where the gradient of NO concentration on the fuel side of the NO peak is sharp due to NO reburn reactions. While probes with small inlet orifice size are desirable for minimizing spatial distortion. this also results in an increased sampling time. For sonic sampling. to collect the same amount of sample. the increase in the sampling time is proportional to the square of the inlet orifice diameter of the probe. Three quartz probes with inlet orifice diameters of 40μm. 70μm and 200μm were used to sample NO from the sooty flame. Measured NO concentration profiles in the sooty flame are shown in Fig. 3.4. There is very good agreement between the peak values measured with all the three probes. While the difference in the measured NO concentration profiles using the 40μm probe and the 70μm probes is small. the 200μm probe was unable to adequately capture the sharp gradient in NO concentration on the fuel side of the NO peak. On the basis of above experiments 70μm probe was selected for further experiments. The repeatability of the NO measurement was excellent as indicated by the NO profile measured using 40μm probe and the 70μm probe in the Fig. 3.4.

Soot deposition in the Probe

In and near the sooty regions of the flame soot deposition in and around the probe tip can be observed in some cases. Furthermore, soot precursor particles can condense on the inner walls of the probe. Jassama and Borman, [51], report that significant absorption of NO on soot may affect measurement of NO emissions. We have noticed a small 'valley' in the NO concentration profile in sooty flames at the onset or within sooty zone that may be attributed to such aberrations due to NO absorption by soot. For instance, there is a small dip in the NO concentration profile on the fuel side in the Fig. 3.4 for the

measurement reported using 40μm probe. The sampling time was the maximum for this probe amongst the three probes and such probe distortion affects were expected to show up more for this probe. Such a dip in NO profile was not noticed for blue hydrocarbon flames or hydrogen flames. Soot deposition can be minimized by working with small sample size in the sooty regions at the expense of increase in experimental uncertainty resulting from larger dilution prior to analysis by NO analyzer. Another technique that can be adopted is to oxidize the deposited soot and soot precursors by moving the quartz probe to the oxidizing region of the flame prior to every new sample collection in the sooty region. There was no evidence of any chemical adsorption/loss of NO on the walls of the sampling lines when samples with known amount of NO were sampled and analyzed through the sampling system.

NO → NO2 conversion

Computed peak NO2 concentration in the sooty flame was about .1 ppm. We did not find any NO2 within the accuracy of the experiment indicating that NO→NO2 conversion was insignificant in these measurements. Recently, Scire et al., [54], concluded that NO→NO2 conversion over hot metal surfaces was not significant on the basis of comparison of in-situ absorption based NO measurement and measurements based on extractive sampling followed by analysis using a chemiluminescent NO analyzer.

Comparison with Computations and In-situ Measurements

The "Blue-Ravi" flame was a diluted methane-air flame with inlet compositions, velocity and temperature boundary conditions as shown in Table 3.1 has identical global strain rate (defined as the sum of inlet speeds divided by the burner gap) and inlet compositions at the "5 sec-1 methane flame" of Ravikrishna and Laurandeau, [46]. In-situ laser based measurement of NO distribution for this flame was reported recently, [46], with peak NO concentration of 43.0. The NO distribution measured in this study using ex-situ measurement is shown in Fig. 3.5. The peak value (42.2 ppm) of NO

measured by the extractive sampling followed by chemiluminesce analysis agreed well with the peak NO (43.0 ppm) reported in the previous work. [46]. Before we compare the NO distribution profiles from the two studies it needs to be emphasized that the inlet port separation for our burner (2.9cm) was different from one used (2.0 cm) in the previous work. [46]. Observation of previous data shows that computed temperature. Fig. 1 in reference [46], and NO distribution for their flame was broader than their measured data. indicating that the global strain rate reported by the authors and the boundary conditions used for OPPDIF computations may have been under-estimated if the authors did not use the measured inlet temperature boundary conditions which can be different from cold flow burner inlet boundary conditions due to heating of the inlet ports. The NO profile measured in this work is broader than the measured NO profile in the previous work. However, the agreement between the measured and computed widths of NO and temperature distribution in this work is better than reported for the previous in-situ measurements. [46].

An important question that pertains counter-flow flame specification, particularly those with low strain rate, is the validity of the global strain rate to provide a complete and accurate description of the thermo-fluid field. For the same global strain rate and inlet compositions, one can have different flames with the peak flame temperature either closer to the fuel side inlet or the oxidizer side inlet resulting in preheating of either the incoming fuel or the oxidizer.

The location of measured and computed NO peaks agreed well, Fig.3.5. GRIMech2.11 under-predicted NO peak concentration while GRIMech3.00 over-predicted the peak NO concentration. The temperature and velocity distribution computed using the two mechanisms was identical indicating that the differences in the chemical kinetic rates for NO in the two mechanisms, rather that different temperature and velocity distributions, are responsible for the difference in NO prediction by the two

mechanisms. Both mechanisms showed a sharper gradient on the fuel side than the experimental data.

The following are the key conclusions from this study:

1. Sonic sampling, small (70μm in this study) probe inlet diameter and positioning of the probe tip in the central 1-dimensional core of the flame are recommended for extractive sampling of NO in counter-flow flames.

2. NO→NO2 conversion in the sampling system was found to be insignificant.

3. The peak NO measured in the blue flame using extractive sampling followed by chemiluminescent analysis agreed well with in-situ laser based measurement reported in literature for a flame with identical inlet compositions and global strain rate. [46]. The disagreement in the with of the NO distribution from the ex-situ and the in-situ measurements may be due to under prediction of strain rate in the previous work rather than due to inadequate spatial resolution of the profile in the ex-situ measurements. Validity of the global strain rate to adequately define the flame flow-field needs further investigation.

4. While the location of NO peak in computations and measurement agreed, GRIMech2.11 under predicted peak NO concentration while GRIMech3.00 over predicted peak NO concentration.

	Fuel Side	Oxidizer Side
Flame 4.0	Global Strain Rate =7.21 1/sec	
	78.7%N2+21.2%CH4 V=8.78cm/sec. T=662K	47.8%He+52.2%O2 V=12.13cm/sec. T=682K
Blue-Ravi	Global Strain Rate =5.44 1/sec	
	25.8%CH4+74.2%N2 V=3.7cm/sec. T=596K	Dry Air V=12.1cm/sec. T= 400K

Table 3.1. Specifications of the flames for NO Measurement study

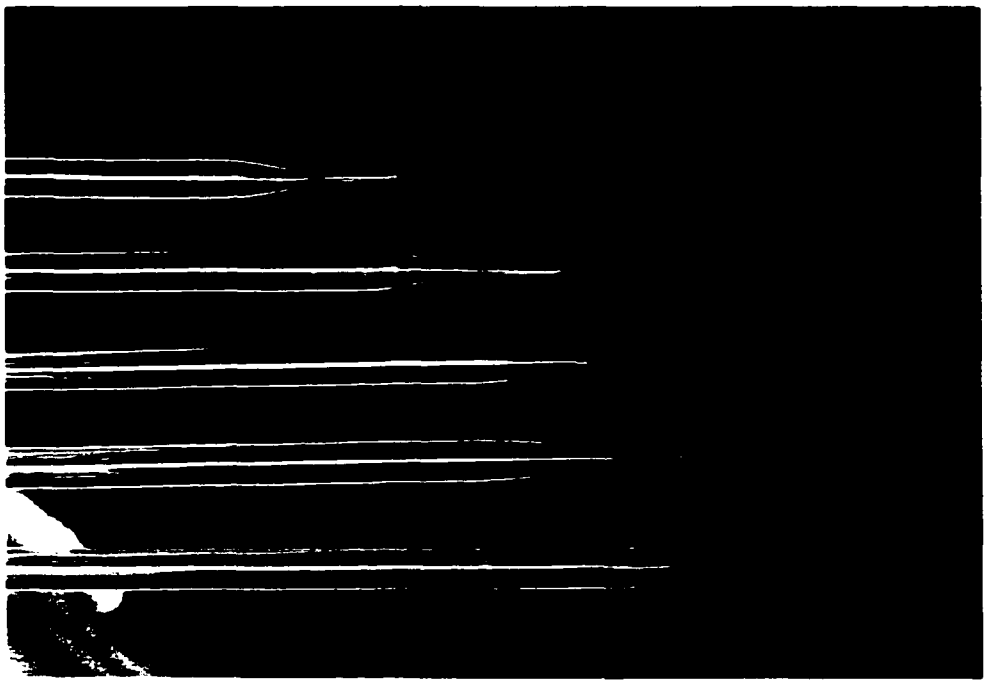

Fig. 3.2 Quartz probes with different tip shapes and inlet orifice sizes

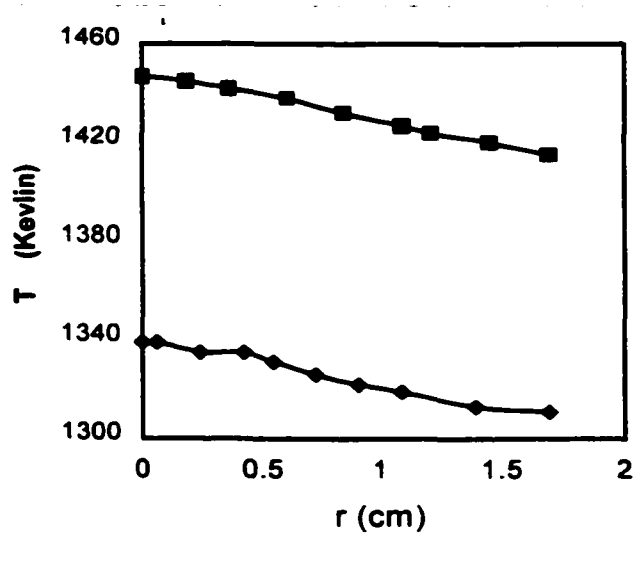

Fig 3.3 Radial distribution of the measured temperature

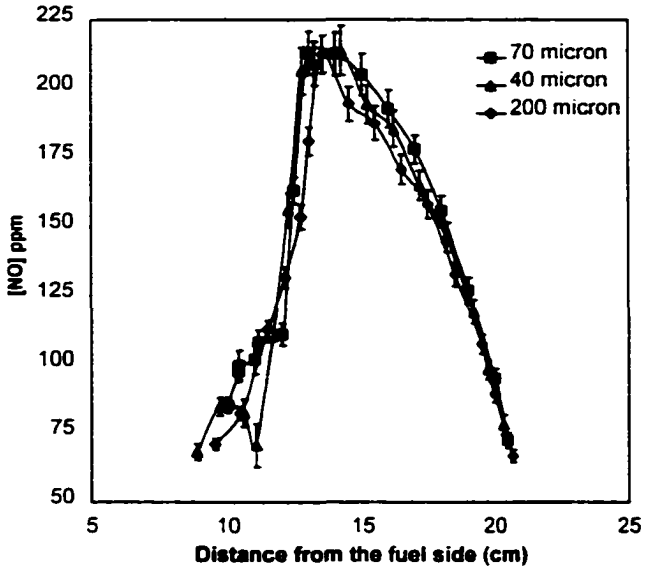

Fig. 3.4 Effect of probe size on the measured NO distribution in Flame 4.0

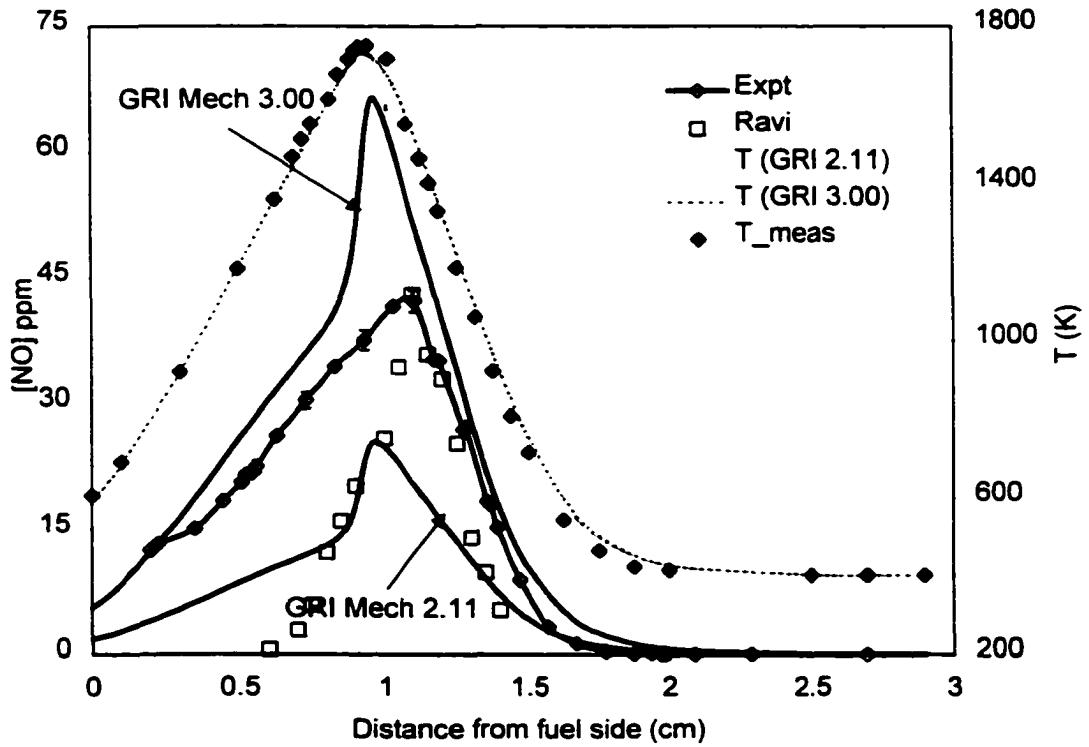

Fig. 3.5 Comparison of measured and computed temperature and NO distribution in the 'Ravi-Blue Flame'

3.2 Gas Chromatographic Analysis

Probe based sampling followed by gas chromatographic analysis on wet-basis was performed for major stable species including CH4, O2, CO, CO2, H2, H2O, N2 and He as well as for C2 hydrocarbons including C2H6, C2H4 and C2H2. Typical errors in measurement of major species are estimated to be about ± 5% except for water where larger errors resulted due to limited calibration standards and polar nature of the water molecule. The design of the sampling system and the sampling procedure has been described in detail by Kim, [33].

Using heated quartz probes of 70μm inlet diameter: gas samples from the central 1-dimensional region of the flame were withdrawn through heated stainless steel line into a heated sampling system where the sample was pressurized and distributed to three gas chromatograms at atmospheric pressure. The first gas chromatogram used Helium as a carrier gas with thermal conductivity detector (TCD) based analyzer to analyze all the major stable species with the exception of Helium. The second gas chromatogram employing Nitrogen as a carrier gas was dedicated to analysis of Helium using a TCD detector. Another gas chromatogram employing flame ionization detector (FID) was used for detection of minor hydrocarbon species, in this case C2 hydrocarbons. All the G.C.s had programmable oven temperature with facility for back-flushing (reversing the flow of carrier gas) though an elaborate system of air-actuated valves.

The voltage signals from the G.C.s were recorded using a PC based data acquisition system. Figure 3.6 shows a sample gas chromatogram for the major species. The area of peaks was identified using best-fit curves using a commercial (PeakFit software, Jandel Corp) curve-fitting program. The gas chromatogram calibration was performed using standard calibration gas samples. A detailed calibration was performed before a set of experiments and a limited calibration was performed prior to and after

G.C. analysis experiments to insure the validity of detailed analysis. Fig. 3.7 shows linearity of calibration for methane over the range of concentrations of interest.

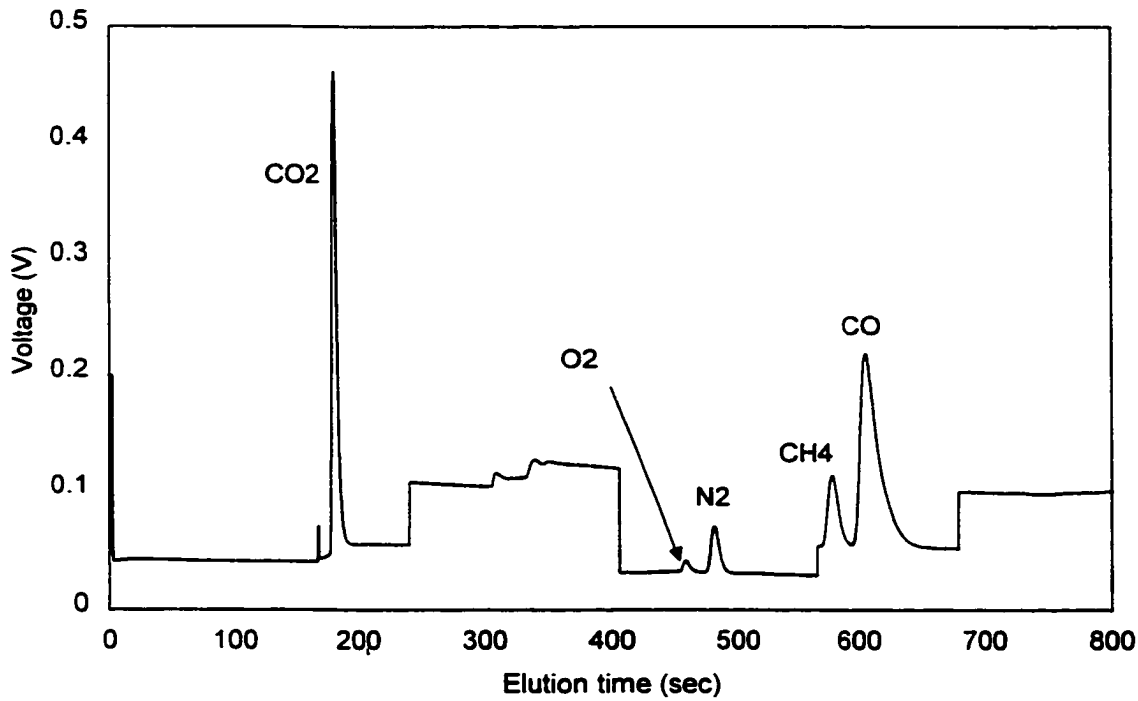

Fig 3.6 A sample gas chromatogram showing major stable species

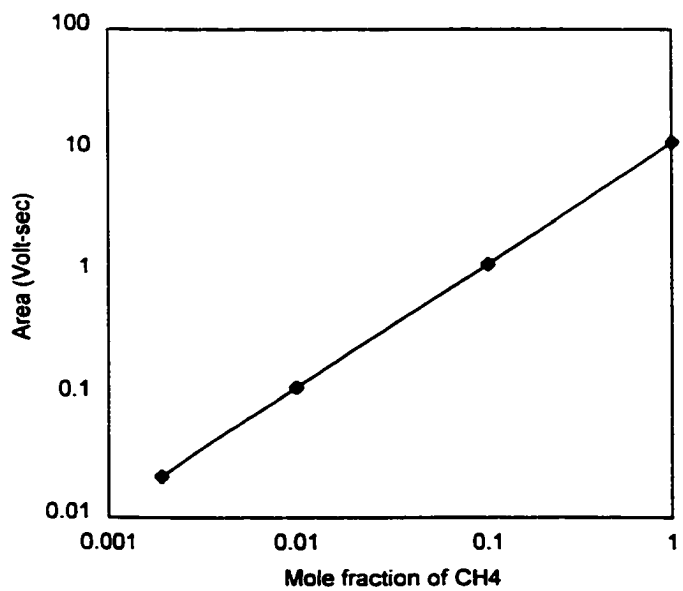

Fig. 3.7 Linearity of the calibration for methane

3.3 Temperature Measurement using SiO_2 coated thermocouples

Thermocouple based temperature measurement in counter-flow flames is described with particular attention to the use of SiO2 for coated thermocouples to prevent catalytic reactions and correction of the temperature measured using the thermocouple for radiative losses in order to infer the flame gas temperature.

Positioning of the thermocouple

The thermocouple wires were shaped in form of a loop and placed in the central 1cm diameter core of the burner, identified as the region with small radial variation of temperature and flow-field identified in previous experiments. The plane of the loop is oriented perpendicular to the burner axis, thereby minimizing heat loss by conduction to the thermocouple wires.

The thermocouple was rigidly mounted on a platform that could be traversed in the direction of the burner axis. A calibrated potentiometer was used to track the vertical position of the thermocouple. Linearity of the potentiometer response was confirmed. The data from the potentiometer and the thermocouple voltage was digitally recorded using a PC based data acquisition system.

SiO Coating

It is a common practice, [57,58], to coat the thermocouples to prevent catalytic reactions on the thermocouple surface. Thermocouple loop was coated with SiO2 to prevent catalytic reaction on Pt alloy surfaces in the flame environment. A uniform translucent coating, 5-6 μm thick (as observed under a calibrated optical microscope 10X optical, 16X digital magnification), was deposited on the thermocouple wire by several passes of the thermocouple loop through a natural gas Bunsen burner flame seeded with Silicone oil (Dow Corning, Polymethylsiloxane, 200 centistokes viscosity). Figure 3.8 shows a photograph of a .008" diameter Pt wire with translucent coating as observed

under an optical microscope. Kent. [58]. has reported that silica present in the thermocouple sheath may bring about the formation of embrittling silicide at higher temperature. Coated thermocouple did not show any evidence of catalytic reaction even when exposed to temperatures 30-40 K lower than the melting point of the thermocouple wire indicating that the effect of reaction of SiO2 with Pt. if such a thing does exist near melting temperatures. did not affect the thermocouple voltage beyond the repeatability of measurement (10K).

Radiation Error Correction

The thermocouple bead receives heat from hot gases by convective heat transfer and cools down by conduction heat transfer along the thermocouple wires and by radiation heat transfer to the surroundings. Pagni et al. [59] and Heitor and Moreira [60] have discussed conduction heat transfer from the thermocouple bead. With steady state temperature assumption and neglecting conduction heat transfer to the thermocouple wires. the energy balance for the thermocouple bead can be written as:

$$h(T_g - T) = \sigma\varepsilon(T^4 - T_{mid}^4) \qquad (3.1)$$

where h,σ and ε are the convective heat transfer coefficient, the Stefan-Boltzman constant and the emissivity of the coated thermocouple. T, T_g and Tmid are the temperatures of the thermocouple, the surrounding gas and the average of the temperature of the two inlet ports. It is a reasonably good assumption that the two inlet ports represent almost 100% of the viewfactor of the thermocouple bead to the surroundings.

With the knowledge of the heat transfer coefficient, the emissivity of the coated thermocouple and the burner inlet port temperatures one can infer the gas phase temperature from the temperature of the thermocouple bead.

Convective heat transfer coefficient

For a small spherical bead of diameter D. in the limit of low Reynolds number. $\mathrm{Re}_D \to 1$. the Nusselt number. $Nu_D = \frac{hD}{k} \to 2$.

Actual thermocouple bead is not exactly spherical in shape. Figure 3.9 shows an image of a thermocouple bead. typical of those commercially available. The actual bead was closer to an oblong ellipsoid rather than a sphere. As a result. a small error may be committed in using Nusselt number for a sphere. The "diameter" for the bead was estimated by averaging several measured dimensions of the bead viewed under an optical microscope. Using the bead 'diameter' and multi-component gas thermal conductivity estimated on the basis of computations with Sandia opposed flow flame code.OPPDIF. one can estimate the heat transfer coefficient. h.

Emissivity of SiO2 coated Pt/Pt-alloy bead

The remainder of this section is devoted to progress made in an ongoing effort. (Zhang et al. [61], [35.43]), to obtain emissivity of SiO2 coated Pt/Pt-alloy bead. especially at high temperature. The following discussion is pertinent to Pt/Pt-alloy thermocouples with SiO2 coating as described before.

The objective of this study was to extend the emissivity data from the previous work to the upper limit of usability of S-type (Pt/Pt-10%Rh) thermocouples reported as ~ 2000 K for short-term exposure by the thermocouple manufacturer (Omega Temperature Catalog, p. H-11,1999,[62]) .

Temperature distribution along the burner axis was measured in two diluted hydrogen-oxygen flames. for which the flame specifications are given in Table A1.1, using SiO2 coated S-type .008" wire thermocouples. Using the measured burner inlet temperatures. thermocouple bead "diameter" and computed distribution of the gas temperature and thermal conductivity, the temperature dependent emissivity of the coated

thermocouple bead was estimated using equation of energy balance for the thermocouple bead. Details of this work are included in Appendix A1

Figure 3.10 shows the new emissivity data for the coated thermocouple (hollow symbols) along with previous data (solid triangles) reported by Zhang et al., [61]. The trend in emissivity of the coated thermocouple was described by the following second order polynomial fit to the experimental data.

$$\varepsilon(T) = 4.75\times10^{-8}T^2 - 3.80\times10^{-4}T + .900 \qquad (3.2)$$

where 300<T<2000K is the temperature of the thermocouple in Kelvin. It is observed that the emissivity decreases with temperature. For coated substrates, both increasing and decreasing trends have been reported by Siegel and Howell [63]. They observe that the radiative properties are influenced by the temperature and spectral characteristics of the underlying material (substrate) when the coating is rather thin. We will compare the observed trend for SiO2 coated Pt/Pt-Rh thermocouple emissivity with that for the uncoated metal and the dielectric oxide coatings. For Pt, Pagni et al. [59], and Pt-10%Rd alloy, Toloukian and Dewitt [64], the total hemispherical emissivity increases with temperature as shown in Fig. 3.10. The emissivity of the uncoated metal is considerably smaller than that of SiO2 coated thermocouple at all the temperatures considered. The trend for total emissivity for SiO2 as a function of temperature could not be found in literature. However, for Zirconium oxide, the reported trend, Siegel and Howell, [63], indicates that for Zirconium Oxide the total emissivity first decreased, reaching a minimum around T~1500K followed by a small increase in the emissitivity as the temperatures approach 2000K.

As discussed before, and shown in Fig. 3.10, the emissivity of the uncoated thermocouple is smaller than that of the coated thermocouple by 30-40% at flame temperatures. Therefore, the SiO2 coating lowers the temperature of the bead due to increased radiation heat transfer as compared to an uncoated bead. Consequently, the

radiation error between the thermocouple temperature and the gas temperature is more for a coated thermocouple. While the lower temperature of SiO2 coated bead increases the radiation error, it is advantageous in high temperature (typ~2400K) flames where an uncoated thermocouple bead would melt (melting point ~2040K). Systematic uncertainty in the new data reported in Fig. 3.10 is estimated as, Appendix A1, at least ± 20-30%. Further details of uncertainty analysis and the technique for obtaining SiO2 coated Pt/Pt-10%Rh thermocouple emissivity are included in Appendix A1.

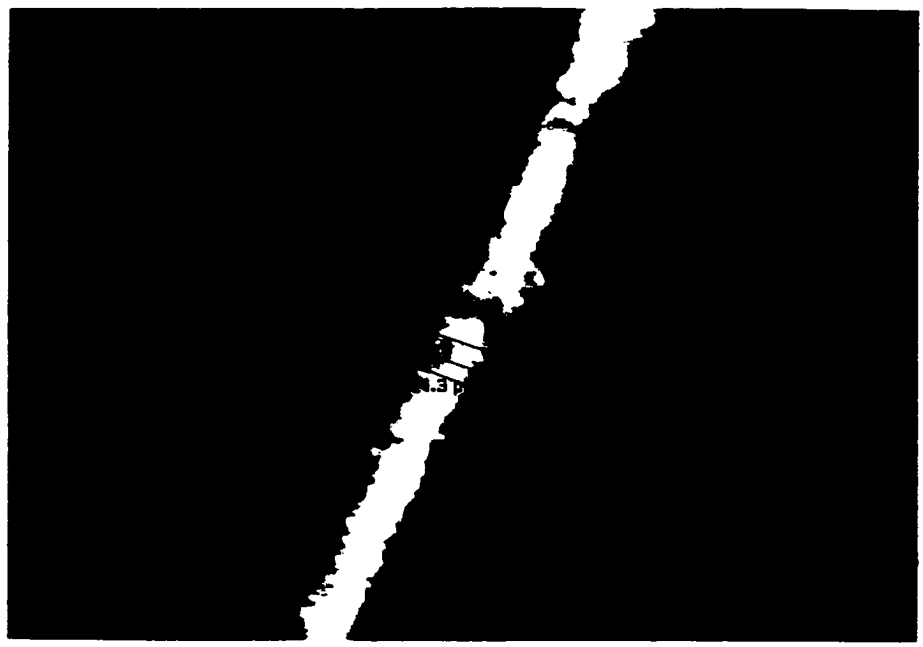

Fig. 3.8 An optical microscope photograph of a coated .008" thermocouple wire

Fig. 3.9 An optical microscope photograph of a thermocouple bead

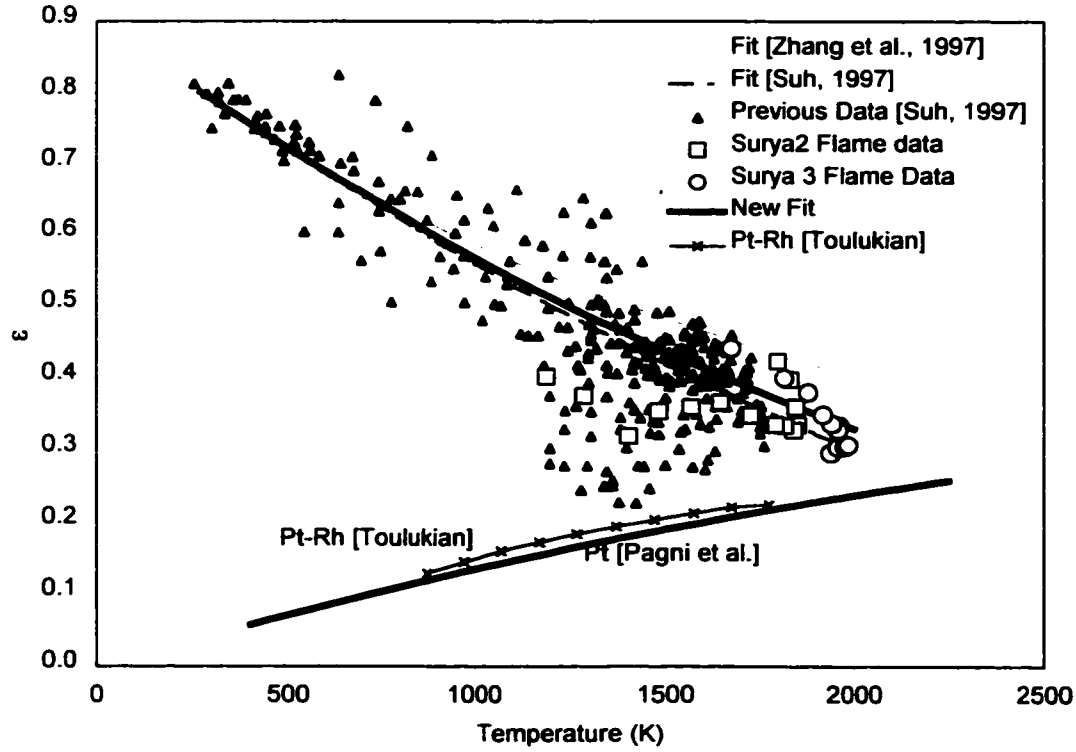

Fig. 3.10 Dependence of emissivity on temperature for SiO2 coated Pt thermocouple

3.4 Flow visualization

The discussion of the flow visualization and particle track velocimetry technique described here is a condensed version of the work previously reported by Mungekar and Atreya, [45]. A laser based particle track imaging technique has been developed and applied to flow visualizations in sooty and nonsooty methane counterflow diffusion flames (CFDF). To the best of our knowledge these flow visualizations have revealed the first visual proof of the existence of sooty methane flames on the fuel side of the stagnation plane. A comparison of the experimentally determined particle velocity with the computed gas phase velocity along the stagnation streamline showed that the thermophoretic forces on the seeding particles should not be neglected while interpreting the results from flow visualizations in flames with low strain rate. These experiments also revealed that the axial component of velocity varied little within the central 1cm diameter cylindrical region around the burner axis.

Experimental Methods

Steady, laminar flames were aerodynamically stabilized between two opposing axisymmetric jets of fuel and oxidizer using the counter-flow burner facility described earlier. A schematic of the flow imaging setup is shown in Fig. 3.11. An Ar+ ion laser beam at 514.5 nm was collimated to 1 mm diameter and then expanded to a 1 mm thick vertical laser sheet by using a cylindrical lens. The sheet was aligned along the burner diameter as shown in the figure. The laser beam was chopped at a known frequency (about 50 Hz) using a mechanical chopper. Close-up still photography equipment was carefully aligned to focus on a graph sheet with 0.2inch × 0.2inch grid placed in the plane of the laser sheet within the burner. The depth of field was about 1 mm for near unity magnification. This insured focusing the camera to the plane of the laser sheet and also gave the calibration scale for quantitative measurements from the flow visualization photographs. The datum for distance from the bottom burner port was fixed using a photograph of a quartz glass mirror with its reflecting surface placed on the lower inlet

port. The height of the quartz glass mirror was measured using Vernier calipers. MgO particles were seeded into the flow using less than 2 cc/sec of Argon gas flow. Detailed simulations with the OPPDIF code, [33], showed negligible impact on the velocity along the stagnation streamline due to the seeding flow. Furthermore, identical location of stagnation plane was obtained whether the flow was seeded from the top side or from the bottom side.

The average MgO particle size was estimated to be about 10 μm. The longest dimension of the MgO particles observed under a microscope was less than 20 μm. On the basis of the calculated axial velocity with the OPPDIF code an exposure time of 1/8 sec sufficed to get the particle tracks over the field of most flames for this study. Actual exposure time of the scattered light from the particles was fixed by the chopper speed. ASA 800-1000 film speed was found to be appropriate for laser beam powers between 500-1000 mW.

To superimpose the blue flame luminosity or the yellow orange soot luminosity double exposed pictures were taken. In the first exposure particle tracks were recorded with a green filter. In the second exposure, of a significantly shorter duration, only blue luminosity or yellow orange soot luminosity was superimposed on the flow field recorded in the previous exposure.

For quantitative measurements of the particle velocity the photographic images were digitized using a negative scanner with a resolution of approximately 90pixels/mm of the film. Calibration of pixels to the physical distance was made with the photograph of a known size grid. Digitized photographs were analyzed using an image processing software to measure the length and the direction of the particle tracks. Information from many such photographs was assimilated to obtain the variation of the axial component of the velocity of the particles lying in the center 1cm diameter core about the burner axis of symmetry. Comparison of experimentally obtained axial velocity in the core with

computed particle velocity along the stagnation streamline was used to ascertain one dimensionality of the axial velocity within the core of the flame.

Quantitative measurements of velocity are reported for a non-sooty flame (the Blue Flame in [41]). The error in the quantitative measurement of the particle velocity arises from the error in measuring the length of the streaklines ($\Delta(\delta x) = \pm$ 10 pixels) and the error in the chopper frequency. This error is estimated as:

$$\Delta v = \frac{\Delta(\delta x)}{\delta t} + \frac{\Delta(\delta t)}{\delta t}\frac{\delta x}{\delta t} \qquad (3.3)$$

The error in $\Delta(\delta t)/\delta t$ due to the error in the chopper frequency is estimated to be about ± 0.01. Neglecting the error in the chopper speed, the lower bound on the error in velocity, Δv, is at least $\pm$ 0.5 cm/sec. The length of the streaklines decreases as the particles approach the stagnation plane. So, the % error in axial velocity close to the stagnation plane is the largest. It is worthwhile to add that the error can be controlled by changing the chopper speed as discussed by Ohmi et al., [65]. Increasing the chopper speed resulted in small streaklines increasing the digitization error in Δx while very low chopper speeds increased the error in the velocity due to averaging over a longer time interval. Additional errors due to overlap of streaklines from multiple particles and uncertainties in measurement of the streakline lengths where the streaklines are obscured partially by the flame luminosity add to the error in measurement of velocity.

Computational Modeling

The gas phase velocity was obtained by using the OPPDIF code with GRIMech 2.11 mechanism, [55], and realistic multicomponent transport and thermodynamic properties. The flow boundary conditions and the species flux were imposed using the burner inlet flow rates measured with calibrated sonic orifices. The temperature distribution and the temperature boundary condition measured with SiO2 coated

thermocouples was corrected for radiation and used instead of solving the energy equation.

Figure 3.12 shows a comparison of the computed gas phase velocity along the stagnation streamline and the measured particle velocity in the Blue flame. There is a considerable discrepancy between the particle velocity and the gas phase velocity that could not be explained on the basis of experimental errors alone. A possible source for the discrepancy noted above could be the thermophoretic forces acting on the seeding particle. To investigate this possibility, the particle velocity along the stagnation streamline was computed using the following governing equation for the particle motion in the flowfield:

$$m\frac{dv_p}{dt} = F_t + F_v \qquad (3.4)$$

where F_t is the thermophoretic force and F_v is the viscous drag force on the particle. For the purpose of these calculations the seeding particles were considered to be spherical(R= 5μm) and with a density of 3.28 gm/cm^3. Particles were assumed to be in thermal equilibrium with the surrounding gas. Calculations for the thermal history of the seeding particle indicated that the particles have low thermal inertia and the maximum temperature lag between the gas and the particle temperature was less than 5 Kelvin for the 10 μm diameter particles. No thermophoresis was considered in the radial direction as it has been confirmed that radial temperature gradients are insignificant in comparison to the axial temperature gradients in this flame.

Stokes drag force with slip correction is given by:

$$F_v = \frac{-6\pi\mu R(v_p - v_f)}{C} \qquad (3.5)$$

where C is the slip coefficient obtained from Knudsen-Weber formula, $C = 1 + Kn\,A$, where $A = \alpha + \beta\exp(-\gamma/Kn)$.

The empirically determined values of α = 1.142, β= 0.558 and γ= 0.999 by Allen and Rabbe, [200], were used. *Kn* is the Knudsen number based on the particle radius and the mean free path of the gas molecules related to the coefficient of viscosity. Thermophoretic force was obtained using Brock's formula for spherical particles with exchange coefficients recommended by Tablot et al.,[201].

$$F_t = \frac{-12\pi\mu\eta RC_s\left(\frac{k_g}{k_p} + C_t Kn\right)\left[\frac{\nabla T}{T}\right]}{(1+3C_m Kn)\left(1+2\frac{k_g}{k_p}+2C_t Kn\right)} \qquad (3.6)$$

C_s = 1.17, C_t = 2.18, C_m = 1.14 are the thermal slip coefficient, thermal and momentum exchange coefficients respectively.

The governing equation for the particle motion, eqn.3.4, was discretized in the finite difference form and the initial value problem was solved by imposing the initial particle velocity to be equal to the gas velocity at the inlet port.

Comparison of Computations with Experiment

Figure 3.12 shows a comparison of the computed gas velocity in the Blue flame and the computed particle velocity for 10 μm diameter MgO particles. Experimental data (symbols) compare well with the computed particle velocity. The same location was obtained for the particle stagnation plane irrespective of seeding from the fuel side or from the oxidizer side. This implies that same stagnation plane can be obtained from flow visualization experiments even though the particles undergo different thermophoretic flow histories depending on whether they are injected from the fuel side or the oxidizer

side. In the Fig. 3.12 the location of computed and measured particle stagnation plane using computed gas velocity agree well. The flow field for the counterflow diffusion flame is laminar and is governed by the continuity equation and the momentum equation and the ideal gas law for a given temperature profile. These equations along with the two velocity boundary conditions constitute a well-posed problem for which the stagnation plane is uniquely defined. Therefore, good agreement between the computed and measured stagnation plane locations gives us confidence in the computed velocity distribution. Thus for many sooty flames, where the seeding particles can not be visualized on the soot side of the stagnation plane, a confirmation of measured and calculated stagnation plane as well as measured velocity on the nonsooty side of the stagnation plane adequately defines the velocity field for the flame.

The symbols shown in the Fig. 3.12 represent data from several flow visualizations using the streaklines located within the center 1 cm diameter core of the flame, indicating that the radial variation of the axial component of the velocity within the core of the flame can be considered as one dimensional within the limits of experimental error.

The effect of thermophoretic force on particles seeded from the fuel side inlet port and the oxidizer side inlet port are shown in Figs. 3.13 and 3.14 respectively. Figure 3.13 shows the variation of the axial temperature gradient and the thermophoretic force on the seeding particles introduced from the fuel side. The temperature gradient is positive in the direction of particle motion. Therefore, the thermophoretic force, which acts in the direction opposite to that of the temperature gradient, opposes the particle motion. As a result a velocity lag is observed between the particle and the surrounding gas phase. This explains why the particle stagnation plane is on the fuel side of the gas stagnation plane for the particles introduced from the fuel side.A more interesting situation arises for the seeding particles introduced from the oxidizer side, Fig. 3.14. Since the flame lies on the

oxidizer side of the stagnation plane, the particles have to pass through a temperature maximum ($dT/dx = 0$) before they reach their stagnation plane. As a result the direction of the temperature gradient, and therefore the direction of the thermophoretic force, seen by the seeding particle changes when the particle goes through the flame as shown in Fig.3.14. The peak flame temperature for the blue flame is at 1.7cm from the fuel side. The temperature gradient is positive in the direction of the particle motion, and the resulting thermophoretic force opposes the particle motion, before it reaches the peak temperature location. As a result, there is a velocity lag between the particle velocity and the surrounding gas velocity for $1.7cm < x < 2.9cm$. At the peak flame temperature location, the thermophoretic force ceases to act and the viscous drag takes over to speed up the particle to match the gas velocity. After the particle has crossed the flame, the temperature gradient is negative in the direction of particle motion. The resulting thermophoretic force accelerates the particle with respect to the gas. As a result the particle overshoots the gas stagnation plane and continues to move till the viscous drag from the gas flow in the opposite direction slows it down. This explains why the observed particle stagnation plane is on the fuel side of the gas stagnation plane.

Flow Visualization Images

Figures 3.15 and 3.16 are flow visualization photographs for the Flame 1 and the Flame 4 respectively, studied by Atreya et al., [41]. The top side in these photographs is the oxidizer and the bottom side is the fuel side. In each of these two photographs the MgO particles were seeded into the flow from the fuel side inlet.

Flame 1 is on the oxidizer side of the stagnation plane as shown by the flow visualization. Soot formation begins on the fuel side of the flame and soot is convected by the flow towards the stagnation plane in the fuel rich zone. It is noted that the soot stagnation plane coincides with the particle stagnation plane in the Fig. 3.15. It is also observed in that as soot gets convected away from the flame towards the stagnation

plane, the color of the soot zone as recorded by the film changes from yellow to orange red as expected from the Wein's law of radiation.

Flame 4 lies on the fuel side of the stagnation plane as shown in Fig. 3.16. In this case soot formation begins on the fuel side of the flame and soot is driven by the flowfield into the flame zone where it gets oxidized. As a result no soot reaches the stagnation plane. Due to very high soot luminosity in this flame, this photograph was taken with a green laser line filter. This is, to the best of our knowledge, the first visual confirmation of sooty methane flame on the fuel side of the stagnation plane. The flow visualization photographs in addition to providing the flowfield information, are instructive of the soot growth and oxidation processes in these flames.

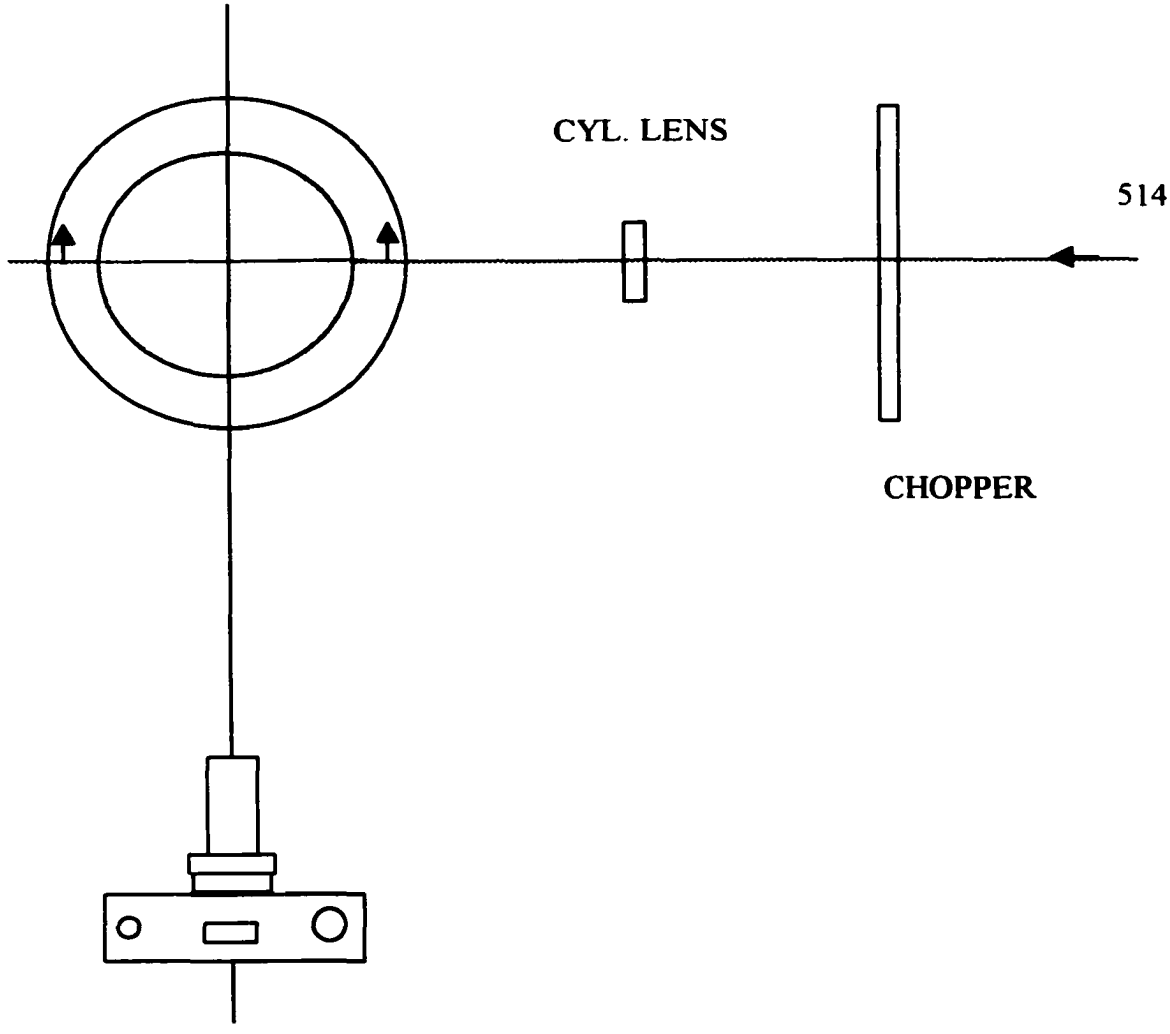

Fig 3.11 Experimental set-up for flow-visualization

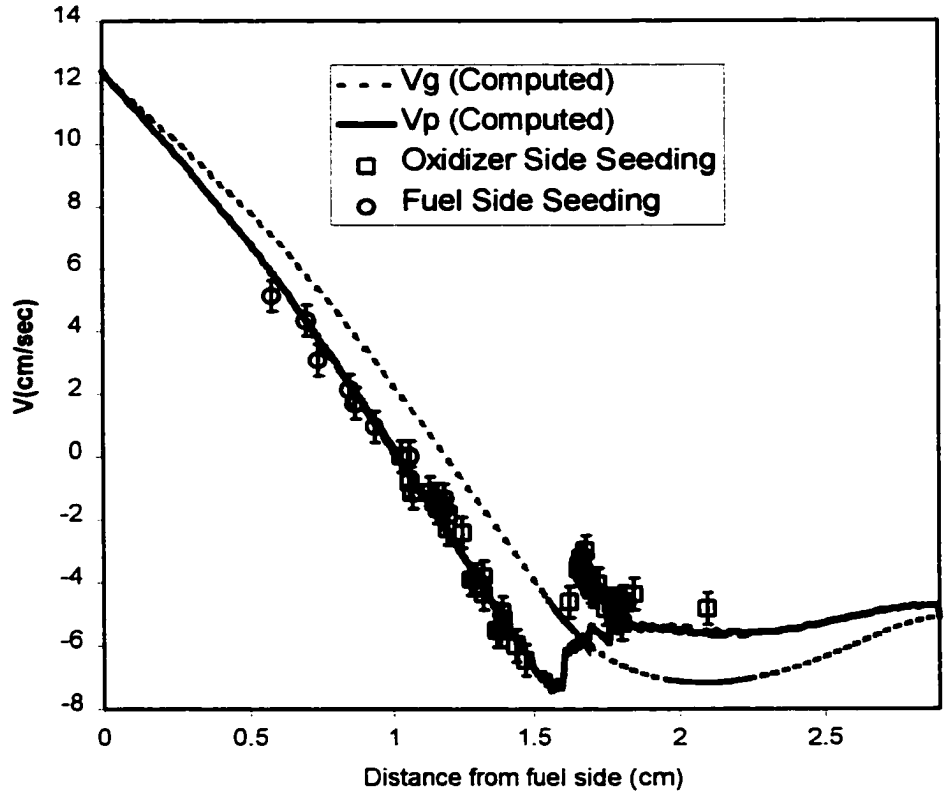

Fig. 3.12 Comparison of computed and measured particle velocity distribution with the gas velocity distribution in the 'Blue-Flame'

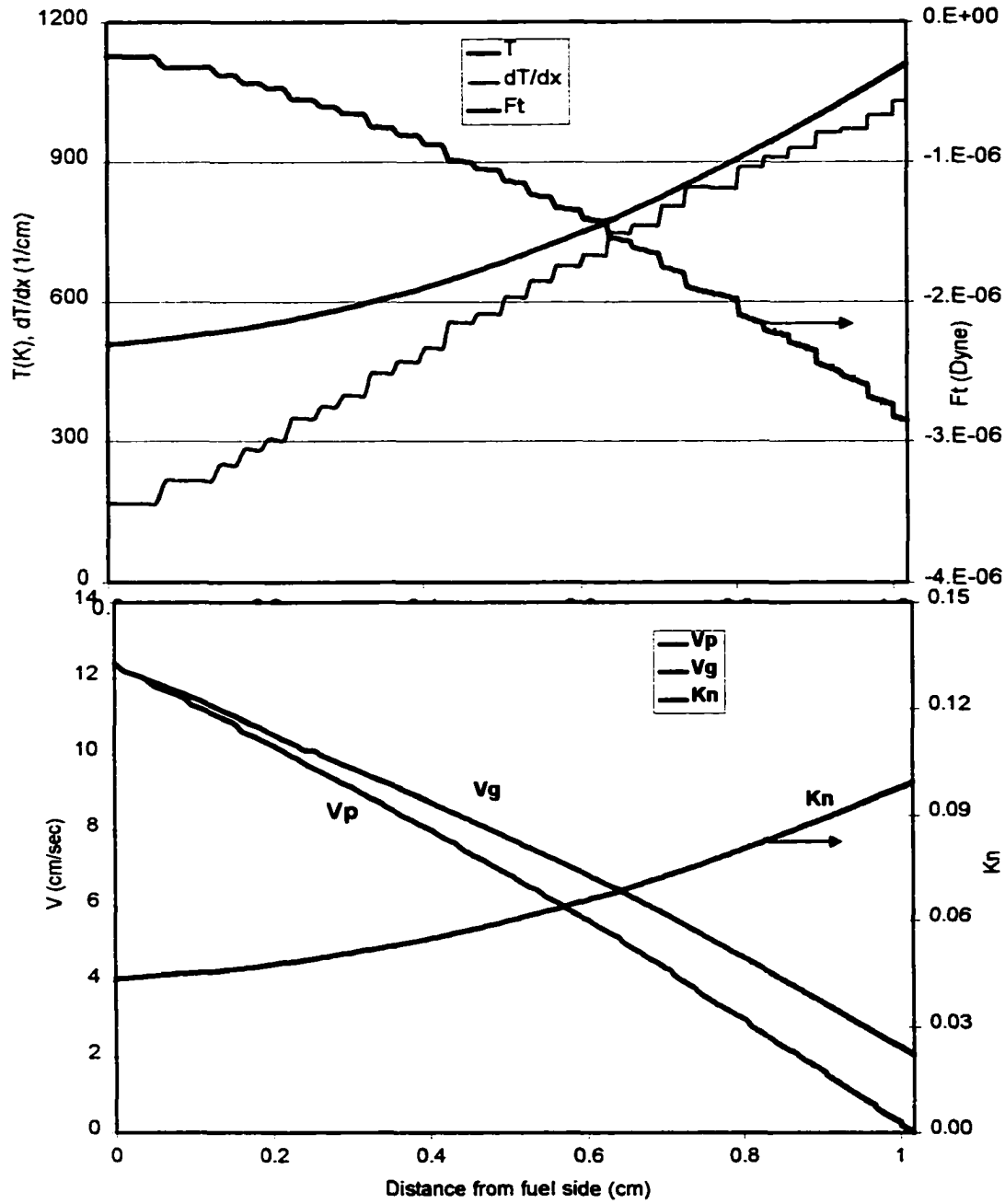

Fig. 3.13 Effect of thermophoresis on particles seeded from the fuel side

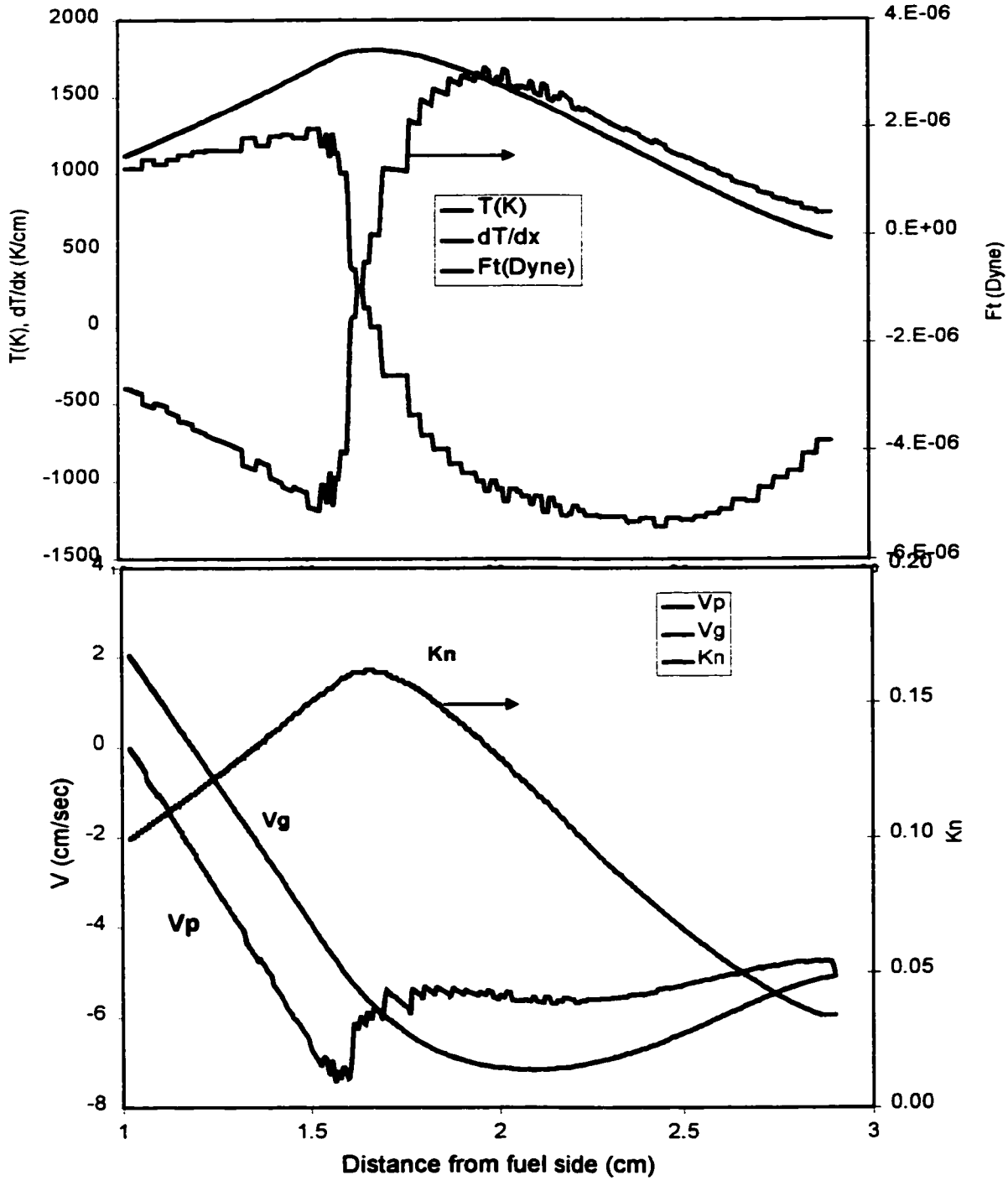

Fig 3.14 Effect of thermophoresis on particles seeded from the oxidizer side

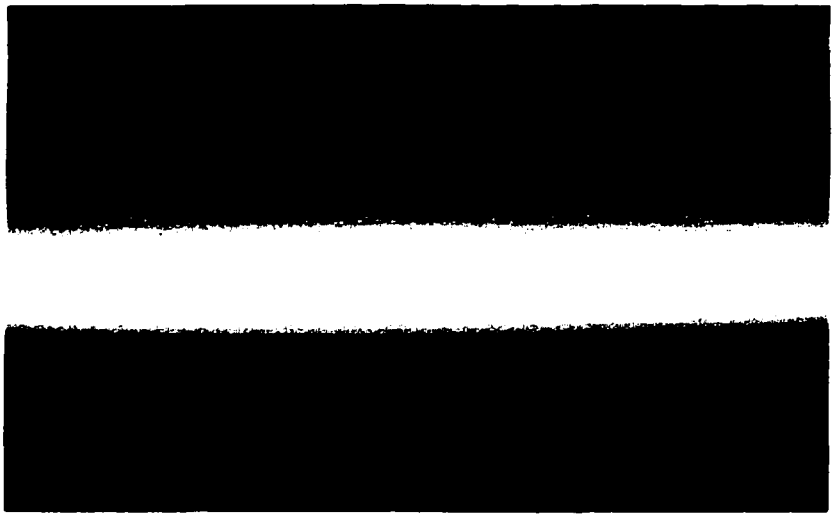

Fig. 3.15 Flow visualization image for Flame 1.0

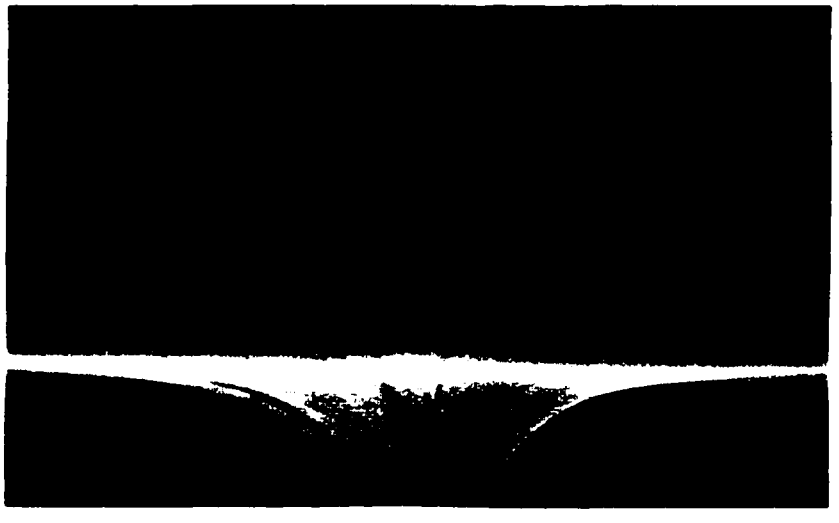

Fig. 3.16 Flow visualization image for Flame 4.0

3.5 OH measurement using Saturated Laser Induced Fluorescence (LIF)

A Laser Induced Fluorescence (LIF) technique for in-situ measurement of OH concentration in the flame is described. Figure 3.17 shows a schematic of the experimental setup. All the optics was rigidly fixed on an optical table while the burner could be moved vertically, perpendicular to the optical table, allowing for measurement of OH distribution along the burner axis. A pulsed NdYAG laser with fundamental emission wavelength of 532nm was operated at a pulse rate of 10 pulses per second with an average pulse power of 300mJ/pulse over a pulse-duration of approximately 10 nsec. The output of the NdYAG laser was used to pump a dye laser using Rhodamine 590 dye. The dye laser was tuned such that its frequency doubled output would excite the $Q_1(3)$ line of the $A^2\Sigma(v'=0)\leftarrow X^2\Pi(v''=0)$ system of OH. This excitation was incorrectly identified as Q_1 (5) in the previous work, Atreya et al., [41], from this laboratory. Figure 3.18 shows an excitation scan, used for identification of OH excitaion, along with theoretical prediction using LIFBASE software. The frequency of excitation was also checked against literature, Dieke and Crosswhite[66].

The U.V. beam was collimated and focused to a 70μm diameter focal volume in the center of the burner. The collection optics consisting of a focusing lens and an optical fiber bundle collected signal from a focal volume approximately 5mm long and 70μm in diameter. The signal collected by the optical fiber bundle was spectrally resolved using an Oriel 257 spectrograph with a 2400line/mm grating and detected using a gated cooled an Instaspec-V ICCD (Intensified CCD). The fluorescence spectrum was averaged over 200 laser excitations. This along with thermoelectric cooling of the CCD to –20°C and background subtraction technique improved the Signal to Noise ratio of the spectrum obtained. The spectrum of the fluorescence signal in the wavelength range of 298-333nm was collected and the peak background corrected signal count, which occurred around 310nm, was recorded.

Figure 3.19 shows the dependence of LIF signal on the laser power (energy/pulse as measured after the 45 degree prism). The regime of Saturated LIF is identified as powers in excess of 7 mJ/pulse where the LIF signal was independent of the signal intensity. This corresponds to power of about 3.5-4.5 mJ/pulse at the burner.

Measured background corrected LIF signal (counts), I_{LIF}, was related to the OH concentration using the following calibration equation:

$$[OH] = C_1 \eta_{OH} I_{LIF} \tag{3.7}$$

where, η_{OH} is the population fraction of OH in the desired ground state at given temperature, T, and C is a calibration constant. Likewise, mole fraction, X_{OH}, can be obtained as:

$$X_{OH} = C\, T \eta_{OH} I_{LIF} \tag{3.8}$$

The ground state population was calculated using:

$$\eta_{OH}(J) = \frac{g_J \exp\left(\frac{-J(J+1)\theta_r}{T}\right)}{\sum_{J=1}^{\infty}(2J+1)\exp\left(\frac{-J(J+1)\theta_r}{T}\right)} \tag{3.9}$$

where, $g_J=2J+1$ is the degeneracy of the energy level with a rotational quantum number of J and $\theta_r=29.35K$ is the rotational temperature, Herzberg [67], for OH assuming a rigid rotor model. The temperature dependence of ground state population fraction, shown in Fig. 3.20, was not included in the previous work reported from this laboratory.

The calibration factor,C, in eqn. 3.8, was determined by comparing the computed peak OH mole fraction in the 'Surya 3 flame' with measured peak fluorescence signal intensity in that flame. The calibration for the 'blue-flame' was checked against a hydrogen flame, Fig. 3.21. The calibration using the blue flame was checked before and after a set of experiments to ensure validity of the calibration. To maximize the S/N ratio the optical fiber was carefully aligned till the fluoresence signal was maximum.

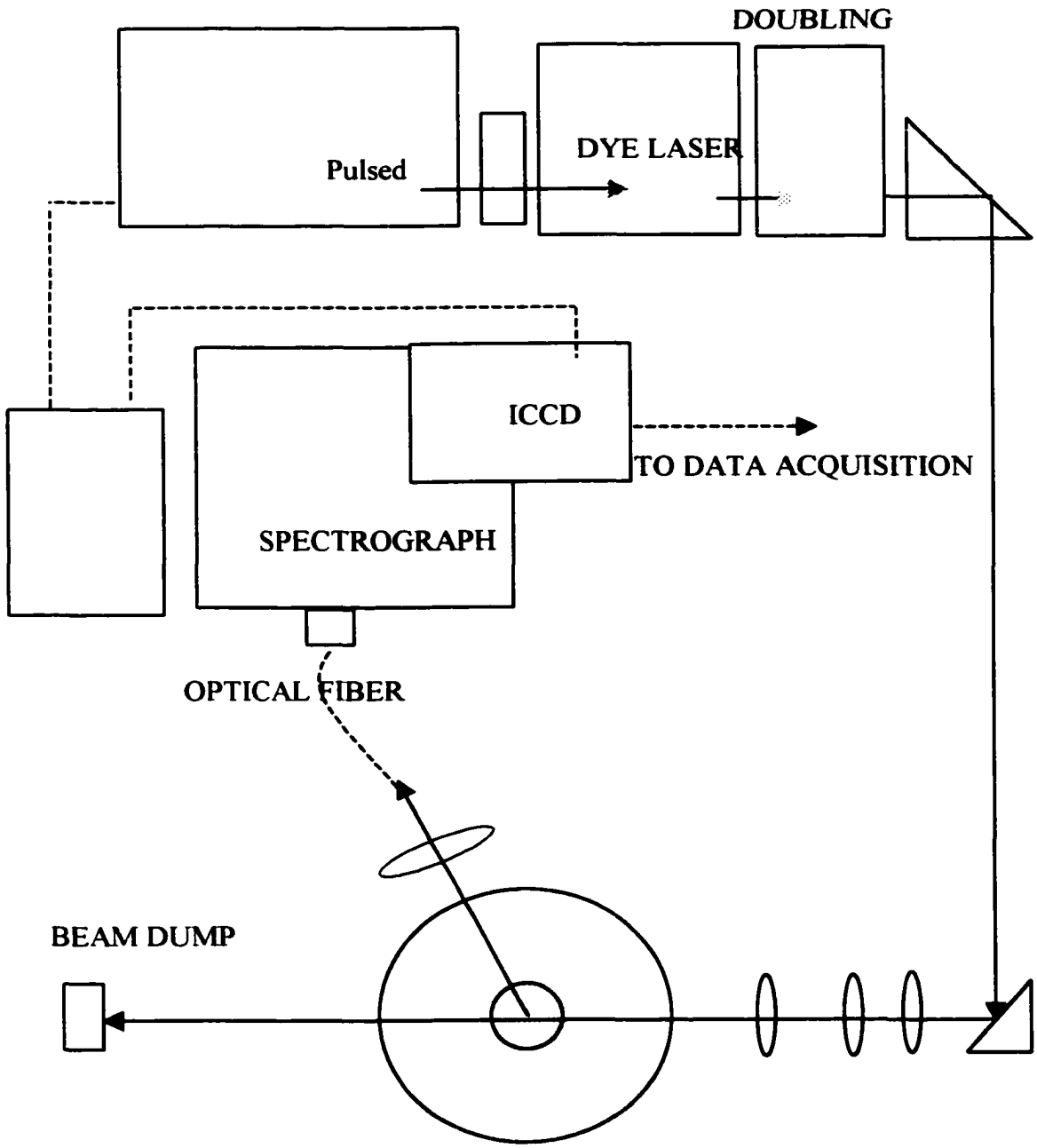

Fig. 3.17 Experimental set-up for OH LIF measurement

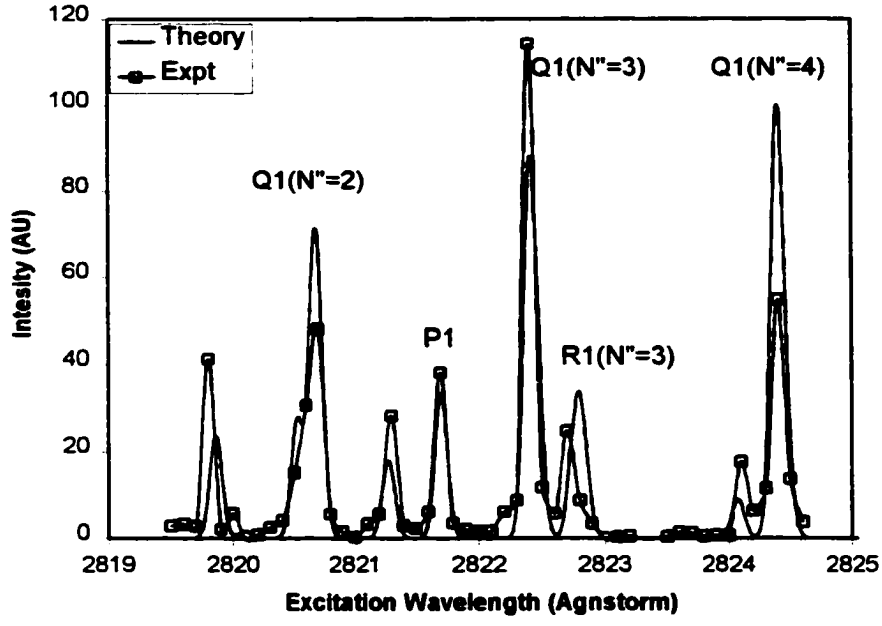

Fig. 3.18 Comparison of experimental excitation scan with theory

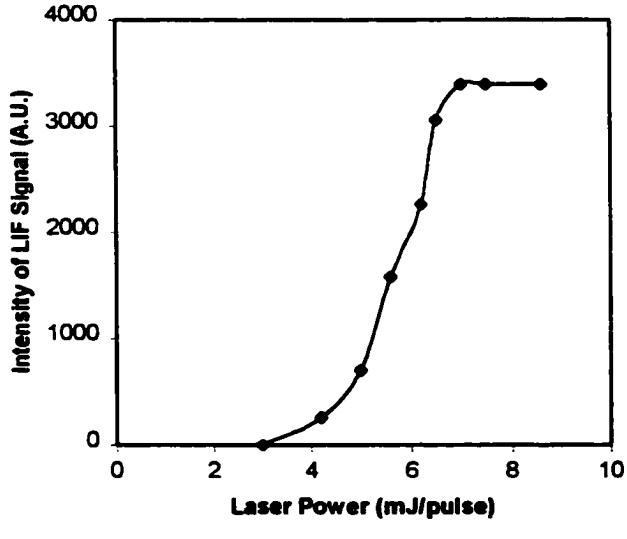

Fig 3.19 Dependence of the OH LIF intensity of the laser power

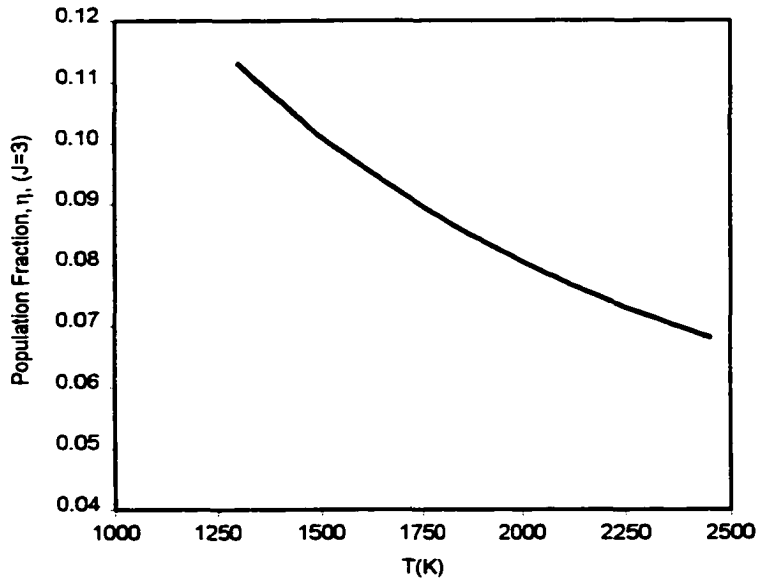

Fig. 3.20 Variation of OH ground state population fraction with temperature

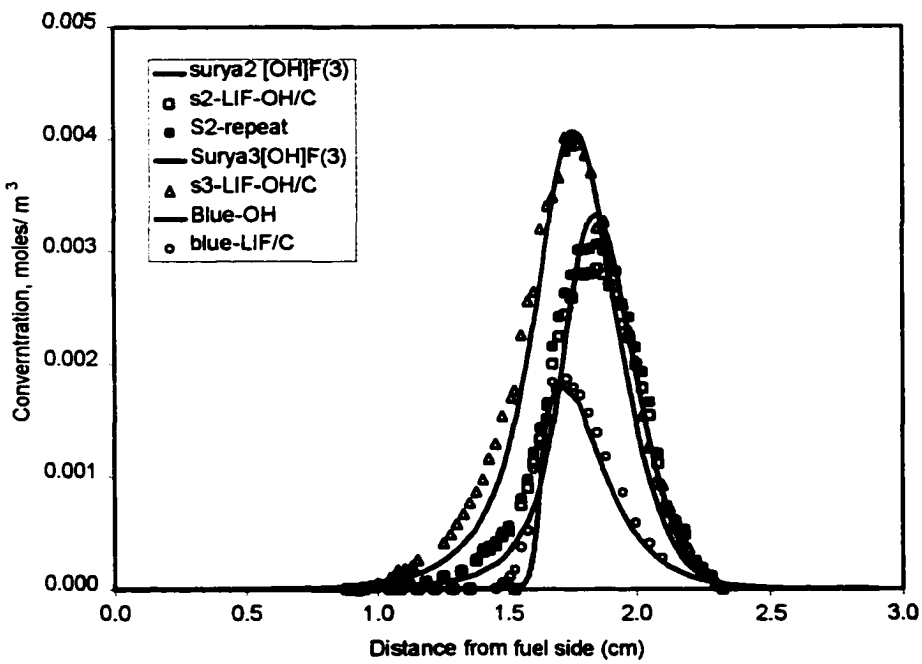

Fig 3.21 Calibration of OH LIF signal using Surya 3 Hyrdogen Flame

3.6 Soot optical diagnostic techniques

A technique for measurement of laser light extinction and scattering by soot in counter-flow flames is described. Interpretation of the measured light extinction and scattering signals to obtain soot morphology using two commonly used theories, Mie Scattering Theory for spheres and Rayleigh-Debye-Gans(RDG) theory for Fractal Aggregates (FA) is discussed.

Non-intrusive light extinction/scattering measurements of flame generated soot aggregates are routinely carried out to infer soot volume fraction and soot particulate size. Early work by Erickson et al.[68] and Dalzell et al.[69] used equivalent Mie sphere theory to interpret the angular light scattering behavior of soot aggregates. Advances in the understanding of soot morphology and light scattering behavior in the last decade, [70-73], have resulted in development of Rayleigh-Debye-Gans(RDG) theory for fractal aggregates(FA). Recently, Farias et al.[74] concluded that RDG-FA theory is a reasonable assumption for a wide range of fractal aggregates and provided error contour charts as guidelines for the suitability of RDG-FA theory for light scattering/extinction measurements in particle-laden environment. Few experimental studies have used RDG-FA theory to interpret soot aggregate morphology in flames. Gangopadhyay et al.[75] and Koylu[76] have used in-situ scattering measurements alone to characterize soot morphology while Dobbins et al.[77] have combined ex-situ TEM measurements with in-situ light scattering/extinction measurements.

We present a study of departure from Rayleigh scattering in a sooty counter-flow methane flame using measurement of scattering signal at two angles. The scattering signals are used to assess the size of the largest soot aggregates and their scattering regime using RDG-FA theory. The measured scattering and extinction coefficients are also interpreted using Mie theory. Experimental challenges in applying RDG-FA theory for optical diagnostics in counter-flow flames are identified.

Experimental Setup and Techniques

Figure 3.22 shows a schematic of the experimental setup. Vertically polarized continuous Ar+ laser beam (λ=514.5 nm) was collimated and focused at the center of the counter-flow burner. Along the extinction pathlength, as defined by the distance between the two quartz guide tubes, the beam diameter was less than 70 μm. The extinction path was limited to about 5cm in length. This technique obviates the need for deconvolution of soot volume fraction measurements by confining the pathlength to the central region of the flame where the soot field is approximately one-dimensional.

VV scattering from the central control volume was collected at two angles, $\theta=15^{o}$ and $\theta=90^{o}$ from the forward direction as shown in Fig. 3.22. These two measurements were sufficient for determination of the radius of gyration of soot aggregates. The choice of the angles was made considering i) limited optical access in the existing experimental setup ii) need to maximize the ratio of scattering signals measured at the two angles in order to study the departure from Rayleigh scattering regime.

The receiving optics for the scattering measurements consisted of an iris, a planoconvex lens, a polarization filter, a laser line interference filter(center wavelength 514.5nm and fwhm of 1 nm) and a photomultiplier tube(PMT). Spatial measurements were made by traversing the burner in the z direction, while the optics was rigidly fixed on an optical table. The reference signal to infer soot scattering coefficient was obtained from methane scattering at room conditions. In addition to this, the scaling factor (error bar ± 5%) associated with different solid angles and optics at the two viewing angles was obtained using VV Rayleigh scattering signal from methane scattering at two angles using same laser power. Linearity of the PMT for measurement of the scattering signal and photodiode for measurement of the extinction signal were checked in the ranges relevant to this study. Signals were detected using a lock-in-amplifier that used lock-in signal from a mechanical chopper located in the incident beam path. The chopper frequency was set to 1000Hz.

Atreya et al., [41], have studied flame structure and soot formation in Flame 3.0. They found that in this sooty methane flame the peak flame temperature is located (14.3 cm form the fuel side inlet) on the fuel side of the gas stagnation plane (14.5cm from the fuel side inlet). The flame has an intensely radiating thin sooty zone similar to the sooty flame shown in Fig. 3.16.

Departure from Raleigh scattering

Figure 3.23 shows a comparison of VV laser light scattering intensity at two different angles, after taking into account the scaling factor due to differences in the solid angles and receiving optics employed for detection of the scattering signal at the two angles. Departure from Raleigh scattering is evident in these measurements as the ratio of $I_{vv,15} / I_{vv,90} = 1.6$ at the peak of the two scattering signals. Such a comparison was not attempted at other points due to sharp gradient in the soot scattering signal. Overcoming the challenge imposed by the sharp gradients in soot optical cross-section in counter-flow flames is critical for reliable application of RDG-FA theory which relies on measurement of the ratio scattering cross section at atleast two angles to furnish information about soot morphology, as will be illustrated shortly.

Interpretation using Mie theory for spheres

Soot particles were considered as spheres with log-normal size distribution and a complex refractive index of m=1.57-.56i for 514.5 nm wavelength to be consistent with previous work. No total scattering correction was applied to the laser light extinction measurements. This results in a small over-estimation of soot volume fraction. the measured light extinction, K_{ext} , and scattering coefficients, $Q_{vv,soot}$, are related to soot volume fraction, f_v, diameter, D_{63}, and the number of Mie spheres per unit volume, N, as follows:

$$f_v = \frac{\lambda}{6\pi}\frac{K_{ext}}{E(m)} \tag{3.10}$$

$$N = \frac{12 f_v}{\pi D_{63}^3} \tag{3.11}$$

$$D_{63} = \lambda\left(\frac{4}{\pi}\frac{E(m)}{F(m)}\frac{Q_{vv,soot}}{K_{ext}}\right)^{1/3} \tag{3.12}$$

$E(m) = -\mathrm{Im}\left[\left(m^2-1\right)/\left(m^2+2\right)\right]$ and $F(m) = \left|\left(m^2-1\right)/\left(m^2+2\right)\right|^2$ are functions of soot refractive index,m. D_{63} is a moment of soot particle diameter defined elsewhere, [70].

The Mie sphere interpretation of the data is presented in Fig. 3.24. The values of peak soot volume fraction and number density are representative of those encountered in laminar flames in this study. Since $D_{63} \propto (Q_{vv,soot})^{1/3}$ while $N \propto Q_{vv,soot}$, the effect of polar variation of scattering cross-section shows up more effectively in the number density distribution rather than in the size distribution. It is further noticed that the difference in the particle sizes estimated on the basis of VV scattering cross-sections at the two angles is about 20% for the largest aggregates in this flame.

Interpretation using RDG-FA theory

The soot aggregates are assumed to be made of monodisperse spherical primary particles of diameter d_p. The radius of gyration, R_g, of the aggregate is related to the number of primary particles per aggregate, n, via the following expression:

$$n = k_f\left(\frac{R_g}{d_p}\right)^{Df} \tag{3.13}$$

where k_f and D_f are the pre factor and the fractal dimension. Although, scale similarity is not applicable for small aggregates (n~100), the above mass fractal relationship can be used to relate soot morphological properties. The average VV

scattering cross-section of the aggregates, $C_{vv,a}$, is related to that of primary particles, $C_{vv,p}$ via the following relationships.

For the small angle (Guiner) regime:

$$\frac{C_{vv,a}(\theta)}{N^2 C_{vv,p}} = \exp\left(\frac{-q^2 R_g^2}{3}\right) \qquad \text{when } q^2 R_g^2 < 1.5\, D_f \tag{3.14}$$

For the large angle regime:

$$\frac{C_{vv,a}(\theta)}{N^2 C_{vv,p}} = \left(\frac{3D_f}{2eq^2 R_g^2}\right)^{D_f/2} \qquad \text{when } q^2 R_g^2 > 1.5\, D_f \tag{3.15}$$

where e is the Neper number and q is defined as:

$$q = \frac{4\pi}{\lambda}\sin\left(\frac{\theta}{2}\right) \tag{3.16}$$

For aggregates that satisfy Guiner Regime the Radius of Gyration, Rg, can be related to the ratio of scattering intensity at the two angles using:

$$R_g^2 = \frac{\ln\left(\frac{I_{vv}(\theta_2)}{I_{vv}(\theta_1)}\right)}{\frac{1}{3}\left(\frac{4\pi}{\lambda}\right)^2\left(\sin^2\left(\frac{\theta_1}{2}\right) - \sin^2\left(\frac{\theta_2}{2}\right)\right)} \tag{3.17}$$

Using $I_{vv}(15^\circ)/I_{vv}(90^\circ)$ value 1.6 for the largest aggregates, the mean radius of gyration values of 70 nm. These indeed were found to satisfy the small angle regime criterion in eqn. 3.14 using the value of D_f =1.6. Commonly quoted values of D_f in literature for soot are 1.6-1.85[8-10]. The value of R_g estimated above is biased to large aggregates. Furthermore, since the RDG-FA theory underestimates $C_{vv,a}(15^\circ)$ with respect to $C_{vv,a}(90^\circ)$,[75-77], the values of R_g presented here have been overestimated. On the basis of error contour charts published by Farias et al.[74] this error is less than 20% for the two cases considered. Since the values of peak $D_{63}/2$ are almost half of the

corresponding R_g values it is concluded that soot aggregates are open structures which is in agreement with $D_f < 2$ reported in several studies of soot morphology [75-77].

Several factors make the use of RDG theory to interpret soot optical cross-section in counter-flow flames a challenging task. Firstly, due to thin soot region, the gradients in the soot scattering cross-section are large, resulting in large errors in obtaining the ratio of scattering cross-sections at two angles. Secondly, to obtain complete information about soot morphology, several angular scattering measurements in both the small angle and large angle regimes are necessary, which may not be possible due to geometric limitations or may need measurements using multiple laser wavelengths. Thirdly, it is difficult to obtain the morphology for evolving particles since for these small particle aggregates the ratio of scattering cross-section of close to unity is difficult to measure with adequate accuracy. Consequently, the measured scattering and extinction coefficients are interpreted in the rest of the chapters using Mie Theory for spheres with log-normal size distribution.

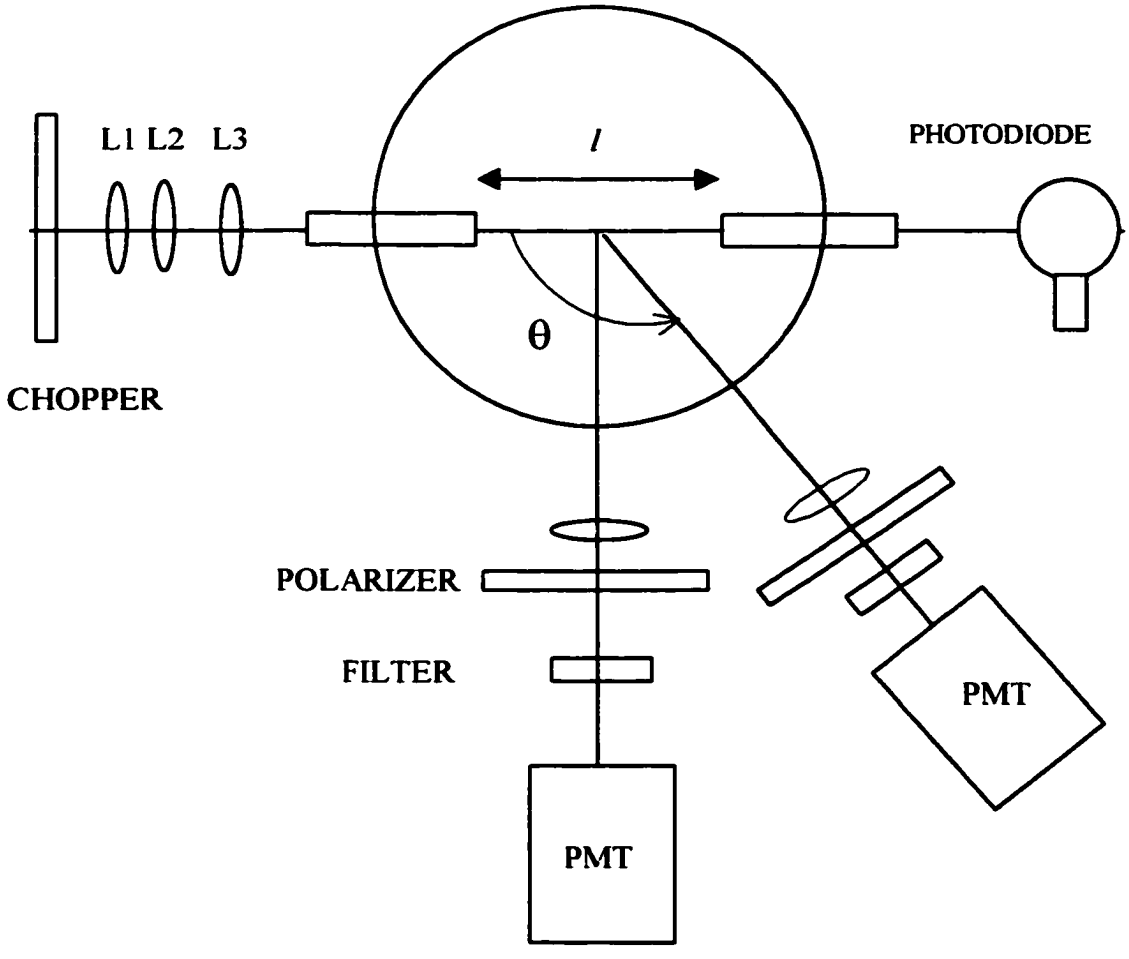

Fig 3.22 Experimental set-up for measurement of soot optical cross-sections

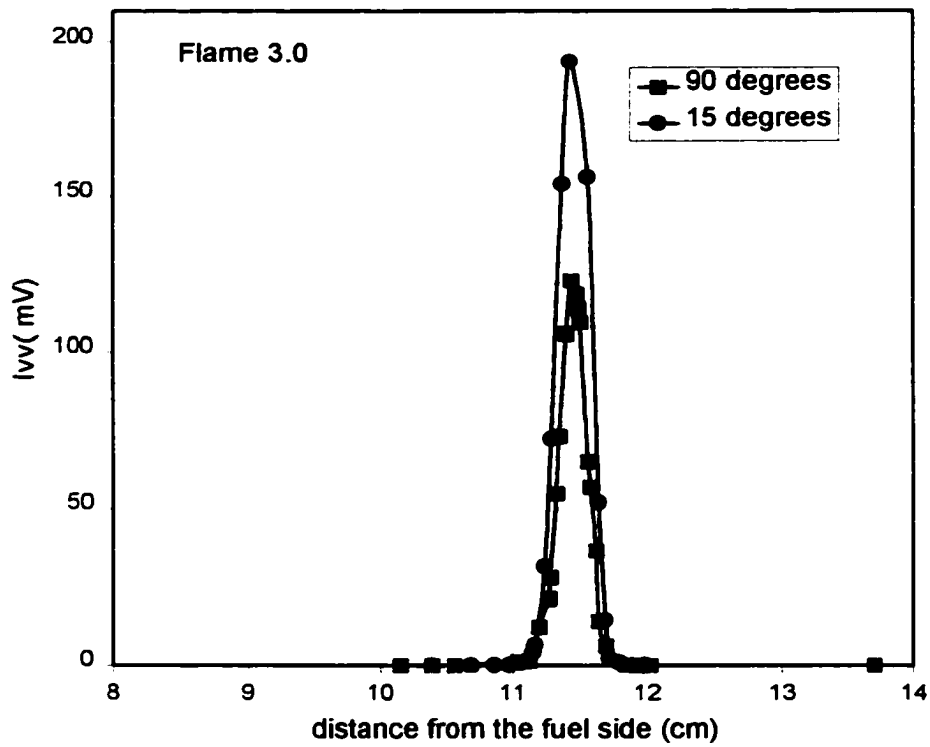

Fig 3.23 Comparison of Ivv at 15° and 90° for the Flame3

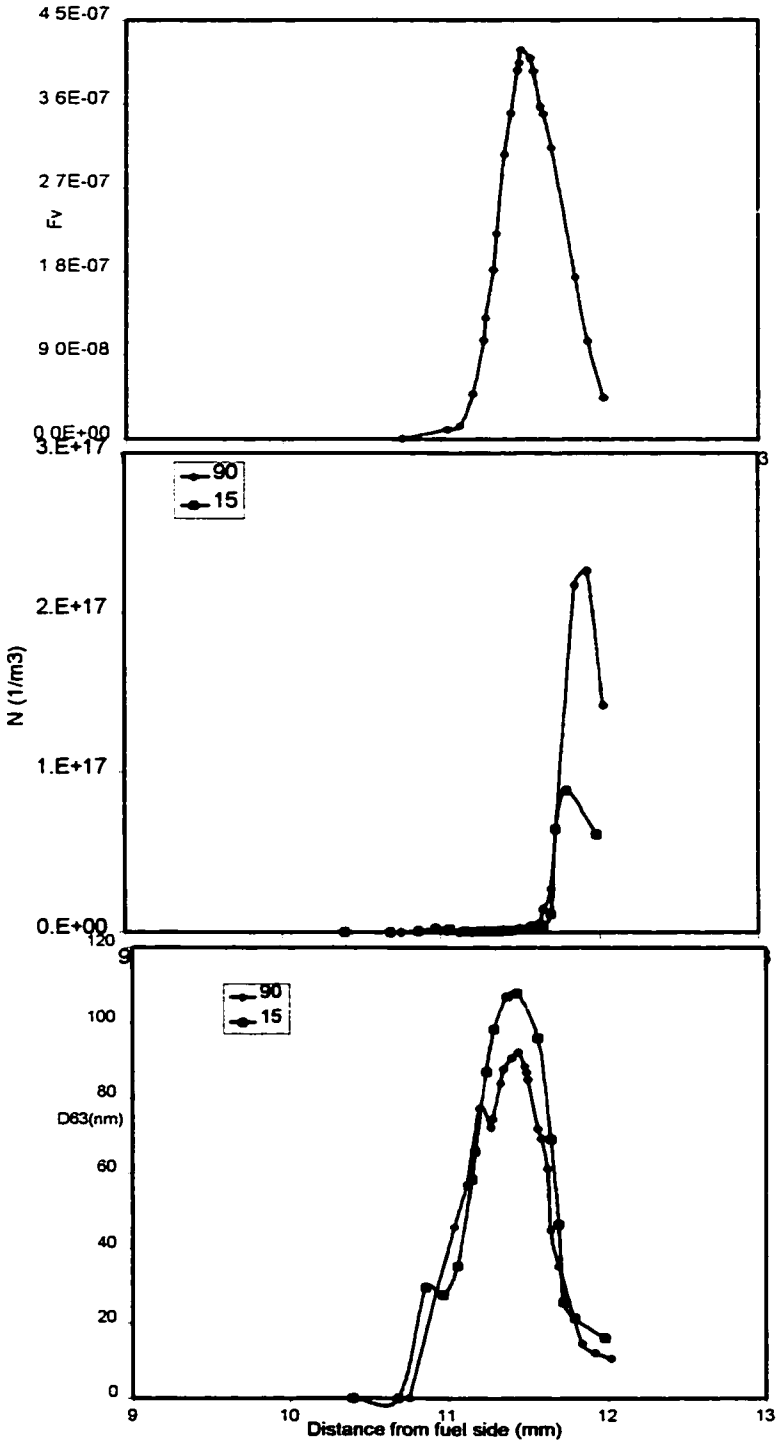

Fig. 3.24 Distribution of fv, D63 and N using Mie theory interpretation of soot optical cross-sections in Flame3.0

CHAPTER 4

ANALYTICAL SOLUTION

4.1 Introduction

With partial premixing, the counter-flow flame consists of two reaction zones, a premixed reaction zone and a non-premixed reaction zone as discussed before in Chapter1. This chapter deals with an analytical solution for locations of the premixed and the non-premixed reaction zones with respect to the stagnation plane.

Pioneering experimental studies of the location of these reaction zones with respect to the stagnation plane for different levels of fuel side partial premixing was studied by Yamaoka and Tsuji [3] in rich laminar methane air counterflow flames stabilized in the stagnation point region of circular cylinder. This flow configuration is called the *planar* counter-flow flame configuration as shown schematically in Fig. 4.1. For small levels of partial premixing (large equivalence ratio of the rich fuel stream), the two reaction zones were indistinguishable and the measured species and temperature distribution in the flame resembled that of a pure non-premixed flame. This regime of partial premixing was called the 'merged flames' regime. As the equivalence ratio of the fuel stream was decreased the spatial separation between the two reaction zones increased. In this regime of partial premixing, termed as the 'interdependent flames' regime, the premixed flame supplied CO and H2 fuel to the nonpremixed flame that in turn supplied the premixed flame with heat and radicals. The transition from the merged flame to the interdependent flames regime was marked by crossover of the premixed reaction zone from the oxidizer side of the stagnation plane to the fuel side of the stagnation plane in the counter-flow flame geometry.

The analytical work described in this chapter was initiated as an attempt to answer the question asked by S.Ito, [3], in the 16th Symposium (International) to seek an understanding for the effect of partial premixing on relative position of the premixed and the non-premixed reaction zones with respect to the stagnation plane. It will be demonstrated in the subsequent chapters that the understanding gained from the analytical model presented in this chapter in an attempt to answer the Ito's question provides valuable insights that can be applied to explain experimental observations of soot and NOx formation.

Similar to experimental data of Tsuji and Yamaoka [2-3] for *planar* counter-flow flames, recently Blevins and Gore [31], presented computed structure of double flames for *axisymmetric* counter-flow methane-air partially premixed flames.

Analytical framework using flame sheet approach has been applied for partially premixed counter-flow flames by Law et al. [6] and Chung et al. [7] to study the flame extinction behavior.

This study investigates the effect of equivalence ratio for the nonpremixed flame crossover using Burke-Schumann analysis [80] and that for the premixed flame using an asymptotic analysis similar to that of Law et al. [6] for the planar counter-flow geometry similar to that of Tsuji and Yamaoka [3]. The analytical results are compared to available experimental data, [2-3], and computational results [31] with detailed modeling of the aero-thermo-chemistry. Experimental data for the reaction zone position with respect to the stagnation plane is compared to the analytical model in section 6.3 and its implications for NO emission from flamelet combustion is discussed.

4.2 Theory

Governing Equations

The governing equations were derived with the assumptions of one step Arrhenius kinetics, steady one-dimensional incompressible flow along the stagnation streamline and

constant thermochemical property data. Lewis number is assumed to be unity and the origin of the coordinate system is located at the stagnation plane. Energy and species equations in the transformed coordinate system are written as:

$$\frac{d^2T}{d\eta^2} + \eta\frac{dT}{d\eta} = w \qquad (4.1)$$

$$\frac{d^2Y_i}{d\eta^2} + \eta\frac{dY_i}{d\eta} = -w \qquad (4.2)$$

i=O,F denote oxidizer and fuel respectively and w represents the reaction rate given by $w = -DaY_OY_F \exp\left(-T_a/T\right)$. The non-dimensional coordinate is defined as $\eta \equiv \sqrt{2}\tilde{\eta} \equiv y'/\sqrt{D'/K'}$. D' is the mixture mass diffusivity and K' is the strain rate. Da is Damkohler number. $T_a=E_a/R$ where E_a is the activation energy and R is the universal gas constant. Y_F is the fuel mass fraction. Y_O is the oxidizer mass fraction scaled by σ (kg oxygen per kg fuel in the stoichiometric equation). T=T'Cp'/q' is the scaled temperature. Primes are used to indicate unscaled quantities. q' is energy released per kg fuel on dry basis.

Boundary Conditions:

Oxidizer Side Boundary ($\eta \rightarrow -\infty$)

$Y_O = Y_{O,-\infty}$, $Y_F = 0$, $T = T_{-\infty}$

Fuel Side Boundary ($\eta \rightarrow +\infty$)

$Y_O = Y_{O,+\infty}$, $Y_F = Y_{F,\infty}$, $T = T_{+\infty}$

Subscripts $+\infty$ and $-\infty$ indicate fuel side and oxidizer side boundary respectively.

Analysis

Figure 4.2 shows a schematic of the premixed and the nonpremixed reaction sheets within the flamesheet approach. The task at hand involves determination of the

five unknowns T_p, T_n,η_p, η_n and $Y_{F,p}$. Subscripts p and n denote values at the premixed and the nonpremixed flame locations.

Nonpremixed Flame

The analytical methodology for determining the location and the temperature of the nonpremixed flame sheet utilizes the well-known Shvab-Zel'dovich transformation, [81], and an error function solution for the similarity variable β.

$$\beta = \frac{1}{2}\left(1 + erf(\tilde{\eta})\right) = \frac{\alpha - \alpha_{-\infty}}{\alpha_{+\infty} - \alpha_{-\infty}} \qquad (4.3)$$

α is an appropriate Shvab-Zel'dovich variable. The Shvab-Zel'dovich variable for fuel-oxidizer coupling is defined as $\alpha_{FO} = Y_F'/M_F \nu_F - Y_O'/M_O \nu_O$. Similarly, Shvab-Zel'dovich coupling variable for fuel-temperature is defined as $\alpha_{FO} = Y_F'/M_F \nu_F + T'C_p'/q'$. Here M_i and ν_i represent species molecular weight and coefficient in the stoichiometric reaction respectively.

The location of the nonpremixed flame is characterized by $\alpha_{FO,n} = Y_F = Y_O = 0$ giving

$$\beta_n = \frac{-\alpha_{FO,-\infty}}{\alpha_{FO,+\infty} - \alpha_{FO,-\infty}} \qquad (4.4)$$

Substituting this value of β_n in Eqn 4.3 the location η_n and the temperature T_n of the nonpremixed flame sheet can be calculated. Using the error function solution we find that at the location of the stagnation plane, η=0, the value of β is 0.5. The equivalence ratio for the nonpremixed flame sheet to crossover from the oxidizer side to the fuel side of the stagnation plane can be computed by setting $\beta_n = 0.5$ in Eqn. 4.4.

Premixed flame sheet

Having determined the location, η_n, and the temperature, T_n, of the nonpremixed flame sheet as indicated above we are left with three unknowns η_p , T_p and Y_{Fp} associated with the premixed flame sheet. However, only two equations relating these

unknowns are provided by the equations for species and energy flux balance at η_p. The closure problem was solved by an asymptotic expansion of the premixed reaction region using analysis similar to that of Law et al.[6].

Solution Procedure

η_n and Tn were determined using the error function solution, Eqn. 4.3, for known boundary conditions. Thereafter, the unknowns η_p, T_p and Y_{Fp} were determined using an iterative procedure so as to satisfy the species and energy flux balance conditions at η_p and an equation, Eqn. 16 in appendix A3, for pseudo-temperature, [6], in the modified coordinate system for the premixed reaction zone. Details of theoretical formulation are presented in the Appendix A3. Present code was checked for domain dependence and initial guess dependence. Previously published computations using the same mathematical framework for oxidizer side partial premixing [6] were reproduced satisfactorily by the present computational procedure. Values of property data used in this work were Cp'=1.77kJ/kgK, $T'_{+\infty} = T'_{+\infty}$= 300K, σ =4.0, q'=11950 kcal/kg fuel, E_a = 40kcal/mol and $Da=10^8$.

Although the analysis is presented here for the planar counter-flow geometry, it can be modified for axisymmetric flow configuration as outlined in [6].

4.3 Results and Discussion

Rewriting Eqn. 4.4 as:

$$\beta_n = \frac{1}{1+\left(\frac{Y_F'}{M_F\nu_F} - \frac{Y_O'}{M_O\nu_O}\right)_{\infty}\left(\frac{M_O\nu_O}{Y_O'}\right)_{-\infty}} \qquad (4.5)$$

We observe that fuel side partial premixing causes the nonpremixed flame to move closer to the fuel side (β_n increases) because of two reasons:

1. consumption of a fraction of the fuel in the premixed flame sheet
2. dilution of the fuel

The equivalence ratio for nonpremixed flame crossover is obtained by setting $\beta_n = 0.5$ in Eqn. 4.5, yielding ϕ =2.11 for methane air partially premixed flame. It is evident from Eqn. 4.5 that the nonpremixed flame cross over equivalence ratio is independent of the strain rate. The value obtained above agrees well with the experimental value of 2.2 reported in [3] for rich methane air flames. It can be shown that an identical value of nonpremixed flame crossover equivalence ratio is obtained for rich axisymmetric methane air counterflow flames which agrees well with detailed computational modeling of Blevins and Gore [31] using detailed chemistry and transport properties.

For several other hydrocarbons including alkane, alkene and alkyne series compounds with up to 4 carbon atoms and benzene, the nonpremixed flame crossover equivalence ratio was calculated to be in the range 2.11-2.16.

The experimentally determined distance of the nonpremixed flame from the stagnation plane, [3], correlated linearly with computed values of η_n for the corresponding equivalence ratios. The length scale $(D'/K')^{1/2}$ for the experiments of Yamaoka and Tsuji [3] was determined using the slope of the straight-line fit, Fig. 4.3, for the above correlation as 0.3 cm. This length scale was used to nondimensionalize the experimental data from [3] presented in Fig. 4.4 along with theoretical results. The agreement for the nonpremixed flame is very good .The values of E_a and Da were chosen to force the premixed flame cross over at ϕ=2.6. The premixed flame crossover equivalence ratio was found to be sensitive to the choice of strain rate (Da number) and chemical kinetics (E_a) with premixed flame crossover equivalence ratio decreasing (higher level of partial premixing required) for higher strain rate. This observation is explained by the fact that the premixed flame has a positive flame speed subsequent to flame cross over and its location with respect to the stagnation plane (η_p) is sensitive to the strain rate field. As the strain rate is increased, the premixed flame tends to merge with the nonpremixed flame. The lower bound for the premixed flame cross over equivalence ratio can be argued to be 2.11 for methane-air flames.

The value of ϕ=2.7 found by Yamaoka and Tsuji[3] for transition from the merged flame regime to the interdependent flame regime and ϕ=2.5 by Blevins and Gore[31] for observation of double peaks in CH distribution profiles for rich methane air counterflow flames should be accepted with the above understanding of dependence of premixed flame cross over on the strain rate. Blevins and Gore [31] reported that "below ϕ=2.5, the two flame zones exist on the opposite side of the stagnation plane". This statement is true only for $2.11<\phi<2.5$ since for $\phi<2.11$ both the flames lie on the fuel side of the stagnation plane.

4.4 Conclusions

Following conclusions can be drawn from this analytical study:

1. Fuel side partial premixing causes the non-premixed reaction zone to come closer to the fuel side by two effects: (i) dilution of the fuel side stream (ii) by consumption of a fraction of the fuel in the premixed reaction zone.
2. Non-premixed reaction zone crossover equivalence ratio for methane air partially premixed flames was obtained to be 2.17, which agreed well with experimental value of 2.11 obtained by Tsuji and Yamaoka [3].
3. Non-premixed reaction zone cross over equivalence ratio was shown to be independent of strain rate and the choice of thermochemical properties. It was further shown that it varied little for a variety of C1-C4 hydrocarbon fuels.
4. Premixed reaction zone cross over equivalence ratio was found to be sensitive to strain rate and choice of thermochemical properties.

The understanding of the double flame structure obtained using the simplified model above will be invoked in the subsequent chapters to explain the experimental observations of formation of soot and NO in counter-flow partially premixed flames.

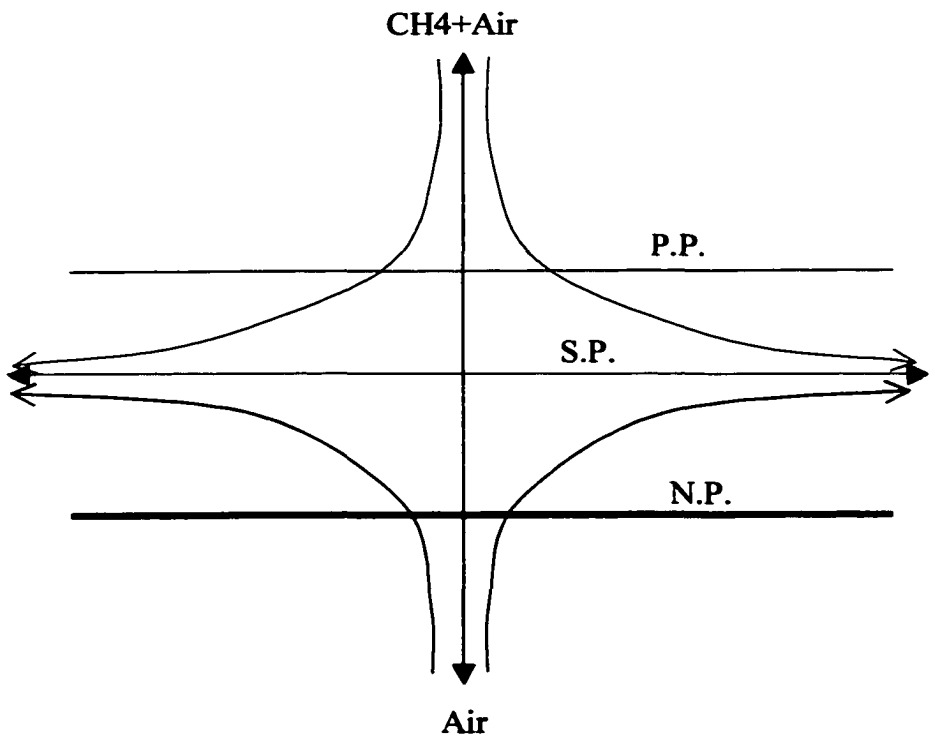

Fig 4.1 Flow configuration for planar counter-flow partially premixed flame

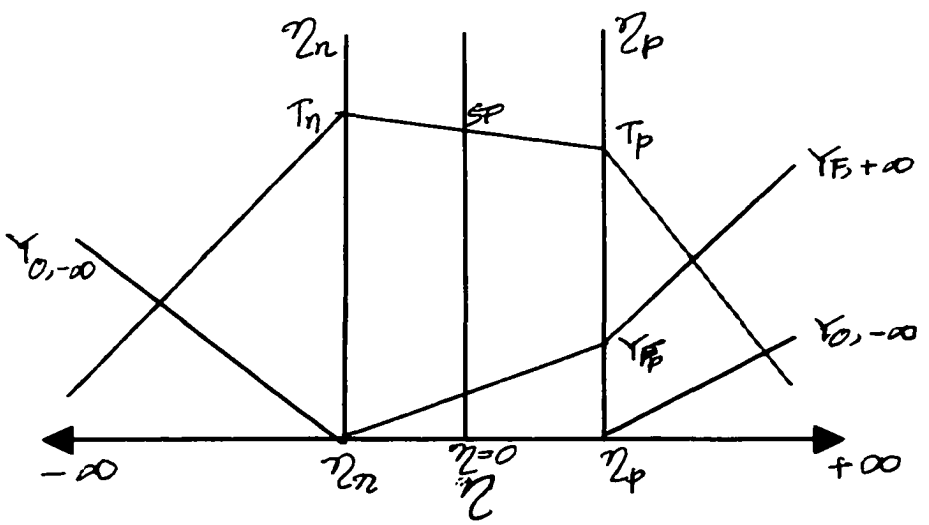

Fig 4.2 Schematic illustration of the flamesheet model

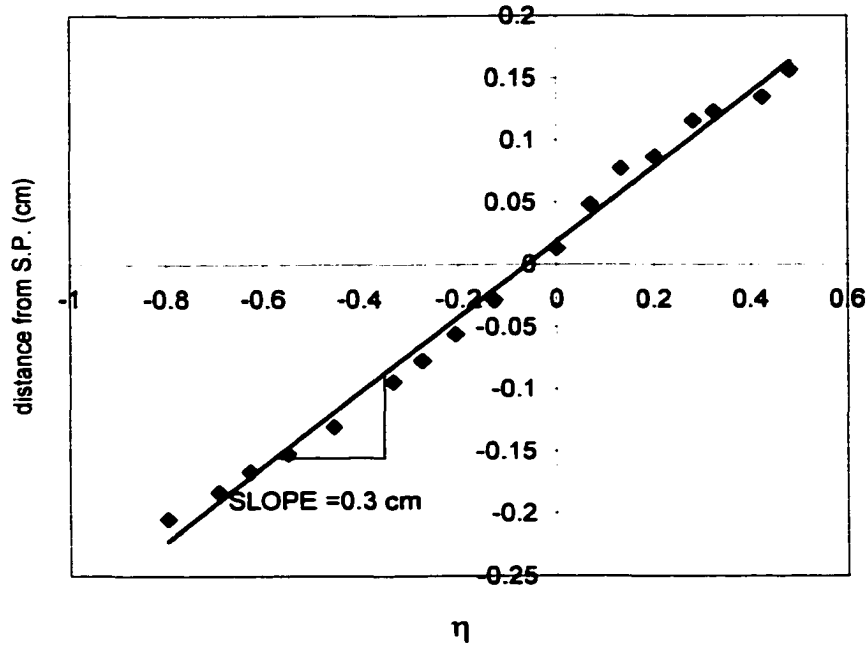

Fig 4.3 Determination of the length scale $\sqrt{\frac{D'}{k'}}$ for data of Tsuji and Yamaoka[3]

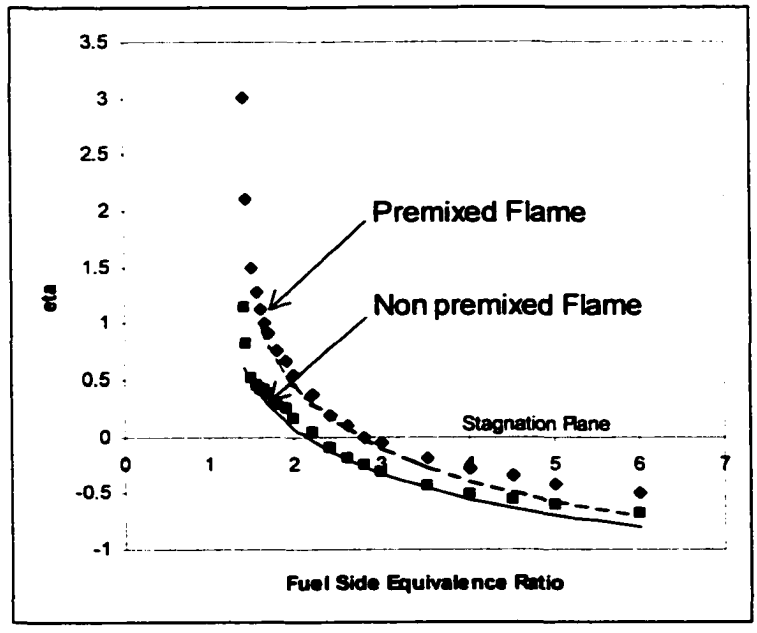

Fig 4.4 Comparison of theory with experimental data of Tusji and Yamaoka [3]

CHAPTER 5

FORMATION AND CONTROL OF SOOT EMISSIONS

5.1 Introduction

Soot formation in flames is of concern because soot radiation is an important mode of heat transfer in industrial furnaces and soot emissions from combustion equipment pose health and environmental hazard.

The term 'partial-premixing' is commonly used to refer to the technique of adding oxygen (in quantities less than required for rich flammability limit) into the fuel. The rich fuel mixture then reacts with air in the combustion chamber. Intentional partial premixing is practiced for the reasons of flame stabilization and pollutant emission control. About 30% of natural gas use takes place in partially premixed mode, Warnatz et al. [1]. Unintentional partial premixing of turbulent flames can occur in practical burners as a result of incomplete mixing due to geometric limitations for premixed combustion and due to flame extinction re-ignition mechanisms in nonpremixed combustion devices.

A commonly used flame configuration used for laboratory studies of flames is the counter-flow flame configuration. Counter-flow flame configuration is a well-defined flame configuration where flames are stabilized between opposing flows of fuel and oxidizer. The counter-flow flame configuration is also pertinent to turbulent combustion via flamelet approach, Carrier et al. [34]. This chapter deals with the effect of partial premixing on the *flame structure, sooting tendency* and *flame radiation* of laminar counterflow diffusion flames (CFDFs) with partial premixing. A partially premixed flamelet within a turbulent flame may have partial premixing either on the fuel side or on

the oxidizer side or on both the sides. We shall consider the effects of both these scenarios:(a) fuel side partial premixing and (b) oxidizer side partial premixing.

Pioneering experimental work for understanding the structure of methane-air partially premixed counter-flow flames was done by Tsuji and Yamaoka [2,3]. They observed that with partial premixing the 'flame' was actually a 'double-flame' with a premixed reaction zone and a non-premixed reaction zone. For small amounts of oxygen added into the fuel the premixed reaction zone was indistinguishable from the non-premixed reaction zone and the temperature and species profiles measured in the flames were similar to that in a non-premixed diffusion flame. Such partially premixed flames were called 'merged-flames'. For progressive levels of partial premixing the premixed flame became stronger and there was clear spatial separation between the two reaction zones, as was evident in the temperature and species profiles measured in these flames. The premixed reaction zone was dependent on the non-premixed reaction zone for supply of heat while it, in turn, supplied CO and H2 'fuel' to the non-premixed reaction zone. Such flames were called double flames in the 'interdependent flame' regime.

A number of studies [8-21] have considered soot formation in partially premixed flames for a variety of hydrocarbon fuels and flame configurations as summarized is the Table 5.1. The effect of small amount of oxygen added into hydrocarbon fuels on 'carbon' formation has been an area of active research. It has been known that addition of small amounts of oxygen promotes pyrolysis of ethylene fuel, Chakraborty and Long [8]. This observation has been used to explain enhancement of soot loading in ethylene flames, Glassman and Hura[12], Mitrovich and Lee[17], for small amounts of oxygen added into the fuel side of originally non-premixed flames. Recent work based on more comprehensive chemical kinetic analysis, Hwang et al. [16], and detailed measurements of non-fuel hydrocarbon species, McEnally and Profile, [18], have emphasized the role of C3 species in order to explain an increase in sooting tendency for small amounts of oxygen added to ethylene fuel.

Although methane is a major component of natural gas, a fuel of commercial importance, and partial premixing accounts for a significant portion of natural gas consumption, limited literature, [10,15,18], is available on effect of partial premixing on soot production in methane flames. It is known that the chemical effect of oxygen added to the methane fuel, [18], and propane, [13], is to inhibit soot formation. There have been no studies of soot growth in partially premixed methane counter-flow flames except for the recent work of Mungekar and Atreya [20,21]. The rest of the chapter is devoted to the description of these two studies in greater detail than reported previously. In the first study the effect of partial premixing on *flame structure and soot formation* was considered. The second study describes various configurations of sooty flames obtained with fuel side partial premixing to control *flame radiation and soot emission* from counter-flow flames.

5.2 Flame Structure and Soot Formation

This primary objective of the study reported in this section was to understand the effect of partial premixing on the flame structure and soot loading.

Previous literature, [13,18], has reported that the effect of oxygen added to methane and alkane fuels is to suppress *soot inception* and soot precursor species formation. Under most common circumstances most of the soot mass comes from *soot growth* processes and not soot nucleation. Soot growth is known to be affected by the temperature time histories of the soot particulate within the flame. Hence, even though the chemical and dilution effects of oxygen added to methane fuel are known to suppress inception of soot-the effect on soot growth has not been studied in the past. The objective of this study is to understand the effect of partial premixing on soot loading in counter-flow flames with particular attention to the effect on soot growth due to changes in temperature-time histories of the soot particles brought about by partial premixing.

As described on the basis of the simplified analytical model presented in the Chapter 4, different effects on movement of the flame with respect to the stagnation plane (thereby affecting the temperature time history of the growing soot particles) are expected depending on :

(1) Location of the non-premixed flame with respect to the stagnation plane

i.) *Case 1* Flame on the oxidizer side of the stagnation plane.

ii.) *Case 2* Flame on the fuel side of the stagnation plane.

(2) Inlet stream which is partially premixed

i.) Partial premixing on the fuel side (oxygen added to the fuel side).

ii.) Partial premixing on the oxidizer side (fuel added to oxidizer side)

Effect of fuel side as well as oxidizer side partial premixing for both the cases of the nonpremixed flame configuration are considered in this study. Although the effect of oxidizer side partial premixing on soot formation, not reported in the previous literature to the best of our knowledge, has been studied herein, more effort was spent on fuel side partial premixing which is of more technological importance.

The experiments were conducted in the unique low strain rate (~10 sec^{-1}) CFDF burner described in Chapter 3. All measurements were carried out along the stagnation streamline. Soot volume fraction and particle size distribution were inferred from laser light extinction and scattering measurements using a 514.5nm Ar+ laser. Mie scattering theory for spheres with lognormal size distribution and soot complex refractive index of 1.57-0.56i was assumed. Temperature in the flame was measured using a Pt/Pt-10%Rh thermocouple of wire diameter 0.20mm. The thermocouple was coated with SiO2 to prevent catalytic reactions. The repeatability of measurement was within ±10K. Gaseous species including CO, H2O, H2, O2, CH4, N2, He as well as C2 species were measured on wet basis using gas chromatographic analysis of gas samples collected from the flame. These species measurements were accurate to within ±5% except for water for which larger variations were observed. OH concentration distribution was

measured using Laser Induced Fluorescence technique. The details of the experimental techniques are described in Chapter 3.

Two nonpremixed flames, Flame1.0 and Flame4.0, studied previously by Atreya et al. [41] were used as the base non-premixed flames to study the effect of partial premixing on soot growth processes. Flame 1.0 is a representative flame for the *case 1* of the non-premixed flame configuration (the flame is located on the oxidizer side of the stagnation plane) as shown in the flow visualization photograph, Fig. 3.15. Flame 4.0 is a representative flame for the *case 2* of the non-premixed flame configuration (the flame is located on the fuel side of the stagnation plane) as shown in the flow visualization photograph, Fig. 3.16. The specifications for the base non-premixed flames are reported in the Tables 5.2 and 5.3 respectively. The burner inlet temperatures of the reactants were used to evaluate the adiabatic flame temperature and the tabulated global strain rate is defined as the difference in the gas axial velocities at the two inlet ports divided by the burner gap. The choice of the inert diluents, Helium and Nitrogen, was made for buoyant stabilization of these low strain rate flames.

In the first set of experiments the effect of partial premixing on Flame 1.0 was considered. Flame1.0 is located on the oxidizer side of the stagnation plane as indicated by βstoic=.1305. Flames1.1, 1.2 and 1.3 corresponding to 6.73%(βstoic=.1917), 9.42%(βstoic=.2211) and 11.96% (βstoic=.2523) oxygen (on molar basis) in the fuel side inlet mixture were studied to investigate the effect of fuel side partial premixing on Flame1.0. Flames1.5 and 1.4 corresponding to 4.37%(βstoic=.1031), 7.75%(βstoic=.08) methane (on molar basis) added to the oxidizer side inlet mixture were studied to see the effect of oxidizer side partial premixing on Flame1.0. The specifications for these flames have been tabulated in the Table 5.2.

In the second set of experiments the effect of partial premixing on Flame 4.0 was considered. Flame4.0 is located on the fuel side of the stagnation plane as indicated by βstoic=.6392. Flames4.1 and 4.2 corresponding to 2.69%(βstoic=.6623) and

4.84%(βstoic=.6817) oxygen (molar basis) in the fuel side inlet mixture were studied to investigate the effect of fuel side partial premixing on Flame4.0. Flame4.3 corresponding to 4.02%(βstoic=.5888) methane (on molar basis) in the oxidizer side inlet mixture was studied to observe the effect of oxidizer side partial premixing on Flame4.0. The specifications for these flames have been tabulated in the Table 5.3.

Computations were carried using the Sandia opposed flow flame code, OPPDIF, [33], modified by Kim, [35], to include an optically thin model of soot and gas radiation as described in the Chapter 2. The GRIMech 3.00, [56], mechanism was used with the recommended multi-component transport and thermo-chemical database. The boundary conditions at the inlets included measured inlet temperature; velocity and the species flux at each of the two inlets 2.9 cm apart. The converged solution was checked for dependence on the initial grid and the choice of convergence parameters.

The results from this study are presented and discussed in the sections 5.2.1 and 5.2.2 for the two cases of the non-premixed configuration.

5.2.1. Case1: Nonpremixed Flame on the Oxidizer side of the Stagnation Plane

Non-premixed Flame

Fig. 3.15 shows flow visualization photograph for flame 1.0. Flame 1.0 is a sooty methane flame with soot zone on the oxidizer side of the stagnation plane. Computed distribution of stable species is shown in fig 5.1 (a). Atreya et al.,[41], found good agreement between computed and measured distribution of major species and C2-species (except acetylene) for this flame. The fuel and the oxidizer diffuse from the respective inlet ports towards the non-premixed flamesheet located on the oxidizer side of the stagnation plane. Energy release distribution in this flame is shown in Fig. 5.3(a). Soot formation begins on the fuel rich side of the peak flame temperature location. Soot particles grow as they are driven by the flow field towards the stagnation plane in a fuel rich region as shown in Fig. 5.5(a). The particles grow in size as well as the mass

(volume) fraction of the soot increases as the particles are driven by the flow-field towards the stagnation plane.

The effects of partial premixing on the *flame structure* and *soot formation* for this flame are discussed next.

Effects of Partial Premixing

The trends observed in the measured soot zone thickness, peak soot volume fraction and peak aggregate sizes with both fuel side partial premixing as well as oxidizer side partial premixing of Flame1.0 are summarized in Fig. 5.6. The choice of the horizontal axis is appropriate for this purpose as the value of β_{stoic} uniquely identifies a partially premixed variant of the given nonpremixed flame. Fuel side partial premixing is indicated by increasing values βstoic and oxidizer side partial premixing is indicated by decreasing values of βstoic in Fig 5.6. The values of β_{stoic} corresponding to different flames used in this work are included in Table 5.2.

The values of the measured peak soot volume fraction, soot zone thickness and the peak soot particle diameter initially decreased and then increased with increasing levels of fuel side partial premixing. The present work shows that the net effect of fuel side partial premixing on *soot growth* can be to increase or to decrease the sooting tendency of the flame.

As shown in the Fig. 5.6 oxidizer side partial premixing caused the peak soot loading in the flame to decrease monotonically with increasing levels of fuel added into the oxidizer side. The peak soot diameter decreased after a small (comparable to the experimental error of ± 4nm) increase.

The effect of *fuel side* partial premixing on the flame structure and soot growth are discussed in more detail next followed by a discussion of *oxidizer side* partial premixing.

Fuel side Partial Premixing

(a) Flame structure

The distribution of major stable species for the non-premixed flame and its partially premixed counterparts flames 1.1, flame 1.2 and flame 1.3 are shown in Figs.5.1. The measurements are indicated by symbols while the computed distribution is indicated by solid lines in these figures. With the exception of water, measured major species distribution shown in figs 5.1 agreed well with computations. Analysis of water was not as good as other species since it is a polar compound and a portion of water was retained in the G.C. column in spite of efforts to condition the column and post-run hold period at high temperature. Recently, Barlow et al. ,[80], have reported good agreement with computed species distribution for major species, measured using Raman technique in rich methane air counterflow flames. In the Fig 5.1 (c) for the partially premixed flame, flame 1.2, the premixed reaction zone can be identified by disappearance of the molecular oxygen added to the fuel side. As shown in the figure, this happens very close to the stagnation plane (indicated by a vertical line) for flame 1.2. Likewise in Fig 5.1 (d) for the partially premixed flame, flame 1.3, the premixed reaction zone is located on the fuel side of the stagnation plane. Tusji and Yamaoka, [3], identified the cross over of the premixed reaction zone from the oxidizer side of the stagnation plane to the fuel side of the stagnation plane as the onset of "interdependent-flames" regime. The spatial separation of the non-premixed and the premixed reaction zones is emphasized by plotting the species mole fraction on a log scale as in Figs. 5.2 (a-c).

It is also evident from Figs. 5.2 that with progressive partial premixed the non-premixed flame sheet, identified with the peak flame temperature for the purpose of this discussion, moved closer to the fuel side (also stagnation plane in this case). This can be qualitatively explained using the theoretical analysis, presented in chapter 4, as a consequence of a) dilution of the fuel b) consumption of a fraction of the fuel in the premixed reaction sheet.

Computed energy release distribution for the non-premixed flame 1.0 and its partially premixed counterparts is shown in Figs. 5.3. For the non-premixed hydrocarbon flame, flame 1.0, the energy release takes place in two major steps shown as 'peak 1' and 'peak 2' in the fig 5.3 (a). In the first step, corresponding to the 'peak 1', fuel is partially oxidized to CO and H2, which in turn are oxidized to CO2 and H2O in the second step corresponding to the 'peak 2'. In partially premixed flames, Figs 5.3(b-d), in addition to these two energy release peaks, energy release takes place in 'peak 3' which corresponds to consumption of oxygen added to the fuel in a rich premixed reaction zone. With progressive partial premixing the relative importance of energy release in the premixed reaction zone, represented by 'peak 3', increases. Furthermore, it is observed that for the non-premixed reaction zone, the relative importance of 'peak 2' increases in comparison to that of 'peak 1' with progressive partial premixing. This is explained by the observation that more and more CO and H2 'fuel' is made available by the premixed reaction zone. In fig 5.1(d) a relatively flat distribution of CO and H2 species is observed for the "interdependent-flames" regime flame, flame 1.3. For this flame the rich premixed energy release ('Peak 3') is indeed on the fuel side of the stagnation plane, Fig.5.3 (d), as expected on the basis of observation of consumption of molecular oxygen added to the fuel side as discussed earlier.

(b) C2 species

Stable c2 hydrocarbon species distribution is shown in Figs. 5.4 (a-d) for the non-premixed flame 1.0 and its counterparts obtained by fuel side partial premixing. C2 hydrocarbon species are important intermediates in oxidation of methane. Furthermore, C2H2 is considered to be an important species for soot inception and surface growth of soot nuclei. Several computational models for soot prediction rely on C2H2 very heavily.

The agreement between the experiments and the measurements for C2 species is good for C2H6 and C2H4, Figs.5.4 (c-d). C2H2 is over predicted in both the cases that the author has experimental data for. Similar observation was reported by Atreya et

al.,[41], for flame 1.0. This result may be a consequence of either incorrect rate of formation of C2H2 or incorrect rates for destruction of C2H2. It is noted that GRIMech3.00 has a limited mechanism for getting from C2 to C3 species.

The computed peak mole fractions of the C2 hydrocarbon species are spatially separated with C2H6 peaking first, then C2H4 followed by C2H2 with increasing distance from the fuel side inlet. The feature was seen in our experimental measurements in figs 5.4 (c-d). Some recent measurements, [81](Gore, 2000), of C2 species in counter-flow non-premixed flames have not been able to show this feature of C2 chemistry. We were able to record this feature of C2 chemistry since a separate gas chromatograph, with higher detector sensitivity, was used to analyze C2 species in the gas samples extracted from the flames.

(c) Soot zone thickness

Measured distribution of soot volume fraction and particle diameter is shown in figs 5.5 for the non-premixed flame 1.0 and its partially premixed counterparts. As summarized earlier, fig 5.6, the thickness of the soot zone first decreased and then increased. In the merged flame regime, which is similar to non-premixed flame, the soot zone is limited to the distance between the non-premixed flame and the stagnation plane. In Figs 5.5 (a-c) that soot formation begins on the fuel rich side of the OH zone and soot mass growth takes place as soot is driven towards the stagnation plane. The initial decrease in the thickness of the soot zone, from flame 1.0 to flame 1.2, is attributed to the decrease in the distance between the non-premixed flame and the stagnation plane in the merged flame regime. Subsequent increase in the thickness of the soot zone is attributed to soot growth taking place in between spatially separated premixed and non-premixed flame sheets in the 'interdependent regime', flame 1.3, as shown in Fig5.5 (d).

(d) Soot growth and importance of flow field effects

Three important factors affecting soot growth are the temperature, residence time and the chemistry in the soot growth region. Previous literature, [13,18], has reported that

the chemical effect of oxygen added to the fuel is to suppress inception of soot and formation of soot precursors in alkane fuel flames. The presence of molecular oxygen in the soot growth region of partially premixed flames 1.2 and 1.3 is evident in the measured species distribution, Figs. 5.1 (c-d). Therefore, soot growth and oxidation can take place simultaneously in these flames unlike in the case of non-premixed flame 1.0. The dilution effect of oxygen added to the fuel side is to suppress the sooting tendency of the flame. As discussed earlier, with progressive partial premixing on the fuel side, the peak flame temperature moves closer to the stagnation plane resulting in increase in temperature in the vicinity of the stagnation plane. This results in favorable temperature time histories for soot particles. The observed initial decrease in the peak soot volume fraction cannot be attributed to the residence time effect and must have come from the combined effects of dilution and suppressive chemical effect of oxygen added to the fuel side. Subsequent increase in the peak soot volume fraction, going from flame 1.2 to flame 1.3, may be attributed to favorable temperature-time effect. In flame 1.3 soot growth takes place in spatially separated premixed and non-premixed reaction zones on either side of the stagnation plane as shown in Fig 5.5(d). The difference in the shapes of soot volume fraction distribution for the merged flame regime flame, flame1.1, and the inter-dependent regime flame, flame 1.3, are noteworthy. In flames 1.0 and 1.1 the soot volume fraction profile shows an increase in soot volume fraction as soot particles are carried towards the stagnation plane. In contrast to the above situation in Fig. 5.5(d) the soot volume fraction profile shows growth taking place on fuel side of the stagnation plane followed by oxidation as soot runs into the OH zone.

Another interesting example to illustrate the effect of flow-field changes due to partial premixing on soot growth is presented next. Size of the soot particles can increase as a consequence of surface mass growth as well as by agglomeration. Observation of the measured soot distribution in Figs. 5.5(b-c) indicates that while the soot mass growth (indicated by the peak soot volume fraction) decreased in going from flame 1.1 to flame

1.2, the largest aggregate size increased. This implies that the flame 1.1 has 'large number of small particles' near the stagnation plane while the flame 1.2 has 'small number of large particles'. The increase in peak particle size for flame 1.2, in spite of suppression of net mass growth, must have come from an increase in aggregation rates. Aggregation rates are directly proportional to the temperature.[i] The increase in aggregation in flame 1.2 in comparison to flame 1.1 can be attributed to an increase in temperature in the high residence time region near the stagnation plane as progressive partial premixing causes the non-premixed flame to come closer to the stagnation plane. This observation clearly highlights the importance of the changes in the flow field and temperature field of soot particles for soot growth process.

Oxidizer side Partial Premixing

The computed distribution of major species, measured temperature and chemical energy release in flame 1.5 obtained by oxidizer side partial premixing is shown in the figs 5.7 (a) and 5.7(b). The location of the stagnation plane is marked by a vertical line in these figures. The temperature profile, Fig.5.7 (a), indicates that the fuel added to the oxidizer side is consumed under fuel lean conditions about 1.5 mm from the oxidizer side port. This is also indicated in the computed energy release distribution, Fig5.7 (b). Comparison of species profiles, Fig. 5.8, plotted on a log scale for the non-premixed flame 1.0 and the flame 1.5 indicate that the non-premixed flame sheet, which is originally on the oxidizer side of the stagnation plane, moves further away from the stagnation plane, as expected on the basis of the flamesheet analysis presented before.

The distribution of the measured soot and OH radical concentration is compared in figs 5.9 for the non-premixed flame 1.0 and flame 1.5. The soot volume fraction profile in both the cases is similar in shape with soot inception beginning at the fuel side

---

[i] Although the difference in the tempearture at the stagnation plane for the two flames is about 100K the effect on aggregation is noticable due to large residence time near the stagnation plane.

edge of the OH region and soot mass growth taking place as the particles are convected towards the stagnation plane by the flow-field. It is observed that the peak soot loading decreased with partial premixing in this case. The fuel added to the oxidizer side for partial premixing can not have any chemical effect on soot formation since it gets consumed under fuel lean conditions. The dilution effect of the less than 1% (by volume) fuel added to the oxidizer can be neglected too. The movement of the (non-premixed) flame away from the stagnation plane resulting in lower temperatures in the high residence time region near the stagnation plane is in line with lowering of the peak soot loading as observed in the experiment.

5.2.2. Case2: Nonpremixed Flame on the Fuel side of the Stagnation Plane

Non-premixed Flame

Figure 3.13 (b) shows a flow visualization photograph of the non-premixed flame, flame 4.0. The soot zone appears as a thin very intensely radiating zone. The flow visualization picture indicated that the flame is on the fuel side of the stagnation plane. The computed distribution of stable species, temperature and energy release are shown in figs 5.10(a-b). Atreya et al., [41], have reported measured major species and C2 species distribution in this flame. The measured distribution of soot volume fraction, OH radical concentration and temperature are shown in fig 5.14 (a). It is observed from fig 5.14(a) that soot formation begins on the fuel rich side of the peak flame temperature. The soot particles are driven into the OH zone by the flow field where they are completely oxidized before reaching the stagnation plane. Soot volume fraction first increases and then decreases as the soot particles are driven towards the stagnation plane by the flow field. As a result, all the soot produced along the stagnation streamline is consumed internally in this non-premixed flame configuration. Soot formation for this configuration is discussed in Atreya et al., [41], and described as "soot formation-oxidation" flame configuration by Chung et al., [82].

The effect of partial premixing on soot formation is discussed next for this non-premixed flame configuration.

Effect of Partial Premixing

Figure 5.13 summarizes the effects of fuel side partial premixing as well as oxidizer side partial premixing of the nonpremixed flame, flame 4.0, which was originally on the fuel side of the stagnation plane. While fuel side partial premixing showed a monotonic decrease in the sooting tendency of the flame with an eventual transition to a nonsooty flame, oxidizer side partial premixing showed an increase in the peak soot loading in the flame.

Fuel side Partial Premixing

Distribution of major species for the partially premixed flames 4.1 and 4.2 are shown in fig 5.11-12(a). Corresponding energy release distribution is shown in figs 5.11-12(b) while the distribution of C2 species and OH are shown in figs 5.11-12(c).

The measured distribution of major species agreed well with computations for the flame 4.1. The agreement for OH is acceptable for flames 4.1 and flame 4.2. Computed C2H6 and C2H4 agreed well with experimental data, fig 5.11(c), while C2H2 was over predicted.

Comparison of soot volume fraction distribution for the non-premixed flame, flame 4.0, and its partially premixed counterpart, flame 4.1, shows an order of magnitude decrease, Fig. 5.14, in the peak soot volume fraction. This decrease cannot be attributed completely to the small dilution effect of approximately 3% (by volume) oxygen added to the fuel side. Instead, the decrease may be attributed to the competition between soot growth and oxidation, as oxygen is present in the soot growth region of the partially premixed flame. The 'chemical' effect of oxygen added to the fuel side of alkane fuels has been identified in the previous literature, [13,18], to suppress soot inception and formation of soot precursor species.

Oxidizer side Partial Premixing

The distribution of major species, energy release and C2 species are shown in figs. 5.15(a-c) respectively for the partially premixed flame 4.3 obtained by oxidizer side partial premixing of the non-premixed flame 4.0. The temperature profile, Fig. 5.15(a), indicates that the premixed reaction zone is located about 2 mm from the oxidizer side inlet where the fuel added to the oxidizer is consumed under fuel lean conditions. The energy release distribution, Fig. 5.15(b), shows corresponding energy release, represented by 'peak 3', due to premixed combustion. In contrast to the fuel rich premixed reaction zone with fuel side partial premixing, where CO and H2 are created, the fuel-lean premixed reaction zone with oxidizer side partial premixing creates CO2 and H2O. The computed OH profile, fig 5.15(c), agrees well with the experimental OH data. The computed OH profile in the 'post-flame region' of the fuel lean flame is quite flat. This flat region (about 8mm from the oxidizer inlet) was not accessible to the optical diagnostics.

The measured soot volume fraction distribution for the non-premixed flame 4.0 and the partially premixed flame 4.3 are shown in figs 5.16 (a-b). The peak soot volume fraction increased with oxidizer side partial premixing for the level of partial premixing studied. The fuel added to the oxidizer side gets consumed under fuel lean conditions and it cannot participate chemically in soot formation. The effect of dilution is small and would inhibit soot formation. Therefore, the observed increase in the peak soot volume fraction may be attributed to the changes in the temperature-residence time effects brought about by the oxygen added to the oxidizer side. Firstly, the original non-premixed flame, flame 4.0, was deficient in fuel; therefore, addition of fuel to the oxidizer side results in an increase in the peak flame temperature. Secondly, as shown in figs 5.16, with addition of fuel to the oxidizer side, the non-premixed flame, which is originally on the fuel side of the stagnation plane, comes closer to the stagnation plane (fuel side), as expected qualitatively on the basis of flamesheet analysis presented before.

Both these factors favor an increase in residence time in the high temperature soot formation zone which in turn results in an increase in the peak soot loading.

Fuel	*Co-flow flames*	***Counter-flow flames***
Methane	• Saito et al.(86) • McEnally and Pfefferle(99) • Guilder (95)	Mungekar and Atreya (00,01)
Ethane	• Long and Chakraborty(68)	
Propane	• Wey et al. (84) • Glassman and Hura(88) • Guilder(95)	• Law et al.(90) • Glassman and Hura (87,88)
n-Butane	• Glassman and Hura (87) • Guilder(95)	
Ethylene	• Long and Chakraborty(68) • Glassman and Hura (87,88) • Mitrovich and Lee (98)	• Glassman and Hura (88) • Law et al.(90) • Chung et al.(98)
Propylene	• Glassman and Hura (87)	
Acetylene		• Peters N. et al. (94,00)

Table 5.1 Previous studies of soot formation in partially premixed flames

	Fuel Side	Oxidizer Side
Flame1.0	Tad = 2662 K Global Strain Rate =6.65 1/sec	
β=.1305	71.1%He+28.9%CH4 V=13.6cm/sec,T=592K	57.4%N2+42.6%O2 V=5.7cm/sec, T=667K
Fuel Side Partial Premixing		
Flame1.1	Tad = 2698 K Global Strain Rate =6.97 1/sec	
β=.1917	66.4%He+26.9%CH4+6.73%O2 V=13.7cm/sec,T=556K	57.4%N2+42.6%O2 V=6.52cm/sec, T=753K
Flame1.2	Tad = 2711 K Global Strain Rate =7.3 1/sec	
β=.2211	64.4%He+26.1%CH4+9.42%O2 V=14.7cm/sec,T=577K	57.4%N2+42.6%O2 V=6.47cm/sec, T=746K
Flame1.3	Tad = 2723 K Global Strain Rate = 7.4 1/sec	
β=.2523	62.6%He+25.4%CH4+11.95%O2 V=15.0cm/sec,T=574K	57.4%N2+42.6%O2 V=6.47cm/sec, T=747K
Oxidizer Side Partial Premixing		
Flame1.5	Tad = 2777 K Global Strain Rate =8.45 1/sec	
β=.1031	71.1%He+28.9%CH4 V=14.1cm/sec,T=612K	54.9%N2+40.7%O2+4.37%CH4 V=10.4cm/sec, T=1145K
Flame1.4	Tad = 2806 K Global Strain Rate =8.41 1/sec	
β=.0800	71.1%He+28.9%CH4 V=13.6cm/sec,T=591K	52.9%N2+39.3%O2+7.75%CH4 V=10.8cm/sec, T=1145K

Table 5.2 Flame specification for flame 1.0 and its partially premixed counterparts

	Fuel Side	Oxidizer Side
Flame4.0	Tad = 2618 K Global Strain Rate =7.21 1/sec	
β=.6392	78.7%N2+21.2%CH4 V=8.78cm/sec,T=662K	47.8%He+52.2%O2 V=12.13cm/sec, T=682K
Fuel Side Partial Premixing		
Flame4.1	Tad = 2628 K Global Strain Rate =7.13 1/sec	
β=.6629	76.6%N2+20.7%CH4+2.69%O2 V=9.71cm/sec,T=712K	47.8%He+52.2%O2 V=10.98cm/sec, T=618K
Flame4.2	Tad = 2651 K Global Strain Rate =7.72 1/sec	
β=.6817	75.0%N2+20.2%CH4+4.84%O2 V=11.07cm/sec,T=794K	47.8%He+52.2%O2 V=11.32cm/sec, T=637K
Oxidizer Side Partial Premixing		
Flame4.3	Tad = 2692 K Global Strain Rate =8.47 1/sec	
β=.5888	78.7%N2+21.2%CH4 V=8.54cm/sec,T=644K	45.9%He+50.1%O2 +4.02%CH4 V=16.04cm/sec, T=866K

Table 5.3 Specifications for the flame 4.0 and its partially premixed counterparts

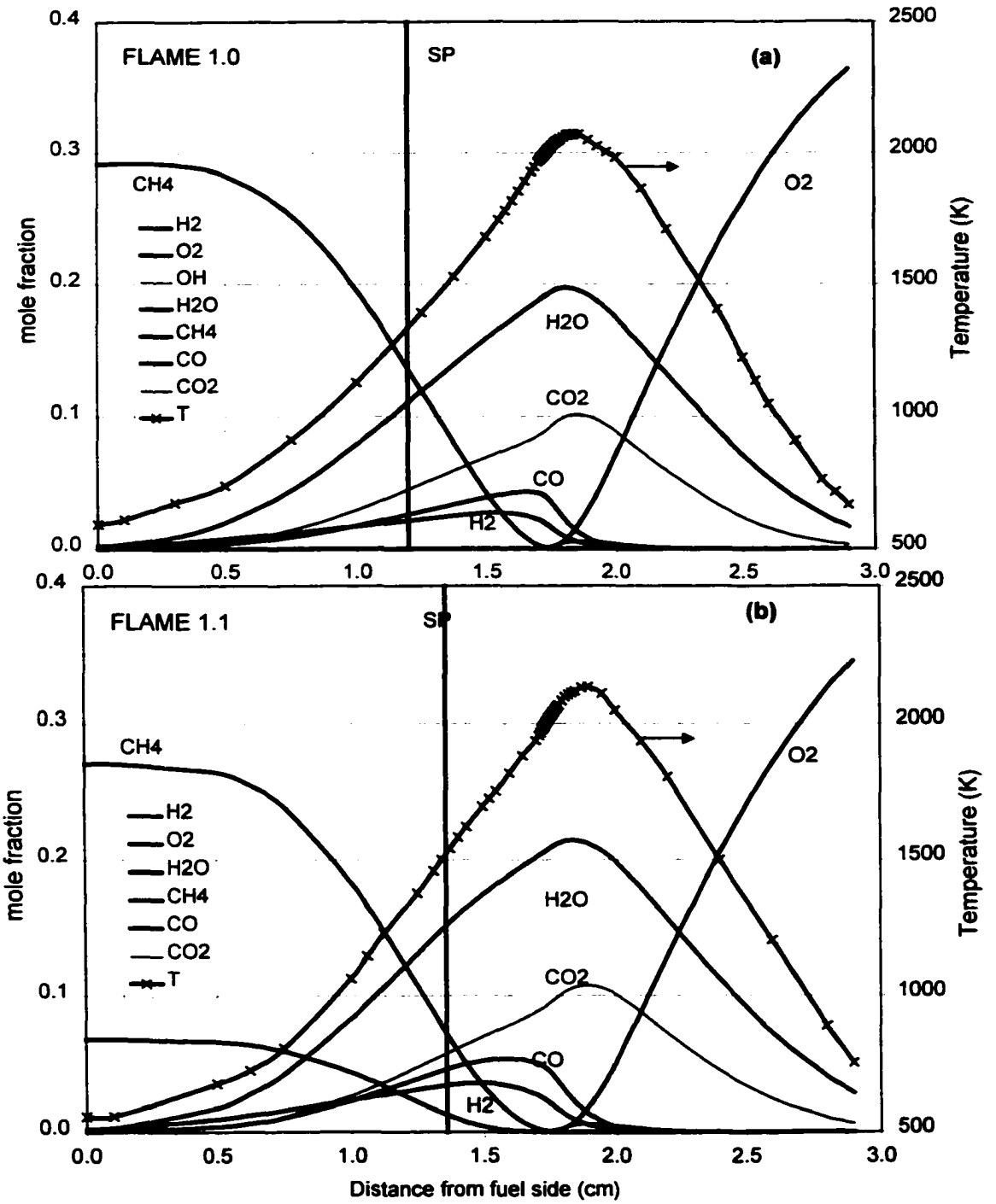

Fig 5.1 Tgiven computed distribution of major species and measured temperature in (a) non-premixed flame 1.0 (b) partially premixed flame 1.1

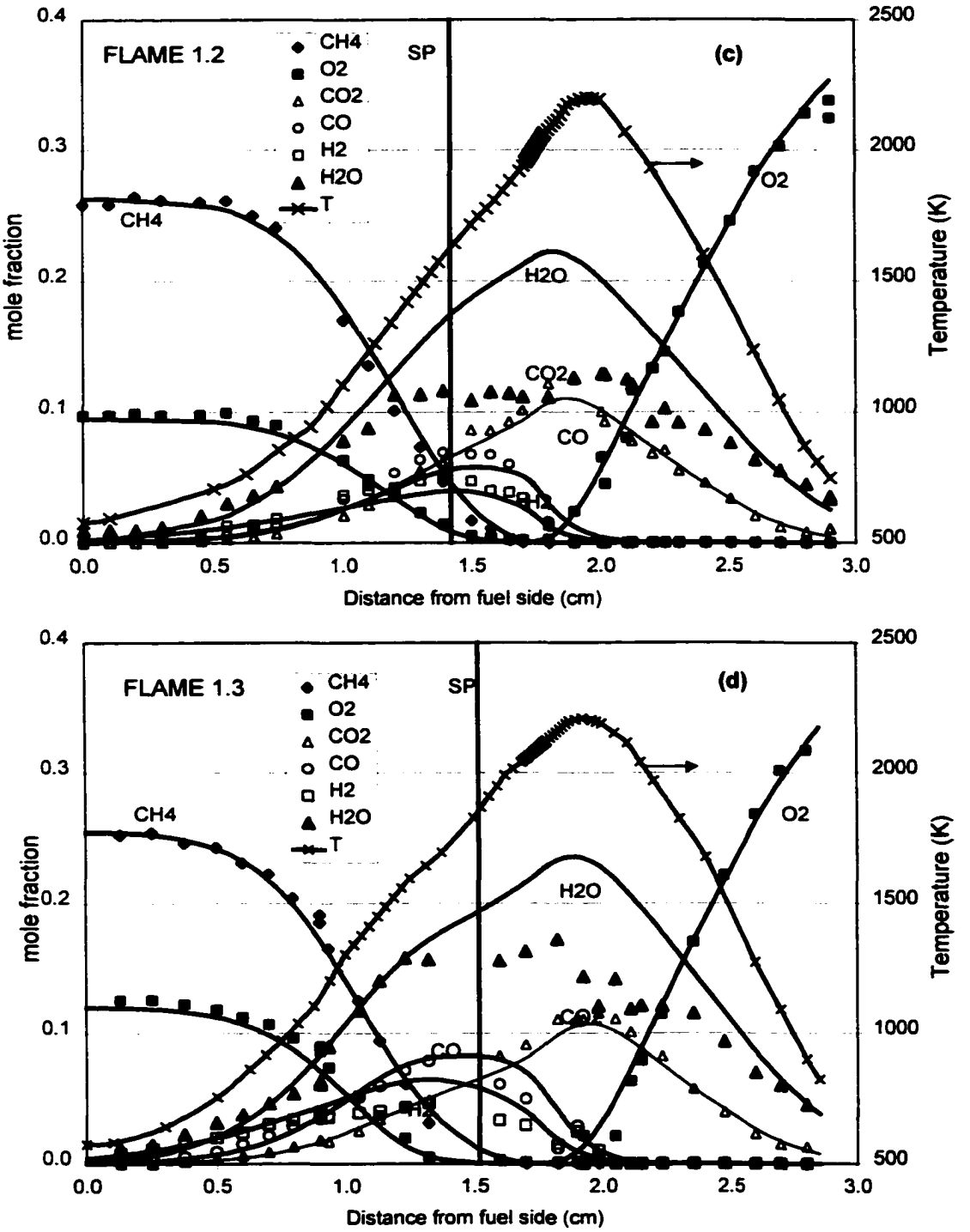

Fig 5.1 Tgiven computed and measured distribution of major species and temperature in Partially-premixed (c) flame 1.2 (d) flame 1.3

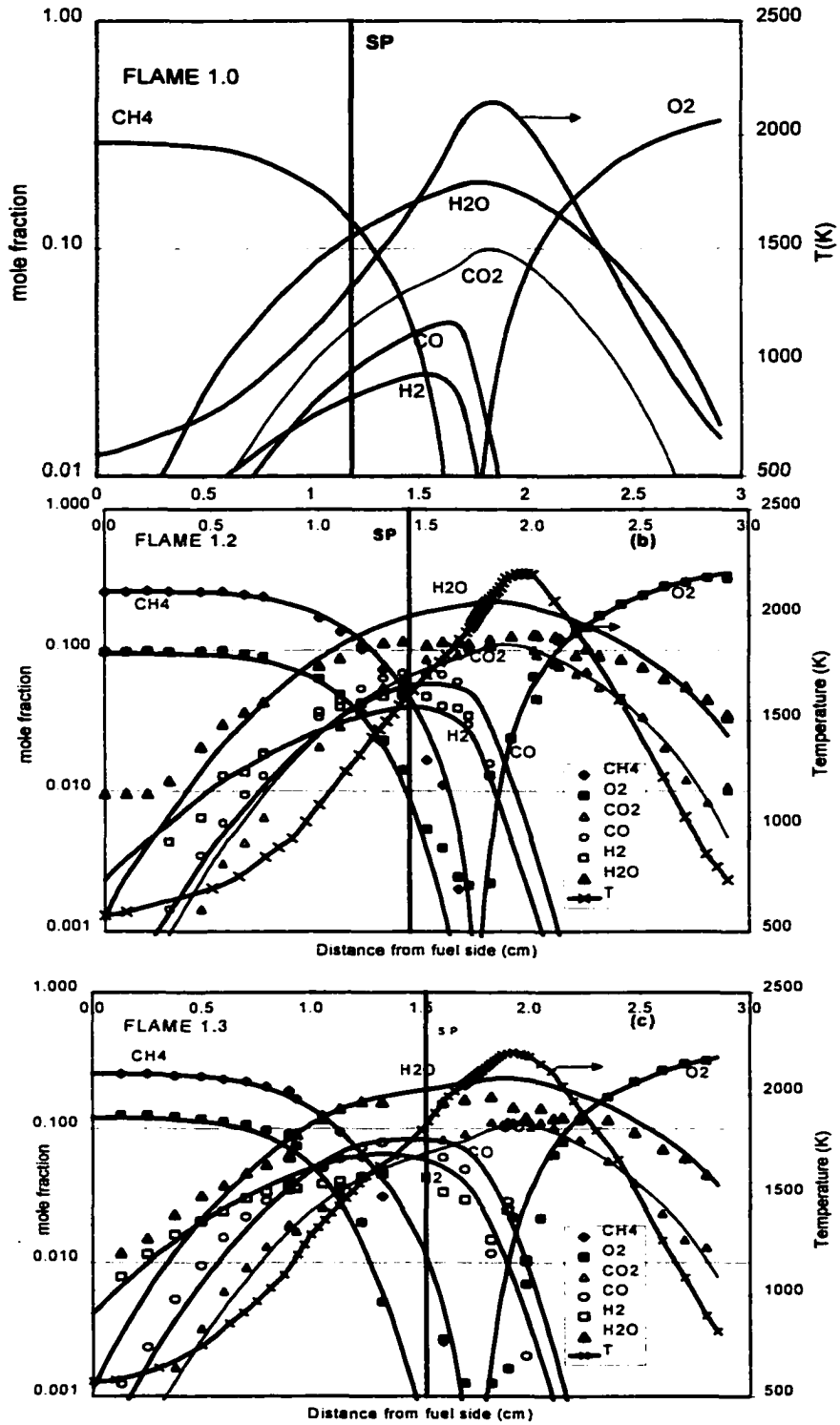

Fig 5.2 Comparison of species distribution in (a) non-premixed flame 1.0 and Partially premixed flames (b) flame 1.2 and (c) flame 1.3

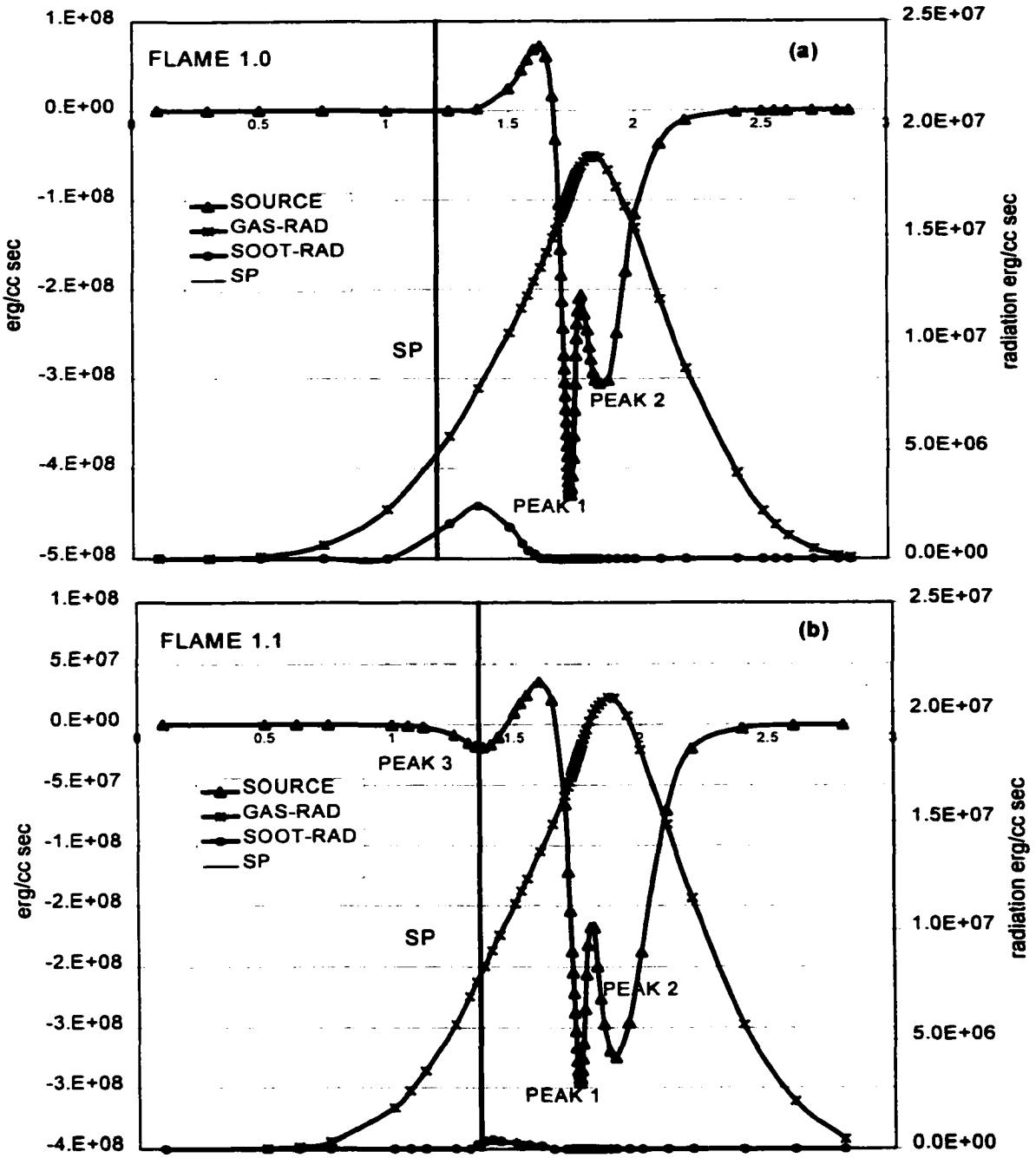

Fig 5.3 Tgiven computed distribution of chemical energy release and flame radiation in a) non-premixed flame 1.0 b) partially premixed flame 1.1

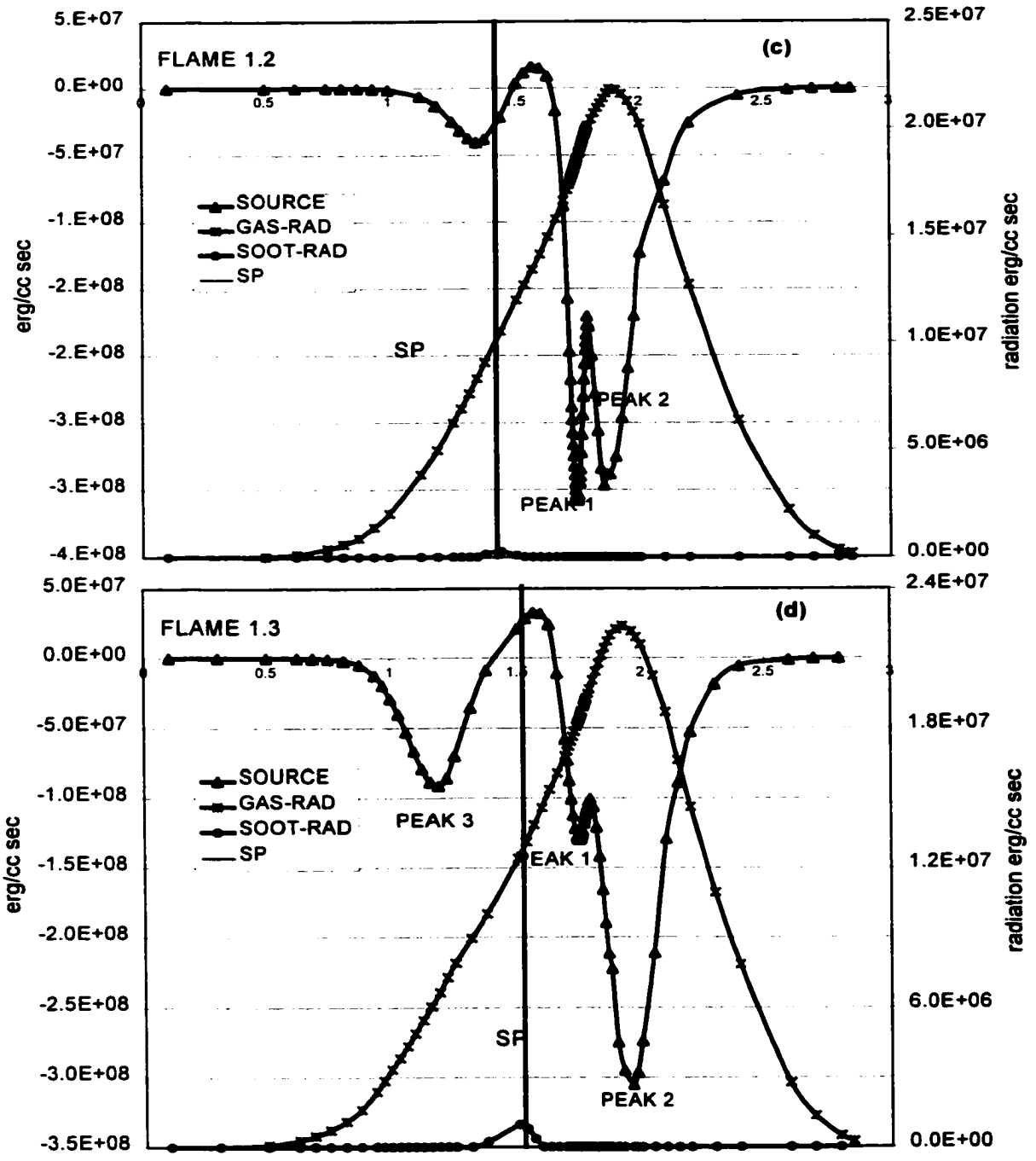

Fig 5.3 Tgiven computed distribution of energy release and flame radiation in Partially premixed flames (c) flame 1.2 and (d) flame 1.3

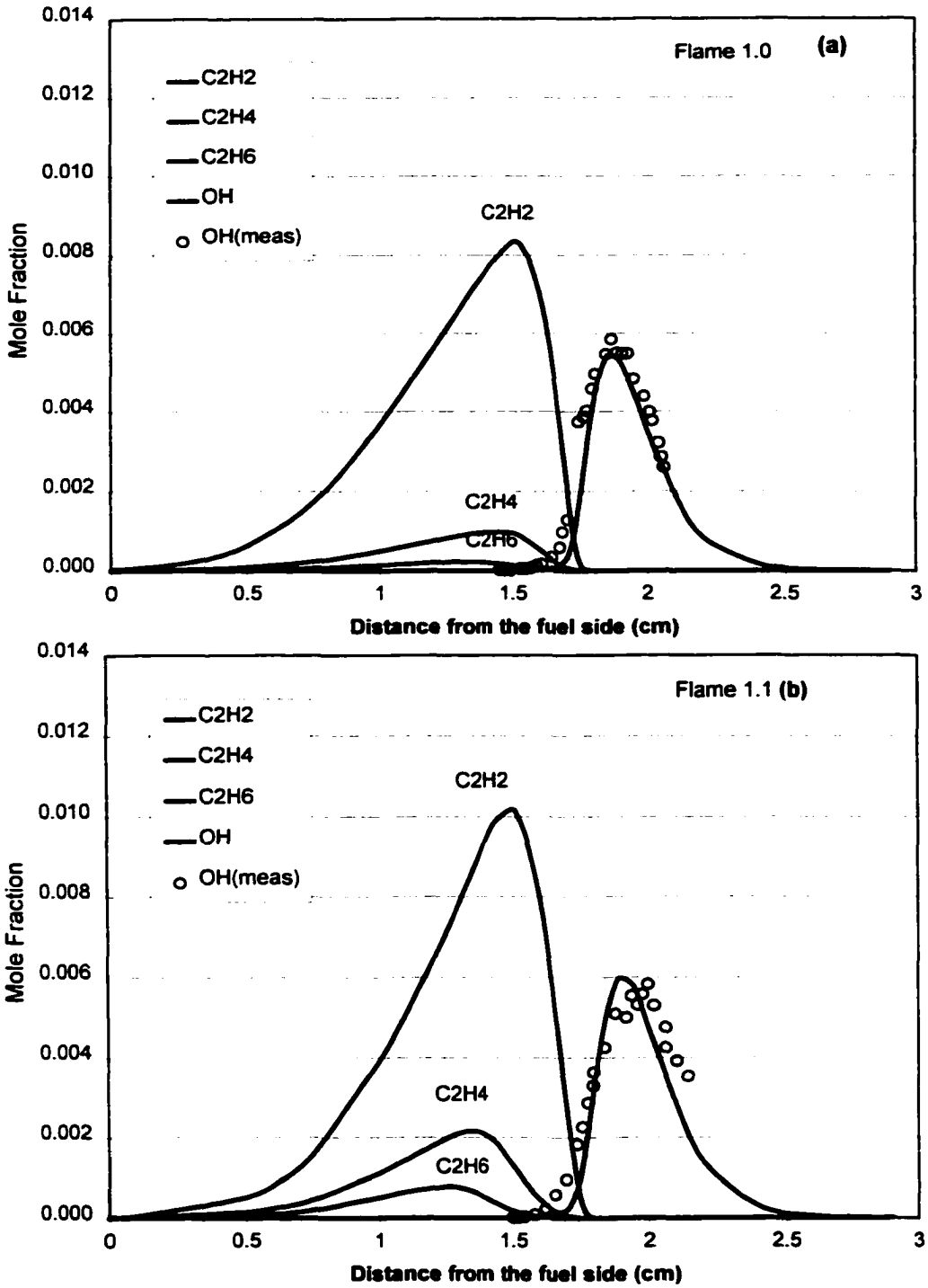

Fig 5.4 Tgiven computed distribution of C2 hydrocarbons and OH radical in (a) non-premixed flame 1.0 (b) partially premixed flame 1.1

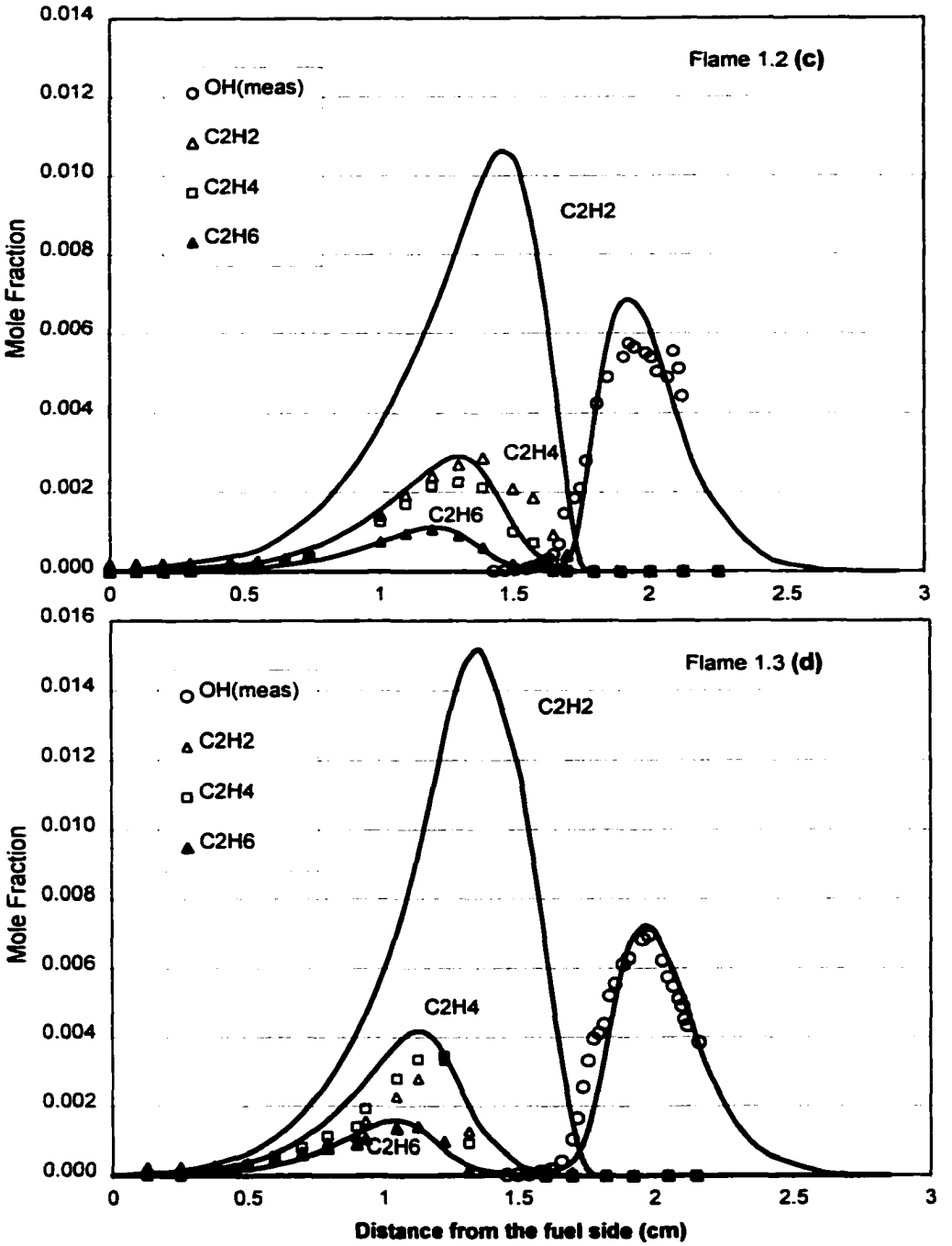

Fig 5.4 Comparison of computed and measured C2 hydrocarbon and OH in Partially-premixed (c) flame 1.2 and (d) flame 1.3

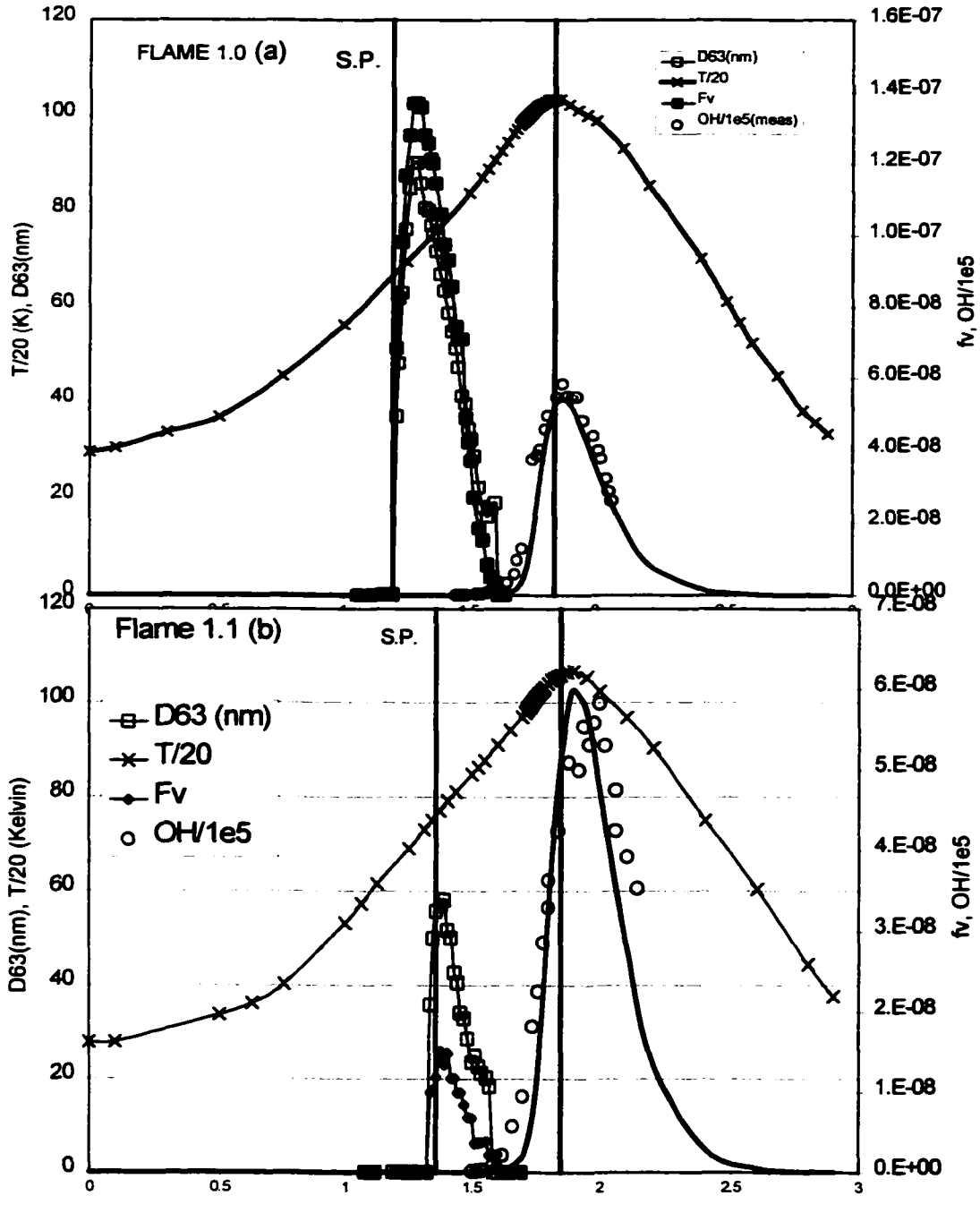

Fig 5.5 Distribution of measured soot, OH and temperature in (a) Non-premixed Flame 1.0 (b) Partially Premixed Flame 1.1

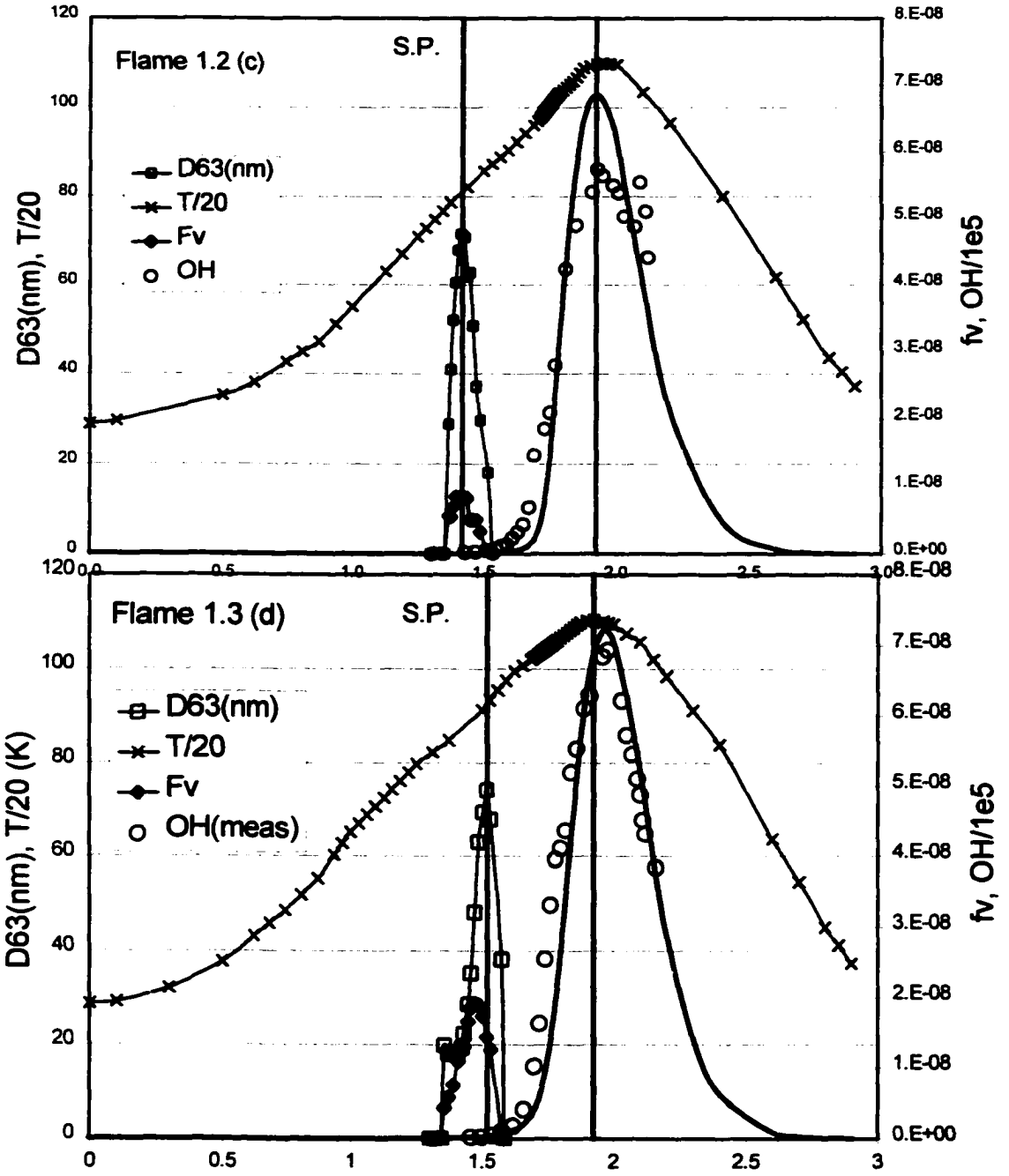

Fig 5.5 Distribution of measured soot, OH and temperature in Partially Premixed Flames c) Flame 1.2 and d) Flame 1.3

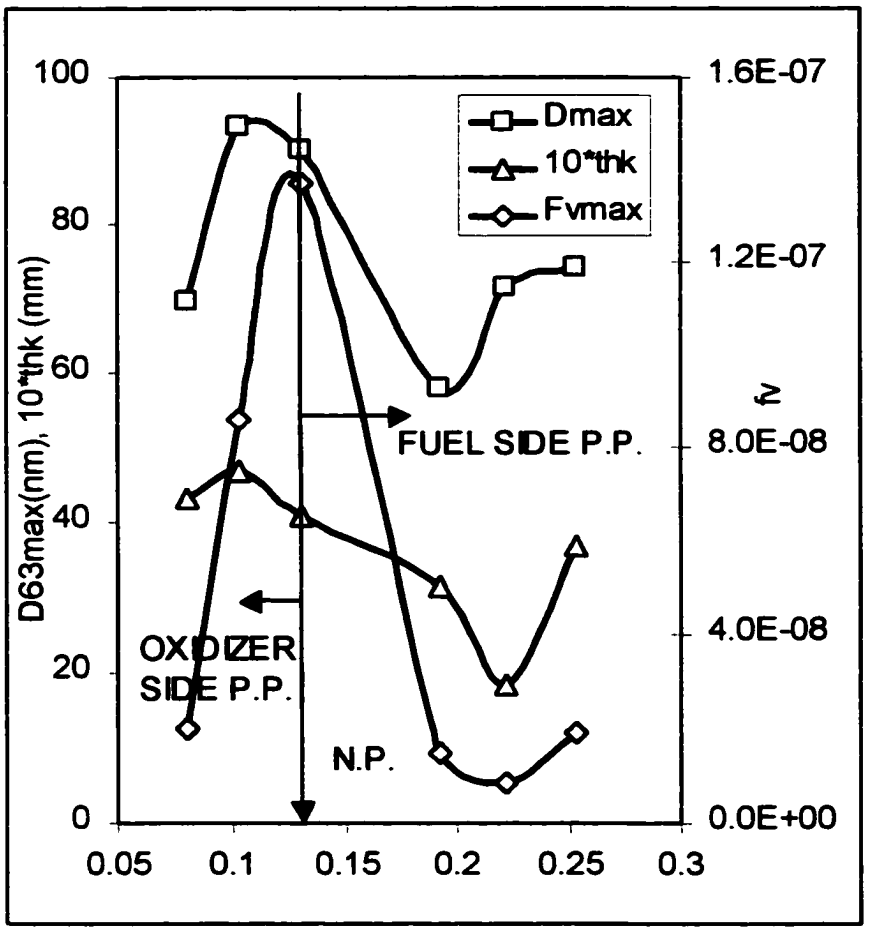

Fig 5.6 Measured trends in Peak Fv, D63 and soot zone thickness with partial premixing of Flame 1.0

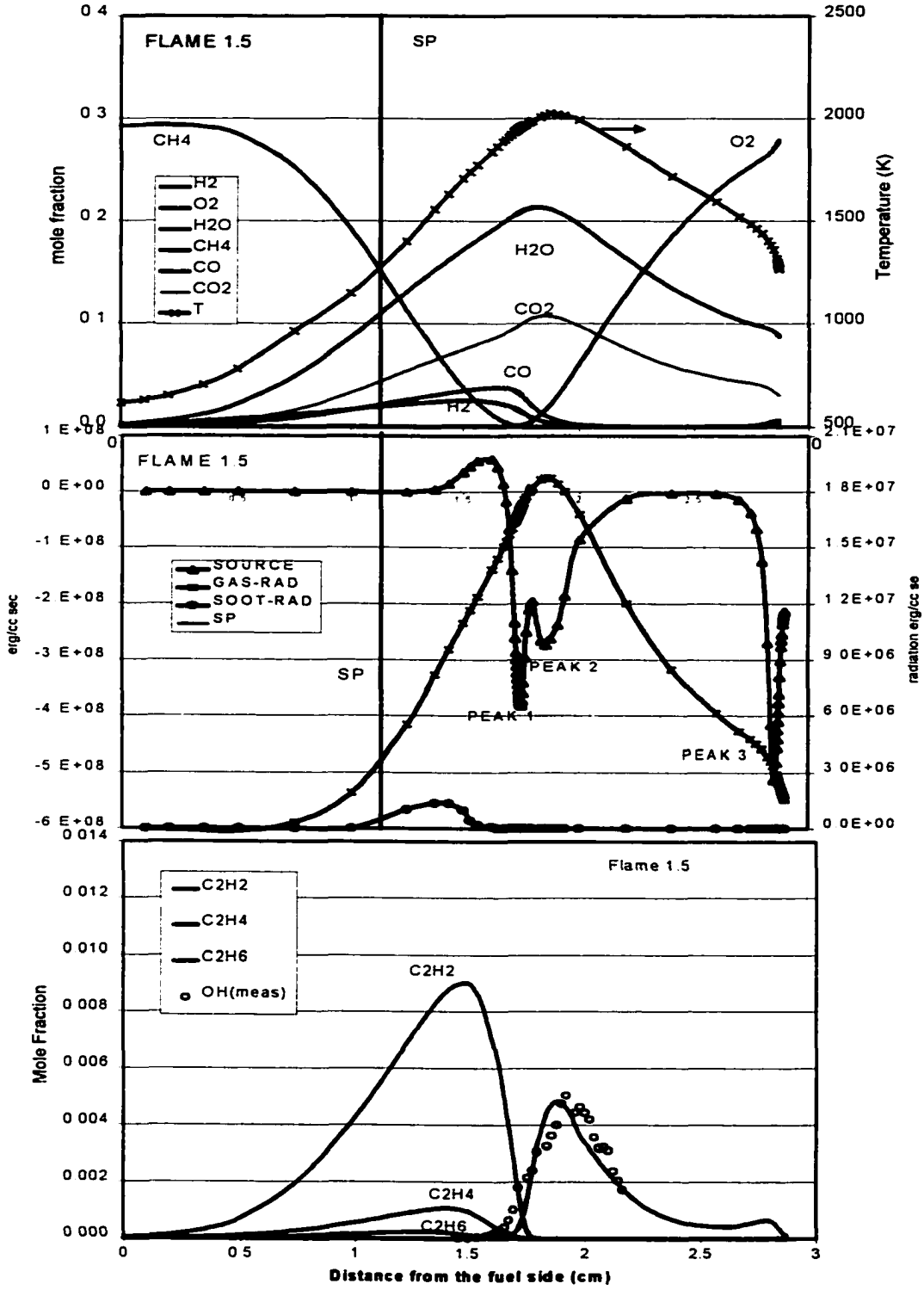

Fig 5.7 Computed distribution of a) major species and temperature b) energy release and flame radiation c) C2 and OH species in Flame 1.5

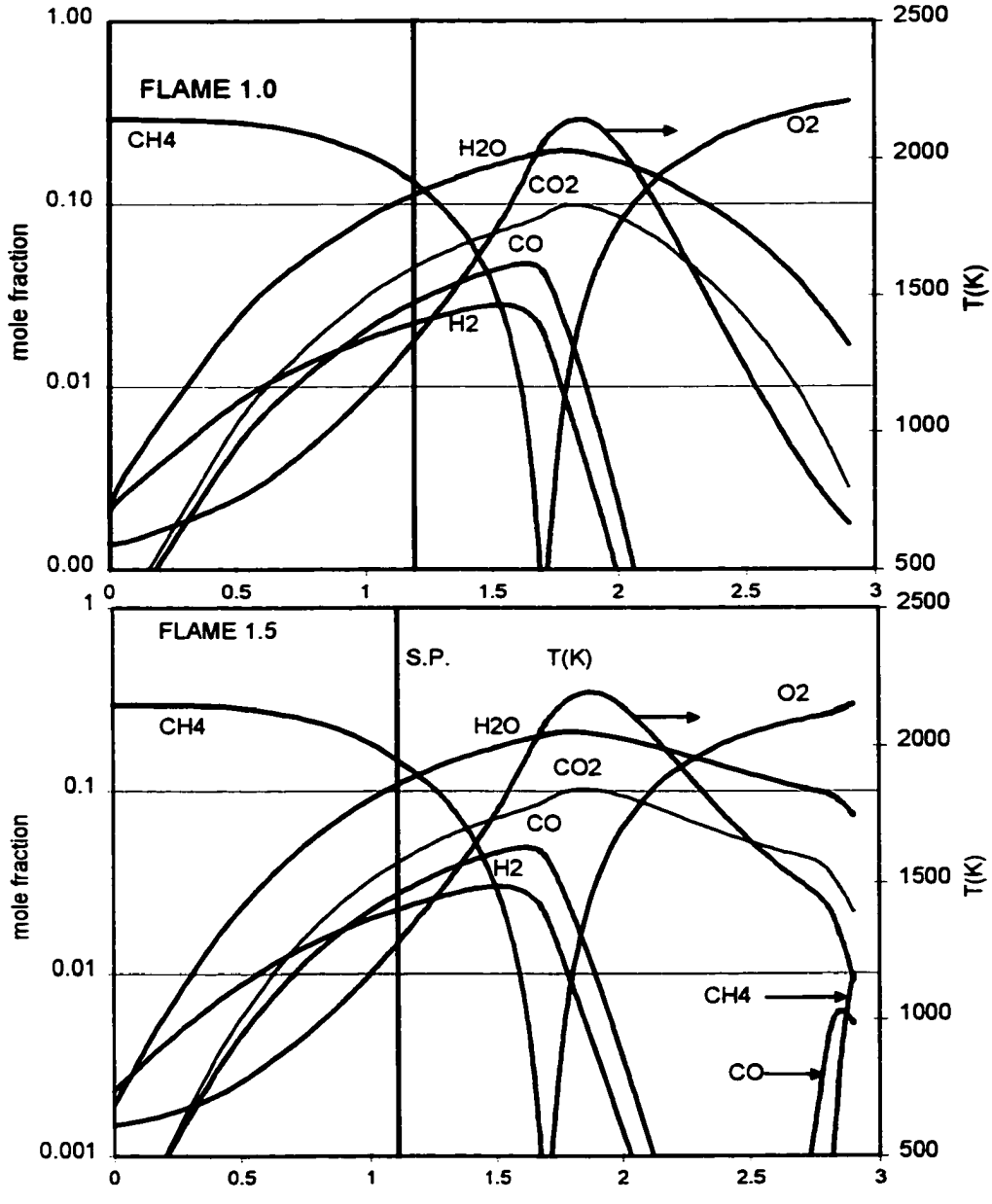

Fig 5.8 Computed distribution of major species and temperature in

(a) non-premixed flame 1.0 (b) partially premixed flame 1.5

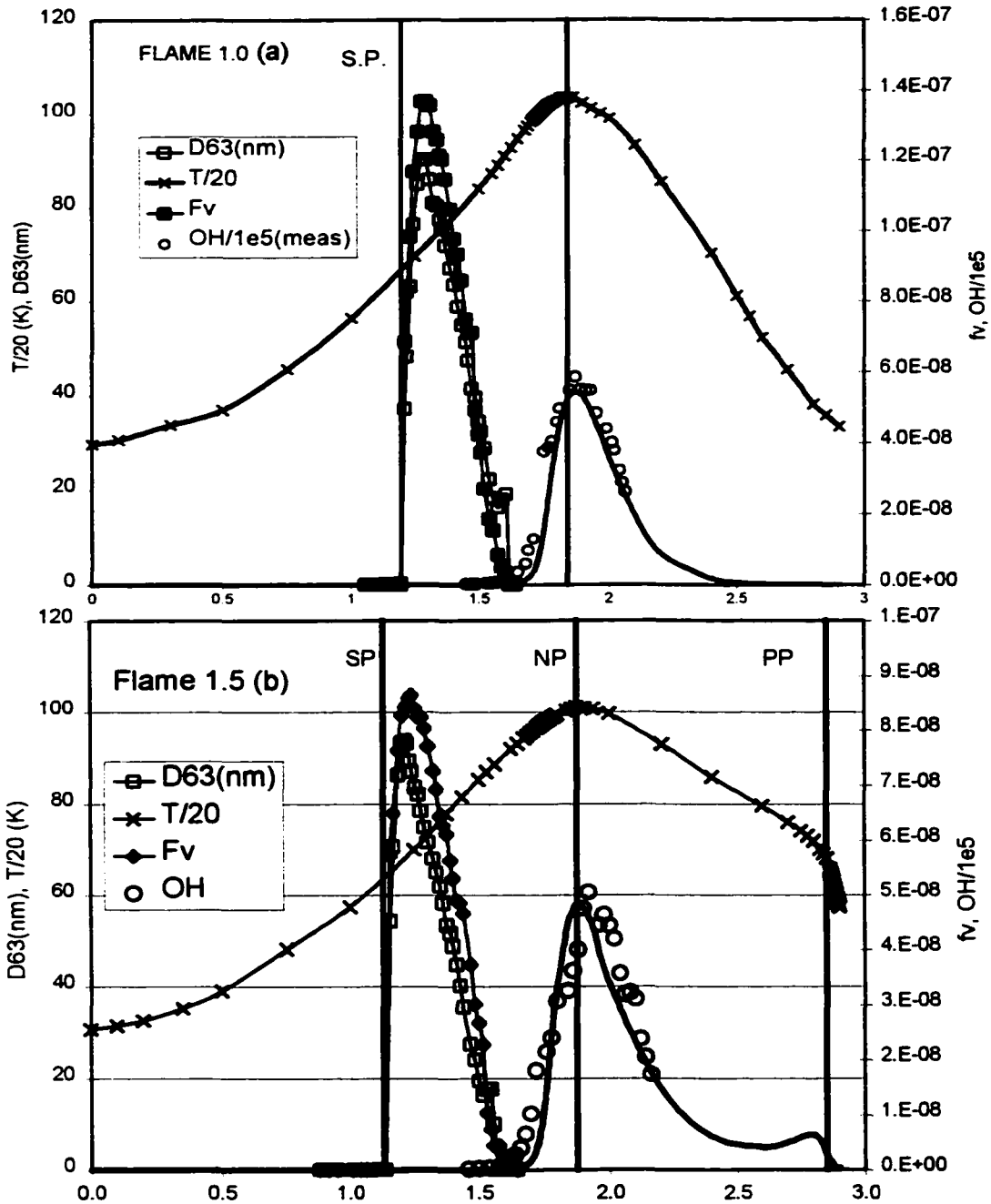

Fig 5.9 Distribution of measured soot, OH and temperature in (a)Non-premixed Flame 1.0 (b) Partially Premixed Flame 1.5

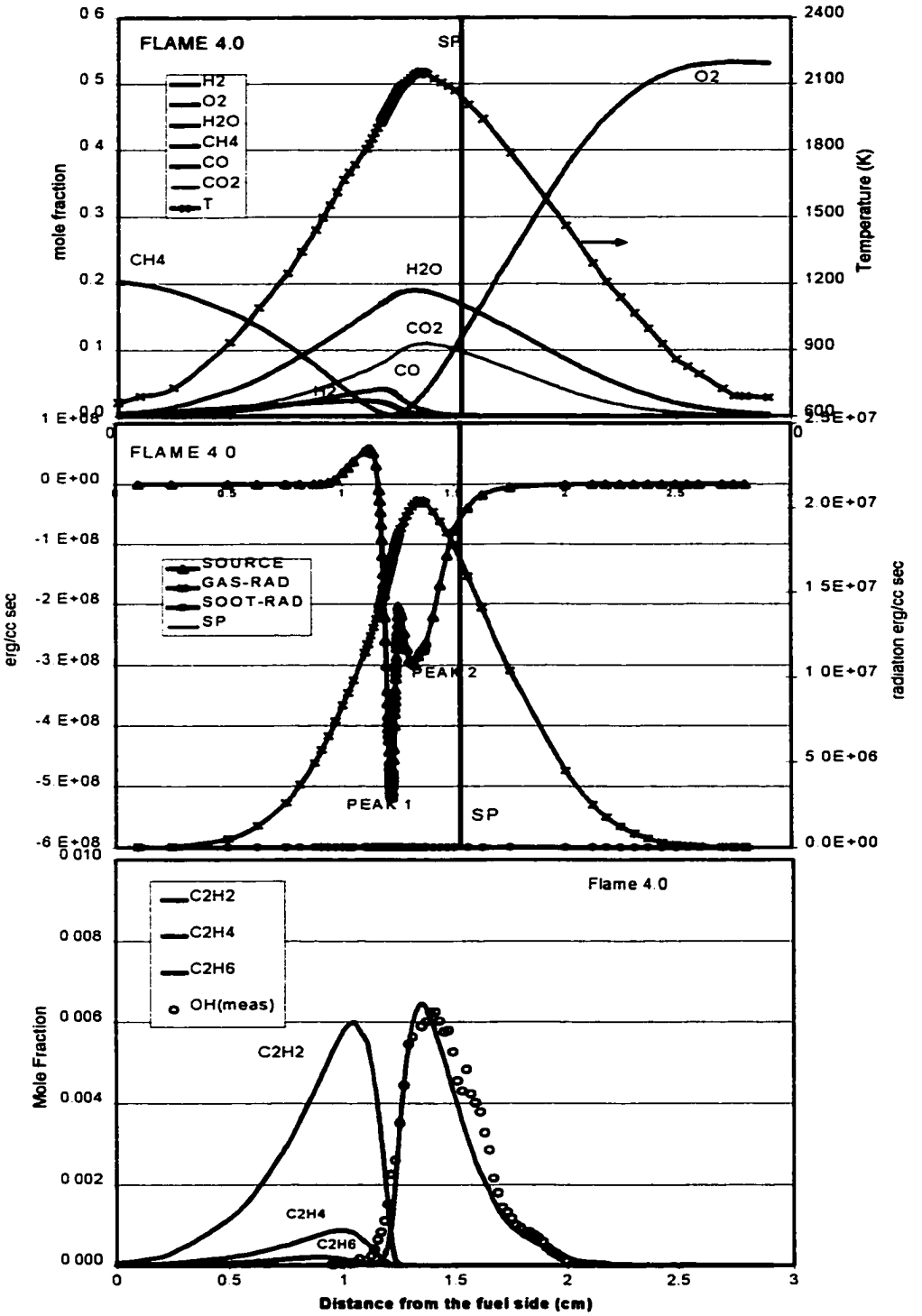

Fig 5.10 Tgiven computed distribution of a) major species and temperature b) energy release and flame radiation c) C2 and OH species in Flame 4.0

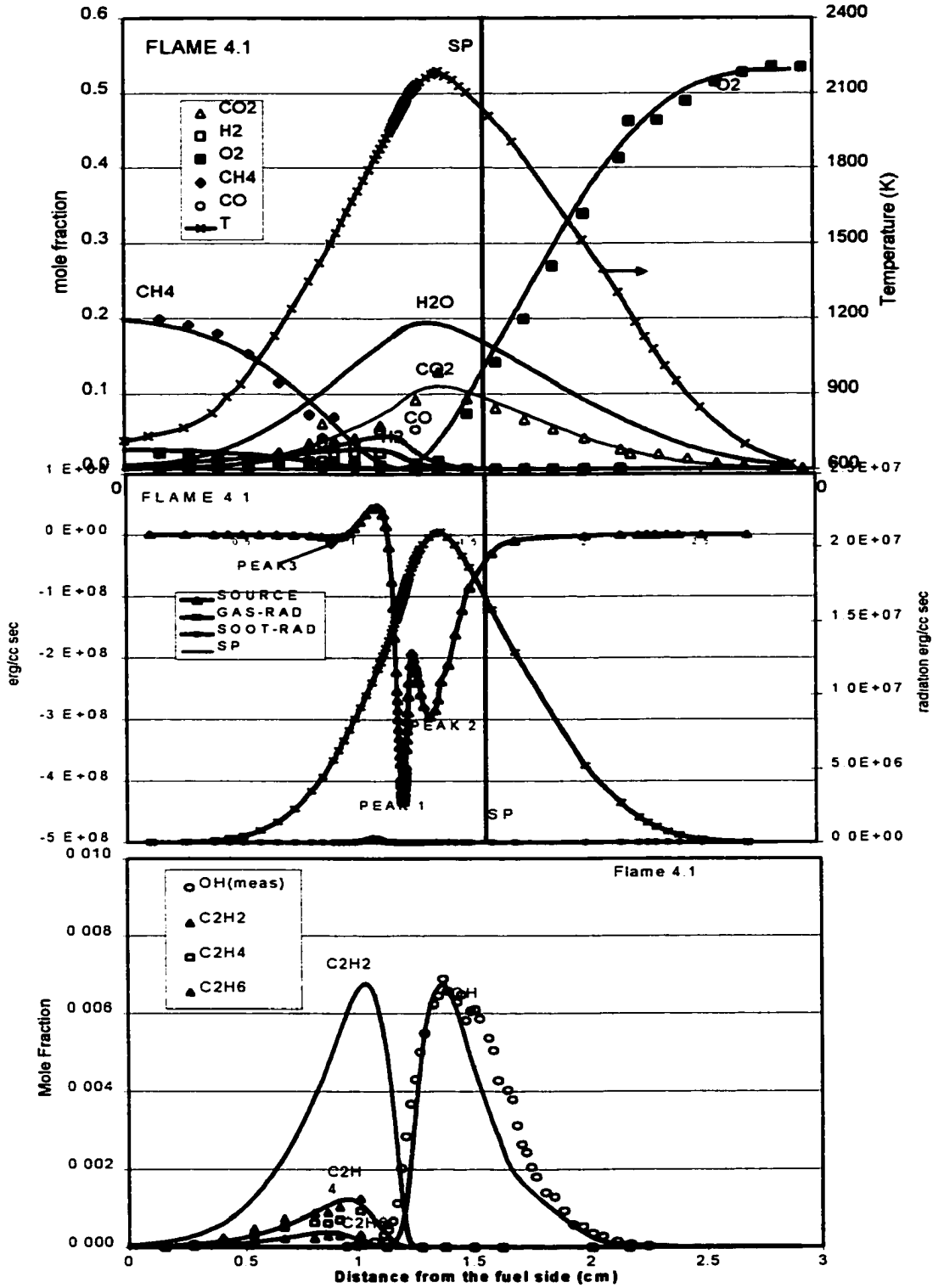

Fig 5.11 Distribution of a) measured major species and temperature computed b) energy release and flame radiation c) C2 and OH species in Flame 4.1

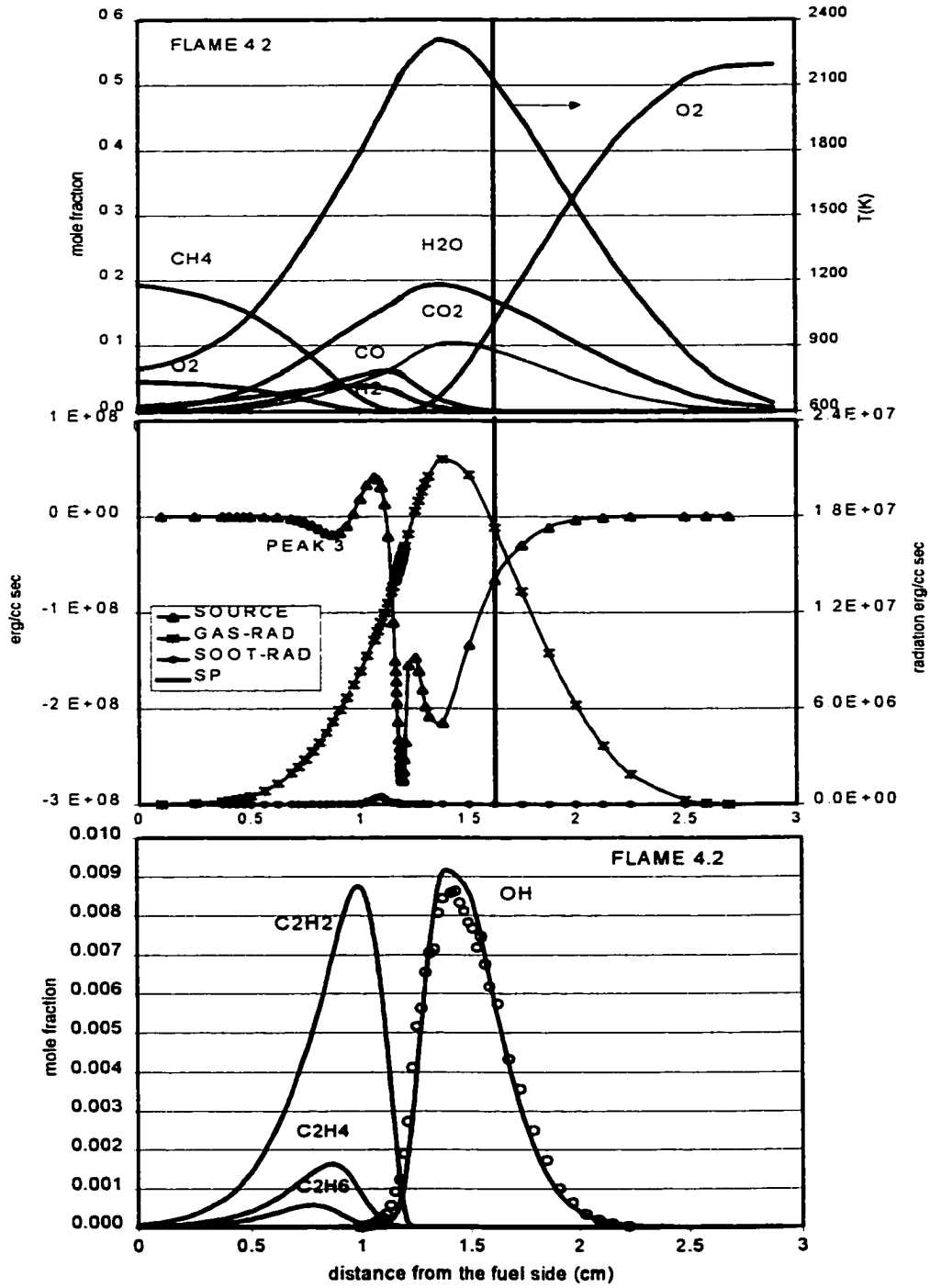

Fig 5.12 Distribution of computed a) species and temperature

b) energy release and flame radiation c) c2 and measured OH species in Flame 4.2

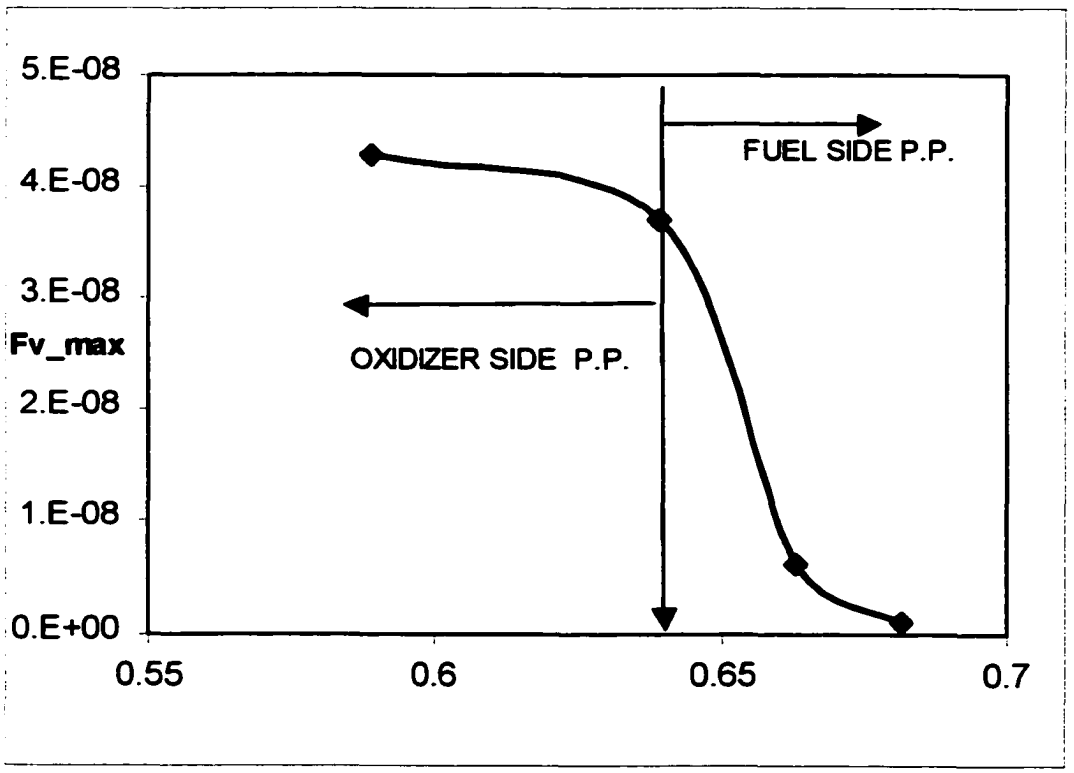

Fig 5.13 Trend in the measured peak soot volume fraction with partial premixing of the non-premixed flame 4.0

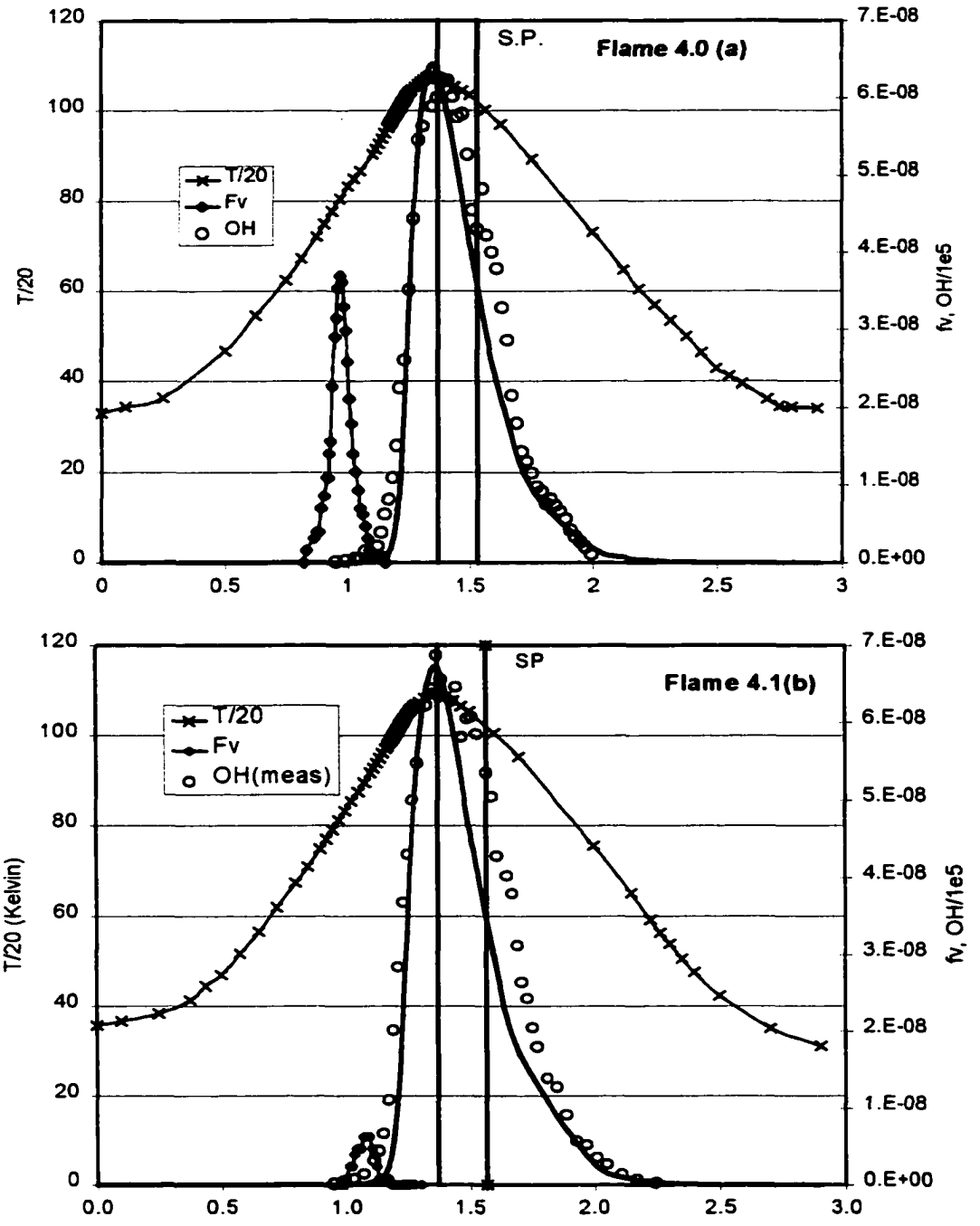

Fig 5.14 Distribution of measured soot, OH and temperature in (a)Non-premixed Flame 4.0 (b) Partially Premixed Flame 4.1

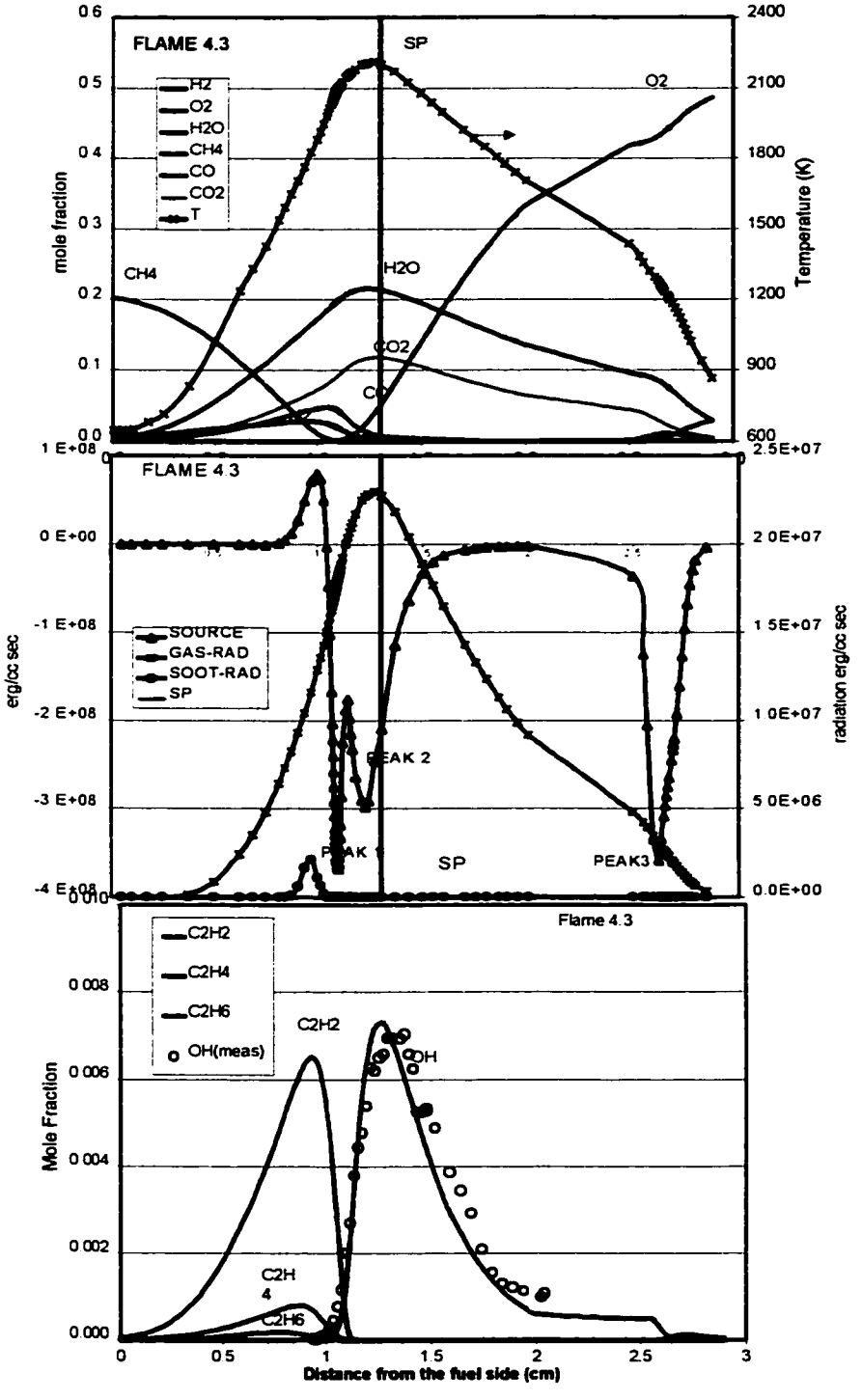

Fig 5.15 Tgiven computed distribution of a) major species and temperature b) energy release and flame radiation c) C2 and OH species in Flame 4.3

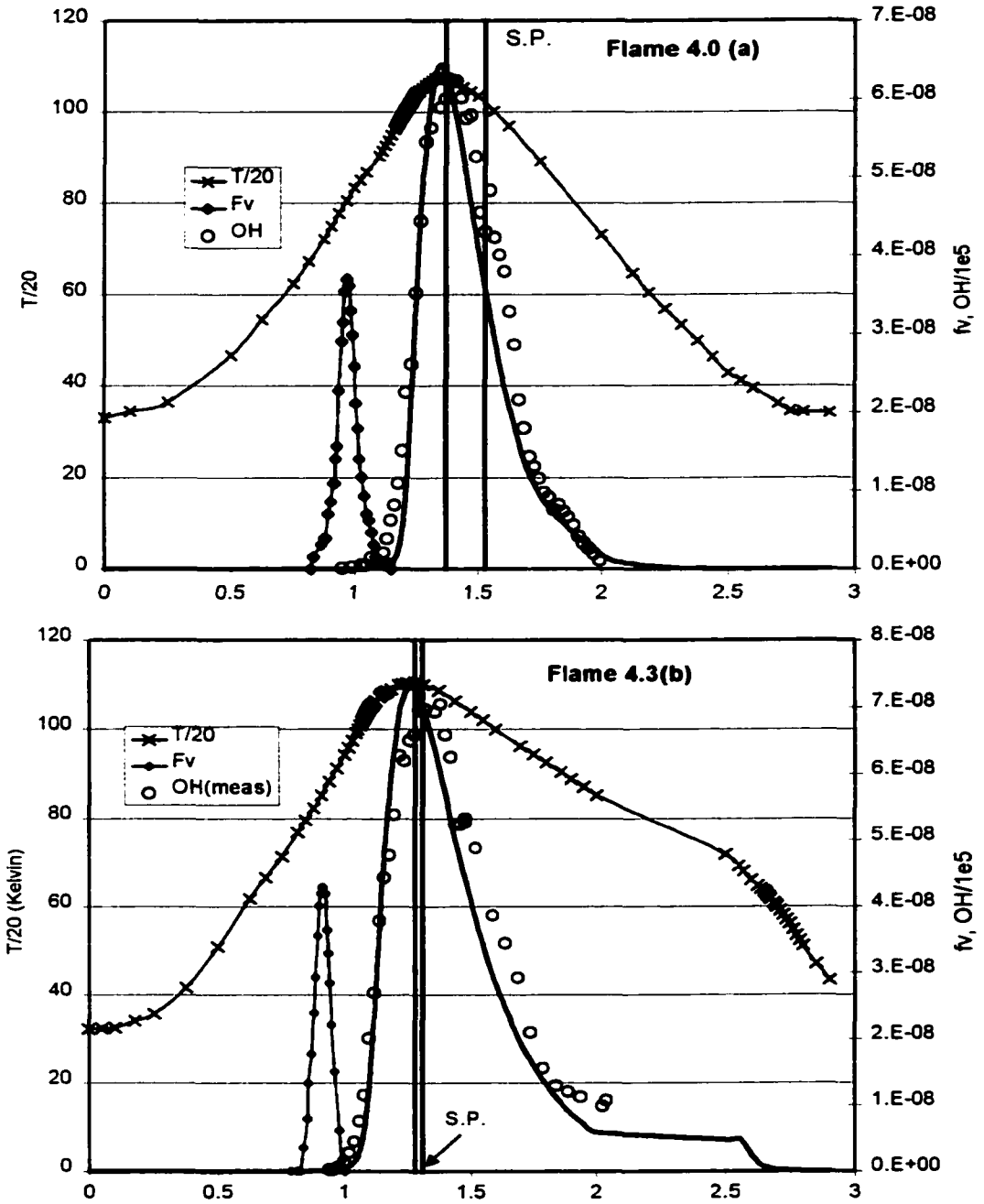

Fig 5.16 Distribution of measured soot, OH and temperature in (a)Non-premixed Flame 4.0 (b) Partially Premixed Flame 4.3

5.3 Control of Flame Radiation and Soot Emission

In the study described in the previous section, among the four cases considered, two each for flame 1.0 and flame4.0, fuel side partial premixing for the Case1 (flame 1.0), where oxygen was incrementally added to the fuel side of the flame originally residing on the oxidizer side of the stagnation plane is technologically most relevant. For progressive addition of oxygen added to the fuel side, the soot zone thickness, the peak soot loading and the peak soot aggregates sizes first decreased and then increased. The previous study emphasized the need to consider the changes in the temperature time histories of soot particles due to changes in the locations of the premixed and the non-premixed reaction zones with respect to the stagnation plane in addition to the chemical and dilution effects of oxygen added into the fuel side.

This section, which forms the second part of the study of soot processes in partially premixed flames, builds on the understanding of soot formation processes gained in our previous work and reports a novel partially premixed flame configuration having the potential of enhanced soot radiation with simultaneous control of soot particulate emissions from flamelet combustion.

Experiments were conducted in a unique low strain rate (typical strain rates 10-15 sec-1) counter-flow flame burner described in Chapter 3. All measurements were carried out along the axis of symmetry. The gases used were of chemical purity grade (99.7% or better) and inlet flow rates of gases were monitored using calibrated sonic orificemeters and rotameters. Soot volume fraction distribution was inferred from laser light extinction measurements using 514.5nm Ar+ ion laser. Mie scattering theory for lognormal distribution of spherical particles and soot complex refractive index of 1.57-0.56i was assumed to infer particle diameter and volume fraction from measured scattering and extinction cross-sections. Temperature in the flame was measured using a Pt/Pt-10%Rh (S-type) thermocouple of wire diameter 0.008 inches. The thermocouples were coated

with SiO2 film to prevent catalytic reactions on the thermocouple surface and measured temperature was corrected for radiation error following Zhang et al. [61].

The specifications of the non-premixed methane flame, flame A, used in this study are given in Table 5.4. This flame was a sooty flame with peak flame temperature on the oxidizer side of the stagnation plane. Four partially premixed flames were obtained from the flame A by progressively adding oxygen to the fuel side while maintaining the same flows on the oxidizer side. The four partially premixed variants A*, B, C and D had 9%, 14.5%, 18% and 22.7% oxygen by volume in the inlet fuel stream. Further addition of oxygen was not attempted due to the risk of flashback in these low strain rate flames. Typical global strain rates in these flames are in the range 10-15 sec-1. Global strain rate is defined as the difference of centerline axial velocities at the two burner inlet ports divided by the burner gap. Specifications of these flames including temperature and velocity boundary conditions are included in Table 5.4.

Computations were carried out using Sandia opposed flow flame code, OPPDIF, [33], using GRIMech 3.00 mechanism with the recommended multi-component transport and thermo-chemical database. The boundary conditions at the inlets included measured inlet temperature, velocity and the species flux at each of the two inlets 2.9 cm apart. The converged solution was checked for dependence on the initial grid and the choice of convergence parameters. The energy equation in the original code was modified by Kim, [35], to include an optically thin model of soot and gas radiation as described before. The author would like to reiterate that the *measured* soot volume fraction distribution was provided as an *input* to the modified OPPDIF code for the purpose of calculating soot radiation. This obviates the need to have a soot model for prediction of soot radiation in the present work.

In order to compare radiation from different flames on a rational basis we define radiative fraction, χ, for the gas radiation, the soot radiation and the net radiation as follows:

$$\chi_{gas} = \int_0^l \nabla q_{gas}\, dz \Big/ \int_0^l \sum_k^K w_k W_k h_k \, dz \qquad (5.1)$$

$$\chi_{soot} = \int_0^l \nabla q_{soot}\, dz \Big/ \int_0^l \sum_k^K w_k W_k h_k \, dz \qquad (5.2)$$

$$\chi = \chi_{gas} + \chi_{soot} \qquad (5.3)$$

The limits of integration in the above definitions are from the fuel side inlet to the oxidizer side inlet. Radiative fraction is directly proportional to radiative heat transfer per unit mass of fuel consumed.

Visual observation of the flames

Figure 5.17 shows soot luminosity photographs of the non-premixed methane flame, flame A, and the partially premixed flames obtained from it for progressive levels of oxygen added into the fuel. The trends of measured peak soot volume fraction and the thickness of the soot are shown in fig. 5.18. For progressive levels of partial premixing:

a) The thickness of the soot zone first decreased and then increased

b) The peak soot loading in the flame first decreased and then increased

Energy release

Measured distributions of soot volume fraction are shown in figs. 5.19-5.22(a) along with computed distribution of temperature, OH radical concentration and location of the stagnation plane. The locations of the premixed and the non-premixed reaction zones as well as computed distribution of gas and soot radiation are shown in figs. 5.19-5.22(b). In the non-premixed hydrocarbon flames conversion of hydrocarbon fuel to CO2

and H2O takes place as a two step process; first the hydrocarbon species is oxidized to CO and H2 which is in turn oxidized to CO2 and H2O in the second step. These two energy release processes represent the two negative peaks in the chemical energy release distribution shown as 'Peak 1' and 'Peak 2' in Fig. 5.19(b). For the partially premixed flames, in addition to the two non-premixed energy release peaks, a third energy release peak, shown as 'Peak 3' in Figs 5.20-5.22(b), is observed which corresponds to consumption of oxygen added to the fuel. For small levels of partial premixing the area under the premixed energy release peak is small compared to the non-premixed energy release peaks as shown in Fig. 5.20(b). Corresponding temperature profile for the flame B is indicative of the 'merged-flame' regime with no evidence of a spatially separated premixed and non-premixed reaction zones. As the level of partial premixing is increased the energy release contribution of the premixed reaction zone becomes comparable to that of the non-premixed flame as shown in Fig. 5.22(b). Corresponding temperature distribution for flame D is representative of the 'interdependent flames' regime where the premixed reaction zone has become strong and shows clear spatial separation from the non-premixed reaction zone. Tsuji and Yamaoka, [3], found that the distribution of temperature and products of combustion is 'broader' in the region between the premixed and the non-premixed reaction zone for the flames in the 'interdependent-flames' regime as indicated by computed species distribution in Fig. 5.22(c) for the flame D.

Soot formation in the non-premixed flame

Figure 5.19(a) shows soot volume fraction distribution in the non-premixed flame, Flame A. With the non-premixed 'flame' (reaction zone) on the oxidizer side of the stagnation plane, soot formation begins on the fuel side of the OH zone and soot growth takes places as soot particles are driven by the flow-field towards the particle stagnation plane. The thickness of the soot zone is limited to the distance between the 'flame' and the (particle) stagnation plane. In this flame the soot volume fraction has a sharp fall off on the fuel side of the soot distribution in Fig. 5.19(a).

Effects of Partial Premixing

(a) Width of the soot zone

As shown in Fig. 5.18, the thickness of the soot zone first decreased and then increased as oxygen was progressively added to the fuel side. The initial decrease in the soot zone thickness takes place as the merged flame moves closer to the stagnation plane (also closer to the fuel side) and soot zone is squeezed in between the flame and the particle stagnation plane. As discussed in section 5.2, the merged flame moves closer to the fuel side for incremental addition of oxygen to fuel because of two effects: (1) the fuel gets diluted (2) a fraction of the fuel is consumed by the reaction of oxygen added into the fuel.

The subsequent increase in the thickness of the soot zone is attributed to transition from the merged flame regime to the interdependent flame regime [20]. In the interdependent flame regime soot formation can take place in between spatially separated premixed and non-premixed reaction zones as shown in Figs. 5.22(a-b).

(b) Peak soot loading

As shown in Fig. 5.18 the peak soot loading first decreased and then increased for progressive levels of partial premixing.

The initial decrease in the peak soot loading is attributed to dilution and suppressive chemical effects of oxygen added to the fuel as observed in similar other studies of methane flames described in section 5.2. The subsequent increase is attributed to favorable temperature time histories. In the earlier study, section 5.2, we have emphasized the importance of considering the temperature time histories of the soot particles resulting from the changes in the locations of the premixed and the non-premixed reaction zones with respect to the stagnation plane to explain the trends in the

peak soot loading and peak particle sizes resulting from progressive partial premixing of methane flames.

Although we notice that the peak soot loading in the flame D is similar to that in the original non-premixed flame, flame A, the two flames have very different soot emission characteristics. In flame A, soot leaves the flame at the stagnation plane where the soot volume fraction has reached its maximum. In contrast to flame A, in flame D all the soot produced along the stagnation streamline is consumed internally in the flame. Here, as soot is driven towards the stagnation plane by the flow-field it encounters the OH radical zone of the non-premixed flame and is oxidized prior to reaching the stagnation plane. We notice in Fig. 5.22(a) that the overlap of OH and soot volume fraction distribution is not insignificant in this flame.

(c) *Soot radiation*

Soot radiation from flame, defined as $\int_0^{\infty} \nabla \overset{\rho}{q}_{soot} dz$, first decreased and then increased for progressive levels of partial premixing as shown in Fig. 5.23 following the trend for peak soot volume fraction. This observation is intuitive considering a reduction in peak soot loading by about half in going from flame A to flame C and an increase in peak soot volume fraction back (to the level of peak soot loading of flame A) in flame D. The soot radiative fraction followed the same trend as shown in Fig. 5.23.

In the case of the non-premixed flame, Fig. 5.19(a), soot volume fraction increases as particles are carried away from the flame by the flow-field. As a result, the temperature at the peak soot loading is also the lowest temperature anywhere in the soot zone. This is not a very favorable situation. In flame D, with peak soot loading similar to that in flame A, soot radiation is significantly enhanced because the broad soot zone benefits from the board temperature profile between the premixed and the non-premixed reaction zones and an overall increase in the flame temperature. This flame configuration

is therefore advantageous not only from soot particulate emission considerations as discussed before but also from the point of view of enhanced soot radiation.

The peak volumetric soot radiation in flame C was about 1.5 times that in flame A although the peak soot loading in the flame C is almost half of that in flame A. Similarly, the peak volumetric soot radiation in flame D, Fig.5.22(b), is about 3 times more than that in flame A although both the flames have similar peak soot volume fraction. The increase in peak volumetric soot radiation is also evident qualitatively in soot luminosity photographs, Fig. 5.17.

(d) *gas radiation*

Gas radiation from the flame, defined as $\int_0^l \nabla \overset{\rho}{q}_{gas} dz$, systematically increased for progressive levels of partial premixing as shown in Fig. 5.24. This increase is attributed to the following two effects of partial premixing. Firstly, the there was an increase in the peak flame temperature. Secondly, the profiles of CO, CO2 and H2O get broader, especially in the interdependent flame regime as shown in Fig. 5.22(c). The broad profiles of the radiating species also coincide with broad temperature distribution as shown in Fig. 5.22(a). These factors lead to an increase in gas radiation from the flame.

It is interesting that in spite of an increase in the radiation from the flame the radiative fraction for the gas radiation decreased. As is evident in figs. 5.19(b)-5.22(b), with progressive partial premixing, the energy release in the flame increases, primarily as more and more fuel is consumed in the premixed reaction zone. The incremental increase in the net energy release was bigger than the incremental increase in gas radiation from the flame as oxygen was progressively added into the fuel stream.

Net radiation from the flame consists of both soot radiation and gas radiation. Combining the trends discussed above for these individual contributions we find that the net radiative fraction first decreased and then increased as oxygen was progressively added to the fuel side of the methane non-premixed flame.

5.4 Conclusions

Main conclusions of this study are summarized below.

Flame structure and soot formation

1. Volumetric energy release increased for progressive partial premixing. With progressive partial premixing the relative importance of energy release in the premixed reaction zone increases.
2. The CO and H2 'fuel' produced by the premixed reaction zone is consumed in the non-premixed reaction zone increasing the relative importance of energy release associated with CO and H2 conversion to CO2 and H2O in comparison to energy release associated with formation of CO and H2 in the nonpremixed reaction zone.
3. Computed as well as measured species distribution showed that the spatial separation between the premixed and the nonpremixed 'flamesheet' increased with progressive partial premixing.
4. Fuel side partial premixing of the:
   i.) Case 1: (Nonpremixed flame residing on the oxidizer side of the stagnation plane) first decreased and then increased the peak soot volume fraction, the thickness of the soot zone and the peak soot aggregate size with progressively increasing levels of partial premixing.
   ii.) Case 2: (nonpremixed flame residing on the fuel side of the stagnation plane) showed a monotonic decrease in the sooting tendency with an eventual transition to a nonsooty flame.
5. Oxidizer side partial premixing of the:
   i.) Case 1: (nonpremixed flame residing on the fuel side of the stagnation plane) resulted in decrease in the peak soot loading with progressive partial premixing.
   ii.) Case 2: (nonpremixed flame residing on the fuel side of the stagnation plane) resulting in an increase in peak soot volume fraction.

6. Although the effect of oxygen added to methane fuel is to suppress soot inception, the effect on soot growth could be a decrease or an increase in peak soot loading depending on the configuration of the non-premixed counterflow flame and the level of partial premixing. The effect of flowfield should be considered in addition to the dilution and chemical effects of oxygen added to the fuel side.

Flame radiation and soot emission

Effects of fuel side partial premixing on sooting tendency and flame radiation were studied for progressive addition of oxygen into the fuel side of methane counter-flow flames. A novel flame configuration is reported (flame D in this study) where soot is formed and oxidized between the premixed and the non-premixed reaction zones on the fuel side of the stagnation plane. This flame configuration has the potential for low soot particulate emission with simultaneous enhancement of soot radiation heat transfer from flamelets.

Following are the key conclusions from the study:

1. The peak soot volume fraction first decreased and then increased for progressive partial premixing. The initial decrease is attributed to a combination of previously established dilution and chemical effects both of which suppress soot formation in methane flames. The subsequent increase is attributed to more favorable temperature time histories for soot particulates resulting from partial premixing.
2. The thickness of the soot zone first decreased and then increased for progressive levels of partial premixing. The initial decrease is attributed to the merged flame coming closer to the stagnation plane and the soot formation zone being squeezed between the flame and the stagnation plane. Subsequent increase in the soot zone thickness is attributed to formation of soot between the spatially separated premixed and the non-premixed reaction zones in the 'interdependent-flame-regime'.

3. Soot radiation from the flame as well as radiative fraction for soot radiation first decreased and then increased. The experimentally observed increase in soot luminosity in the partially premixed flames was explained using computed volumetric soot radiation in the flames.
4. Gas radiation increased with partial premixing due to broadening of profiles of products of combustion and a flatter temperature profile between the premixed and the non-premixed reaction zone. The radiative fraction for the gas radiation, however, decreased due to a bigger increase in the net chemical energy release in the partially premixed flames.

Similar effects should be expected for flamelet combustion under similar conditions of chemistry and strain rate. Since soot formation is very sensitive to the fuel type above results pertaining to soot loading and soot radiation should be extrapolated with due care noting the sooting tendency of the fuel, particularly with partial premixing. It is of interest to point out that for ethylene, the effect of small amounts of oxygen added to the fuel side was to promote soot loading as presented in Appendix A4.

	Fuel Side	Oxidizer Side
Flame A	Tad = 2928 K Global Strain Rate =11.38 1/sec	
β=.3605	50.7%CH4+49.3%N2 V=10.68cm/sec,T=531K	23.9%He+76.1%O2 V=22.33cm/sec, T=717K
Fuel Side Partial Premixing		
Flame A*	Tad = 2933 K Global Strain Rate =12.12 1/sec	
β=.3861	48.5%CH4+47.2%N2+4.3%O2 V=12.09cm/sec,T=547K	23.9%He+76.1%O2 V=23.06cm/sec, T=741K
Flame B	Tad = 2939 K Global Strain Rate =12.78 1/sec	
β=.4579	43.3%CH4+42.2%N2+14.5%O2 V=13.10cm/sec,T=557K	23.9%He+76.1%O2 V=23.98cm/sec, T=770K
Flame C	Tad = 2942 K Global Strain Rate = 13.63 1/sec	
β=.4894	41.4%CH4+40.4%N2+18.2%O2 V=14.22cm/sec,T=578K	23.9%He+76.1%O2 V=25.33cm/sec, T=812K
Flame D	Tad = 2956 K Global Strain Rate =15.65 1/sec	
β=.5318	39.1%CH4+38.1%N2+22.8%O2 V=15.98cm/sec,T=614K	23.9%He+76.1%O2 V=29.16cm/sec, T=935K

Table 5.4 Specifications of flames studied
for control of flame radiation and soot emission

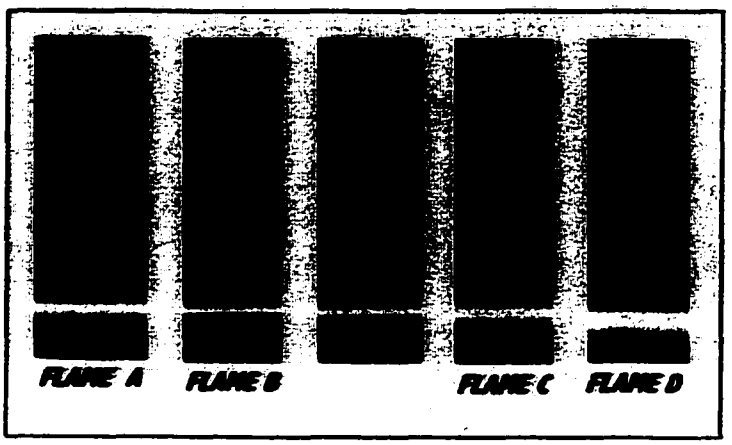

Fig. 5.17 Soot luminosity photographs

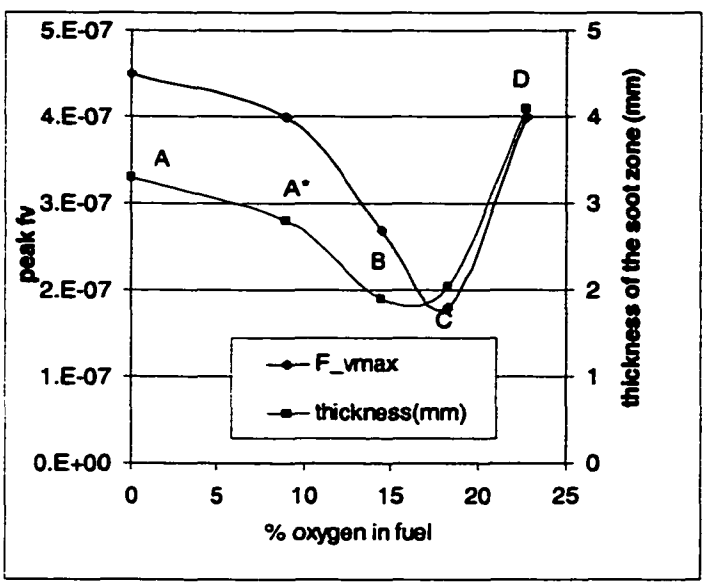

Fig. 5.18 Trends in peak soot loading and soot zone thickness

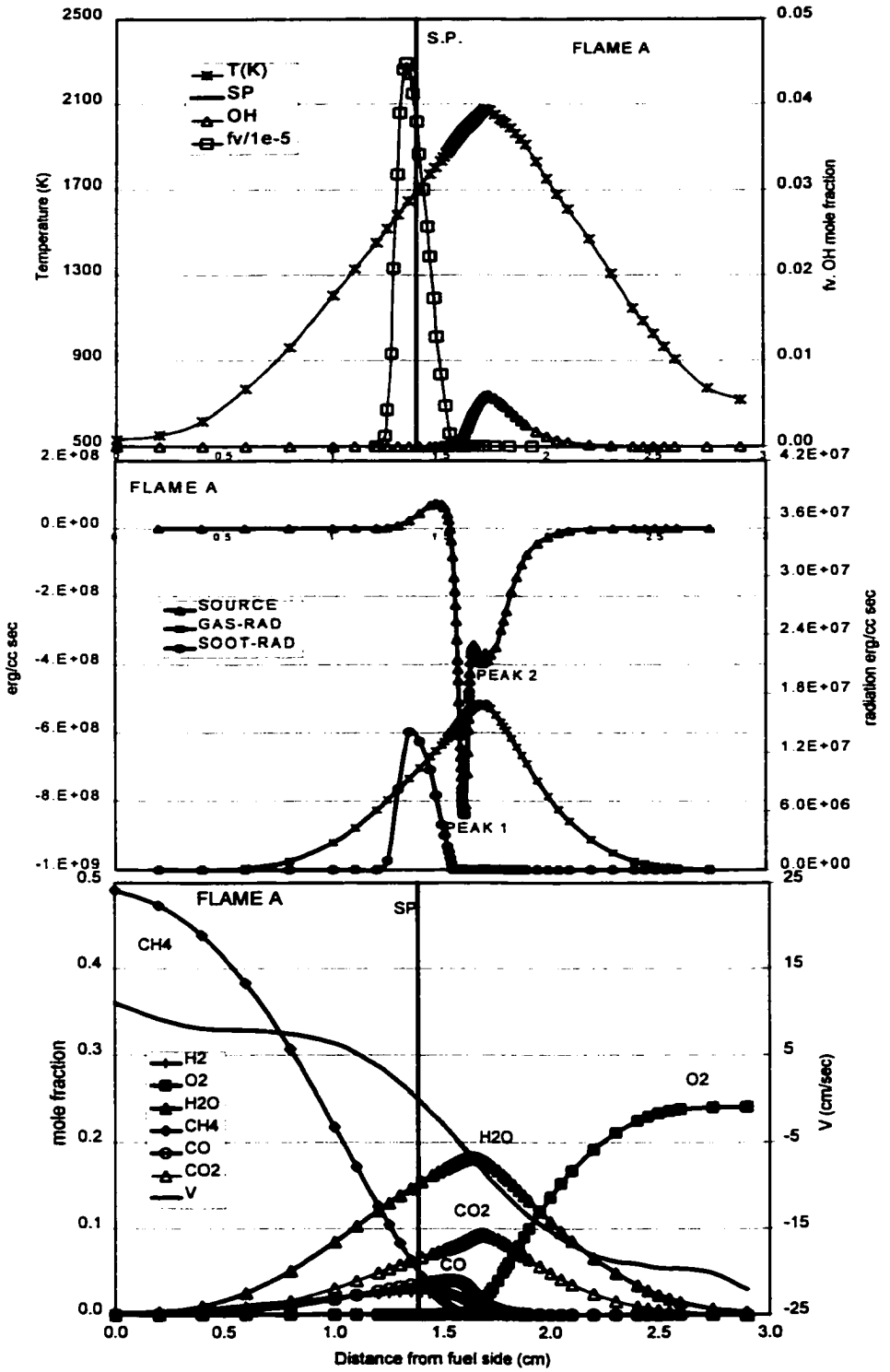

Fig 5.19 Distribution of measured (a) T, fv and OH , computed (b) Energy release rate and radiation (c) Species for the nonpremixed flame, flame A

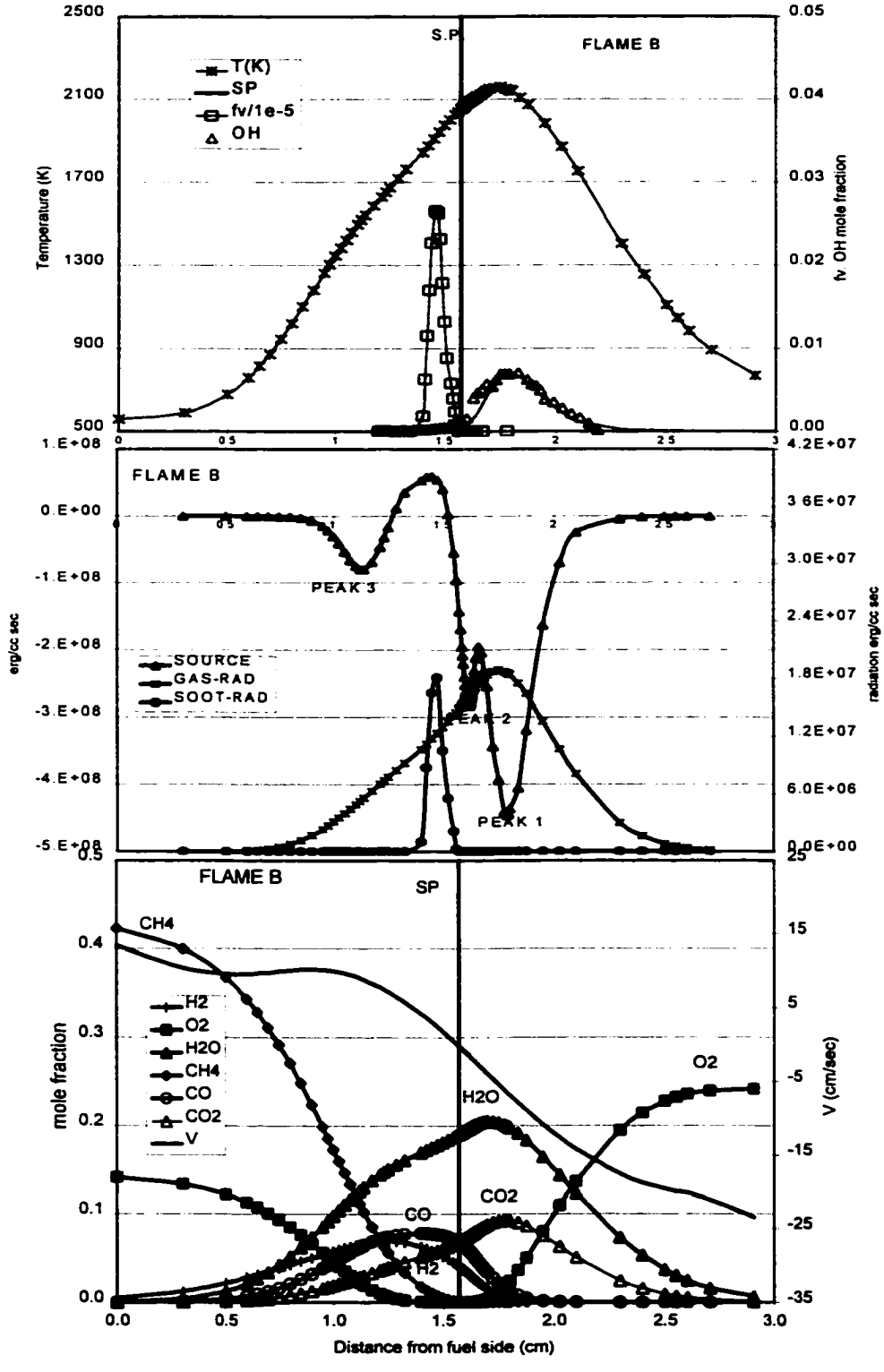

Fig 5.20 Distribution of measured (a) T, fv and OH

Computed (b) Energy release rate and radiation (c) Species for flame B

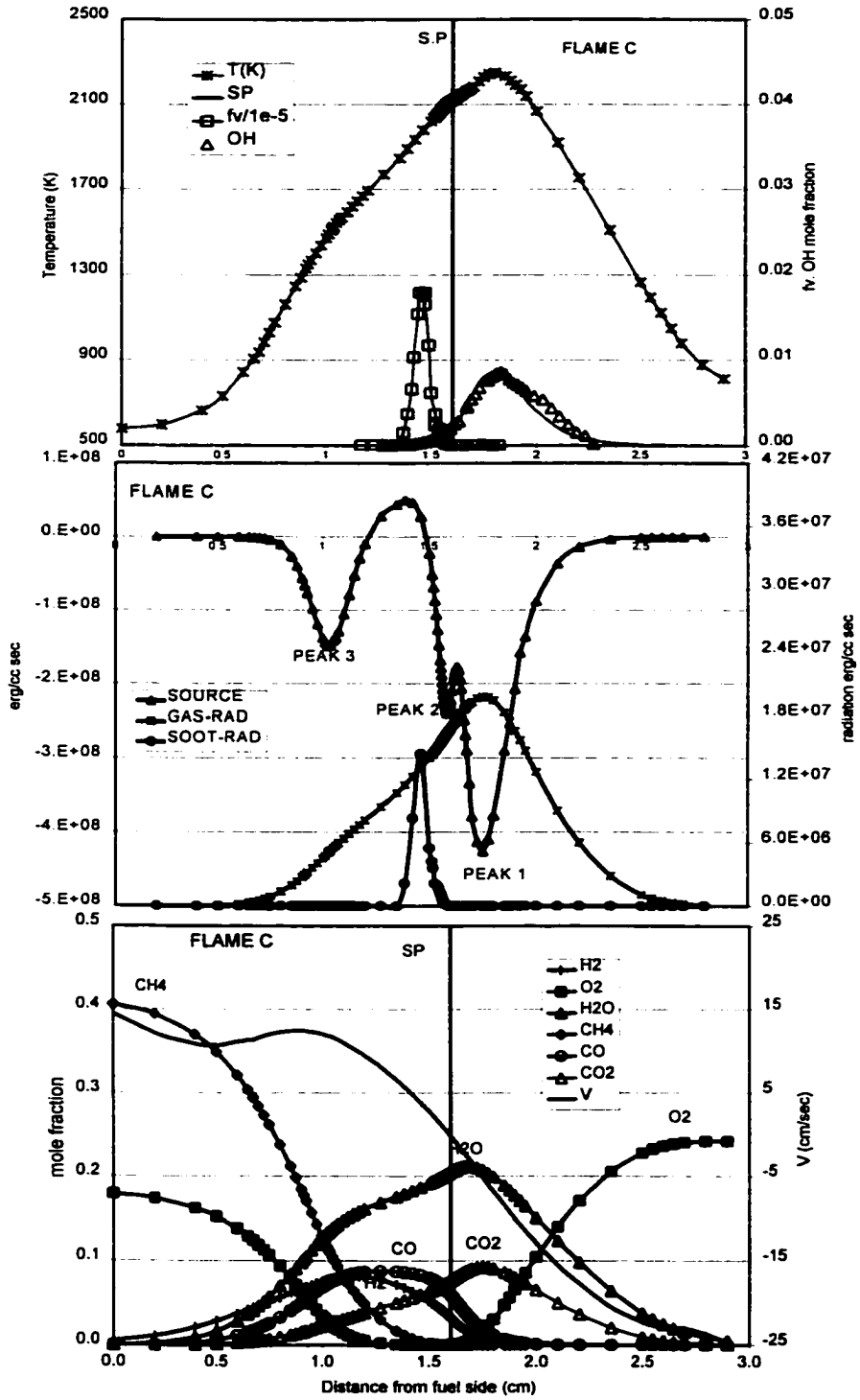

Fig 5.21 Distribution of measured (a) T, fv and OH, computed (b) Energy release rate and radiation (c) Species for flame C

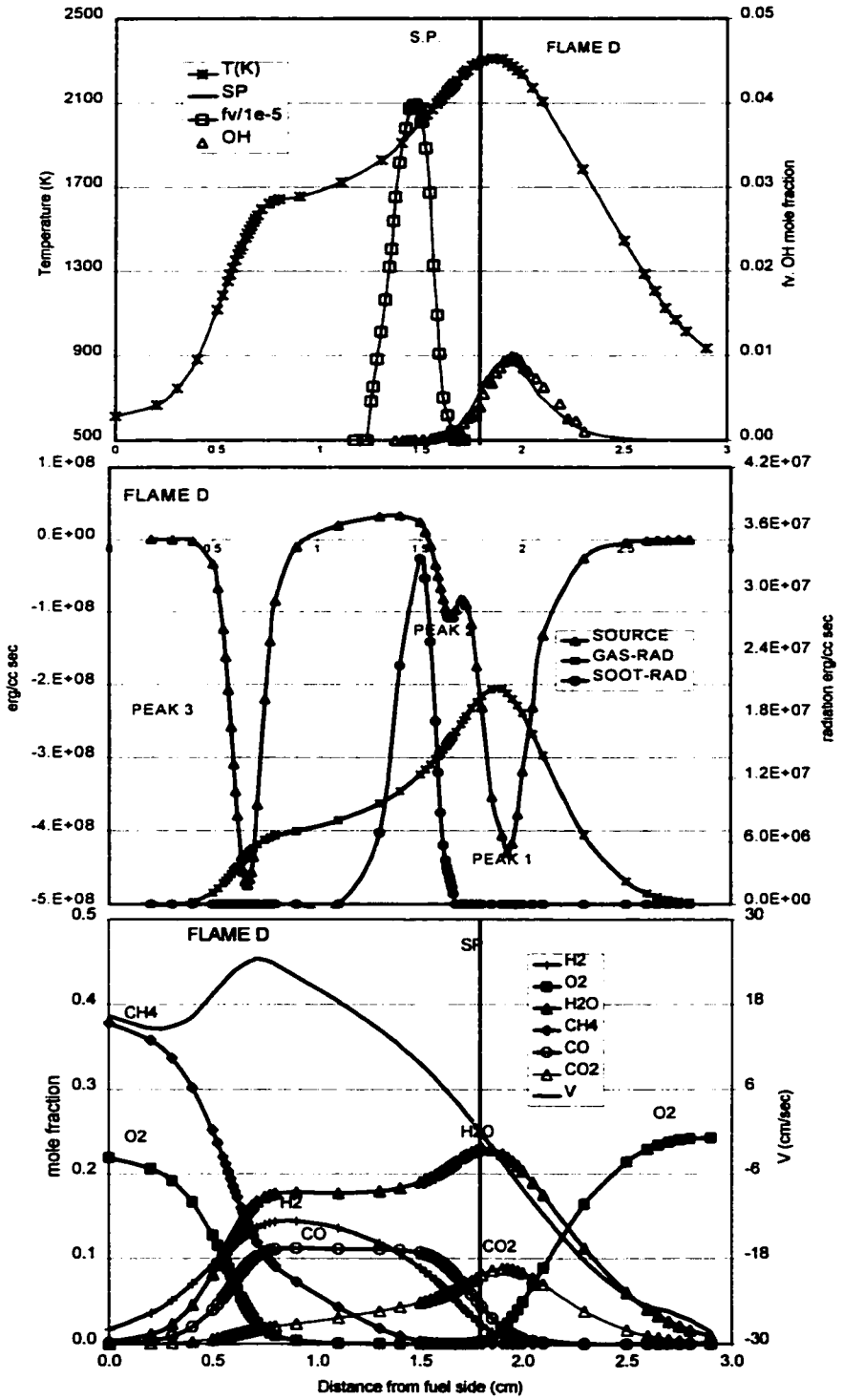

Fig 5.22 Distribution of measured (a) T, fv and OH

computed (b) Energy release rate and radiation (c) Species for Flame D

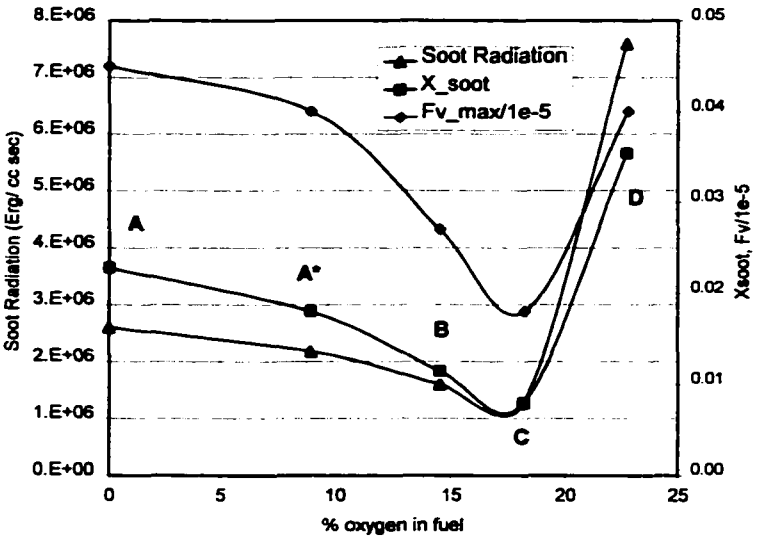

Fig. 5.23 Trend for max fv, χsoot and soot radiation

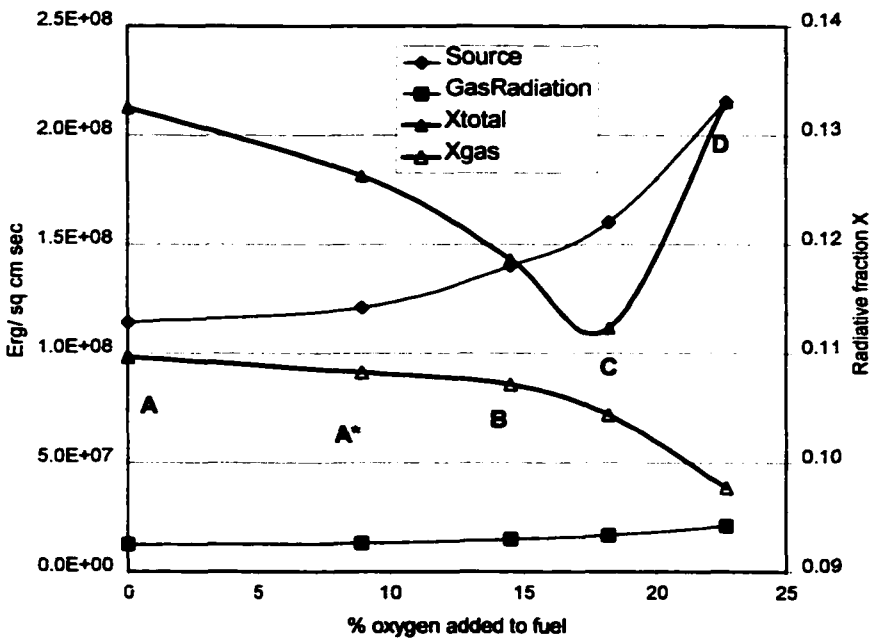

Fig. 5.24 Trend for gas radiation, energy release and radiative fraction with progressive partial premixing

CHAPTER 6

NO EMISSION IN PARTIALLY PREMIXED FLAMES

6.1 Introduction

Combustion of fossil fuels is a primary source of NO emissions into the atmosphere. NO emissions are of concern due to their role in the photochemical smog formation, acid rain and the depletion of the ozone layer and these emissions are controlled by various environmental regulations.

The term 'partial-premixing' is commonly used to refer to the technique of adding oxygen (often in quantities less than required for the rich flammability limit) into the fuel. The rich fuel mixture then reacts with air in the combustion chamber. Intentional partial premixing is practiced for the reasons of flame stabilization and pollutant emission control. About 30% of natural gas use takes place in partially premixed mode, Warnatz et al. [1].

Energy release and radiation characteristics of flames are of concern for burner and combustion equipment design. Flame radiation is an important mode of heat transfer in many practical combustion equipments. It is also important for the control of NO emissions due to the high temperature sensitivity of the thermal NO formation reactions.

Motivated by environmental and technological importance of the subject, NO formation in partially premixed flames has received significant attention in combustion literature [22-32] in the last decade. Several studies in both co-flow and counter-flow configurations encompassing laminar as well as turbulent flow regimes have been reported in the literature for a variety of fuels.

Most of the previous work [22-28] has concentrated on the co-flow geometry. Key findings from these studies are summarized in Table 6.1. It was observed that with partial premixing the energy release took place in: (i) an inner reaction zone where the rich fuel-air mixture issuing from the central tube reacted in a premixed mode, and (ii) an outer non-premixed reaction zone where the excess fuel reacted with an outer co-flowing supply of the 'secondary' air as shown in Fig.1.1. The flame length decreased progressively for increasing levels of partial premixing. Measurement of the radiative fraction (energy radiated per unit chemical energy release,χ) indicated that, [23,27], it decreased systematically with progressive increase in partial premixing. This resulted in an increase in the peak flame temperature. The importance of the effect of flame radiation on NO formation in partially premixed flames was discussed by Driscoll et al. [22]. The effects of partial premixing on the Emission Index of Nitrogen Oxides (EINOx), defined as grams of NO emission per kg of fuel consumption, is also summarized in Table 6.1. Of particular interest for the NO emission control is the minimum in EINO reported by several studies for the rich mixture equivalence ratio of $\Phi \sim 2.2$ with progressive partial premixing. While these studies in co-flow flames provide significant insight and incentive for further studies of NO formation pathways and effects of flame radiation, almost all such work in the past has been conducted using computational modeling of flames and analysis of reaction pathways for which counter-flow flame configuration is more attractive.

Several studies have considered NO formation in counter-flow partially premixed flames [28-32]. These studies considered NO formation over a range of global strain rates from 5 –200 sec^{-1} in methane-air partially premixed counter-flow flames. In the low strain rate studies (5-20 sec^{-1}), EINO first increased and then decreased reaching a maximum around Φ~2, while at higher strain rates EINO decreased monotonically with progressive partial premixing as summarized in Table 6.2.

Except for one recent work [32] all these studies of counter-flow flames have used computational modeling of NO formation. The dearth of experimental data of NO measurements in partially premixed counter-flow flames, especially at low strain rates, may be due to experimental difficulties in establishing stable flames well acknowledged by the previous workers, [31,46]. In some of the previous work radiation effects have been ignored although this cannot be assumed a-priori, at-least for low strain rate flames where significant effect of radiation on flame temperature has been demonstrated [35,40]. Kim [35,41] studied NO formation in non-premixed counter-flow methane flames at low strain rates with significant attention to both soot and gas radiation. He observed that in low strain rate flames the effect of flame radiation on NO formation is important. Significant effect of partial premixing on soot and gas radiation in low strain rate methane partially premixed counter-flow flames was observed in the study reported in the last chapter. Previous literature has not addressed the effect of energy release and the flame radiation on NO formation in counter-flow partially premixed flames or discussed how these aspects in counter-flow flames are pertinent to turbulent flame results available in the literature.

Motivated by environmental and technological concerns and the importance of above issues not addressed in the previous literature an experimental and computational study of low strain rate counter-flow partially premixed methane flames was undertaken.

The experimental and computational techniques used in this study are described in the following section.

6.2 Experimental and Computational Methods

The specifications of the flames used in this study have been tabulated in the Table 5.4. These flames were used in the previous chapter to study control of soot emission and flame radiation in partially premixed flames. The non-premixed methane flame, flame A, used in this study was a sooty flame with peak flame temperature on the oxidizer side of the stagnation plane. Four partially premixed flames were obtained from

the flame A by progressively adding oxygen to the fuel side while maintaining the same flows on the oxidizer side. The four partially premixed variants A*, B, C and D had 9%, 14.5%, 18% and 22.7% oxygen by volume in the inlet fuel stream. Further addition of oxygen was not attempted due to the risk of flashback in these low strain rate flames. Typical global strain rates in these flames are in the range 10-15 sec^{-1}.

In addition to the temperature, OH and soot distribution measurements reported in the previous chapter, additional measurements performed for this study included measurement of NO distribution along the stagnation streamline. Gas samples were collected from the flame using a quartz microprobe with an inlet orifice diameter of 80 μm. The samples were collected in an evacuated metal cylinder through stainless steel sampling lines with sampling pressure below –20"Hg (34kPa absolute) to ensure sonic conditions at the probe. Allen, [49], has emphasized the need for sonic sampling to quench reactions in the sampling system. The probe, the sampling lines and the sample collection cylinder were heated to 70-100 °C to prevent condensation of water from the sample. The sample collected in the metal cylinder was pressurized and diluted by a factor of about five to ten with nitrogen. The dilution of the sample with nitrogen was necessary to prevent condensation of water in the sample on the cold surfaces of the NO analyzer for subsequent measurement of NO concentration. The diluted and pressurized sample was analyzed using a NOx chemiluminescence analyzer (Model 42H from Thermo-Environmental Inc.). The NOx analyzer was calibrated using known samples of NO and its linearity was checked for the range of NO levels encountered in this work. The NO analyzer had a least count of 0.01 ppm for detection of NO and NO2.Typical uncertainties while measuring a 50 ppm sample at a five fold dilution (with N2) level were about ± 2 ppm, though the repeatability of the measurement was much better. This error estimate does not include the uncertainties due to probe distortion or the sample distortion effects. Calibration of the NOx analyzer was performed before and after every experiment to ensure validity of the calibration during the experiment.

Computations were carried using the Sandia opposed flow flame code, OPPDIF, [33], with the GRIMech 3.00 mechanism and the recommended multi-component transport and thermo-chemical database. The boundary conditions included measured inlet temperature, velocity and the species flux at each of the two inlets 2.9 cm apart. The converged solution was checked for dependence on the initial grid and the choice of convergence parameters. Further details of computational methods used are presented in Chapters 2 and 5.

6.3 Results

Figure 5.17 shows soot luminosity photographs of the non-premixed flame, flame A, and its partially premixed counterparts as oxygen was progressively added to the fuel side. It is observed that the soot zone thickness first decreased and then increased and soot luminosity became intense. The effect of partial premixing on soot loading, soot emissions and soot radiation has been presented before in Chapter 5. The effect of partial premixing on energy release and flame radiation for these flames was discussed in section 5.3. These results are briefly revisited and their implication for NO formation in turbulent partially premixed flames is presented in this chapter.

Energy Release

Figure 5.24 shows the trend for volumetric energy release rate distribution integrated over the stagnation streamline between the fuel and oxidizer ports. With progressive partial premixing, the net chemical energy release in the flame increased. An increase in volumetric energy release for flamelet combustion is consistent with decrease in length of turbulent co-flow flames with progressive partial premixing as reported in previous studies, Driscoll et al. [22], Turns et al. [23]. The decrease in flame length for the turbulent co-flow flames in turn is responsible for decrease in the flow residence time for NO formation reactions.

Flame Radiation

Gas radiation from the flame systematically increased for progressive levels of partial premixing as shown in Fig. 5.24. This increase is attributed to the following two effects of partial premixing. Firstly, the there was an increase in the peak flame temperature. Secondly, the profiles of CO, CO2 and H2O get broader, especially in the interdependent flame regime as shown in Fig. 5.22(c). The broad profiles of the radiating species also coincide with the broad temperature distribution as shown in the Fig. 5.22(a). These factors lead to an increase in the gas radiation from the flame.

It is interesting that in spite of an increase in the radiation from the flame the radiative fraction for the gas radiation decreased. As is evident in Figs. 5.19(b)-5.22(b), with progressive partial premixing, the energy release in the flame increases, primarily as more and more fuel is consumed in the premixed reaction zone. The incremental increase in the net energy release was bigger than the incremental increase in gas radiation from the flame as oxygen was progressively added into the fuel stream.

Net radiation from the flame consists of both the soot radiation and the gas radiation. Combining the trends discussed above for these individual contributions we find that the net radiative fraction first decreased and then increased as oxygen was progressively added to the fuel side of the methane non-premixed flame.

Turns et al. [23] found that with progressive partial premixing the radiative fraction decreased in the turbulent co-flow flames of hydrocarbon fuels. On the basis of the above observations in counterflow flames in the present work, it is expected that the radiative fraction of gas radiation (which is a major component of the net radiative fraction) owing to flamelet combustion should systematically decrease with progressive levels of partial premixing. The decrease in the radiative fraction manifests as an increase in the peak flame temperature [23].

While previous studies of counter-flow partially premixed flames have not directly discussed the effect of partial premixing on the radiative fraction, a small

increase in measured peak flame temperature with progressive partial premixing in the experiments of Tsuji and Yamaoka [3] is consistent with a decrease in the radiative fraction with progressive partial premixing.

NO formation

NO distribution

Figures 6.1(a-d) show the measured and computed NO concentration distribution in the counter-flow flames for progressive partial premixing. As oxygen was progressively added to the fuel side the measured peak NO concentration increased from about 25 ppm in the non-premixed flame, flame A, to about 130 ppm in the partially premixed flame, flame D. The computations agree well with the measured trend and show a widening of the NO peak with progressive partial premixing.

Previous research with methane-air partially premixed counter-flow flames has shown, (Tanoff et al. [30], Dupont and Williams [28], Ravikrishna and Laurandeau [32]), a decrease in the peak NO concentration with progressive partial premixing for flames with global strain rate more than 20 sec-1 while for low strain rate calculations, Blevins and Gore [31], the peak NO concentration first increased and then decreased reaching a maximum at $\Phi \sim 2.2$. While the trend in the peak NO concentration in this study differs from previous work on methane-air partially premixed flames, the broadening of the NO distribution profile in the interdependent flame regime is consistent with previous work [30,32]. To explore and explain these similarities and differences a discussion of spatial distribution of NO production rates is presented next.

NO production rates

The computed distribution of volumetric molar NO production rate is shown in Fig. 6.2 for progressive partial premixing. There are three distinct regions-two corresponding to positive formation peaks and one negative NO destruction region.

Spatial distribution of NO production rates

It is observed that with progressive partial premixing the spatial separation between the two production peaks increases, Fig. 6.2. The increased spatial separation accounts for the broadening of the NO concentration distribution.

To understand the above observation, total NO production contribution from the three thermal mechanism reactions is shown along with the net NO production rate distribution for flames A and D in Figs. 6.3a and 6.3b respectively.

Thermal NO reactions:

$N + NO \leftrightarrow N2 + O$ *R178*

$N+O2 \leftrightarrow NO + O$ *R179*

$N+OH \leftrightarrow NO+H$ *R180*

It was observed that the production 'peak1' consisted almost entirely of contribution due to the three thermal reactions above. Furthermore, the relative importance of 'peak1' increased with progressive partial premixing. It is expected that with an increase in the flame temperature the thermal mechanism, which is more sensitive to temperature, is favored over the Fenimore mechanism.

The importance of $HCCO+NO \leftrightarrow HCNO+CO$ reaction, shown as reaction number 274 in the Figs. 6.3(a-b), for NO destruction has been discussed by previous workers [30-31,83]. We found that the NO consumption rate due to this reaction closely mimicked the NO reburn region on the fuel side of the two NO production peaks.

Although the present discussion of the NO rates is based on computations, the trends and the features of NO rate distribution reported can be trusted as the agreement of computed and measured NO and OH radical distributions in Figs. 6.1(a-d), in the light of increasingly important role of thermal NO pathway, supports the computations of NO chemistry in these flames.

Relative importance of NO formation pathways

Figure 6.4 shows the path integrated NO formation (area under the two positive peaks) and destruction (area under the negative NO destruction region) rates as oxygen is progressively added to the fuel side. In this study both these rates increased while in the previous work with methane-air partially premixed flame, Blevins and Gore [31], both these rates decreased with progressive partial premixing. This apparent disagreement can be understood upon considering the different effect on dilution and flame temperature depending on the choice of oxidizer added to the fuel side and whether flame radiation is included or not. Firstly, with the use of air or oxygen, Table 5.4, for partial premixing in an original methane-air non-premixed flame, the adiabatic mixture temperature (CET-93 calculations) does not change significantly with progressive partial premixing. However, adiabatic calculations with OPPDIF code indicate an increase in the peak flame temperature. When the progressive decrease in radiative fraction with partial premixing is accounted for, the flame temperature increases, as shown in experiments and our temperature given calculations that account for soot and gas radiation. The effect of flame radiation on NO rates is important, especially for low strain rate counterflow flames. This effect is not accounted for in the calculations of Gore and Blevins[31]. The increase in the flame temperature favors increase in the NO formation and destruction rates. Secondly, with the use of air there is a large dilution effect due to nitrogen in air, unlike in the case when pure oxygen is mixed with the fuel for partial premixing. While the trend for the path integrated NO formation and destruction rates in this work differs from that in previous research on methane-air partially premixed flames, the trend for net NO production rate is in agreement with the previous work [31]. Path integrated net NO production rate increased with progressive partial premixing indicating that partial

premixing favored NO formation over NO destruction. The ratio of path-integrated NO destruction to NO formation rate decreased with progressive partial premixing.

EINO

Following previous work in counter-flow flames, [29-31], the EINO for counter-flow flames is defined as:

$$EINO = \frac{\int_0^l MW_{NO}\,\omega_{NO}\,dx}{-\int_0^l MW_{CH4}\,\omega_{CH4}\,dx} \qquad (6.1)$$

where the numerator and the denominator represent path-integrated rates of NO production and methane fuel consumption along the stagnation streamline. Figure 6.5 shows the trend in the EINO for the present study. For the levels of partial premixing studied EINO first increased and then decreased. Flame-sheet analysis indicates that the non-premixed flame reaches the stagnation plane when 19.4% oxygen is added to the fuel. While we could not study the effect of partial premixing beyond 22.7% oxygen due to burner limitations, this was sufficient to move the non-premixed flame from the oxidizer side to the fuel side of the stagnation plane. The maximum in EINO for 19.4% oxygen when the non-premixed flame is close to the stagnation plane is consistent with previous low strain rate calculations showing maximum in EINO for Φ~2.2 for rich methane air counter-flow flames. It was shown in Chapter 4 that Φ~2.2 is the equivalence ratio for methane-air partially premixed flames for the non-premixed flamesheet cross-over. The importance of the location of the reaction zone with respect to the stagnation plane for NO formation in partially premixed flames is discussed next.

Location of the reaction zone with respect to the stagnation plane

Nishioka et al. [29] found that in EINOx reached a maximum value for Φ~2 in their methane-air partially premixed flames at a global strain rate of about 20 sec-1. Blevins and Gore [31] found that the peak NO concentration and the EINOx reached

maximum at the rich methane-air equivalence ratio of Φ~2.2. This observation is of interest because Tsuji and Yamaoka [3] found that the non-premixed reaction zone, which originally lies on the oxidizer side of the stagnation plane, reaches the stagnation plane for Φ=2.11 in their experiments with rich methane-air flames in planar 2-D counter-flow flames. The importance of this equivalence ratio can be understood by observing that the peak thermal NO production rate is in the vicinity of the peak flame temperature and that the residence time for NO production via the thermal NO pathway is maximum when the flame is close to the stagnation plane. Using a simplified flame-sheet model we demonstrated, in Chapter 4, that the equivalence ratio for methane-air mixture for the non-premixed flamesheet to cross over from the fuel side to the oxidizer side is 2.17 independent of the strain rate, the choice of counter-flow flame geometry (2-D planar or axi-symmetric) or the choice of thermo-chemical property data. It was further shown that the non-premixed flame cross over equivalence ratio was Φ~2.2 for a large variety of hydrocarbons including alkanes, alkenes and alkynes till C6. This is a useful result to help determine the equivalence ratio for which the residence time for thermal NO formation is most favorable.

Equally important is the premixed flame crossover equivalence ratio, defined as the equivalence ratio of the rich fuel-air mixture when the premixed reaction zone lies at the stagnation plane. Tsuji and Yamaoka [3] found that this event happened at Φ~2.7 for their methane-air partially premixed flames. It indicated the equivalence ratio for transition from 'merged-flames' regime to 'interdependent' flame regime. Gore and Blevins [31] observed two CH peaks in the computed structure of low strain rate methane-air partially premixed flames for Φ<2.5. The equivalence ratio for the premixed flame cross over is dependent on the strain rate as indicated earlier, by Gore and Blevins [31], and Mungekar and Atreya [84]. Thus, a generalized result, like the one for the non-premixed flame crossover, cannot be made.

6.4 Conclusions

The effects of fuel side partial premixing on the energy release rate, flame radiation and NO formation were studied for progressive addition of oxygen to the fuel side of methane counter-flow flames. Following are the key conclusions from this study.

1. The measured peak NO concentration increased and the NO profile broadened with progressive partial premixing. These observations were reproduced reasonably well by computations with using the GRIMECH 3.00 mechanism.
2. With partial premixing, the NO production rate distribution showed two positive NO production peaks and one NO destruction region. One production peak was accounted for by thermal NO reactions alone. Contribution of this peak to total NO production increased with progressive partial premixing indicating that thermal mechanism was favored as the flame temperature increased with progressive partial premixing.
3. With progressive partial premixing the spatial separation between the two NO formation peaks increased. This observation accounted for the observed broadening of the NO concentration profile with progressive partial premixing.
4. Fuel side partial premixing favored the NO formation reactions over the NO reburn reaction.
5. EINO first increased and then decreased with progressive partial premixing for the levels of partial premixing studied. Careful review of previous literature indicated that in low (<20 sec^{-1}) strain rate methane air flames EINO reached maximum around Φ~2.2 irrespective of strain rate. This observation, along with the maximum in EINO around 19.4% oxygen content in the fuel in the present work, indicates that EINO in low strain rate partially premixed flames peaks around the non-premixed flame cross over equivalence ratio.

Similar effects should be expected for flamelet combustion under similar conditions of chemistry and strain rate.

Fuel	Co-Flow Flames	Flamelength	X_r	EINO
Methane (Laminar)	Gore and Zhan(96), Dupont and Williams (98)	↓		↓ and then ↑ (minimum~2.0)
Methane (Turbulent)	Driscoll et al. (92), Turns et al. (93), Lyle et al. (99), Lee et al. (00)	↓	↓	↓ and then ↑ (minimum~1.5)
Ethane (Laminar)	Kim et al. (95)	↓		↓ and then ↑ (minimum~2.2)
Propane (Turbulent)	Turns et al. (93)		↓	↑
Propane (Laminar)	Rokke et al. (94)			↑
Ethylene (Turbulent)	Turns et al. (93)		↓	↑
Hydrogen (Turbulent)	Driscoll et al. (92)	↓	↓	↓

Table 6.1 Summary of results from previous work on co-flow flames

	K(Hz)	ϕ	[NO]max	EINOx	Tmax	Radiation
Tsuji & Yamaoka(76)		1.45-∞			↑	Yes
Nishioka et al. (94)	~20	1.55-∞	↓	↑ and ↓ (max ϕ~2)	Const	No
Tanoff et al. (96)	~150	1.3-2	↓		↑	Yes
Dupont and Williams(96)	~20	1.4-2.4		↑ and ↓ (max ϕ~2.2)	↑(?)	No
	50-200	1.4-2.4			↑(?)	No
Blevins & Gore(98)	5	1.6-∞	↑ and↓ (maxϕ~2)	↑ and ↓ (max ϕ~2.2)	↑(?)	No
Ravikris& Laurandeau(00)	~20	1.45-2	↓			Yes
Flamesheet analysis					Const	No

Table 6.2 Summary of results from previous work on counter-flow flames

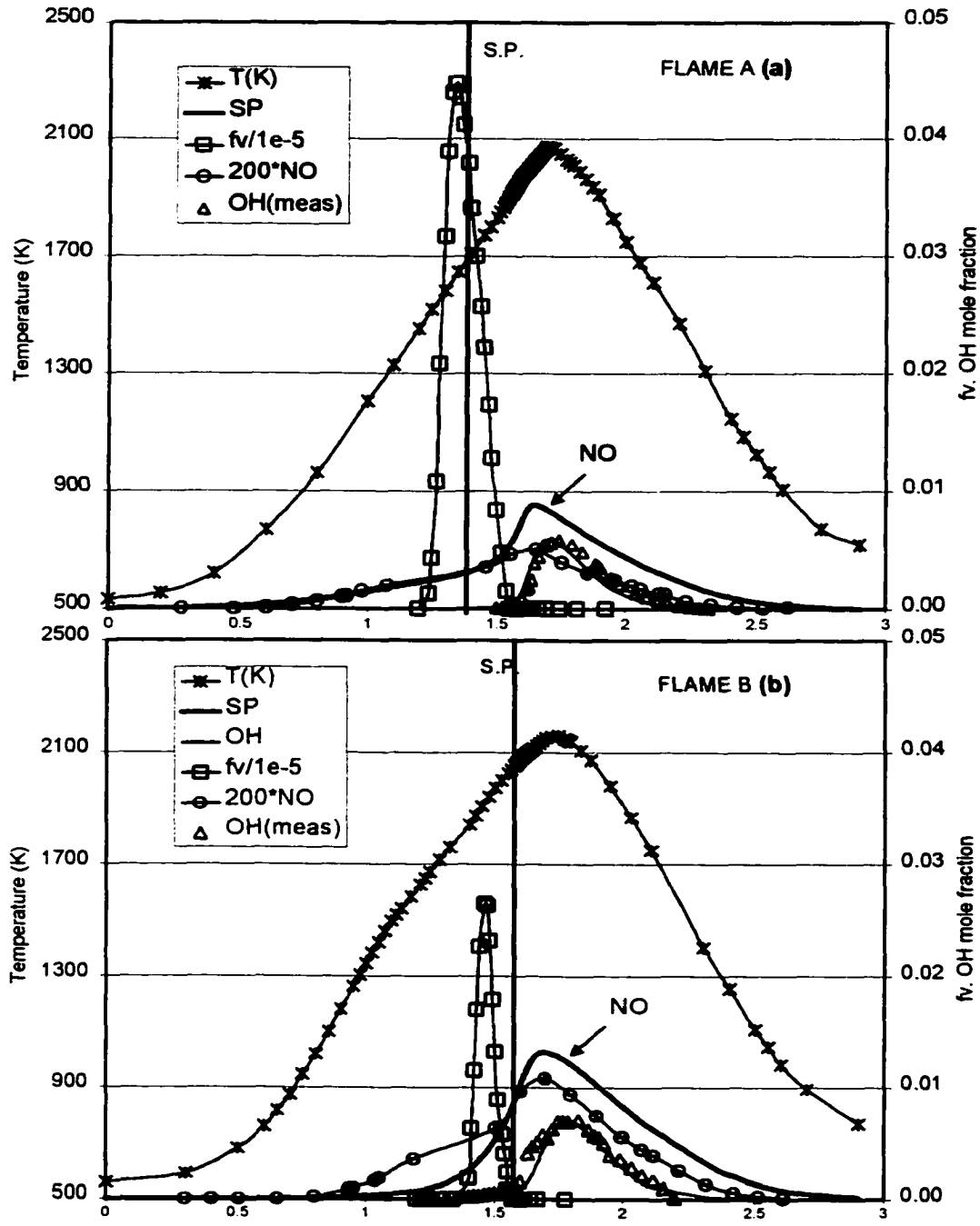

Fig 6.1 Distribution of computed and meaured NO, OH, T and soot in (a) non-premixed flame, Flame A (b) partially premixed flame, Flame B

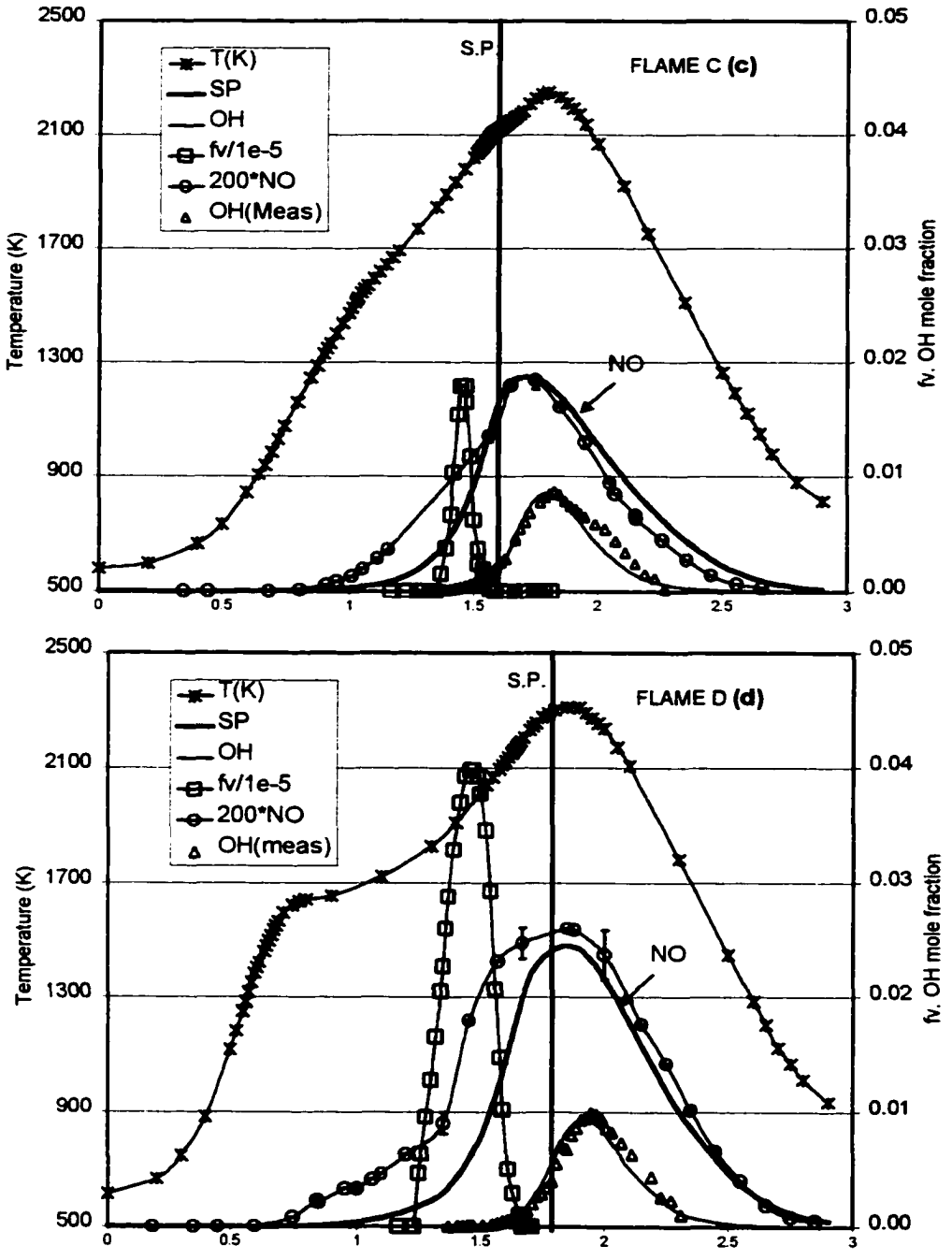

Fig 6.1 Distribution of computed and measured NO, OH and measured T and soot in Partially premixed flames (c) Flame C (d) Flame D

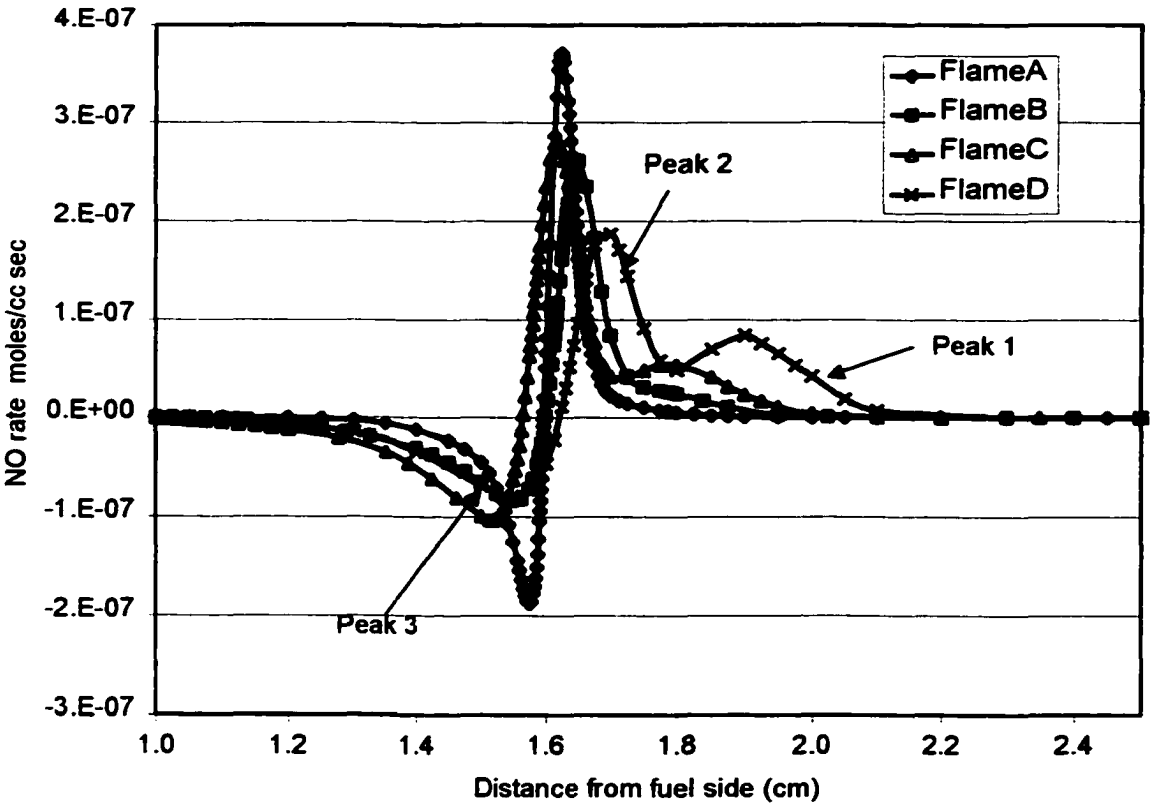

Fig. 6.2 Computed NO production rate distribution

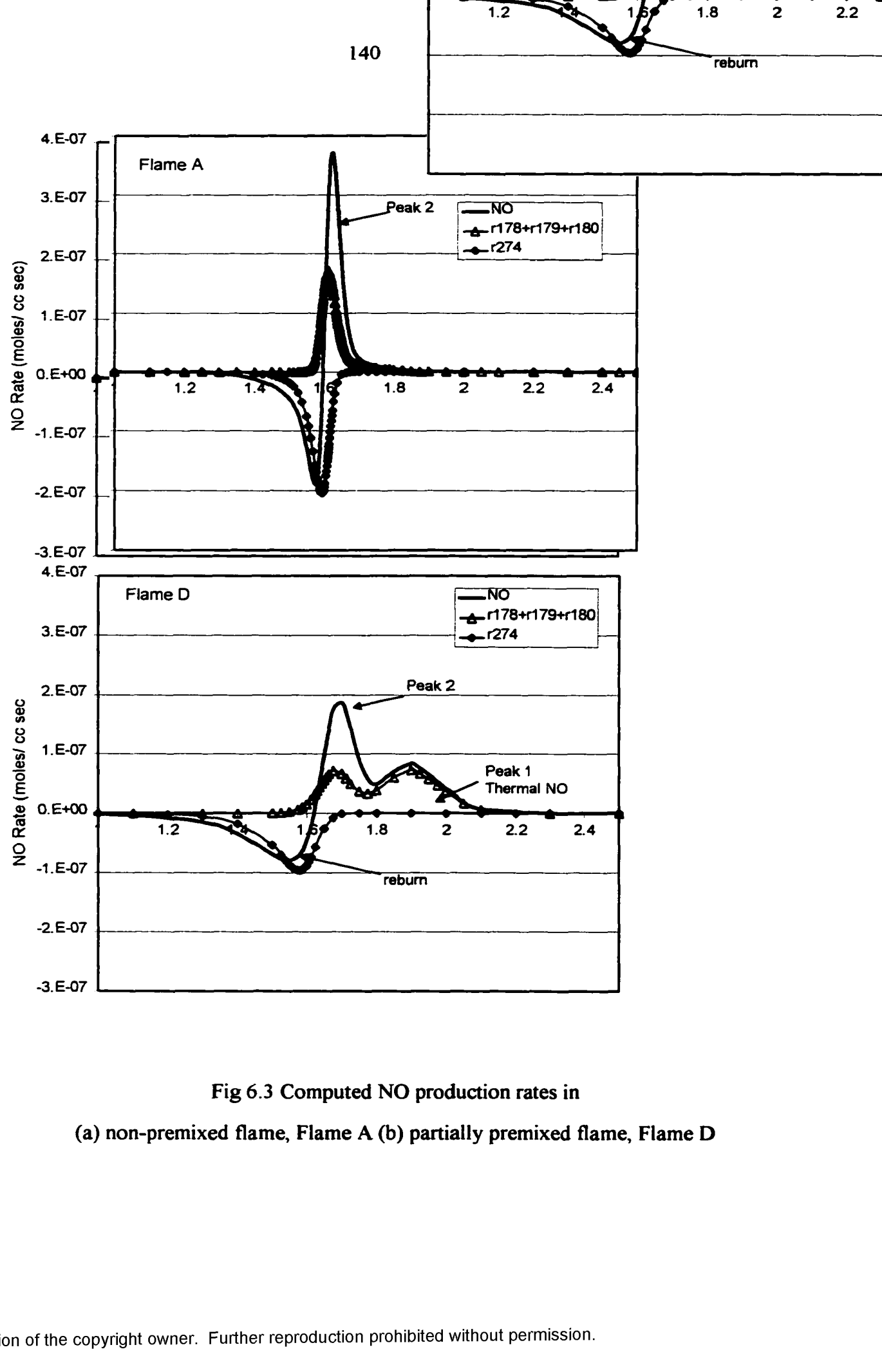

Fig 6.3 Computed NO production rates in

(a) non-premixed flame, Flame A (b) partially premixed flame, Flame D

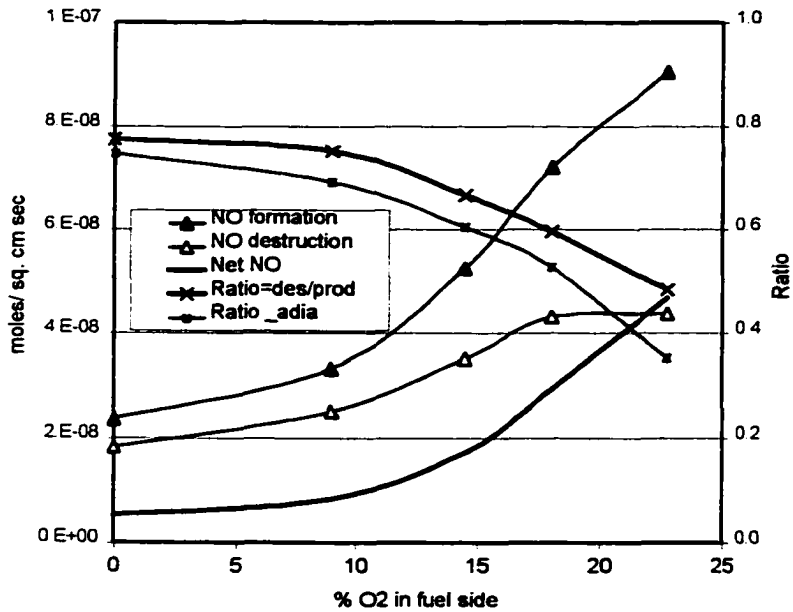

Fig. 6.4 Path integrated NO formation and destruction rates

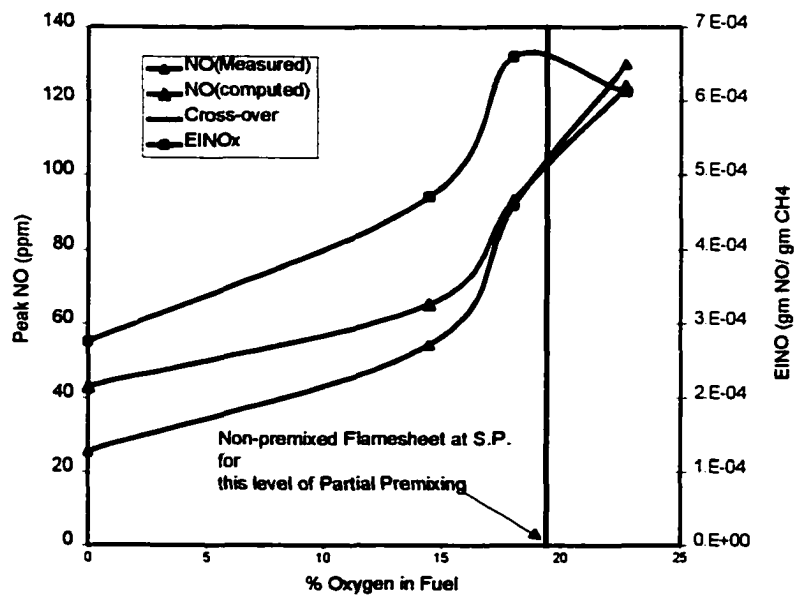

Fig 6.5 Trend in computed EINO with progressive partial premixing

CHAPTER 7

TRANSITION TO SOOTING

7.1 Introduction

Combustion generated soot particles are of interest due to their health and environmental concerns. Soot radiation from flames is an important mode of heat transfer in industrial furnaces. Motivated by these concerns efforts for development of computational models for quantitative prediction of soot formed in flames and emitted in combustion exhaust is an active area of research, [85-89], Validation of such models against experiments in well defined laboratory flames is necessary before the models can be used for modeling soot processes in practical combustion equipment.

Soot obtained from a variety of fuels and combustion sources has shown invariance of chemical composition, physical and optical properties [90]. When observed under transmission electron microscope (TEM), soot particles appear as aggregates with open structure consisting of nearly spherical primary particles (~10-40nm). Observation of primary particles using X-ray diffraction techniques shows crystalline structure showing randomly oriented laminated structures. The existence of these laminar structures is attributed to large Polycyclic Aromatic Hydrocarbons (PAH), which are planar compounds. PAH compounds are believed to be important precursors in the pathway to soot formation. Therefore for most commercial fuels, which are aliphatic compounds, formation of first benzene ring is an important step in the chemical pathway to soot formation. The role of acetylene in growth of PAH species via hydrogen abstraction carbon addition (HACA) mechanism is recognized in literature [86]. In addition to this mechanism, it is proposed, [91,92], that large PAHs can coalesce in

highly effective reactive collisions of these large molecules (typically 300-500 amu). Studies based on TEM observation of thermophoretically sampled material in regions where tarry material (characterized by insolubility in organic solvent indicating molecular weight of >1000 amu) showed [93] existence of single particles which are typically 2-10nm is size and are more transparent to electron beam than more mature soot particles. The author has noticed brown tarry deposits on gas sampling probes use to collect material from the dark region between the blue chemilumeniscent zone and the yellow sooty zone in counter-flow flames. The process of carbonization of these nuclei has received attention in recent combustion literature, [94,95]. The nuclei form the primary particles that collide with each other and form soot agglomerates. Usually, most of the soot mass produced in flames comes from surface growth of primary particles rather than from formation of soot nuclei. Soot inception is the first step where experimentally identifiable particle matter forms in the flame. The importance of soot inception for an accurate representation of soot processes in a soot model is emphasized by the following considerations:

1. Incorrect location of soot inception manifests in incorrect T-t history of growing soot particles resulting in incorrect soot surface growth rates
2. Incorrect size and/or number of soot nuclei results in incorrect surface area (resulting in incorrect aggregate morphology and soot volume fraction due to incorrect surface growth rates)
3. Both the factors above can result in incorrect radiation heat transfer and soot exhaust emission calculations.

To validate a soot model carefully designed experiments in well-defined flame geometry are needed. Counter-flow flame configuration is a well-defined flame configuration where the flame is established between opposing flows of fuel and oxidizer. The counter-flow flame configuration is pertinent to turbulent combustion via flamelet approach, [34]. This flame configuration is convenient for computational

modeling along the stagnation streamline due to numerical simplicity of the one-dimensional problem. Furthermore, approximate one-dimensionality of scalar variable within central 'core' region around the burner centerline allows for comparison of computational modeling with experimental measurements.

Several experimental and computational studies, [89, 96-100], of soot inception in counter-flow flames have been reported in literature. These studies have utilized transition from blue (soot free) flames to yellow (soot-containing) flames to explore the effect of a variety of variables on soot inception as summarized in Table 7.1. The study of 'transition to sooting' is a convenient technique to study soot inception without overwhelming the experiment and the model with the complexities of soot growth. In this work we shall use the phenomenon of 'onset of sooting' or 'transition to sooting' to study soot inception in methane and ethylene counter-flow diffusion flames. Transition to sooting may be induced by varying one or more of the following parameters: (i) strain rate (ii) composition (fuel, oxidizer or diluents concentration) (iii) fuel/oxidizer preheat (iv) pressure. All the previous studies, save one [100], have used strain rate to induce sooting. Chung et al., [100], mapped the 'transition curve' demarcating soot free and soot containing flames in a constant (global) strain rate study of propane-oxygen flames using nitrogen as diluent on the fuel and oxidizer side to change the inlet fuel and oxidizer concentrations. They observed that the transition curve, Fig. 7.1, had two asymptotes: (i) for flames with low Y_F, transition to sooting occurred for Y_F~constant (ii) for flames with low Yo, transition to sooting occurred for Y_o~constant. Other studies have provided useful quantitative, Senkan and co-workers, [101,102], and qualitative, [103], measurements of PAH species and computational modeling of PAH chemistry in hydrocarbon counter-flow flames.

Constant strain rate transition experiments, similar to those of Chung et al.[100], were performed for low strain rate (5-7 1/sec) methane and ethylene counter-flow flames to study the behavior of the 'transition curve' for these fuels. It is shown that the concept

of the 'transition curve' can be used to compare the sooting tendency of different fuels or to assess the effectiveness of additives for soot suppression.

Experiments were performed for a series of methane and ethylene counter-flow flames having similar global strain rate and located at (or near) the stagnation plane to study onset of sooting by altering inlet fuel and oxidizer side composition. Measured scattering and extinction coefficients for 514.5 nm laser light were used to study the optical characteristics of the flames across the threshold of transition to sooting. Computations with Sandia opposed flow flame code, OPPDIF [33], were used to gain understanding of flow-field and species distribution using GRIMech 3.00, [56],C2 chemistry.

7.2 Transition Curves

The 'transition curve' is defined as the curve separating the domain of soot free flames from sooty flames in the Yf-Yo plane as shown in Fig. 7.1. In Fig. 7.1 the axes indicate the inlet fuel and oxidizer mass fractions for constant strain rate non-premixed counter-flow flames. The region on the convex side of this curve (the region containing the origin) is the domain of soot-free flames for the given fuel-oxidizer-global strain rate combination. The curves presented in Fig. 7.1 are for atmospheric pressure flames. The discussion presented here does not include any effects of pressure dependence on transition.

The previous authors, Chung et al. [100], accounted for this interesting observation by noting that the inlet fuel concentration may be the most crucial independent variable for flames having small fuel (and therefore small soot precursor) concentration while the flame temperature (which in turn depends on the inlet oxygen concentration) may be the most important variable for flames where the fuel is in excess.

We have reported the transition curves for diluted methane-oxygen and ethylene oxygen flames with global strain rate of ~7sec^{-1} in Fig. 7.1. The two inlet ports were 2.9cm apart in these experiments, unlike 1.4cm for Chung et al., [100], and the diluents used were a 1:1 (by volume) mixture of helium and nitrogen for the oxidizer side and argon for the fuel side. Transition to sooting was identified by a sudden, almost two to three orders of magnitude, change in the measured peak Qvv laser light scattering signal across the 'transition curve'. The peak scattering coefficient measured in the flame increased about 2-3 orders of magnitude for a small, typically less that 1%, change in the fuel/oxidizer concentration at the threshold of transition to sooty flames.

The transition curves for methane and ethylene, shown in Fig. 7.1, exhibit the same general behavior as reported for propane flame by Chung et al. [100]. The transition behavior for ethylene flames at large Y_F values could not be studied as the excess unburnt fuel escaping the combustion zone formed a hazardous flammable mixture with room air and burnt in the annular space around the burner.

Encouraged by the similarity in the behavior of the constant global strain rate transition curves for a variety of fuels using different diluent and at different global strain rates as shown in Fig.7.1, the concept of the transition curve in Y_F-Y_O plane as a tool to rank the sooting tendencies of different fuels appears promising. One difficulty in using the curves as shown in Fig. 7.1 is that any given point, (Y_O, Y_F), for two different fuels does not, in general, represent flames at same location of the non-premixed flamesheet from the stagnation plane. This apparent difficulty is overcome by scaling the Y_F axis by $M_F\nu_F/M_O\nu_O$. With the choice of this scaling, lines of constant nondimensional flame position are represented by straight lines of the form:

$$\frac{Y_F}{(M_F\nu_F/M_O\nu_O)} = \left(\frac{1}{\beta_{stoic}} - 1\right) Y_O \qquad (7.1)$$

where βstoic is defined for given inlet compositions of fuel and oxidizer side by eqn 4.5. Representative lines are shown in Fig. 7.2 with corresponding βstoic numbers.

As discussed before in Chapter 4, βstoic>.5 indicates flamesheet on the fuel side of the stagnation plane and βstoic<.5 indicates flamesheet on the oxidizer side of the stagnation plane.

Since the choice of diluents was identical for methane and ethylene transition curves shown in Fig. 7.2, the observation that the transition curve for ethylene is located on the convex (inner) side of the methane transition curve indicates that ethylene fuel soots more easily than methane. While this conclusion is not new, the approach adopted here in arriving at this conclusion is novel. This approach can be adopted to study other transition phenomena like flame extinction. The effectiveness of an additive to suppress sooting or to aid flame suppression can be identified by comparing the transition curves as outlined above.

In Fig. 7.2, the straight line for βstoic=0.5 separates the fuel side flames from the oxidizer side flames. An investigation of transition to sooting for βstoic=0.5 flames of methane and ethylene fuels is described in the next section.

7.3 Transition to Sooting for βstoic=0.5 flames

From the study of transition curves for three different fuels presented in the last section it is observed that transition for flames along βstoic =0.5 takes place away from either asymptotes to the transition curve. While the importance of the fuel concentration is emphasized for low Yf values (βstoic ~1) the importance of peak temperature is emphasized for flames with βstoic <0.2. Both the flame temperature and the inlet fuel concentration can be expected to be important variables for transition to sooting in βstoic ~0.5 flames. An interesting aspect of studying transition in flames with βstoic =0.5 is that the 'flamesheet' is located at the stagnation plane and the strain rate distribution is constant and almost identical for the flames as we undergo transition, along βstoic =0.5 line in Fig. 7.2. This aspect is presented and discussed in more detail in the following

section of on the flame structure. The simplicity of the flow-field in soot inception region may be advantageous for future analysis of soot inception models. Starting with blue flames, the inlet fuel and oxidizer side compositions were varied so as to maintain βstoic, defined by eqn. 4.5, constant at 0.5. Argon was use as a diluent for the fuel side while a 1:1 (by volume) mixture of helium and nitrogen was used as a diluent for the oxidizer side. The inlet compositions and boundary conditions for βstoic =0.5 methane and ethylene flames across the threshold of transition to sooting are tabulated in tables 7.1 and 7.2 respectively. Experimental measurements included distribution of temperature, laser light extinction, Kext, and scattering coefficient, Qvv, for 514.5nm wavelength along the axis of symmetry of the counter-flow burner. Details of the burner and experimental methods are described in Chapter 3. The laser light extinction setup was modified for improved accuracy in the measured extinction coefficient as described in Appendix A5. The new laser light extinction technique allowed for detection of extinction signal down to 0.2% extinction. This is important for lightly sooting flames near the threshold of transition to sooting.

(a) Flame Structure

Two issues are addressed in the following discussion. Firstly, the implication of finite rate chemistry and non-unity Lewis number for a formal definition of a 'flame' for non-premixed hydrocarbon flames. Secondly, a unique feature of the flow-field distribution for βstoic=0.5 flames, not observed for other (oxidizer side or fuel side of stagnation plane) flames, is presented.

In the infinite rate chemistry framework all the energy release takes place in a 'thin' flamesheet (Yf=Yo=0) that coincides with the peak flame temperature. With Le=1 assumption and infinite rate chemistry, βstoic=0.5 indicates that the peak flame temperature, the stagnation plane and the flamesheet all coincide.

With finite rate chemistry, the energy release for hydrocarbon combustion is distributed in two major spatially separated steps as discussed Chapter 5. In the first step,

the hydrocarbon fuel is partially oxidized into CO and H2, which are, in turn, oxidized into CO2 and H2O in the second step. Computed species distribution, using GRIMech 3.00 mechanism, in βstoic=0.5 methane flame with 23% inlet methane concentration is shown in Fig. 7.3(a). Corresponding computed energy release and similarity variable, β (defined by eqn. 4.3), distribution are plotted in Fig 7.3(b). The locations of the stagnation plane and the peak flame temperature are shown in these figures. The βstoic=0.5 and the peak temperature locations are located at the fuel side and the oxidizer side extremes of the energy release distribution with the stagnation plane sandwiched in-between. The OH, fig. 7.3(c), zone extends to the fuel side of the stagnation plane and the fuel side edge of the OH profile coincides with the computed βstoic=0.5 location in the flame. An implication of this for soot formation is that these flames can be expected to have soot formation and oxidation confined to the fuel side of the stagnation plane, as was the case for the 'fuel side' flame, Flame 4.0 reported in Chapter 4.

Fig 7.3(a) shows computed distribution of velocity and temperature in the 23% methane flame. The small separation between the locations if the peak flame temperature and the stagnation plane in Fig. 7.3(c), in spite of the choice of inlet compositions to ensure βstoic=0.5, is due to the effects of finite rate chemistry and non-unity Lewis number. It is interesting to note that the strain rate (gradient of the axial velocity) is almost constant over a significant portion of the energy release distribution on both the fuel and oxidizer side of the stagnation plane. The gas does not accelerate as it approaches the flame located near the stagnation plane. Unlike this situation, when the flame is located away from the stagnation plane, Fig. 3.17, the gas first accelerates as it approaches the flame and then decelerates as it approaches the stagnation plane. The uniform flow-field near the flame is significant in future efforts to analytically understand strain rate effects on the transition phenomena.

Computed and measured distributions of temperature for βstoic=0.5 methane and ethylene flames are shown in Fig. 7.4(a) and Fig. 7.4(b) respectively. Corresponding

distributions of axial velocity and similarity variable β are shown in Figs. 7.5 and 7.6 respectively. The peak temperature location and the stagnation plane location are nearly the same. For 20% and 21% methane flames the peak flame temperature is at 1.70 cm from the fuel side inlet. For 22%, 23% and 24% methane flames the peak flame temperature is at 1.65 cm from the fuel side inlet. . The stagnation plane is located typically .2-.4 mm on the fuel side of the peak flame temperature location. Starting at 1790K for the 20% methane flame, the peak flame temperature increases by about 60-70K for every 1% increase in inlet fuel concentration for methane flames. The strain rate distribution in the vicinity of the flame around the stagnation plane is almost uniform and similar for several flames shown in Figs. 7.5(a-b). This indicates that not merely the design global strain rate, reported in Tables 7.2 and 7.3, is same for these flames, but the actual strain rate is also maintained approximately the same in the vicinity of the flame and soot nucleation zone. Distribution of similarity variable, β, in Fig 7.5(a) shows that βstoic=0.5 is located between 1.50-1.56cm from the fuel side inlet for 22-24% inlet methane concentration flames. This indicates that in the flames considered, the flamesheet, (Yf=Yo=0), indicated by βstoic=0.5, is located on the fuel side of the stagnation plane. Computations for ethylene βstoic=0.5 flames, Figs.7.4 (b)-7.6(b), showed similar behavior for the distribution of temperature, velocity and the similarity variable, β.

(b) Visual Observation of the Flames

Observation of yellow luminosity as a marker for transition to sooting can be deceptive for counter-flow flames because the central 1-d region may still be blue and particle free while the edges of the flames may have a yellow tinge due to reduced strain rate. The visual observation of blue flames is still a simple, yet reliable way to ascertain flames free of incandescent soot particles. The methane flames were blue for 16-19% inlet methane concentration, with a tinge of yellow luminosity appearing on the fuel side

of the blue zone for 20% inlet methane concentration. The yellow luminosity became stronger with progressive increase in the inlet methane concentration. The soot zone was confined to a thin, about 2 mm in thickness, zone with high soot luminosity that increased progressively from 22% to 24% inlet methane concentration flames. The fact that the OH zone extends to the fuel side of the stagnation plane, Fig. 7.3(c), indicates that soot formation and oxidation take place in a thin zone on the fuel side of the stagnation plane.

Similar observations were made for ethylene flames. Starting with blue 11% ethylene flame, the first tinge of yellow luminosity was observed for 12% ethylene flame with the central region still appearing blue. Further increase in inlet fuel concentration to 12.5% resulted in an increased yellow luminosity, though it was unclear if the central region was still blue on the basis of visual observation. 13% and 14% inlet ethylene concentration flames were sooty flames with thin intensely radiating soot zone.

(c) Distribution of Scattering Coefficient, Qvv

Measured Qvv scattering coefficient distribution for 514.5nm wavelength are shown in Figs 7.7 for the methane flames. The distribution of Qvv in the 20% flame indicates that the scattering coefficient decreases and reaches a minimum around 1.7 cm from the fuel side inlet, which coincides well with the location of the peak flame temperature. The distribution of scattering coefficient is representative of a flame where no large soot precursor molecules or soot particles are present. For an ideal gas scattering cross section, $Qvv \propto 1/T$, indicating about 5 fold decrease in the scattering coefficient for temperatures corresponding to ~2000K near the peak flame temperature location. In 21% methane flame, Fig. 7.7, the scattering signal first increased and then decreased reaching a minimum around the peak flame temperature location. An order of magnitude increase in the scattering coefficient observed with a mere 1% change in the fuel concentration indicates presence of scattering species other than major stable molecules in the flame. Further increase in fuel concentration shows a rapid increase in peak scattering coefficient. There is almost three orders of magnitude change in the peak scattering

coefficient in going from 21% methane flame to 22% methane flame. Subsequent change in the peak scattering coefficient from 22% to 24% methane flames is less abrupt. It is interesting to note that when the scattering coefficients profiles in 22%, 23% and 24% methane flames were scaled with the peak scattering coefficient in the corresponding flames, Fig 7.8, the scaled scattering coefficient profiles looked almost identical. Within the Mie Sphere interpretation of the scattering coefficient, $Q_{VV} \propto f_v D_{63}^3$, indicating that the growth and decay process for the above parameter is identical in these flames. This observation of Qvv can be used to verify whether the soot growth models are able to capture the physical and chemical process responsible for the above aspect of growth and oxidation of soot in these flames. Similar observations are reported for ethylene. Qvv distribution in 11% and 12% ethylene flames, shown in Fig. 7.9, is typical of particle/large-molecule free flames. There is almost an order of magnitude increase in the scattering coefficient going from 12% ethylene flame to 12.5% ethylene flame, Fig. 7.10(a), while the increase is almost three orders of magnitude in going from 12.5% ethylene flame to 13% ethylene flame. Subsequent increase in the peak scattering coefficient is not as pronounced. Scattering coefficient distributions in 13% and 14% ethylene flames, when scaled with the peak scattering coefficient values in the corresponding flames, Fig 7.10(b), showed that the scaled profiles were almost identical.

(d) Distribution of Extinction Coefficient, Kext

The experimental setup for measurement of extinction coefficient, described in Appendix 4, allowed for measurement of extinction of laser light with a systematic experimental uncertainty of ± 0.1%. For an extinction path length of 5cm this translates to a lower limit of detection for Kext of $0.02m^{-1}$, which in turn sets the lower limit of detection of soot volume fraction as $2x10^{-9}$ for an assumed soot complex refractive index of 1.57-0.56i.

Distribution of measured ratio of attenuated to incident laser intensity, I/Io, and the extinction coefficient, Kext, for methane flames is shown in Fig 7.11 and 7.12

respectively. No measurable extinction of the laser light was observed for flames with less than 22% inlet methane concentration. This is particularly interesting for the 21% inlet methane concentration flame, in which a maximum in scattering coefficient distribution, Fig. 7.7, was observed for the first time The scatterers in this flame may be large polyaromatic compounds or early soot precursors which have scattering cross-section significantly larger than that of major molecular stable species in the flame, yet having low extinction cross-section.

Distribution of measured ratio of attenuated to incident laser intensity, I/Io, and the extinction coefficient, Kext, for methane flames is shown in Fig 7.13 and 7.14 espectively. No measurable extinction of the laser light was observed for flames with less than 13% inlet methane concentration. For the 12.5% ethylene flame no extinction of laser light, within the limits of experimental uncertainty, was observed though for the first time a maximum in the distribution of the scattering coefficient was observed in this flame, similar to the case of 21% methane flame.

(e) Interpretation using Mie Scattering Theory

Before we embark upon an interpretation of the measured scattering and extinction coefficients using Mie scattering theory for spheres, it is important to acknowledge that the interpretation is limited by uncertainties in the complex refractive index of soot precursor particles and newly formed soot particles as well as approximation of actual soot aggregate morphology by a Mie equivalent sphere.

Reliable Mie theory interpretation can be attempted only for 23% and 24% methane flames and 13% and 14% ethylene flames. For these flames the distribution of fv, D63 and OH in shown in Figs. 7.15-7.18. Soot formation begins on the fuel side of the stagnation plane, soot volume fraction and peak diameters increase and then decrease as soot is driven into the OH zone. All the soot is consumed prior to reaching the stagnation plane. Largest Mie sphere equivalent diameters in these flames are in the range of 35-90nm while the peak soot volume fraction in these flames are in between 3x10-8 and

1.5x10-7. These flames are clearly sooty flame. More interesting is 22% methane flame in which laser light extinction could be barely measured using the experimental setup used in this study. Using measured extinction and scattering coefficients, Kext~0.011m-1 and peak Qvv of 6.4x10-5m-1 , and an assumed soot complex refractive index, m=1.57-0.56i, soot volume fraction in this flame is estimated to be about 10^{-9} and for this peak soot volume fraction the Mie equivalent sphere diameter is estimated as 72.6 nm, This size appears large. Since there is a large (±100%) uncertainty in measured extinction coefficient this uncertainty is also reflected in the Mie sphere diameter reported above. Since the nature of the scattering particles, which can be large molecules or soot precursor particles or carbonized soot particles, is not known the uncertainty in the assumed refractive index further increases the error associated with estimation of particle diameters in such flames.

Above data of scattering and extinction coefficients is useful to check the prediction of computational model provided a reliable way to predict particle morphology and to relate it to particle optical properties become available. At the least the scattering and extinction data presented for a set of methane and ethylene flames can be used to benchmark a soot model for its ability to predict transition from particulate containing flames to particle free flames. The identity of scatterers in 12.5% ethylene and 21% methane flames, where no laser light extinction was observed within the limit of experimental uncertainty, needs to be confirmed. This may be confirmed by TEM observation of thermophoretically sampled material from these flames.

7.4 Conclusions

A study of transition from blue particle free flames to sooty flames was carried out for diluted methane-oxygen and ethylene oxygen counter-flow flames at constant global strain rate. Following are the key conclusions from this study:

1. Constant global strain rate transition curves for methane and ethylene had two asymptotes: (i) for flames with low YF, transition to sooting occurred for

Yo~constant (ii) for flames with low Yo, transition to sooting occurred for Yf~constant. These trends qualitatively agree with previous work , Chung et al. (1997), for propane flames.

2. The transition curves can be used to rank the sooting tendency of different fuels or the effectiveness of additives to suppress sooting by using the scaling $M_F v_F / M_O v_O$ for the Yf axis.
3. Laser light scattering and extinction coefficients in a set of methane and ethylene flames located very close to the stagnation plane is reported. These measurements were used to identify transition from particle free flames to soot containing flame. Intermediate flames (where large scattering, beyond what can be accounted for by major stable species in the flame, however, without any measurable extinction of visible laser light) need further investigation and the nature of scattering molecules/particles in such flames needs to be ascertained.

Since the transition to sooting took place over a 1% change in fuel concentration, the reported data should be used taking into consideration uncertainties in the orificemeter and rotameters calibrations.

Limiting Strain Rate Studies (Strain rate, K, varied to induce transition to sooting)	
Du et al. (1988)	E_a for soot inception
Du et al. (1995a)	βstoic effect on soot inception
Du et al. (1995b)	The effect of diluents on soot inception
Du et al. (1998)	Effect of pressure on soot inception
Constant Strain Rate Studies (Strain rate, K, held constant)	
Chung et al. (1997)	Identified transition curve for propane-oxygen diluted with N2 for global strain rate of about 30 sec^{-1}.

Table 7.1 Previous studies of transition to sooting in counter-flow flames

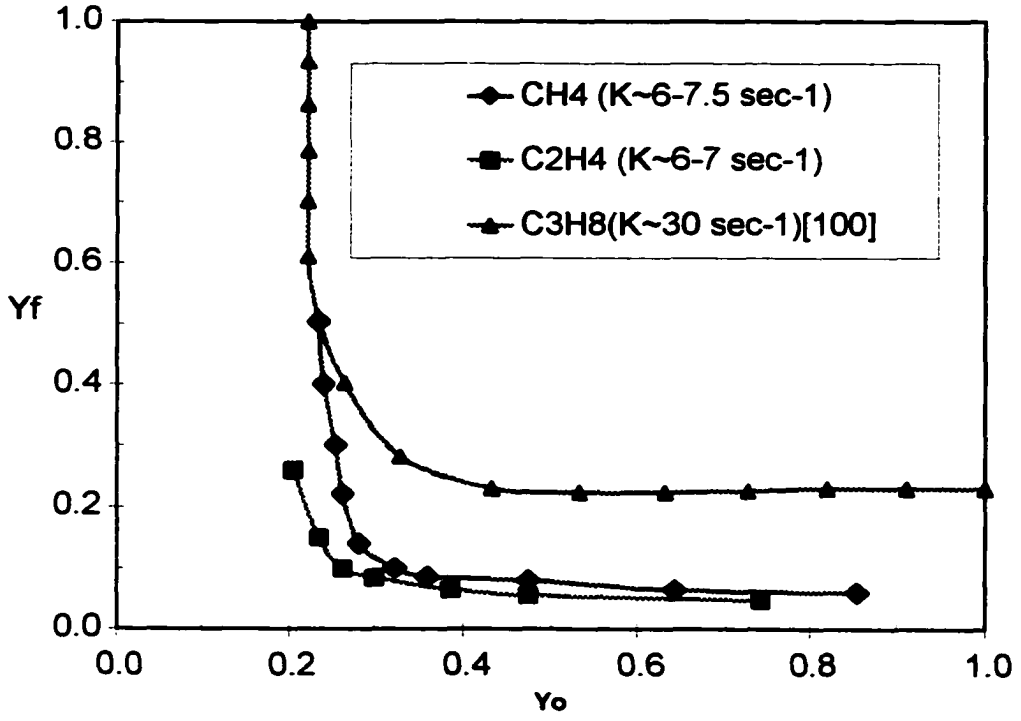

Fig. 7.1 Transition curves in Y_F-Y_O plane

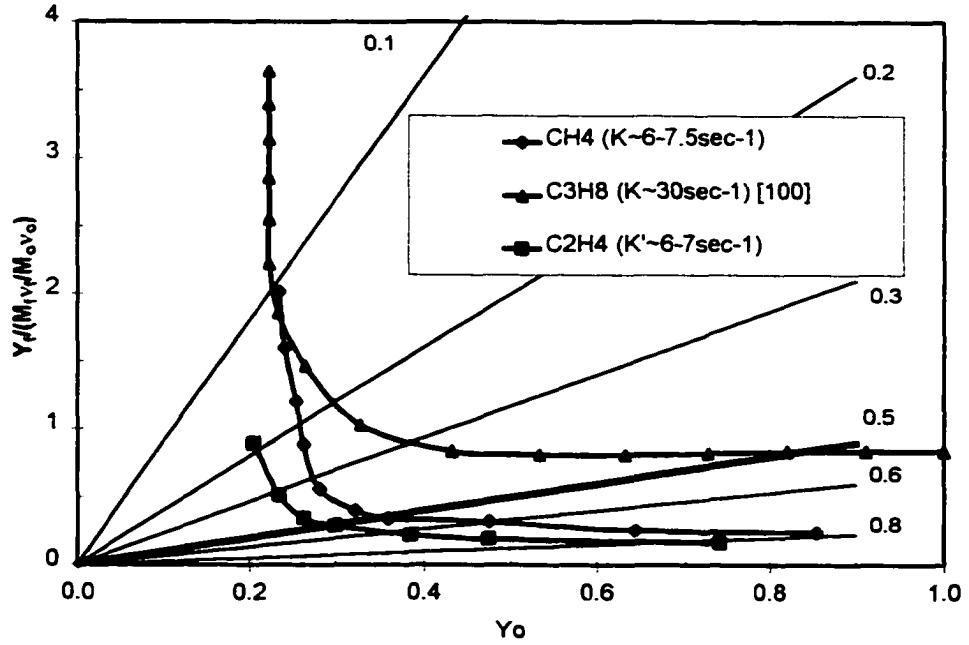

Fig. 7.2 Transition curves in $Y_F/(M_F v_F/M_O v_O)$-Y_O plane

	Fuel Side	Oxidizer Side
18%	Tadia = 2101 K	Global Strain Rate =6.3 1/sec
β=.5	82.11%Ar+17.89%CH4 V=7.78cm/sec,T=456K	18.34%O2+41.01%N2+40.64%He V=10.51cm/sec, T=520K
19%	Tadia = 2173 K	Global Strain Rate =6.43 1/sec
β=.5	80.90%Ar+19.09%CH4 V=7.89cm/sec,T=470K	19.72%O2+40.32%N2+39.95%He V=10.77cm/sec, T=524K
20%	Tadia = 2237 K	Global Strain Rate =6.631/sec
β=.5	79.99%Ar+20.00%CH4 V=8.08cm/sec,T=476K	21.07%O2+39.65%N2+39.29%He V=11.16cm/sec, T=534K
21%	Tadia = 2309 K	Global Strain Rate = 6.85 1/sec
β=.5	78.93%Ar+21.07%CH4 V=8.60cm/sec,T=505K	22.66%O2+38.55%N2+38.79%He V=11.27cm/sec, T=551K
22%	Tadia = 2365 K	Global Strain Rate =7.09 1/sec
β=.5	78.04%Ar+21.96%CH4 V=8.84cm/sec,T=519K	24.16%O2+37.80%N2+38.04%He V=11.74cm/sec, T=563K
23%	Tadia = 2418 K	Global Strain Rate =7.23 1/sec
β=.5	76.96%Ar+23.04%CH4 V=8.99cm/sec,T=532K	25.78%O2+37.17%N2+37.04%He V=11.99cm/sec, T=580K
24%	Tadia = 2466 K	Global Strain Rate =7.45 1/sec
β=.5	76.06%Ar+23.94%CH4 V=9.14cm/sec,T=541K	27.55%O2+36.29%N2+36.16%He V=12.49cm/sec, T=590K

Table 7.2 Falme specifications for βstoic=0.5 methane flames

	Fuel Side	Oxidizer Side
11%	Tadia = 2038 K	Global Strain Rate =6.13 1/sec
β=.5	89.08%Ar+10.91%C2H4 V=8.36cm/sec,T=496K	15.07%O2+42.46%N2+42.47%He V=9.43cm/sec, T=472K
12%	Tadia = 2150 K	Global Strain Rate =6.21 1/sec
β=.5	87.96%Ar+12.03%C2H4 V=8.26cm/sec,T=493K	16.67%O2+41.85%N2+41.47%He V=9.76cm/sec, T=493K
12.5%	Tadia = 2240 K	Global Strain Rate =6.261/sec
β=.5	87.55%Ar+12.45%C2H4 V=8.33cm/sec,T=500K	17.40%O2+41.48%N2+41.11%He V=9.83cm/sec, T=492K
13%	Tadia = 2258 K	Global Strain Rate = 6.4 1/sec
β=.5	87.05%Ar+12.94%C2H4 V=8.54cm/sec,T=505K	18.50%O2+40.62%N2+40.87%He V=10.02cm/sec, T=516K
14%	Tadia = 2350 K	Global Strain Rate =6.8 1/sec
β=.5	86.04%Ar+13.96%C2H4 V=8.74cm/sec,T=516K	20.17%O2+39.79%N2+40.03%He V=10.98cm/sec, T=554K

Table 7.3 Flame specifications for βstoic=0.5 ethylene flames

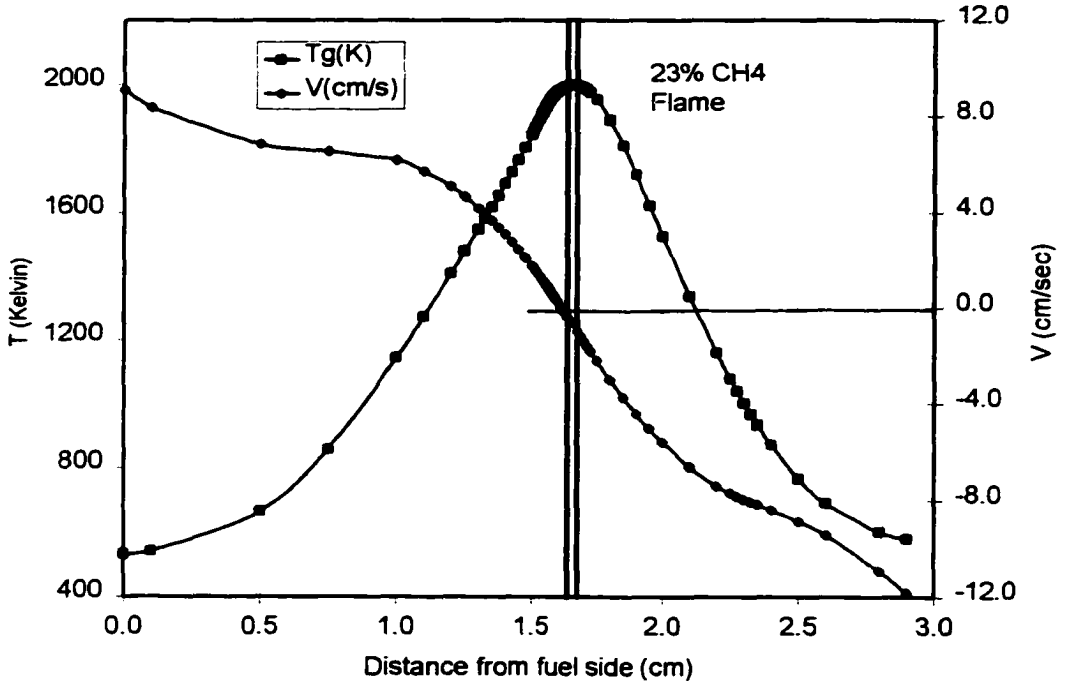

Fig 7.3(a) Distribution of T and V in 23% methane flame

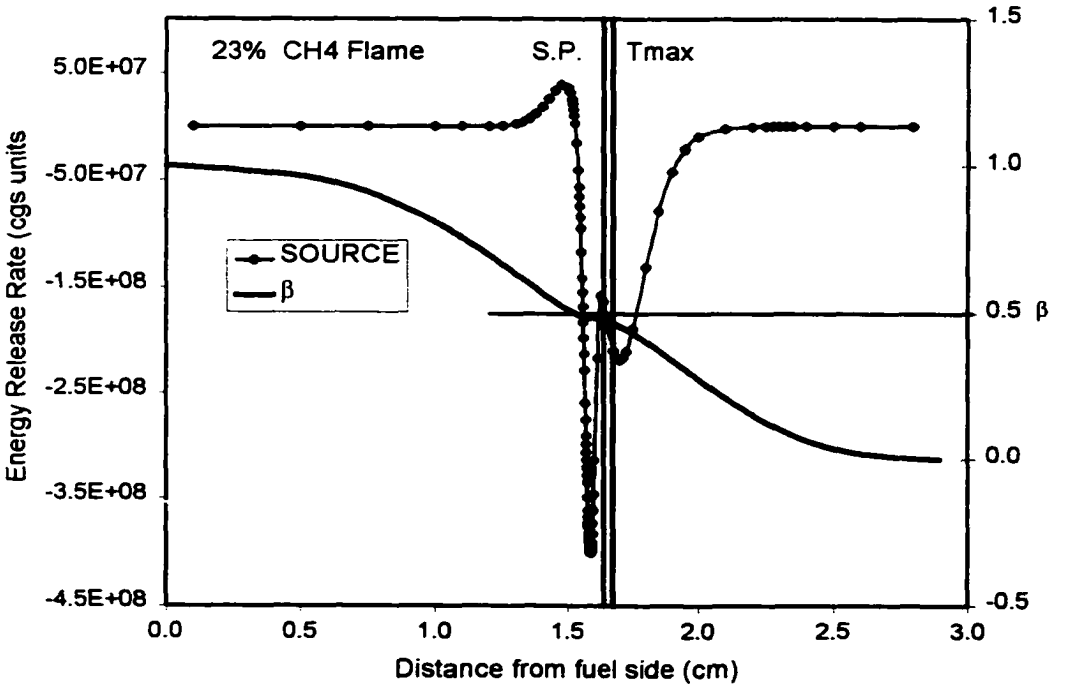

Fig. 7.3(b) Distribution of chemical energy release and β in 23% CH4 flame

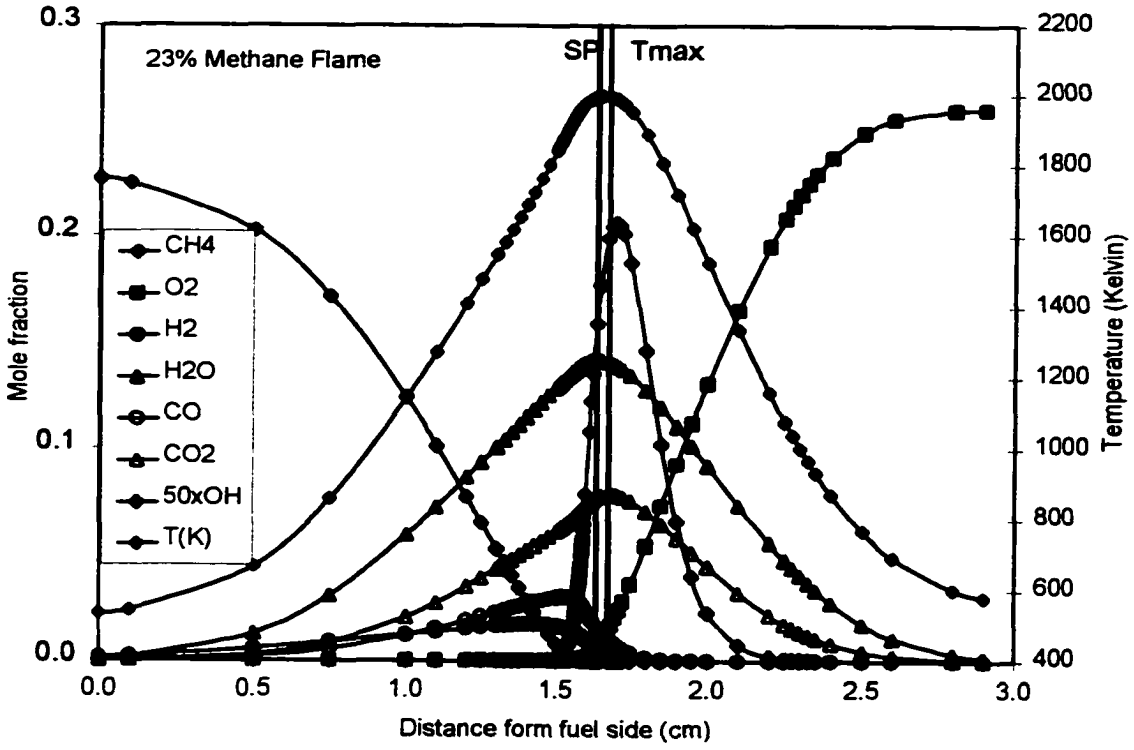

Fig 7.3(c) Species distribution in 23% CH4 Flame

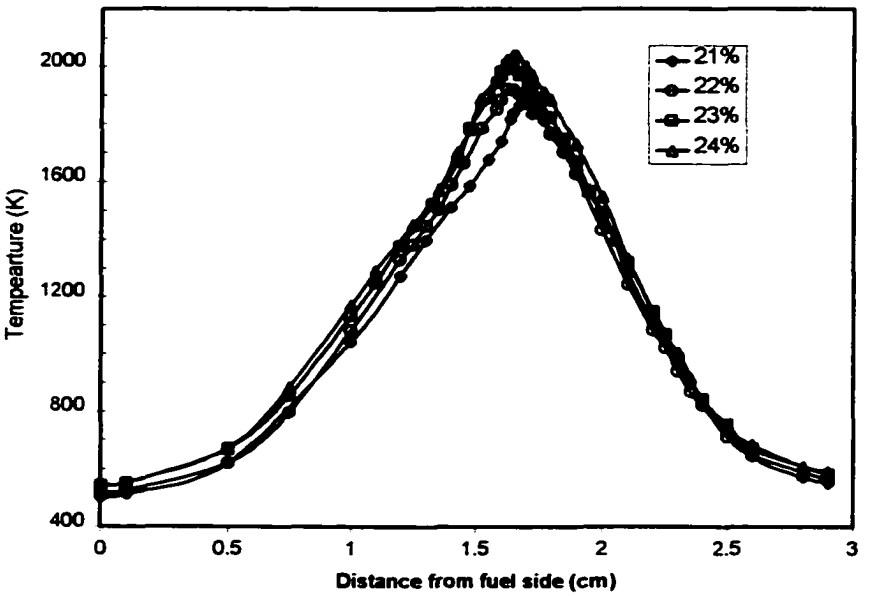

Fig 7.4(a) Measured temperature distribution in βstoic=.5 methane flames

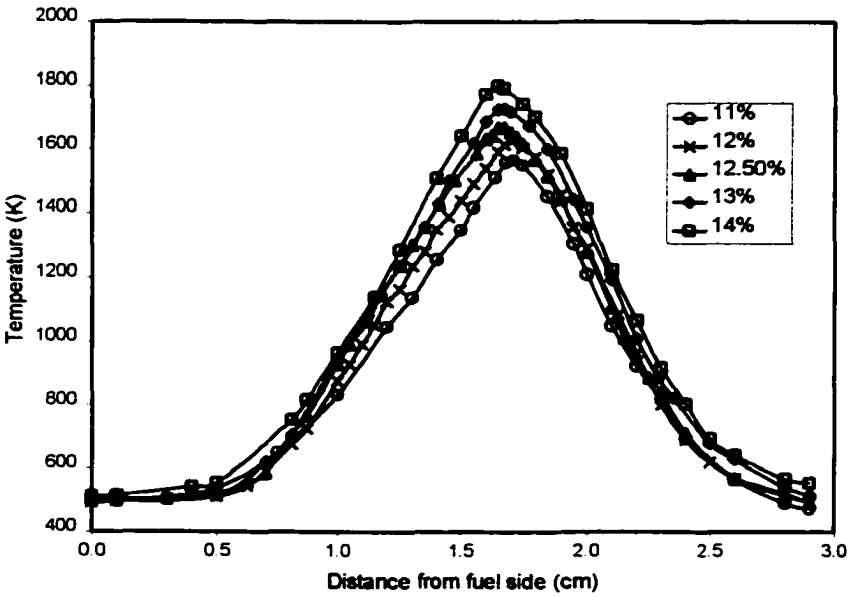

Fig 7.4(b) Measured temperature distribution in βstoic=.5 ethylene flames

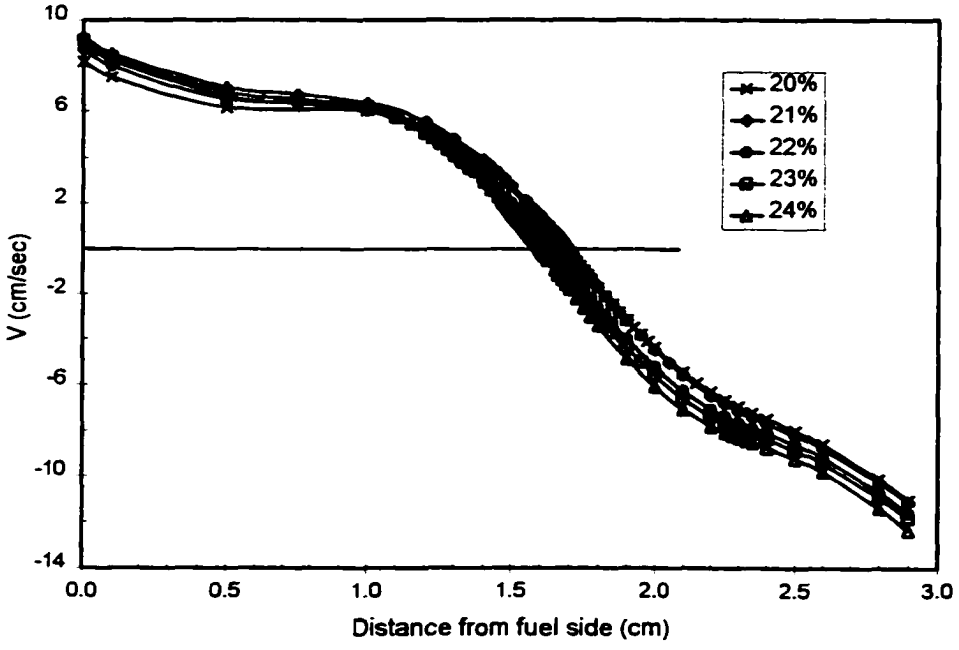

Fig 7.5(a) computed velocity distribution in βstoic=0.5 methane flames

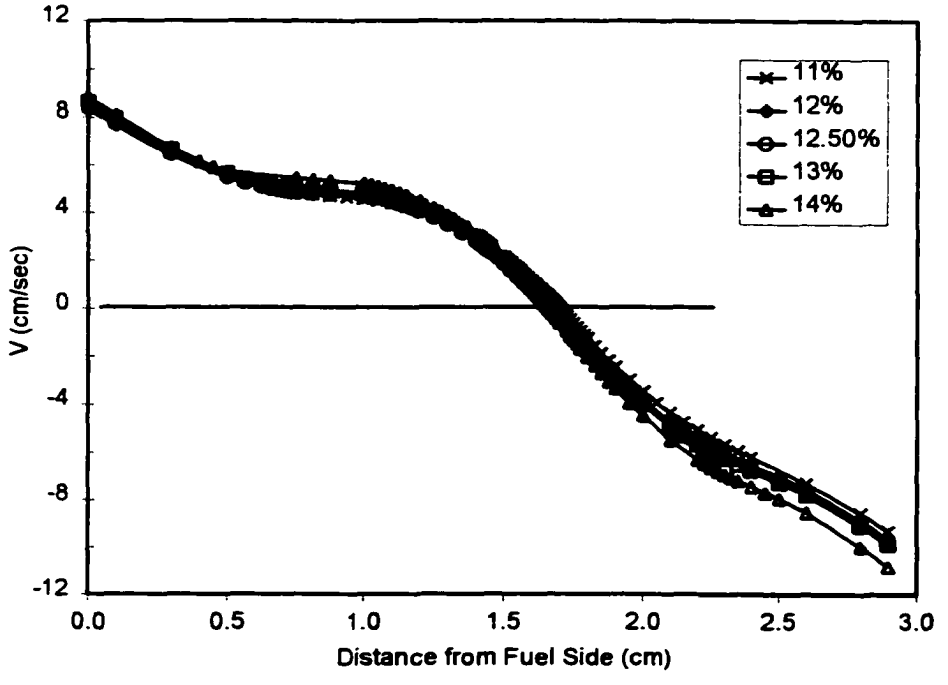

Fig 7.5(b) computed velocity distribution in βstoic=0.5 ethylene flames

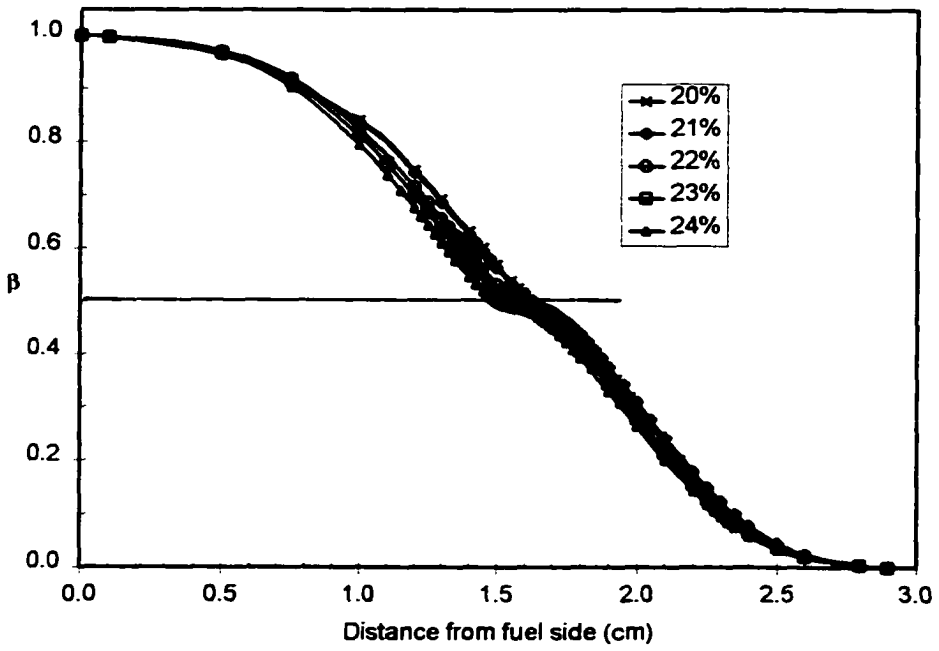

Fig 7.6(a) Computed β distribution in βstoic=0.5 methane flames

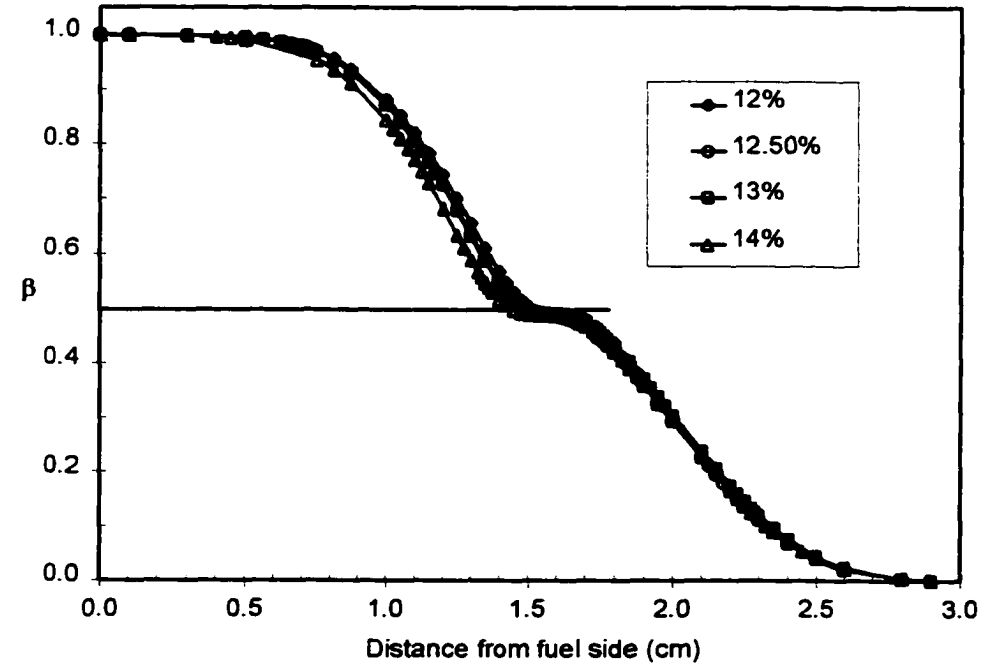

Fig 7.6(a) Computed β distribution in βstoic=0.5 ethylene flames

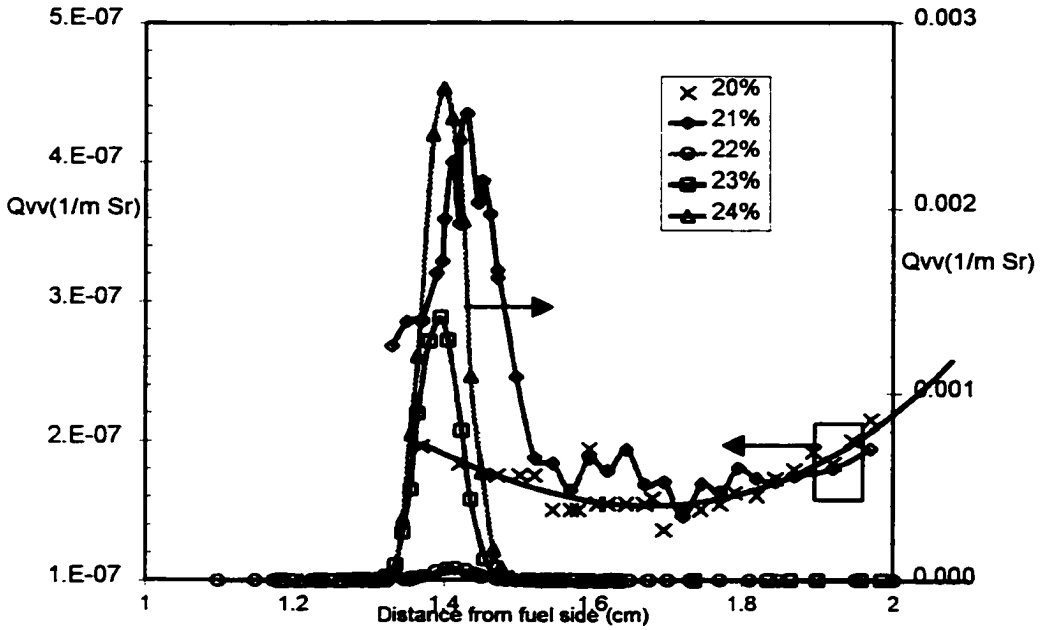

Fig 7.7 Qvv distribution in βstoic=0.5 methane flames

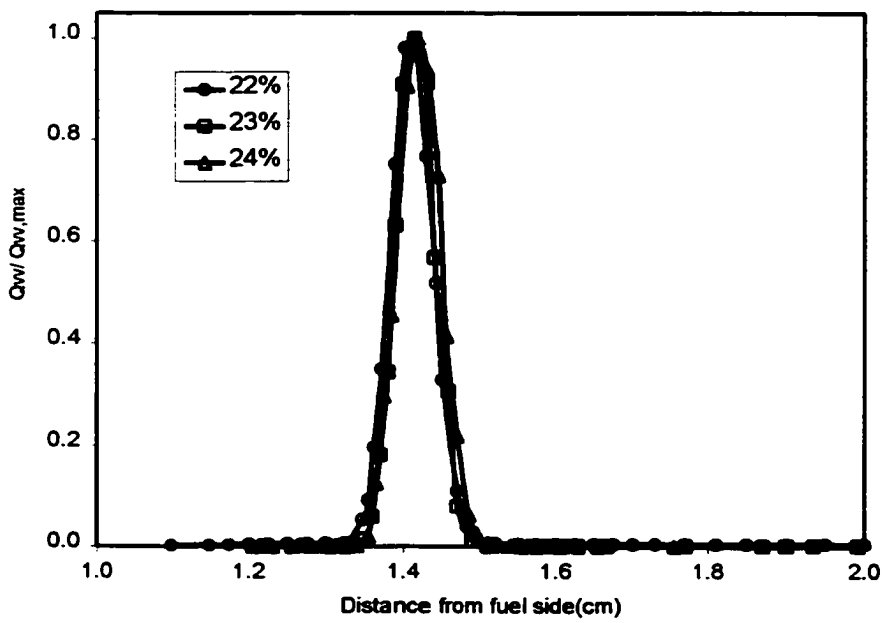

Fig 7.8 Scaled Qvv distribution in βstoic=0.5 methane flames

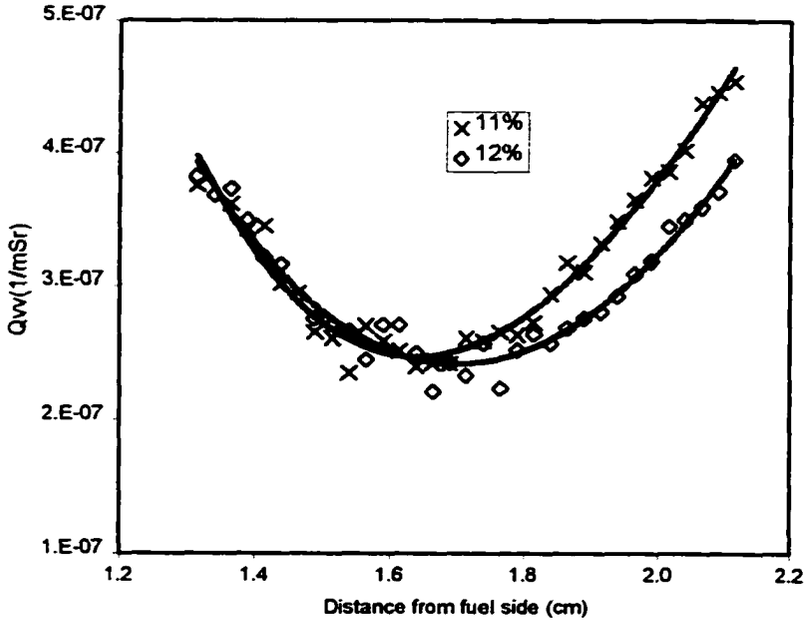

Fig. 7.9 Qvv distribution in 11% and 12% ethylene flames

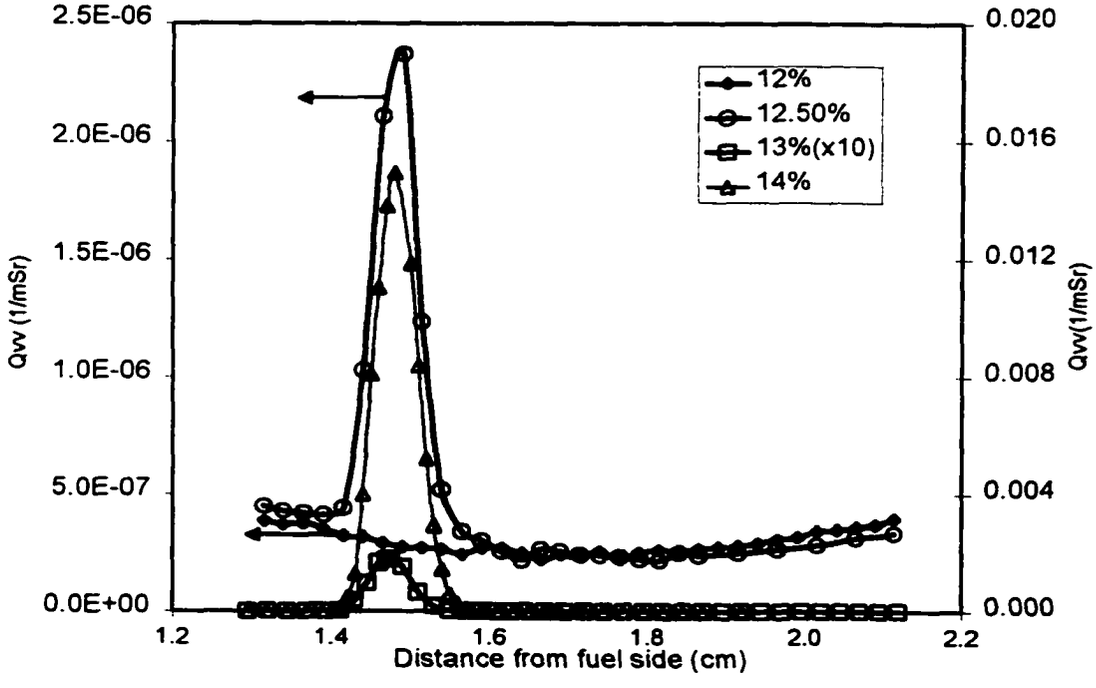

Fig 7.10(a) Qvv distribution in βstoic=0.5 ethylene flames

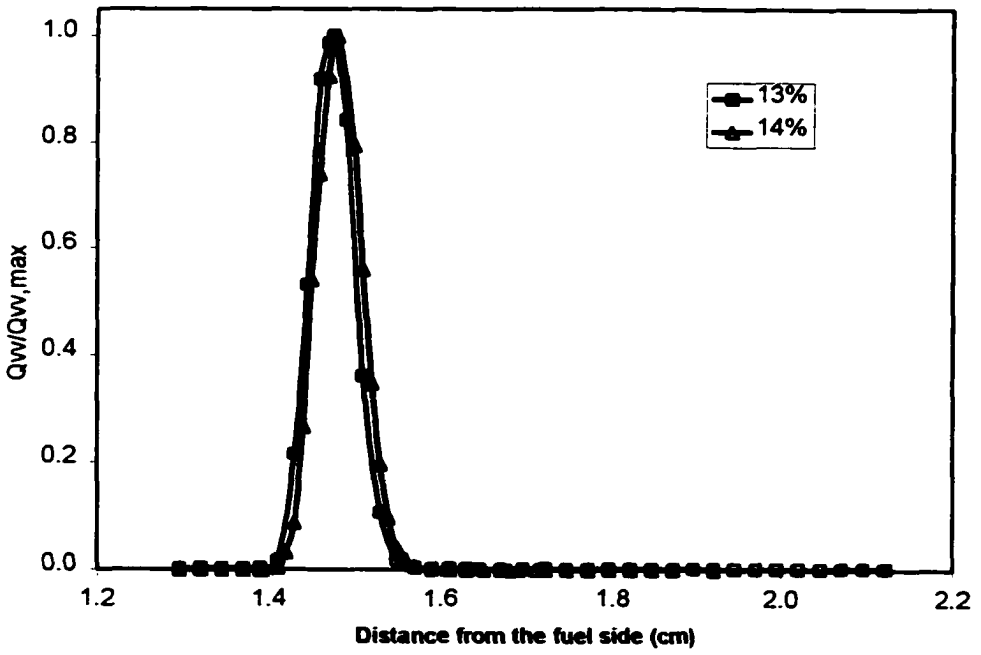

Fig. 7.10(b) Scaled Qvv distribution in βstoic=0.5 ethylene flames

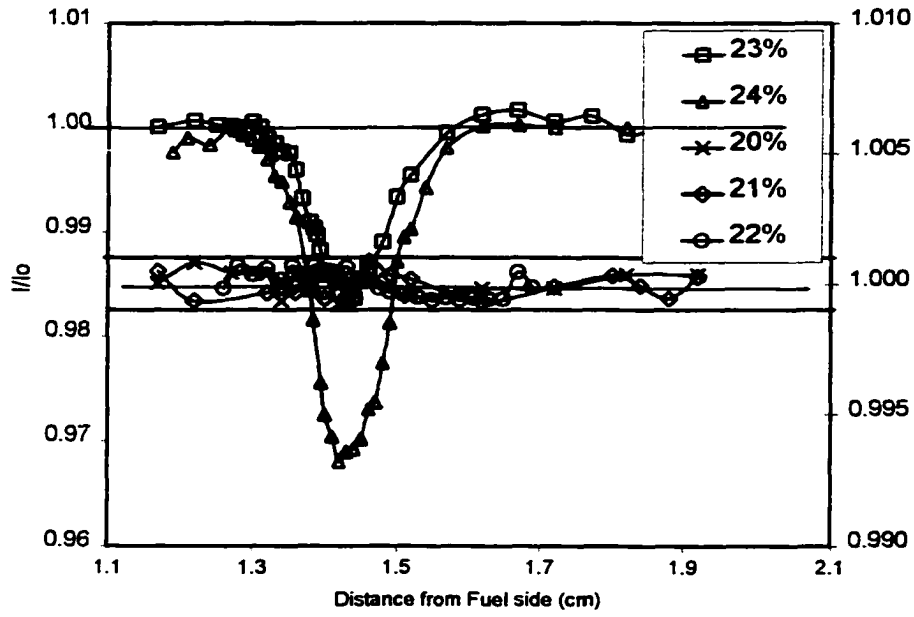

Fig 7.11 I/Io distribution in βstoic=.5 methane flames

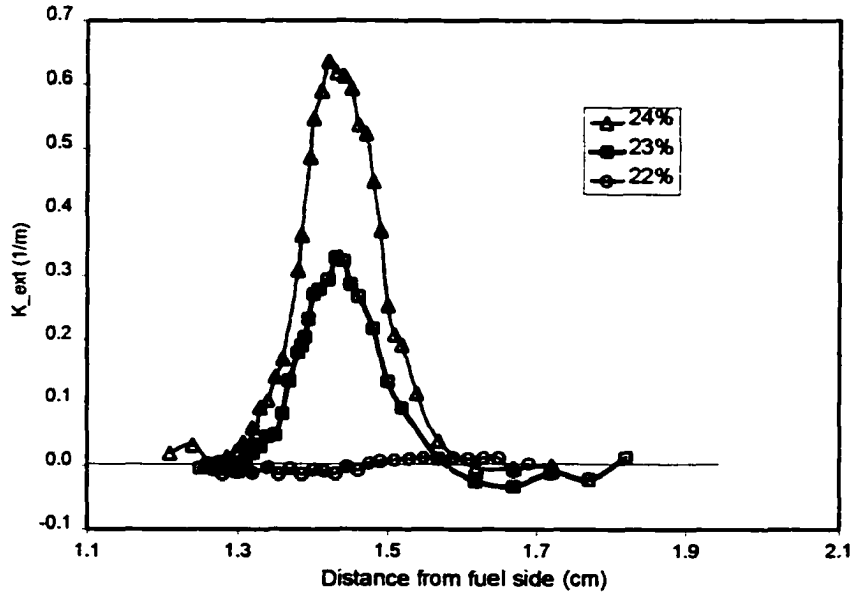

Fig 7.12 Kext distribution in βstoic=.5 methane flames

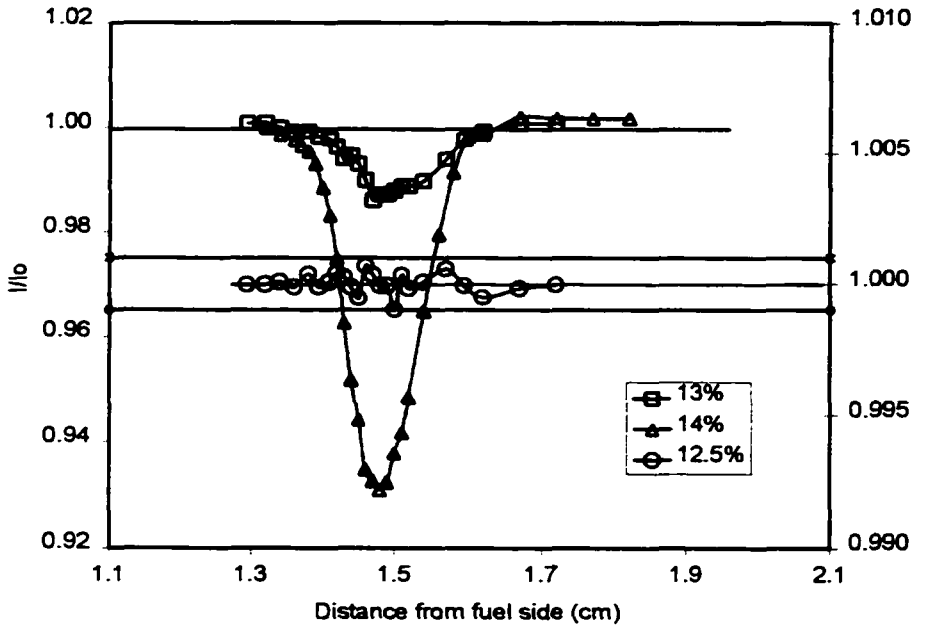

Fig 7.13 I/Io distribution in βstoic=.5 ethylene flames

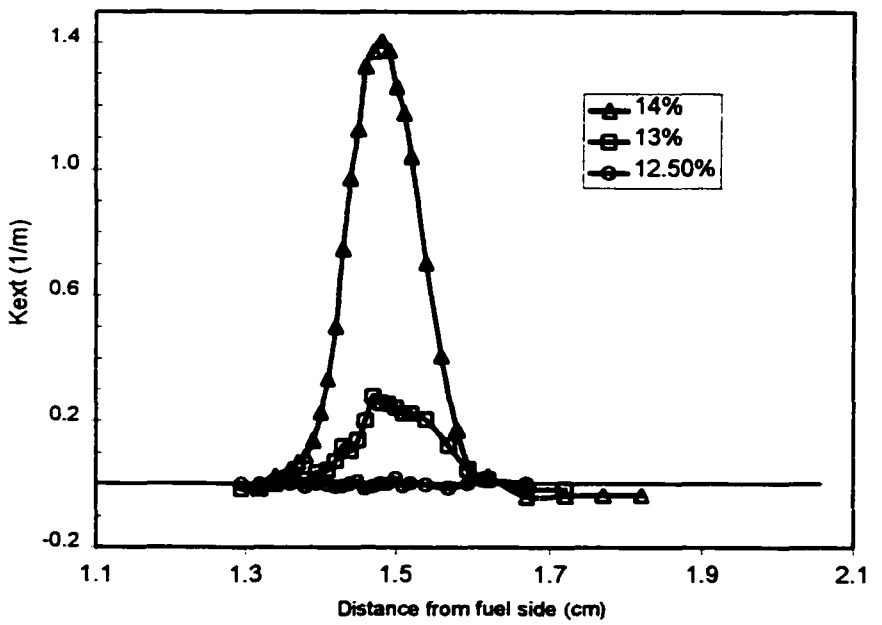

Fig 7.14 Kext distribution in βstoic=.5 ethylene flames

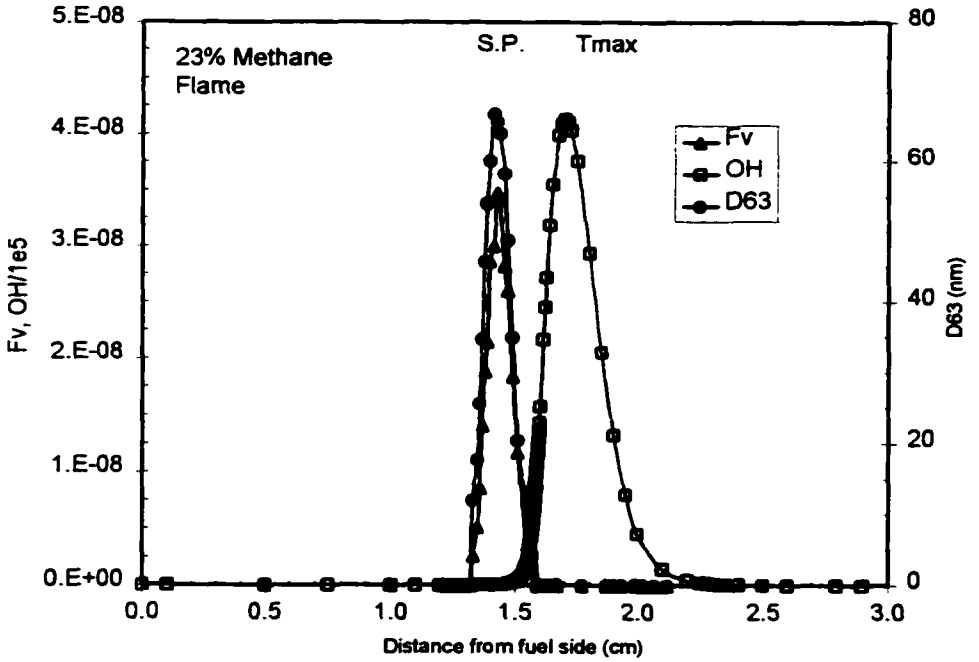

Fig 7.15 Distribution of Fv, D63 and computed OH in 23% CH4 flame

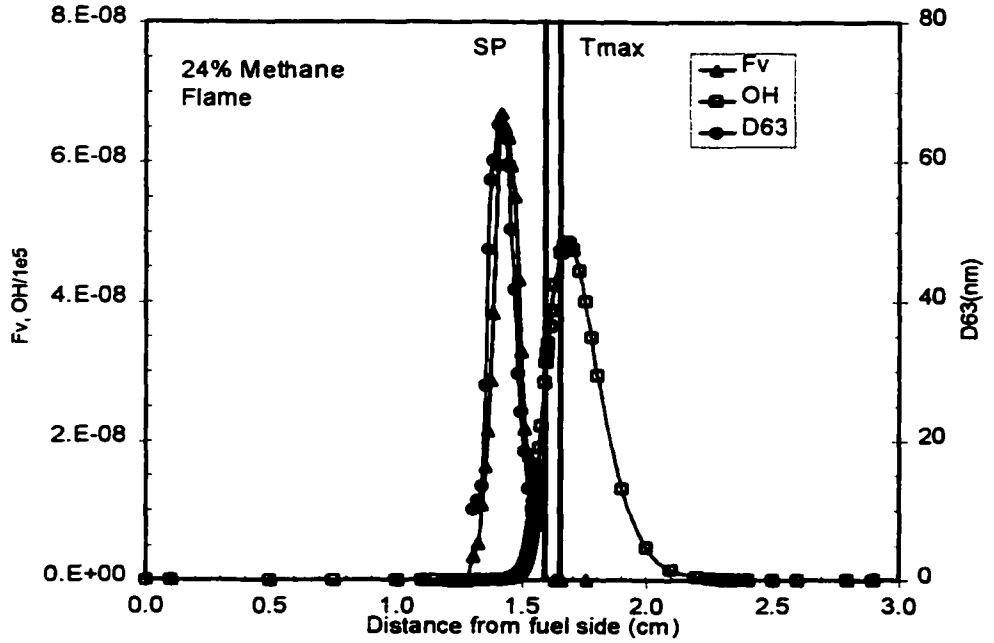

Fig. 7.16 Distribution of Fv, D63 and computed OH in 24% CH4 flame

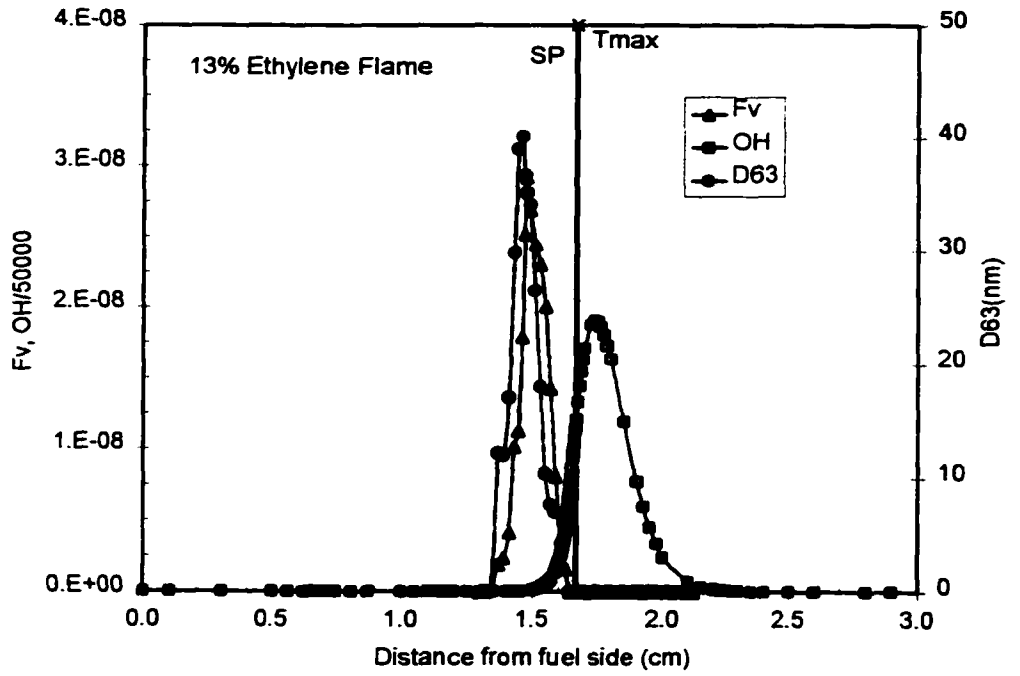

Fig. 7.17 Distribution of Fv, D63 and computed OH in 13% C2H4 flame

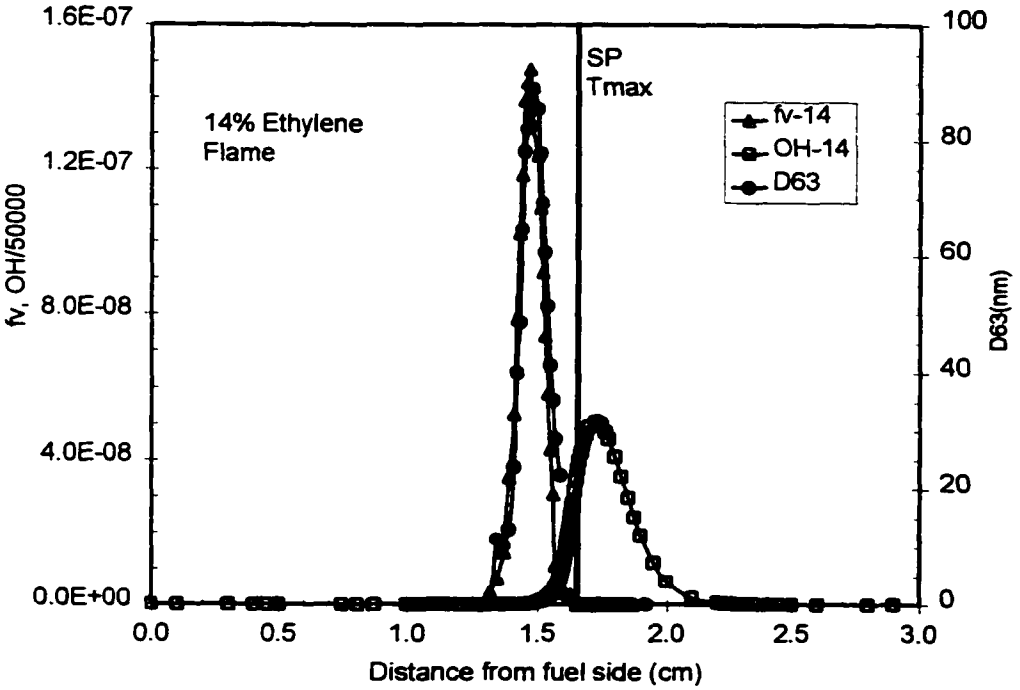

Fig. 7.18 Distribution of Fv, D63 and computed OH in 14% C2H4 flame

CHAPTER 8

SUMMARY AND CONCLUSIONS

An experimental study of flame structure, soot and NO formation in low strain rate methane partially premixed counterflow flames was conducted. The key contributions of this work are summarized below.

8.1 Analysis of location of premixed and non-premixed reaction zone location

1. Fuel side partial premixing causes the non-premixed reaction zone to come closer to the fuel side by two effects: (i) dilution of the fuel side stream (ii) by consumption of a fraction of the fuel in the premixed reaction zone.
2. Non-premixed reaction zone crossover equivalence ratio for methane air partially premixed flames was obtained to be 2.17, which agreed well with experimental value of 2.11 obtained by Tsuji and Yamaoka [3].
3. Non-premixed reaction zone cross over equivalence ratio was shown to be independent of strain rate and the choice of thermochemical properties. It was further shown that it varied little for a variety of C1-C4 hydrocarbon fuels.
4. For low strain rate flames, the previous computational work as well as the present experiments showed, Chapter 6, that the EINO for flamelet combustion reached its peak near the non-premixed cross-over equivalence ratio.

8.2 Energy release and radiation heat transfer in partially premixed flamelets

1. In a non-premixed hydrocarbon counter-flow flame, the energy release takes place in two major steps, first the fuel breaks down into CO and H2 that in turn is oxidized in the second step into CO2 and H2O. In addition to these two energy release peaks, an

additional energy release peak is observed due to premixed flamesheet with partial premixing.

2. Volumetric energy release increased for progressive fuel side partial premixing of a non-premixed flame that was originally located on the oxidizer side of the stagnation plane. With progressive partial premixing the relative importance of energy release in the premixed reaction zone increases.
3. The CO and H2 'fuel' produced by the premixed reaction zone is consumed in the non-premixed reaction zone increasing the relative importance of energy release associated with CO and H2 conversion to CO2 and H2O in comparison to energy release associated with formation of CO and H2 in the nonpremixed reaction zone.
4. The increase in energy release in the flamelets is consistent with decrease in the length of the turbulent flame with progressive partial premixing. The decrease in flame length in turn implies decreased residence time for pollutant formation in the flame.
5. Gas radiation increased with partial premixing due to broadening of profiles of products of combustion and a flatter temperature profile between the premixed and the non-premixed reaction zone. The radiative fraction for the gas radiation, however, decreased due to a bigger increase in the net chemical energy release in the partially premixed flames. The decrease in radiative fraction for gas radiation for flamelet combustion is consistent with previous experimental evidence of decrease in radiative fraction for turbulent partially premixed flames.

8.3 Soot formation in partially premixed flamelets

1. Fuel side partial premixing of the:
   i.) Case 1: (Nonpremixed flame residing on the oxidizer side of the stagnation plane) first decreased and then increased the peak soot volume fraction, the thickness of

the soot zone and the peak soot aggregate size with progressively increasing levels of partial premixing.

ii.) Case 2: (nonpremixed flame residing on the fuel side of the stagnation plane) showed a monotonic decrease in the sooting tendency with an eventual transition to a nonsooty flame.

2. Oxidizer side partial premixing of the:

i.) Case 1: (nonpremixed flame residing on the fuel side of the stagnation plane) resulted in decrease in the peak soot loading with progressive partial premixing.

ii.) Case 2: (nonpremixed flame residing on the fuel side of the stagnation plane) resulting in an increase is peak soot volume fraction.

3. Although the effect of oxygen added to methane fuel is to suppress soot inception, the effect on soot growth could be a decrease or an increase in peak soot loading depending on the configuration of the non-premixed counterflow flame and the level of partial premixing. The effect of flowfield should be considered in addition to the dilution and chemical effects of oxygen added to the fuel side.

8.4 Partial premixing for radiation enhancement and soot emission control

Effects of fuel side partial premixing on sooting tendency and flame radiation were studied for progressive addition of oxygen into the fuel side of methane counter-flow flame.

1. The peak soot volume fraction first decreased and then increased for progressive partial premixing. The initial decrease is attributed to a combination of previously established dilution and chemical effects both of which suppress soot formation in methane flames. The subsequent increase is attributed to more favorable temperature time histories for soot particulates resulting from partial premixing.

2. The thickness of the soot zone first decreased and then increased for progressive levels of partial premixing. The initial decrease is attributed to the merged flame coming closer to the stagnation plane and the soot formation zone being squeezed between the flame and the stagnation plane. Subsequent increase in the soot zone thickness is attributed to formation of soot between the spatially separated premixed and the non-premixed reaction zones in the 'interdependent-flame-regime'.
3. A novel flame configuration is reported (flame D in this study) where soot is formed and oxidized between the premixed and the non-premixed reaction zones on the fuel side of the stagnation plane. This flame configuration has the potential for low soot particulate emission with simultaneous enhancement of soot radiation heat transfer from flamelets.

8.5 Effect of fuel side partial premixing on NO formation and emission

1. The measured peak NO concentration increased and the NO profile broadened with progressive partial premixing. These observations were reproduced reasonably well by computations with using the GRIMECH 3.00 mechanism using the measured temperature distribution as an input to the OPPDIF code.
2. With partial premixing, the NO production rate distribution showed two positive NO production peaks and one NO destruction region. One production peak was accounted for by thermal NO reactions alone. Contribution of this peak to total NO production increased with progressive partial premixing indicating that thermal mechanism was favored as the flame temperature increased with progressive partial premixing.
3. With progressive partial premixing the spatial separation between the two NO formation peaks increased. This observation accounted for the observed broadening of the NO concentration profile with progressive partial premixing.
4. EINO first increased and then decreased with progressive partial premixing for the levels of partial premixing studied. Careful review of previous literature indicated that

in low (<20 sec^{-1}) strain rate methane air flames EINO reached maximum around Φ~2.2 irrespective of strain rate. This observation, along with the maximum in EINO around 19.4% oxygen content in the fuel in the present work, indicates that EINO in low strain rate partially premixed flames peaks around the non-premixed flame cross over equivalence ratio.

A study of transition from blue particle free flames to sooty flames was carried out for diluted methane-oxygen and ethylene oxygen counter-flow flames at constant global strain rate. Following are the key conclusions from this study:

8.6 Transition Curves

1. Constant global strain rate transition curves for methane and ethylene had two asymptotes: (i) for flames with low YF, transition to sooting occurred for Yo~constant (ii) for flames with low Yo, transition to sooting occurred for Yf~constant. These trends qualitatively agree with previous work , Chung et al. (1997), for propane flames.
2. The transition curves can be used to rank the sooting tendency of different fuels or the effectiveness of additives to suppress sooting by using the scaling $M_F \nu_F / M_O \nu_O$ for the Yf axis.

8.7 Concluding Remarks

Experimental measurements and computational analysis of energy release, flame radiation and soot and NO formation in low strain rate counter-flow methane flames presented in this thesis are helpful in understanding these aspects of partial premixing at flamelet level in turbulent combustion. The results presented above should be helpful in understanding the role of partially premixed combustion in several practical applications where partial premixing can be expected, for instance in stratified charge SI engine

combustion or in natural gas turbine engines where partial premixing is known to occur due to insufficient mixing. Although soot emission from partially premixed methane flamelets initially decreased and then increased, the emission index of NO first increased and then decreased, indicating that, it may be challenging to achieve simultaneous suppression of soot and NO emissions from flamelet combustion by partial premixing. In applying the present results to practical systems, due care should be exercised to note the effect of fuel type and strain rate on soot formation. The strain rate dependence on EINO has been reported in the previous literature to be different for strain rates above 20 sec-1. The general aspects of energy release and flame gas radiation seem to be applicable for a variety of fuel types and strain rates. Understanding of these aspects at flamelet level is believed to be helpful in exploiting the partial premixing as a control variable for design of practical combustion devices with fundamental knowledge of the underlying processes.

APPENDICES

APPENDIX A1

HYDROGEN FLAME EXPERIMENTS

An investigation of two high temperature hydrogen flames studied to obtain the emissivity data of SiO_2 coated Pt/Pt-10%Rh thermocouples, reported in Chapter 3, is described. Temperature was measured in two hydrogen flames using .008 inch wire diameter thermocouples coated with 5-6 micron SiO2 film. The choice of rather large thermocouple size was necessitated by high flame temperature to which the thermocouple is exposed resulting in bead temperatures approaching the melting point (~2000K). The technique for obtaining the emissivity of the SiO2 coated thermocouple using the calculated gas temperature and thermal conductivity is presented. Sources of systematic uncertainty in obtaining the emissivity are identified and their implications for the measurement technique are discussed. Several chemical kinetic mechanisms for hydrogen oxidation reported in literature [33,35,80,105] were considered to evaluate the effect of chemical kinetic mechanism on the computed gas temperature and thermal conductivity. A comparison of measured and computed NO concentration is presented to assess the validity of corrected thermocouple temperature for prediction of temperature sensitive NO formation in flames.

Reduction of experimental data for emissivity calculation:

The flame specifications for the two hydrogen flames, Surya 2 and Surya 3, have been shown in Table A1.1. The selection of chemical kinetic mechanism for hydrogen combustion used for these computations, using the computational model discussed in Chapter 2, is presented later in this section.

Emissivity was estimated using eqn 3.1, the energy balance equation for the thermocouple bead, which can be re-written as:

$$\varepsilon(T) = \frac{Nu\lambda}{D\sigma}\frac{(T_g - T)}{(T^4 - T_{mid}^4)} \qquad \text{(A.1.1)}$$

where T, Tg and Tmid are the measured thermocouple temperature, the computed gas temperature and the average of the measured temperature at the two inlet ports. Nu is the Nusselt number for a thermocouple of bead 'diameter', D. λ and σ the thermal conductivity of the gas surrounding the thermocouple and Stefan Boltzmann constant.

On the basis of observation under a calibrated optical microscope the 'diameter' of the bead was estimated as D=.45±0.03 mm. Gas thermal conductivity at the temperature of the thermocouple bead was inferred from the thermal conductivity at the 'free-stream'gas temperature using $\lambda \propto \sqrt{T}$ dependence of thermal conductivity. This is particularly important when the difference between the thermocouple bead temperature and the gas temperature is large, as is the case for large thermocouple bead and high temperature flames.

Experimental data for emissivity of SiO2 coated bead is shown in Fig. 3.9 along with a curve fit, eqn. 3.2, to the experimental data from this work combined with previous data reported by Zhang et al. (1997).

Analysis of experimental uncertainty

Systematic uncertainty in the emissivity is estimated as:

$$\frac{\Delta\varepsilon}{\varepsilon} \approx \left[\left(\frac{\Delta Nu}{Nu}\right)^2 + \left(\frac{\Delta\lambda}{\lambda}\right)^2 + \left(\frac{\Delta D}{D}\right)^2 + \left(\frac{\Delta T}{T_g - T}\right)^2 + \left(\frac{\Delta T_g}{T - T_g}\right)^2 + \left(\frac{4\Delta T}{T}\right)^2\right]^{0.5} \qquad \text{A1.2}$$

Assuming an uncertainty of ±10% in the estimated Nusselt number and the gas thermal conductivity, a ±5% uncertainty in the bead 'diameter', a ±10-15K uncertainty in the measured thermocouple temperature and the computed gas temperature, the

uncertainty in emissivity is estimated to be about 25-30% over a the high temperature region of the flame. Larger uncertainty in the emissivity is expected for smaller thermocouple bead since in eqn. A1.2 the bead diameter D and the temperature difference, Tg-T, both decrease. This technique is not advisable in the lower temperature (typically T < 1000K) regions of the flames to obtain emissivity as $\Delta T, \Delta T_g \rightarrow (T_g - T)$ in the eqn. A1.2.

Selection of chemical kinetic mechanisms for hydrogen-oxidation

A study of several chemical kinetic mechanisms for hydrogen combustion was conducted in order to obtain the distribution of gas temperature and thermal conductivity required for determining the emissivity of SiO2 coated thermocouple bead using the procedure outlined earlier. Of particular interest is the distribution of temperature, major stable species and thermal conductivity computed using various mechanisms. Computed OH concentration using different mechanisms was also compared as OH radical is a key species in chain-branching reaction for hydrogen oxidation. Computations were carried using the OPPDIF code, Sandia report, [33], modified by Kim,[35], to include an optically thin model of gas radiation as described in Chapter 2.

GRIMech 2.11 and GRIMech 3.00, [56,57], are detailed C2 hydrocarbon oxidation and NO chemical kinetic mechanisms optimized for premixed methane flames. The mechanisms reported by Masten, [105], and the one reported in, OPPDIF report [33], are compilations of individual rate constants from a variety of sources. The later shall be referred to as 'SandiaMech' in this report. Another mechanism studied was reported by Barlow et al., [80] which consisted of chemical kinetics for hydrogen oxidation and NO formation in H2/O2/N2 flames. They used this mechanism to compare computed flame structure and NO concentration in non-premixed turbulent H2/O2/N2 flames with experimental data. Three of these mechanisms, SandiaMech, Barlowmech and MastenMech, have been tabulated in Appendix 2.

Computed distribution of gas temperature and gas thermal conductivity is shown in Figs. A1.1 and A1.2 for Surya 2 and Surya 3 flames. Thermal conductivity distribution, computed using Sandia transport database, for all the cases agreed well with each other. While the located of computed peak temperature predicted using different mechanisms is consistent, the value of the peak temperature was within 40K of each other for Surya 2 flame and within 120 K of each other for Surya 3 flame. Actually for Surya 3 flame the predicted peak flame temperatures, Fig. A1.2(b), using the four mechanisms other than Barlow et al. mechanism agreed within 30 K of each other. Similar agreement for peak temperature was reported recently by Chen et al., [106], who compared prediction using several popular hydrocarbon combustion mechanisms for partially premixed methane-air counter-flow flames.

Computed distribution of major stable species and OH radical concentration is shown in Figs A1.3 and A1.4 for Surya 2 and Surya 3 flame respectively. The major stable species agreed well with each other for both the flames. Therefore, the small difference in thermal conductivity distribution among various mechanisms, Figs A.1.1-2(a) is due to the difference in temperature distribution for different mechanisms. OH concentration distribution calculated using various mechanisms agreed well with the peak concentrations within 10% of each other. In the case of both the flames Barlow et al. mechanism consistently under predicted OH by about 10% compared to the other mechanisms. The agreement between SandiaMech and MastenMech mechanisms is excellent with the difference almost unnoticeable in most cases and both these mechanisms showed reasonable agreement with the two GRI Mechanisms. Since the former two mechanisms are derived from compilation of experimentally determined individual reaction rates for hydrogen oxidation mechanism, these two mechanisms were selected for the purpose of computed the gas temperature and thermal conductivity distribution required to obtain emissivity using eqn A1.1.

	Fuel Side	Oxidizer Side
Surya 2	Global Strain Rate =5.55 1/sec	
	75.03%H2+24.97%N2 V=8.8cm/sec, T=719K	Dry Air V=7.3cm/sec, T=576K
Surya 3	Global Strain Rate =6.24 1/sec	
	75.03%H2+24.97%N2 V=10.3cm/sec, T=837K	72.57%N2+27.43%O2 V=7.8cm/sec, T= 626K

Tabel A1.1 specifications for hydrogen Flames, Surya 2 and Surya 3

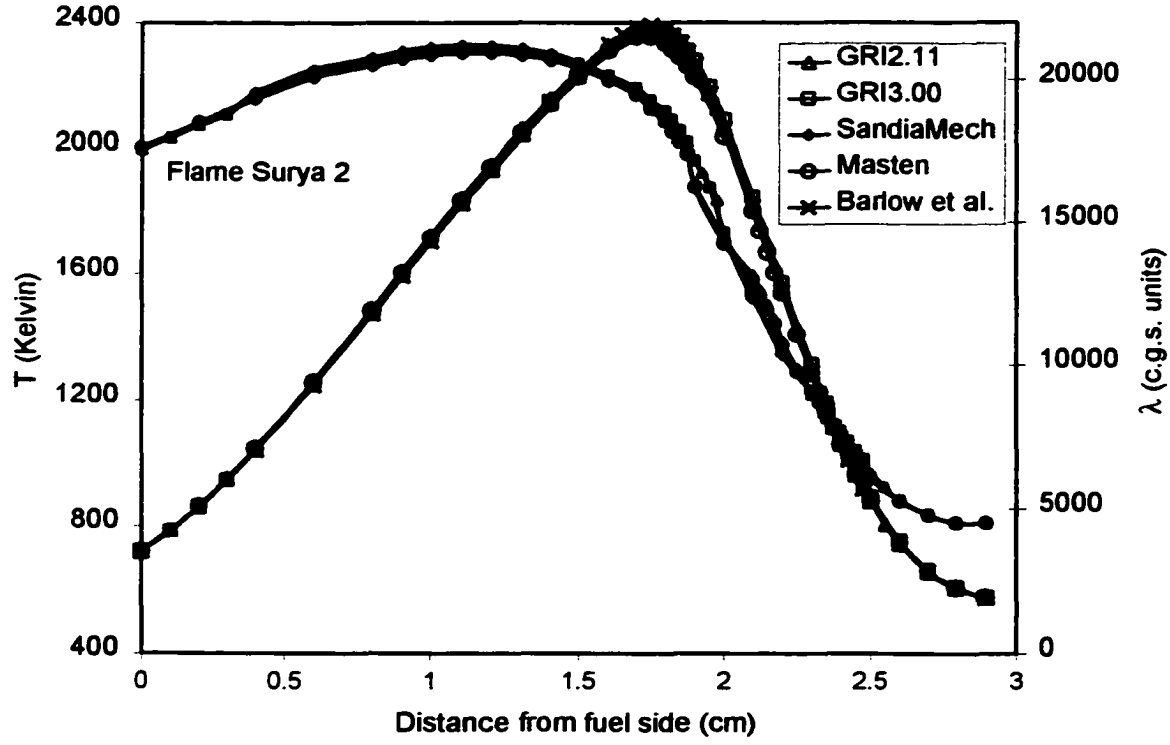

Fig. A1.1(a) Computed distribution of temperature and λ in Surya 2 flame

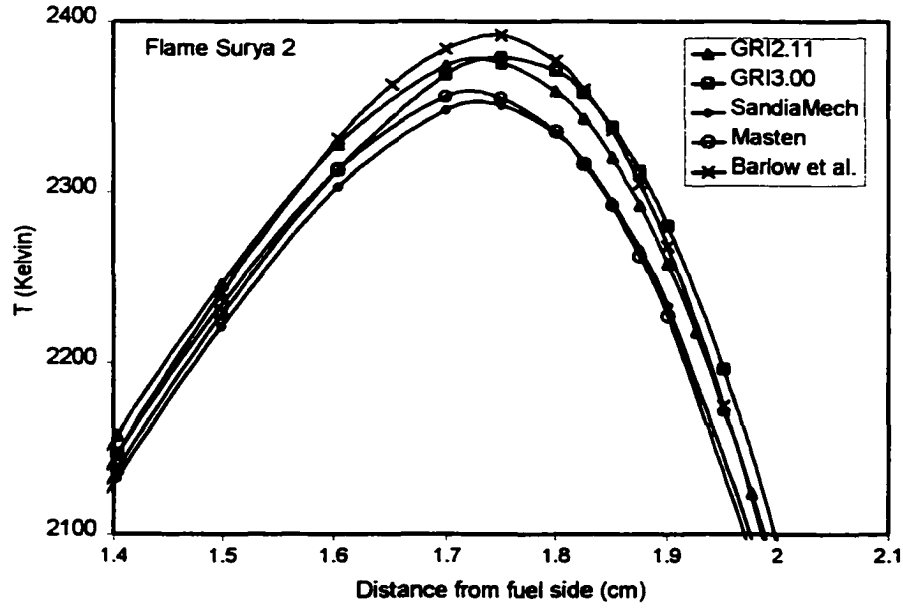

Fig A1.1(b) Computed distribution of temperature in Surya 2 flame

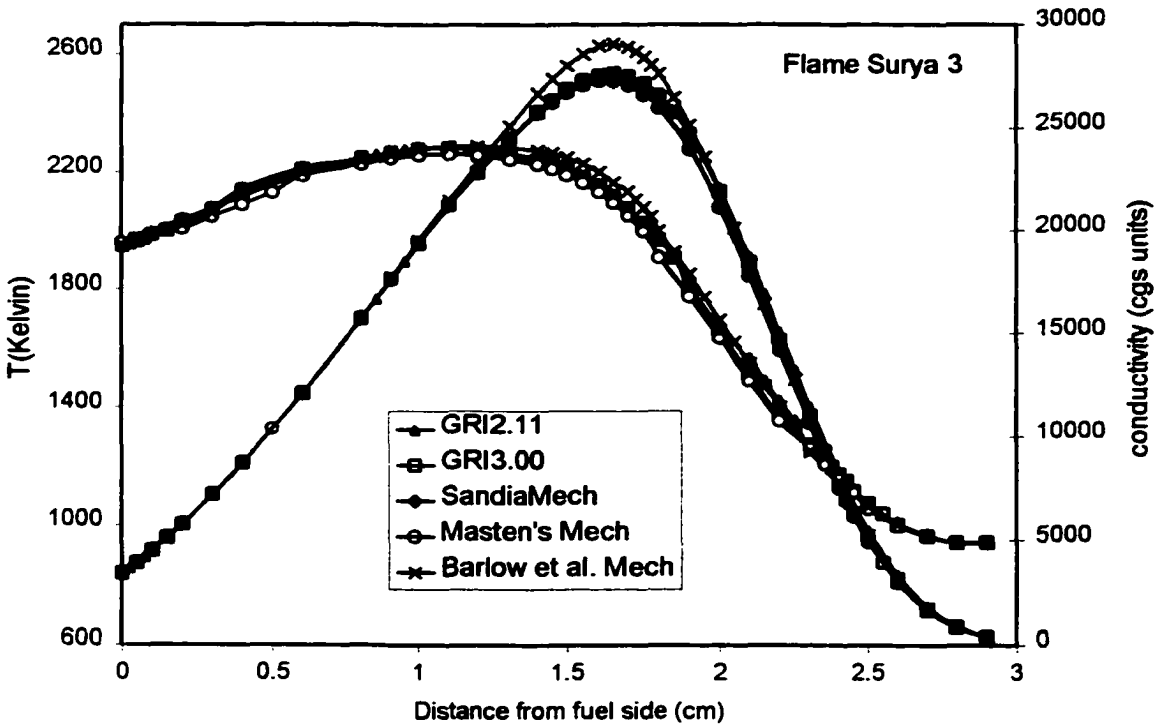

Fig. A1.2(a) Computed distribution of temperature and λ in Surya 3 flame

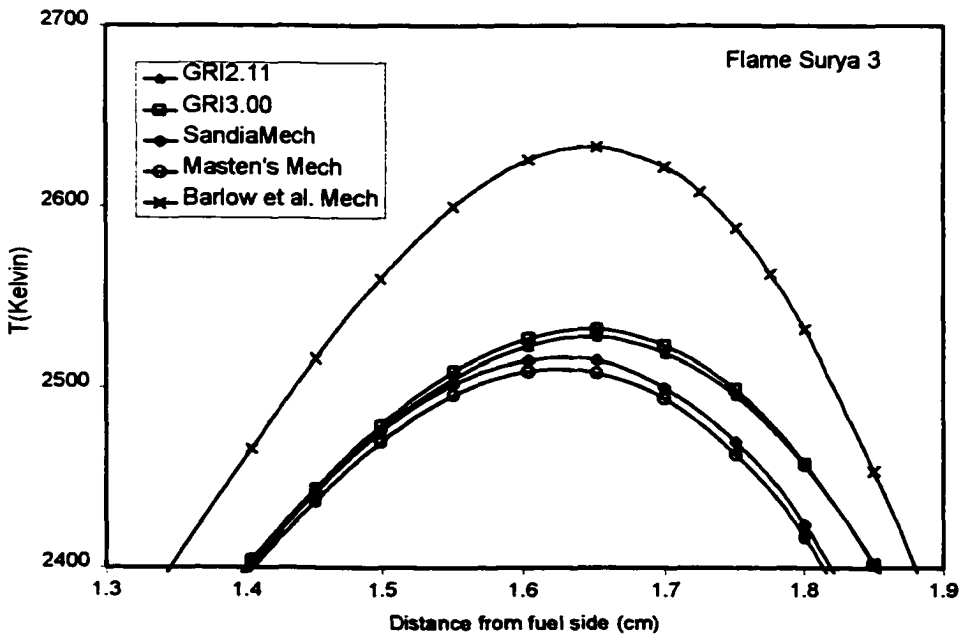

Fig. A1.2(b) Computed distribution of temperature in Surya 3 flame

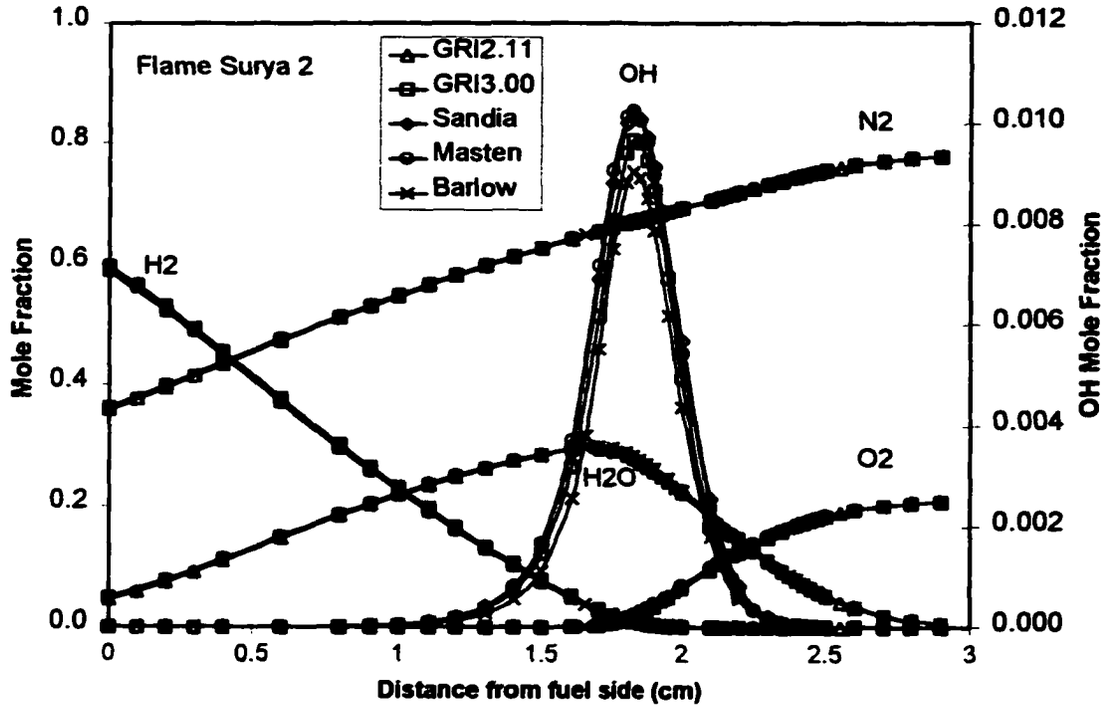

Fig. A1.3 Computed species distribution in Surya 2 Flame

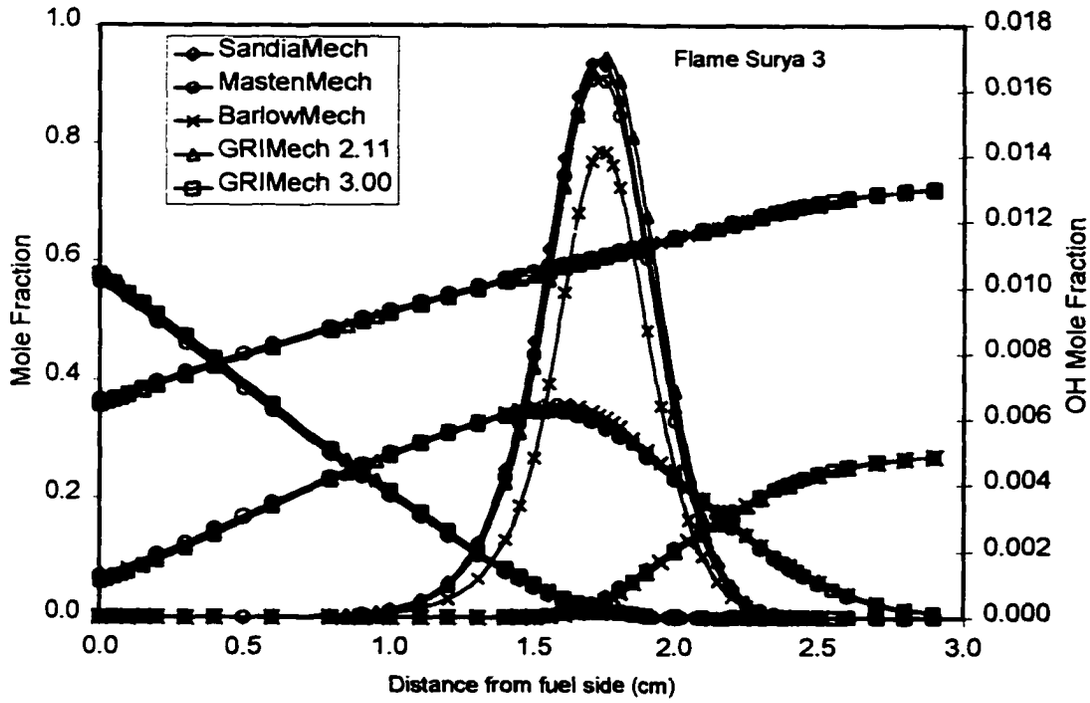

Fig. A1.4 Computed species distribution in Surya 3 Flame

Temperature Sensitivity of NO

Since the peak NO concentration in the flame is sensitive to temperature, a good comparison between the measured peak NO and computed peak NO concentration indicates that the temperature used for computations is correct provided that the fuel-oxidation and NO chemical kinetics can be relied upon. For diluted hydrogen-oxgyen flames Surya2 and Surya3 the mechanisms for hydrogen oxidation and NO formation is reasonably well studied. On the basis of previous discussion of hydrogen oxidation mechanisms, Masten's mechanism with NO chemisty by Dean et al., [107], was selected for comparison of computed and measured NO. Individual steps in these reaction mechanisms have been stuidied in detail and are not merely a product of an optimization procedure like some other commonly used oxidation and NO chemistry for hydrocarbon flames. The NO mechanism has been tabulated in Appendix 2.

To obtain the effect of sensitivity of peak NO to the peak flame temperature the radiation term in the energy equation was artificially enhanced numerically. This allowed us to control the flame temperature and see the effect on peak NO. The peak temperature and the peak NO both decreased almost linearly with the radiation enhancement factor as shown in figs. A1.5 and A1.6. There is about 80 ppm change for every 10 K increase in Surya 3 flame, Fig A1.5, and about 30 ppm change for every 10K change in Surya2 flame, Fig. A1.6. With measured peak NO concentrations of 815 and 330ppm in the Surya3 and Surya 2 flames respectively, the peak NO concentration is very sensitive to NO. The ability of emmisivity correlation to reproduce the NO levels in both these flames using the thermocouple temperature corrected using the emmisivity correlation can be therefore used as a technique for validation of the emmisivity correlation.

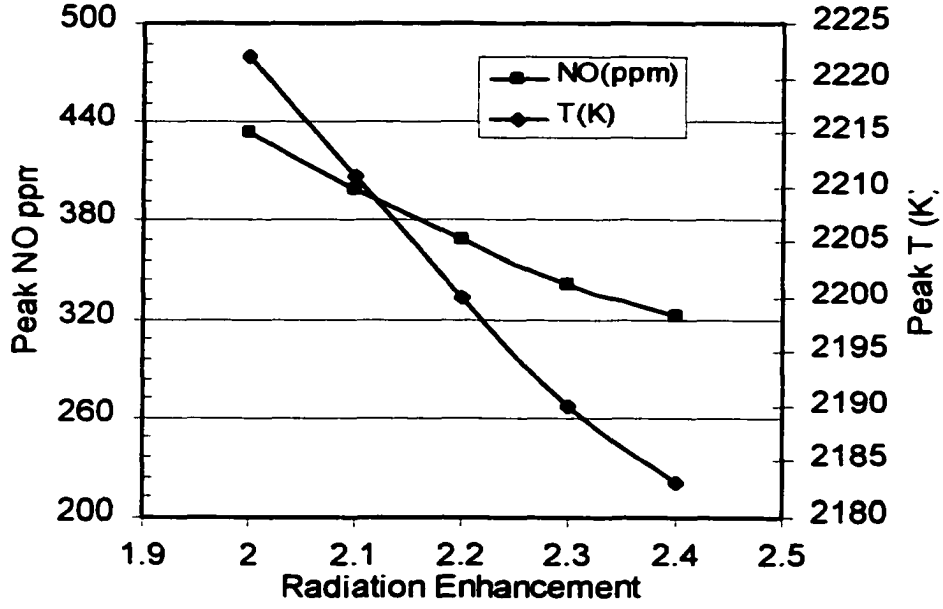

Fig A.1.5 Sensitivity of peak NO to peak flame temperature for Surya 2 Flame

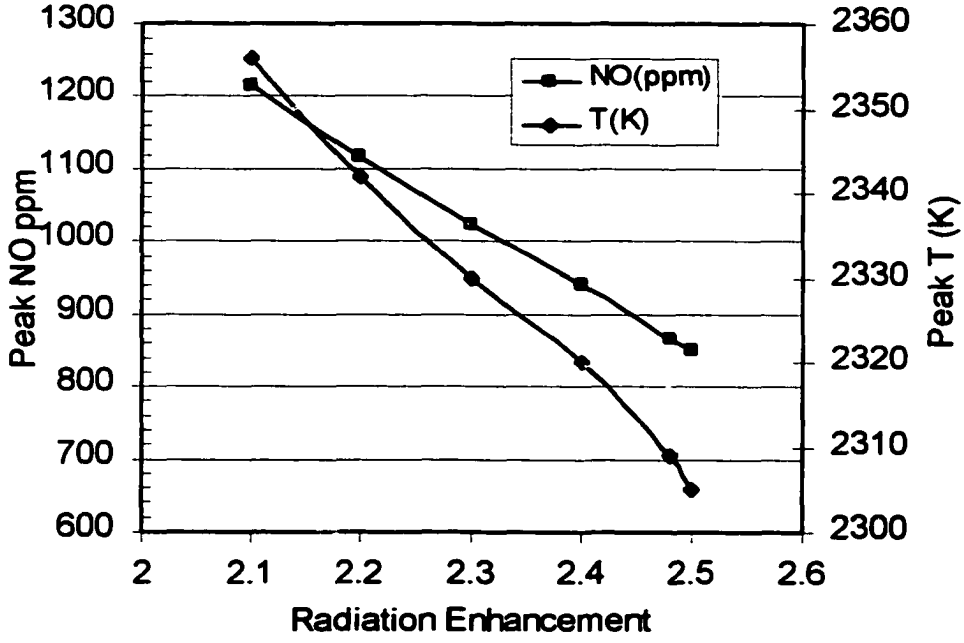

Fig A.1.6 Sensitivity of peak NO to peak flame temperature for Surya 3 Flame

Comparison of computations with corrected thermocouple emmisivity with experiments

Figs. A1.7 and A1.8 show the measured thermocouple temperature and the corrected temparature after accounting for radiation error using the new emmisivity correlation eq.3.2. The emmisivity correlation is a slight modification of the earlier correlation reported by Suh (1997) as shown in Fig. 3.9. The correlation was selected so as to yield good agreement for temperature sensitive peak NO in both the hydrogen flames, as shown in Figs. A1.7 and A.1.8, as well as a good agreement for OH distribution in both the hydrogen flames. The agreement for OH radical distribution is shown in Fig. 3.20. Furthermore, the calibration factor for OH LIF signal obtained using Surya 3 flame agreed well with the "Blue" methane flame OH concentrations as shown in Fig. 3.20.

On the basis of the agreement experimental and computed NO and OH concentrations, the use of present emmisivity correlation to correct the flame temperatures is considered reasonably accurate.

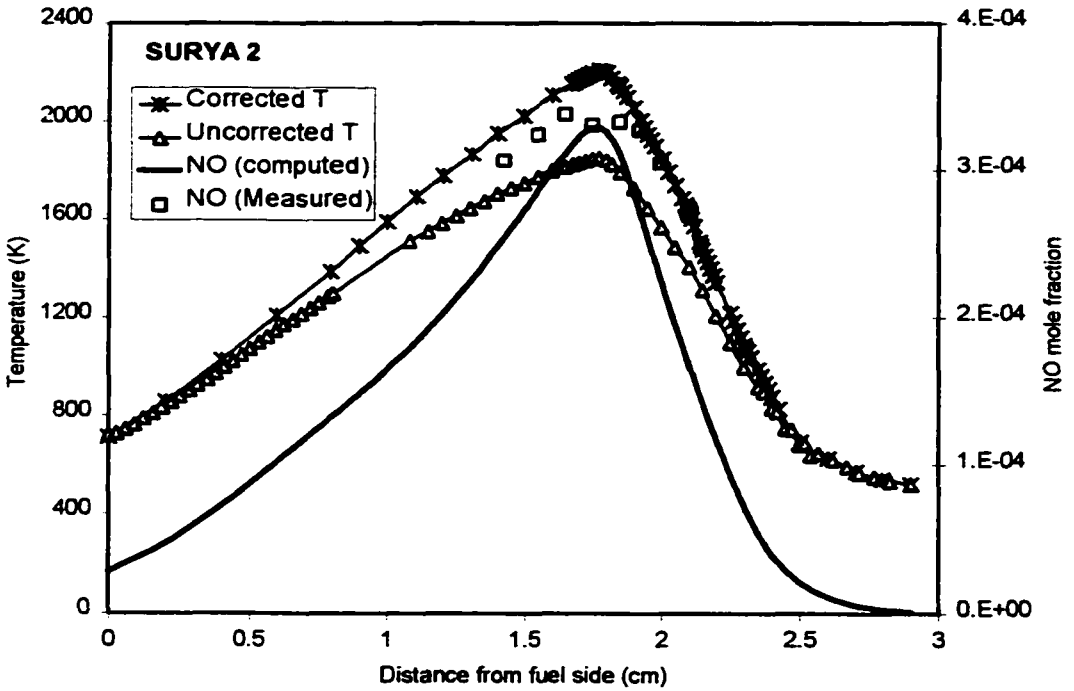

Fig A1.7 Comparison of measured and computed T and NO in Surya2 flame

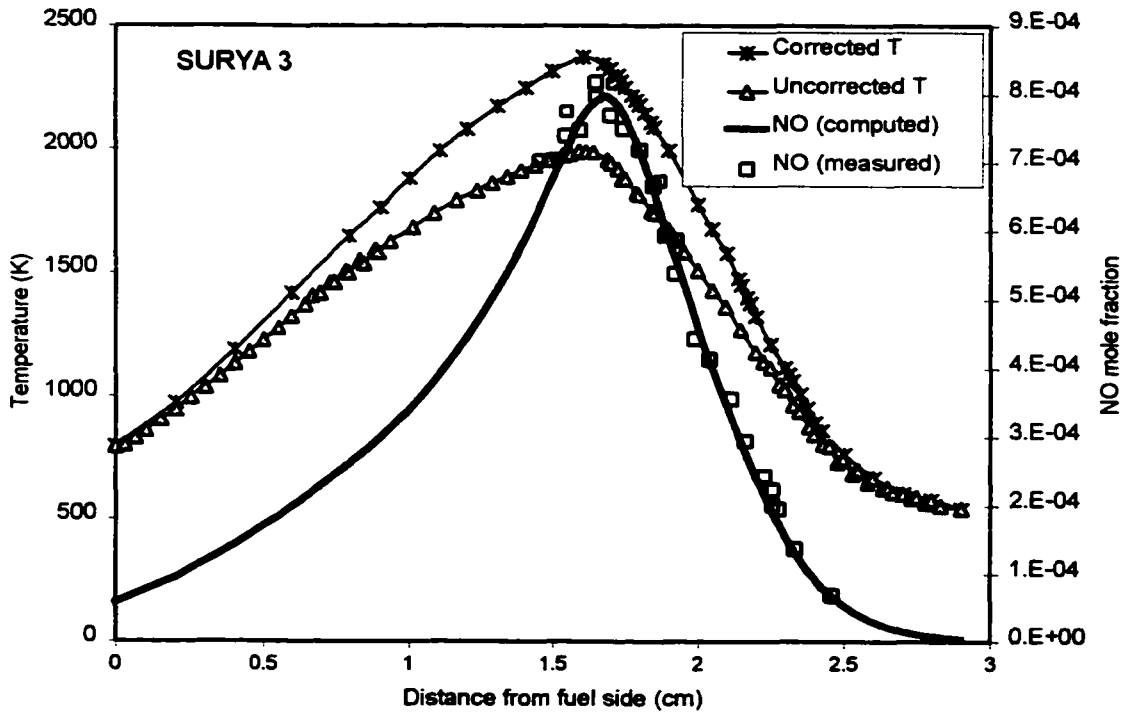

Fig A1.8 Comparison of measured and computed T and NO in Surya3 flame

APPENDIX 2

HYDROGEN OXIDATION MECHANISMS

A2.1 Masten's [105] mechanism

Following is the hydrogen combustion mechanism of Masten [105] with NO chemistry from Dean [107] in Chemkin readable format.

```
! Masten's Mechanism : given by Prof. Wooldridge on 10th May
ELEMENTS
O  H  AR N
END
SPECIES
H2      H     O       O2      OH      H2O     HO2     H2O2
N2      AR
NH3 NO N2O NO2
N   NH NH2 NNH
HNO
END
THERMO
END
REACTIONS
! Units are cm3, mole, cal; k = A T**n exp(-E/RT)
!
!
OH+H2=H2O+H                              1.170E+09    1.300   3626.00
H+O2=OH+O                                9.330E+13    0.00   14800.00
H2+O=OH+H                                5.060E+04    2.670   6290.00
OH+OH=O+H2O                              6.000E+08    1.300      0.00
O+HO2=O2+OH                              1.400E+13    0.000   1073.00
H+HO2=2OH                                1.400E+14    0.000   1073.00
H2+O2=H+HO2                              3.300E+13    0.000  53900.00
OH+HO2=H2O+O2                            7.500E+12    0.000      0.00
HO2+HO2=H2O2+O2                          2.000E+12    0.000      0.00
H2O2+OH=H2O+HO2                          1.000E+13    0.000   1800.00
H2O2+H=H2O+OH                            1.000E+13    0.000   3600.00
H2O2+H=HO2+H2                            1.600E+12    0.000   3800.00
H2O2+O=HO2+OH                            2.800E+13    0.000   6400.00
H2O2+M=2OH+M                             1.300E+17    0.000  45500.00
2O+M=O2+M                                1.890E+13    0.000  -1788.00
H+OH+M=H2O+M                             1.600E+22   -2.000      0.00
H2O/5.0/
H2+M=H+H+M                               2.200E+14    0.000  96000.00
H2/4.0/ H2O/18.6/
H+O2+M=HO2+M                             3.610E+17   -0.720      0.00
H2O/18.6/ H2/2.9/
H+O+M=OH+M                               6.200E+16   -0.600      0.00
H2O/5.0/

!   5/25/00
!   Following is a subset of Dean's NO chemistry mechanism that
!   includes R178-R216 from GRI3 with rates of dean
!   R211  has a C containg species and does not appear in this subset
```

```
!************************************************************************
! Beginning of nitrogen chapter mechanism
O+N2=N+NO    1.95E+14    0.00  76817   !178
N2O+M=N2+O+M       4.00E+14    0.00  56093 !185
N2/1.5/  O2/1.5/  H2/1.5/  H2O/10./
N2O+O=N2+O2 1.40E+12    0.00  10809   !181
N2O+O=2NO   2.90E+13    0.00  23149   !182
HO2+NO=NO2+OH      2.20E+12    0.00  -477    !186
N2O+H=N2+OH 2.20E+14    0.00  16750 !183
H+N2O=NH+NO 8.50E+20    -1.62 35369   !199
H+N2O=NNH+O 2.40E+19    -1.26 47092
NH+NO=N2+OH 1.40E+17    -1.49 1311    !198
NH+NO=NNH+O 1.70E+14    -0.20 12200   !208
NH+O2=NO+OH 7.60E+10    0.00  1530    !195
NH+O2=HNO+O 4.60E+05    2.00  6497    !194
NH2+O=HNO+H 4.60E+13    0.00  0       !201
NH2+O=NH+OH 7.00E+12    0.00  0     !200
DUPLICATE
NH2+O=NH+OH 3.33E+08    1.50  5077  !200
DUPLICATE
NH2+OH=NH+H2O      2.40E+06    2.00  50    !203
!NH2+NO=NNH+OH     3.50E+10    0.34  -765  !  UPDATED 9/25/96
N+O2=NO+O    9.00E+09    1.00  6497    !179
N+OH=NO+H    1.10E+14    0.00  1123  !180
NH+N=N2+H    1.50E+13    0.00  0     !196
NH+OH=HNO+H 2.00E+13    0.00  0       !192
NH+OH=N+H2O 1.20E+06    2.00  -487  !193
NH+H=N+H2    3.50E+13    0.00  1728  !191
NH+O=NO+H    6.00E+13    0.00  0     !190
NNH=N2+H     3.00E+08    0.00  0     !204
DUPLICATE
NNH+M=N2+H+M       1.00E+13    0.50  3060  !205
DUPLICATE
AR/0.7/  H2O/7.0/
NNH+O2=N2+HO2      1.20E+12    -0.34 149     !206
NNH+H=N2+H2 2.40E+08    1.50  -894  !209
NNH+OH=N2+H2O      2.40E+22    -2.88 2454  !210
DUPLICATE
NNH+OH=N2+H2O      1.20E+06    2.00  -1192 !210
DUPLICATE
NNH+O=N2+OH 1.70E+16    -1.23 497   !207
DUPLICATE
NNH+O=N2+OH 1.70E+08    1.50  -894  !207
DUPLICATE
NO2+H=NO+OH 1.30E+14    0.00  358     !189
NO2+O=NO+O2 3.90E+12    0.00  -238    !188
NO2+M=NO+O+M       4.00E+15    0.00  59988 !187
N2/1.5/  O2/1.5/  H2/1.5/  H2O/10./
N2O+OH=N2+HO2      1.29E-02    4.72  36561 !184
HNO+M=H+NO+M       1.80E+16    0.00  48682 !212
N2/1.5/  O2/1.5/  H2/1.5/  H2O/10./
HNO+OH=NO+H2O      1.30E+07    1.88  -954  !215
HNO+H=H2+NO 4.50E+11    0.72  656     !214
HNO+O=OH+NO 4.50E+11    0.72  656   !213
HNO+O2=NO+HO2      2.00E+13    0.00  15896   !216
!****************************************
END
```

A2.2 'SandiaMech' Hydrogen Oxidation Mechanism [33]

The following is the Hydrogen Oxidation mechanism in Chemkin Format as outlined in the Sandia report [33].

```
ELEMENTS
O  H  N  AR  HE
END
SPECIES
H2      H       O       O2      OH      H2O     HO2     H2O2
N2      AR    HE
END
THERMO
END
REACTIONS
! Units are cm3, mole, cal; k = A T**n exp(-E/RT)
!Sandia Report SAND96-8243 UC-1409, Page 21
!
H+O2+M=HO2+M                              3.610E+17   -0.720       0.0
H2O/18.6/ H2/2.86/
H+H+M=H2+M                                1.000E+18   -1.000       0.0
H+H+H2=H2+H2                              9.200E+16   -0.6000      0.0
H+H+H2O=H2+H2O                            6.000E+19   -1.2500      0.0
H+OH+M=H2O+M                              1.600E+22   -2.0000      0.0
H2O/5/
H+O+M=OH+M                                6.200E+16   -0.600       0.0
H2O/5/
O+O+M=O2+M                                1.890E+13    0.000   -1788.0
H2O2+M=OH+OH+M                            1.300E+17    0.000   45500.0
H2+O2=2OH                                 1.700E+13    0.000   47780.0
OH+H2=H2O+H                               1.170E+09    1.300    3626.0
O+OH=O2+H                                 3.610E+14   -0.500       0.0
O+H2=OH+H                                 5.060E+04    2.670    6290.0
OH+HO2=H2O+O2                             7.510E+12    0.00        0.0
H+HO2=2OH                                 1.400E+14    0.00     1073.0
O+HO2=O2+OH                               1.400E+13    0.00     1073.0
2OH=O+H2O                                 6.000E+08    1.30        0.0
H+HO2=H2+O2                               1.250E+13    0.00        0.0
HO2+HO2=H2O2+O2                         2.000E+12    0.00         0.0
H2O2+H=HO2+H2                             1.600E+12    0.00     3800.0
H2O2+OH=H2O+HO2                           1.000E+13    0.00     1800.0
END

EOF
```

A2.3 Barlow et al. [80] mechanism

Following is the hydrogen oxidation and NO formation mechanism in Chemkin format as reported by Barlow et al. [80].

```
ELEMENTS
O  H  N  AR  HE
END
SPECIES
H2       H        O        O2       OH       H2O      HO2      H2O2
N2       AR     HE         N        NO       NO2      N2O      HNO
END
THERMO
END
REACTIONS
! Units are cm3, mole, cal; k = A T**n exp(-E/RT)
!Barlow et al., Chaperon efficiencies as per eqn 6 in the paper
!(1)
O2+H=>OH+O                                  2.000E+14    0.000  16800.00
OH+O=>H+O2                                  1.570E+13    0.000    841.30
H2+O=>OH+H                                  5.060E+04    2.670   6286.00
H+OH=>O+H2                                  2.220E+04    2.670   4371.00
H2+OH=>H2O+H                                1.000E+08    1.600   3298.00
H2O+H=>H2+OH                                4.310E+08    1.600  18274.00
O+H2O=>OH+OH                                1.470E+10    1.14   16991.00
2OH=>H2O+O                                  1.590E+09    1.14     100.40
H+O2+M=>HO2+M                               2.300E+18   -0.80       0.00
H2/ 1.00/ H2O/6.5/ N2/0.4/ O2/0.4/ HE/0.4/
HO2+M=>H+O2+M                               3.190E+18   -0.80   46699.30
H2/ 1.00/ H2O/6.5/ N2/0.4/ O2/0.4/ HE/0.4/
!(11)
H+HO2=>2OH                                  1.500E+14    0.00    1004.00
H+HO2=>H2+O2                                2.500E+13    0.00     693.10
OH+HO2=>H2O+O2                              6.000E+13    0.00       0.00
H+HO2=>H2O+O                                3.000E+13    0.00    1721.00
O+HO2=>OH+O2                                1.800E+13    0.00    -406.30
2HO2=>H2O2+O2                               2.000E+12    0.00       0.00
2OH+M=>H2O2+M                               9.860E+14    0.00   -5070.00

H2O2+M=>2OH+M                               1.300E+17    0.00   45500.00
H2O2+H=>HO2+H2                              1.600E+14    0.00    3800.00
DUPLICATE
HO2+H2O=>H2O2+OH                            2.860E+13    0.00   32790.00
!(21)
H2O2+OH=>HO2+H2O                            1.000E+13    0.00    1800.00
H+H+M=>H2+M                                 1.800E+18   -1.00       0.00
H2/ 1.00/ H2O/6.5/ N2/0.4/ O2/0.4/ HE/0.4/
OH+H+M=>H2O+M                               2.200E+22   -2.00       0.00
H2/ 1.00/ H2O/6.5/ N2/0.4/ O2/0.4/ HE/0.4/
2O+M=>O2+M                                  1.890E+15    0.00   -1788.00
H2/ 1.00/ H2O/6.5/ N2/0.4/ O2/0.4/ HE/0.4/
H2O2+H=HO2+H2                               4.790E+13    0.00    7945.80
DUPLICATE
OH+O+M=HO2+M                                1.000E+16    0.00       0.00
H2/ 1.00/ H2O/6.5/ N2/0.4/ O2/0.4/ HE/0.4/
H2+O2=2OH                                   1.700E+13    0.00   47780.00
```

```
H+O+M=OH+M                                  6.200E+16   -0.60        0.00
H2/ 1.00/ H2O/6.5/ N2/0.4/ O2/0.4/ HE/0.4/
O+N2=NO+N                                   1.400E+14    0.00    75800.00
NO+O=N+O2                                   3.800E+09    1.00    41356.00
!(31)
NO+H=OH+N                                   2.630E+14    0.00    50393.60
NO+M=N+O+M                                  3.980E+20   -1.50   149945.60
H2/ 1.00/ H2O/6.5/ N2/0.4/ O2/0.4/ HE/0.4/
N2O+M=N2+O+M                                1.600E+14    0.00    51600.00
H2/ 1.00/ H2O/6.5/ N2/0.4/ O2/0.4/ HE/0.4/
N2O+O=2NO                                   6.920E+13    0.00    26615.80
N2O+O=N2+O2                                 1.000E+14    0.00    28006.20
N2O+N=N2+NO                                 1.000E+13    0.00    19862.10
N+HO2=NO+OH                                 1.000E+13    0.00     1985.30
N2O+H=N2+OH                                 7.600E+13    0.00    15096.10
HNO+O=NO+OH                                 5.010E+11    0.50     1985.30
HNO+OH=NO+H2O                               1.260E+12    0.50     1985.30
!(41)
NO+HO2=HNO+O2                               2.000E+11    0.00     1985.30
HNO+HO2=NO+H2O2                             3.160E+11    0.50     1985.3
HNO+H=NO+H2                                 1.260E+13    0.00     3972.90
HNO+M=H+NO+M                                1.780E+16    0.00    48663.90
H2/ 1.00/ H2O/6.5/ N2/0.4/ O2/0.4/ HE/0.4/
NO+HO2=NO2+OH                               2.110E+12    0.00     -480.00
NO2+H=NO+OH                                 3.500E+14    0.00     1500.00
NO2+O=NO+O2                                 1.000E+13    0.00      500.00
NO2+M=NO+O+M                                1.100E+16    0.00    66000.00
H2/ 1.00/ H2O/6.5/ N2/0.4/ O2/0.4/ HE/0.4/
END

EOF
```

APPENDIX A3

The following mathematical formulation uses flamesheet analysis concept of Burke-Schumann (1924) and analytical framework for asymptotic analysis of the premixed reaction zone developed by Law et al. (1988).

In the following analysis all the unscaled properties are primed while the scaled quantities are unprimed. One step reaction between fuel (subscript F) and oxidizer (subscript 0) of the form $\nu_F F + \nu_0 0 \rightarrow$ products is assumed where ν_F and ν_0 are the stochiometric coefficients for fuel and oxidizer.

The reaction rate is assumed of the form:

$$\dot{w}_f{}''' = \rho' B' Y_0{}' Y_F{}' \exp\left(\frac{-E_a{}'}{R'T'}\right)$$

where E_a' is the activation energy, Y_0' and Y_F' are oxygen and the fuel mass fraction, ρ' is the mixture density, T' is the temperature and $\dot{w}_f{}'''$ is the fuel consumption rate in (kg/m^3Kec).

The flow field is approximated by potential flow"

$$\begin{aligned}\vec{V} &= u'\hat{i} + v'\hat{j} \\ &= k'x'\hat{i} - k'y'\hat{j},\end{aligned}$$

where k' is the strain rate, x' and y' are x and y co-ordinates with x-axis aligned with the stagnation plane and y-axes aligned with the stagnation streamline.

Using the scaling $\eta = y'/\sqrt{K'D'}$, $Y_F = Y_F{}'$ and $Y_0 = Y_0{}'/\sigma$ the species conservation equation can be written as:

$$\frac{d^2Y_i}{d\eta^2} + \eta\frac{dY_i}{d\eta} = -w \qquad (1)$$

where

$$w = D_a Y_0 Y_F \exp(-E_a'/R'/P')$$

$$D_a = B'\sigma / K'$$

σ is kg oxygen per kg fuel in the stoichiometric equation.

Assuming Lewis no- 1 and using the scaling, $T = T'/(q'/C_p')$ where q' is energy released per kg of fuel the energy equation along the stagnation streamline can be rewritten as:

$$\frac{d^2T}{d\eta^2} + \eta\frac{dY_i}{d\eta} = -w \qquad (2)$$

We further define

$$T_a \equiv (E_a'/R')*(C_p'/q')$$

The boundary conditions for the system consist of temperature and species values at the fuel and the oxidizer side boundaries:

$$T = T_{+\infty}, \quad Y_F = Y_{F,\infty}, \quad Y_0 = Y_{0,\infty} \qquad \eta \to \infty \qquad ..(3a)$$

$$T = T_{-\infty}, \quad Y_F = 0, \quad Y_0 = Y_{0,-\infty} \qquad \eta \to \infty \qquad ..(3b)$$

A schematic diagram of the spatially separated flamesheets is shown in Fig. 4.2. there are five unknowns that we wish to determine – locations η_n, η_p the temperatures T_n, T_p of the two flamesheets and the fuel concentration $Y_{F,p}$ at the premixed flamesheet. $Y_0 = 0$ at the premixed flamesheet.

The regions, labelled as A, B and C in Fig. 4.3 are identified by two flamesheets and the two boundaries.

Outer Solution

The outer solution (indicated by superscript 0) is written as:

(i) Region (A)

$$Y_{F,A}^o = 0 \qquad ..(1.1)$$

$$Y^o_{0,A} = Y_{0,-\infty}\left\{1 - \frac{\int_{-\infty}^{\eta} Hd\eta}{\int_{-\infty}^{\eta_n} Hd\eta}\right\} \qquad ..(1.2)$$

$$T^o_A = \frac{T_n - T_{-\infty}}{\int_{-\infty}^{\eta_n} Hd\eta} \int_{-\infty}^{\eta} Hd\eta + T_{-\infty} \qquad ..(1.3)$$

(ii) Region (B)

$$Y^o_{0,B} = 0 \qquad ..(1.4)$$

$$Y^o_{F,B} = Y_{F,p}\left\{\frac{\int_{\eta_n}^{\eta} Hd\eta}{\int_{\eta_n}^{\eta_p} H}\right\} \qquad ..(1.5)$$

$$T^o_B = T_n + (T_p - T_n) \qquad ..(1.6)$$

where $H \equiv e^{-\eta^2/2}$.

(iii) Region (C)

$$T^o_B = T_\infty + (T_p + T_\infty)\left\{\frac{\int_{\infty}^{\eta} Hd\eta}{\int_{\infty}^{\eta_p} Hd\eta}\right\} \qquad ..(1.7)$$

$$Y^o_{0,C} = Y_{0,\infty}\left\{1 - \frac{\int_{\infty}^{\eta} Hd\eta}{\int_{\infty}^{\eta_p} Hd\eta}\right\} \qquad ..(1.8)$$

$$Y_{F,C}^{o} = Y_{F,\infty} + (Y_{F,p} - Y_{F,\infty})\left\{\frac{\int_{\infty}^{\eta} H d\eta}{\int_{\infty}^{\eta_p} H d\eta}\right\} \qquad ..(1.9)$$

(iv) Jump conditions at the nonpremixed flame:

Energy flux

$$\frac{T_n - T_{-\infty}}{\int_{-\infty}^{\eta_n}\left(\frac{H}{H_n}\right)d\eta} - \frac{T_p - T_n}{\int_{\eta_n}^{\eta_p}\left(\frac{H}{H_n}\right)d\eta} = \frac{Y_{F,p}}{\int_{\eta_n}^{\eta_p}\left(\frac{H}{H_n}\right)d\eta} \qquad ..(1.10)$$

species flux

$$\frac{Y_{F,p}}{\int_{\eta_n}^{\eta_n}\left(\frac{H}{H_n}\right)d\eta} = \frac{Y_{0,-\infty}}{\int_{-\infty}^{\eta_n}\left(\frac{H}{H_n}\right)d\eta} \qquad ..(1.11)$$

(v) Jump conditions for premixed flames

Energy:

$$\frac{(Y_{F,p} - Y_{F,\infty})}{\int_{\infty}^{\eta_p}\left(\frac{H}{H_n}\right)d\eta} - \frac{Y_{F,p}}{\int_{\eta_n}^{\eta_p}\left(\frac{H}{H_n}\right)d\eta} = \frac{(T_p - T_n)}{\int_{\eta_n}^{\eta_p}\left(\frac{H}{H_n}\right)d\eta} - \frac{(T_p - T_\infty)}{\int_{\infty}^{\eta_p}\left(\frac{H}{H_n}\right)d\eta} \qquad ..(1.12)$$

Species flux:

$$\frac{-Y_{0,\infty}}{\int_{\infty}^{\eta_p}\left(\frac{H}{H_n}\right)d\eta} = \frac{(Y_{F,p} - Y_{F,\infty})}{\int_{\infty}^{\eta_p}\left(\frac{H}{H_n}\right)d\eta} - \frac{Y_{F,p}}{\int_{\eta_n}^{\eta_p}\left(\frac{H}{H_n}\right)d\eta} \qquad ..(1.13)$$

We have 5 unknowns $Y_{Ep}, \eta_n, \eta_p, T_n$ and T_p related by 4 jump conditions (1.10)-(1.13). We have a closure problem. In what follows, we shall address the closure problem by considering an asymptotic analysis of the structure of the premixed flame.

Premixed Flame Structure

The inner and outer expansions for the premixed flame structure are given as:

(i) Outer expansion

$$T_{out}^{-} = T_C^o + \in a^{-}\left\{\frac{\int_{\infty}^{\eta} Hd\eta}{\int_{\infty}^{\eta} Hd\eta}\right\} + \vartheta(\in) \qquad ..(1.14)$$

$$T_{out}^{+} = T_B^o + \in a^{+}\left\{\frac{\int_{\eta_n}^{\eta} Hd\eta}{\int_{\eta_n}^{\eta_p} Hd\eta}\right\} + \vartheta(\in) \qquad ..(1.15)$$

$$Y_{i,out}^{-} = Y_{i,C}^o + \in b_i^{-}\left\{\frac{\int_{\infty}^{\eta} Hd\eta}{\int_{\infty}^{\eta_p} Hd\eta}\right\} + \vartheta(\in) \qquad ..(1.16)$$

$$Y_{i,out}^{+} = Y_{i,B}^o + \in b_i^{+}\left\{\frac{\int_{\eta_n}^{\eta} Hd\eta}{\int_{\eta_n}^{\eta_p} Hd\eta}\right\} + \vartheta(\in) \qquad ..(1.17)$$

$a^{\mp}$ and $b_i^{\mp}$ are six integration constants to be determined.

(ii) Inner Expansion

The inner expansions are written in the form

$$T_{in} = T_p - \in (\theta + m\xi + \alpha) + \vartheta(\in) \qquad ..(1.18)$$

$$Y_{i,in} = \in \beta_i + \vartheta(\in) \qquad ..(1.19)$$

Where we define rescaling of the coordinate system as:

$$\xi = \frac{A(\eta_p - \eta)}{\epsilon} + \lambda \qquad ..(1.20)$$

and $\epsilon = \frac{T_p^{\,2}}{T_a}\left(\epsilon << \frac{E_a'}{R_a'}\right)$.

where m, A, α, λ are four free parameters to be chosen to clean up the governing equations later.

Fig. A3.1 shows coordinates systems ξ and η

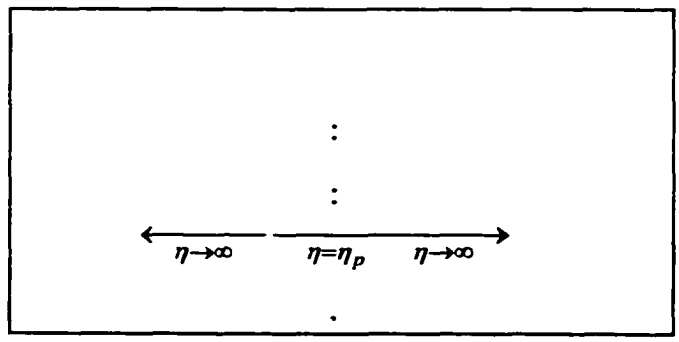

(iii) Governing equations for inner region

Substituting inner expansions into the original governing equations we have

$$\frac{d^2\theta}{d\xi^2} = \left[\frac{D_a \epsilon^3}{A^2}\exp\left(\frac{-T_a}{T_p}\right)\right]\beta_0\beta_F \exp\left(-(\theta + m\xi + \alpha)\right) \qquad ..(1.21)$$

$$\beta_i - \theta = C_i\xi + d_i \qquad ..(1.22)$$

equation (1.21) is an equation for pseudo-temperature (θ) and equation (1.22) is an equation for coupling function (β_i - θ). c_i and d_i are integrating constants expressible in terms of the known boundary conditions, the five unknowns and the four previously introduced free parameters.

(iv) Matching:

Matching the inner and outer expansions at the premixed flame yields:

$$\theta \to \left\{ \frac{(T_p - T_\infty)/A}{\int_\infty^{\eta_p} \left(\frac{H}{H_p}\right) d\eta} - m \right\} \xi - \frac{(T_p - T_\infty)/A}{\int_\infty^{\eta_p} \left(\frac{H}{H_p}\right) d\eta} \lambda - a^- - \alpha \quad \text{as } \xi \to -\infty \quad ..(1.23)$$

$$\theta \to \left\{ \frac{(T_p - T_\infty)/A}{\int_{\eta_n}^{\eta_p} \left(\frac{H}{H_p}\right) d\eta} - m \right\} \xi - \frac{(T_p - T_\infty)/A}{\int_{\eta_n}^{\eta_p} \left(\frac{H}{H_p}\right) d\eta} \lambda - a^- - \alpha \quad \text{as } \xi \to -\infty \quad ..(1.24)$$

for convenience we choose A and m such that

$$\frac{d\theta}{d\xi} \to 0 \quad \text{as } \xi \to \infty \qquad ..(1.25)$$

$$\frac{d\theta}{d\xi} \to -1 \quad \text{as } \xi \to -\infty \qquad ..(1.26)$$

which yields

$$A = \frac{(T_p - T_n)}{\int_{\eta_n}^{\eta_p} \left(\frac{H}{H_p}\right) d\eta} - \frac{(T_p - T_\infty)}{\int_\infty^{\eta_p} \left(\frac{H}{H_p}\right) d\eta} \qquad ..(1.27)$$

$$m = \frac{(T_p - T_n)/A}{\int_{\eta_n}^{\eta_p} \left(\frac{H}{H_p}\right) d\eta} \qquad ..(1.28)$$

With the above choice of A and m

$$\theta \to -\xi + (1-m)\lambda - a^- - \alpha \qquad \xi \to -\infty \qquad ..(1.29)$$

$$\theta \to -m\lambda - a^+ - \alpha \qquad \xi \to +\infty \qquad ..(.130)$$

$$\beta_0 \to -(\xi - \lambda) + b_0^- \qquad \xi \to -\infty \qquad ..(1.31)$$

$$\beta_0 \to b_0^+ \qquad \xi \to +\infty \qquad ..(1.32)$$

$$\beta_F \to y_f + b_F^- - (\xi - \lambda) \qquad \xi \to -\infty \qquad ..(1.33)$$

$$\beta_F \to y_f + b_F^+ \qquad \xi \to +\infty \qquad ..(1.34)$$

where $y_f \equiv Y_{F,p} / \epsilon$.

In deriving (1.33) and (1.34) we have used

$$A = \frac{-Y_{0,\infty}}{\int_{\infty}^{\eta_p} \left(\frac{H}{H_p} \right) d\mu}$$

which can be shown by using (1.29) and (1.12 – 1.13). Furthermore, we invoked that the factor

$$\frac{-Y_{F,p[}}{\epsilon A} \frac{1}{\int_{\eta_n}^{\eta_p} \left(\frac{H}{H_p} \right) d\eta}$$

is always $\theta(\epsilon)$ lower than y_f and can therefore be neglected.

We solve for c_l, d_l in (1.22) using the conditions (1.31 – 1.34) to yield:

$$\beta_0 = \theta + (m\lambda + \alpha) + (a^- + b_0^-) \qquad ..(1.35)$$

$$\beta_F = \theta + y_f + (b_F^+ - b_0^+) + (m\lambda + \alpha) + (a^+ + b_0^+) \qquad ..(1.36)$$

we impose

$$m\lambda + \alpha = 0 \qquad ..(1.37)$$

Furthermore we choose $a^- + b_o^- = a^+ + b_0^+ = 0$

$$a^+ + b_F^+ = a^- + b_F^- = 0$$

following previous work of Linan (1974) and Law et al. (1988).

This yields

$$\beta_0 = \theta \qquad ..(1.38)$$

$$\beta_F = \theta + y_F \qquad ..(1.39)$$

So, far we have imposed three constraints (1.25), (1.26) and (1.37) for four free parameters A, m, λ, α. If we further choose

$$\frac{D_a \epsilon^3}{A^2} \exp\left(\frac{-T_a}{T_p}\right) \exp(-\alpha) = \frac{1}{2(2+y_f)} \qquad ..(1.40)$$

We can reduce eqn.(1.21) for pseudo-temperature to:

$$2(2+y_f)\frac{d^2\theta}{d\xi^2} = \theta(\theta+y_f)\exp\left(-(\theta-m\xi)\right) \qquad ..(1.41)$$

which can be solved subject to boundary conditions:

$$\frac{d\theta}{d\xi} \to 0 \qquad \text{as } \xi \to \infty \qquad ..(1.42)$$

$$\frac{d\theta}{d\xi} \to -1 \qquad \text{as } \xi \to -\infty \qquad ..(1.43)$$

Adopting Linan's closure scheme (1974) for the premixed flames by setting

$$a^- \equiv 0 \qquad ..(1.44)$$

we have (using (1.44), (1.29) and (1.39))

$$\theta + \xi \to \lambda \qquad \text{as } \xi \to \infty \qquad ..(1.45)$$

or

$$\alpha \to -m(\theta+\xi) - \infty \qquad ..(1.46)$$

This problem is now closed

Solver for stiff ODE

Numerical solution of eqn 1.41, pseudo-temperature equation, with boundary conditions specified by 1.42 and 1.43 was carried out using FORTRAN code acdc.f by Cash and Wright, [2000]. This software package is designed to solve stiff two point boundary value probems for ordinary different equations using continuation. Fig. A3.2 shows dependence of solution on three domain sizes (-5,5), (-10,10) and (-15,15). The converged solution for θ in each of the three cases is independent of the domain size. Calculations were carried using domain size of (-10,10).

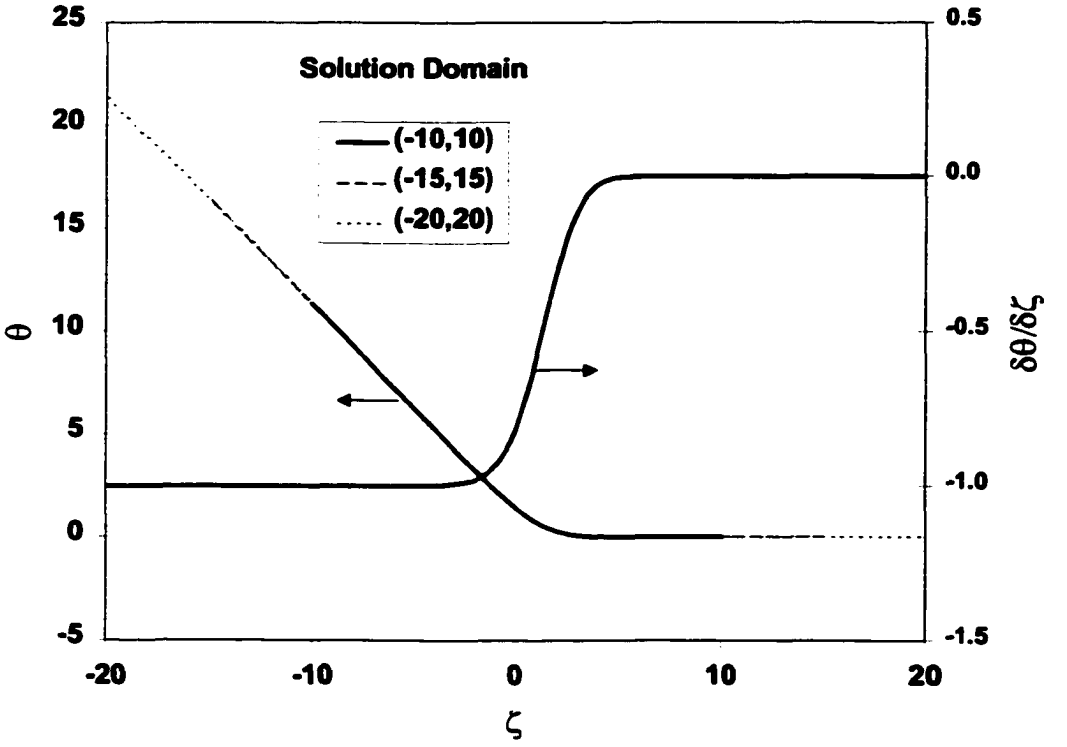

Fig A3.2 Dependence of solution on domain size (m=-.4923, Yfp=.059, ε=3.17306)

APPENDIX A4

Limited experiments and computational analysis of soot loading, flame radiation and energy release for progressive partial premixing of diluted initially non-premixed ethylene flames was conducted to explore the similarities and differences with methane fuel.

The flame specifications for the nonpremixed ethylene flame, EA, and its four partially premixed counterparts with progressive partial premixing are given in Table A4.1. The global strain rate for these flames is in the range 6-7 sec-1. Further partial premixing was not attempted due to danger of flash-back of the premixed flame into the fuel side port.

The trend for peak soot loading with progressive addition of oxygen to the fuel side is shown in Fig. A4.1. The increase in soot loading for addition of small amounts of oxygen to fuel is consistent with previous work of Glassman and Hura(1988). The increase in sooting tendency of ethylene with small amounts of oxygen is attributed in literature to chemical role of oxygen in enhancing soot loading. In Fig. A4.1 for .5% oxygen added to the fuel side of the non-premixed flame almost 100% increase in peak soot volume fraction cannot be attributed to changes in thermo-fluid enviroment in the flame and this effect must be of chemical nature.

Measured soot volume fraction distribution is shown with computed distribution of major stable species, chemical energy release , soot and gas radiation in Figs. A4.2-A4.6. The aspects of energy release distribution observed here are similar to those reported in Chapter5 for methane flames. The details of the trends in the energy release, radiation and radiative fractions are summarized in Fig. A4.7.

With progressive partial premixing the energy relase in the flame increase, Fig. A4.7. The relative importance of the three major energy release regions Peaks 1, 2 and 3

changed with progressive partial premixing in the same fashion as reported in Chapter 5 for methane flames.

Gas radiation increased with progressive partial premixing, Fig. A4.7, and the distribution of gas radiation broadedend due to broadening of the profiles of temperature and product species, Figs. A4.2(b)-A.4.6(b). Even though the gas radiation from the flame was enhanced, the radiative fraction for the gas radiation decreased as shown in Fig. A.4.7, similar to the observation for methane flames, Fig. 5.24.

Soot radiation and soot radiative fraction both increased following the trend for peak soot loading as shown in Fig. A.4.7. The net radiative fraction, combining the contributions of both soot and gas radiation increased with progressive partial premixing.

To conclude, although, the similarities in energy release and gas radiation aspects of both methane and ethylene flames are encouraging and point towards general features of effect of fuel side partial premixing, the effect on soot loading and soot radiation is dependent on the fuel type.

	Fuel Side	Oxidizer Side
Flame EA	Global Strain Rate = 5.83 sec-1	
	87.52% He+ 12.48%C2H4	71.9% N2+ 28.1 %O2
	V=10.4 cm/sec, T=630 K	V=6.5cm/sec, T=568 K
Fuel Side Partial Premixing		
Flame EB	Global Strain Rate = 5.85 sec-1	
	87.09% He+ 12.41%C2H4+.5%O2	71.9% N2+ 28.1 %O2
	V=10.5cm/sec, T=630 K	V=6.5cm/sec, T=568 K
Flame EC	Global Strain Rate= 5.99 sec-1	
	86.31% He+ 12.31%C2H4+1.38%O2	71.9% N2+ 28.1 %O2
	V=11.6 cm/sec, T=673 K	V=6.6cm/sec, T=574 K
Flame ED	Global Strain Rate= 6.62 sec-1	
	82.33% He+ 11.74%C2H4+5.93%O2	71.9% N2+ 28.1 %O2
	V=12.4 cm/sec, T=705 K	V=6.8cm/sec, T=593 K
Flame EE	Global Strain Rate= 6.79 sec-1	
	81.32% He+ 11.59%C2H4+7.08%O2	71.9% N2+ 28.1 %O2
	V=12.9cm/sec, T=725 K	V=6.9cm/sec, T=595 K

Table A4.1 Flame Specifications for ethylene Flames

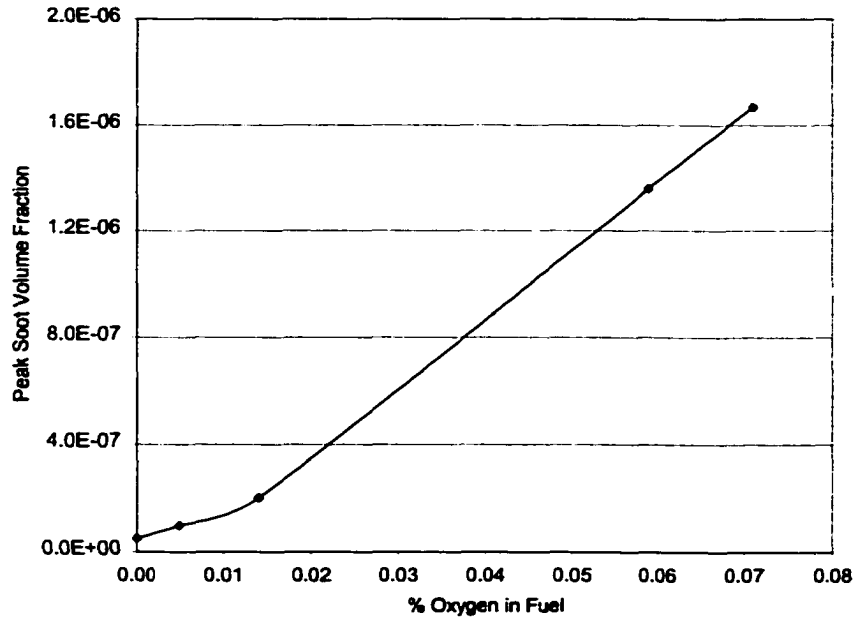

Fig A4.1 Variation of peak soot volume fraction with progressive partial premixing

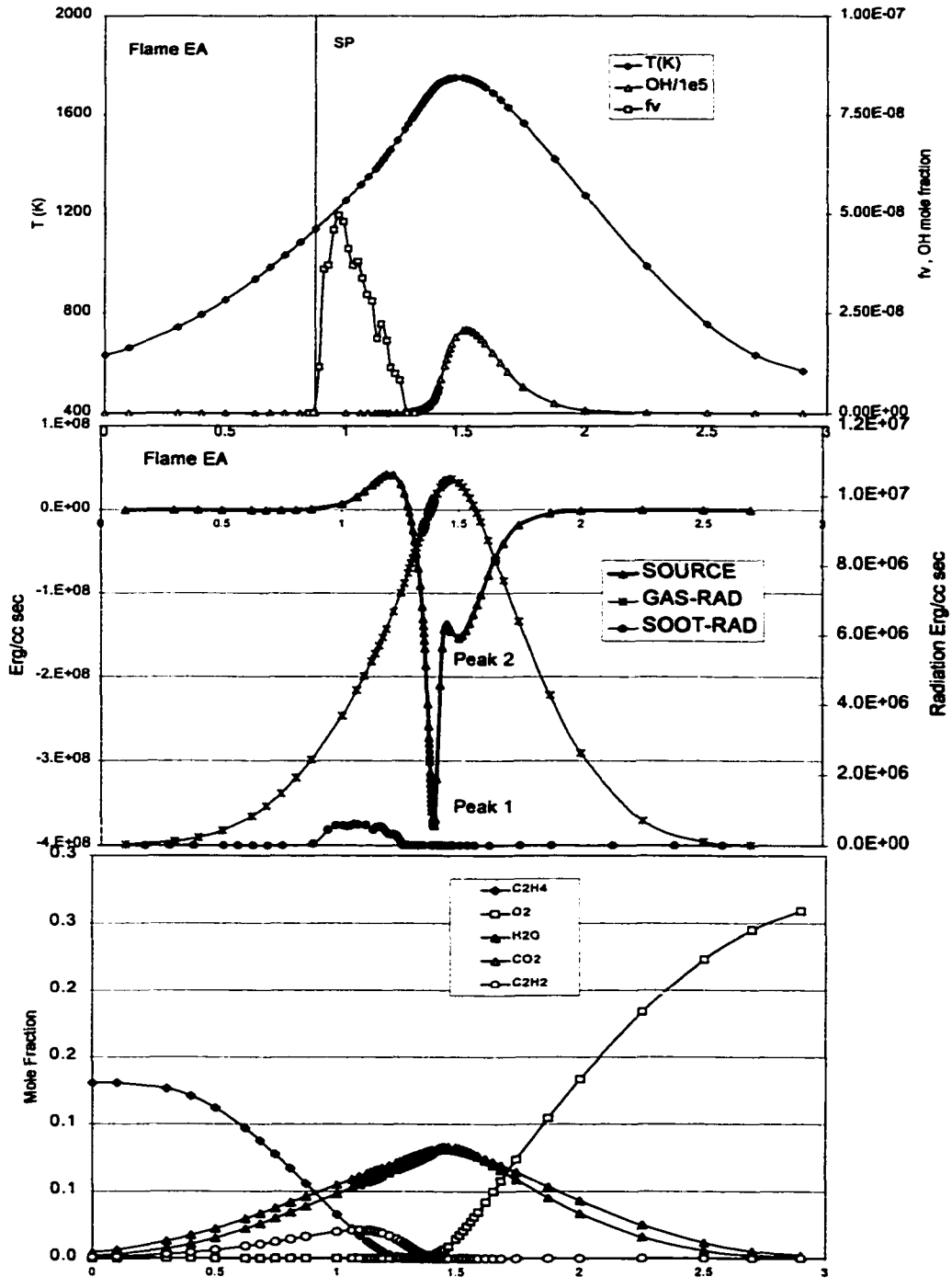

Fig A4.2 Distribution of (a) T, fv and OH (b) chemical energy release and radiation (c) major stable species in non-premixed ethylene flame EAd

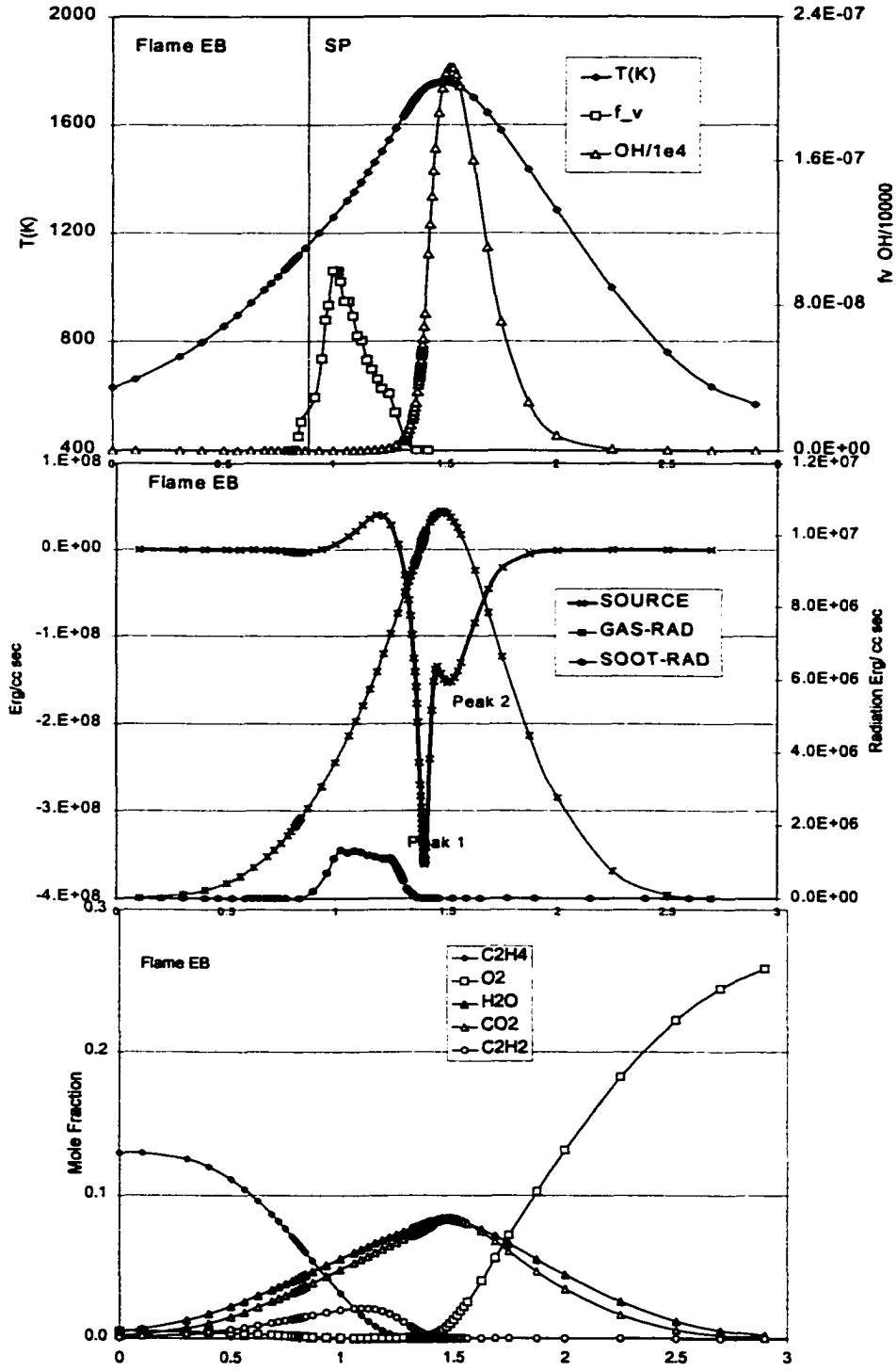

Fig A4.3Distribution of (a) T, fv and OH (b) chemical energy release and radiation (c) major stable species in partially-premixed ethylene flame EB

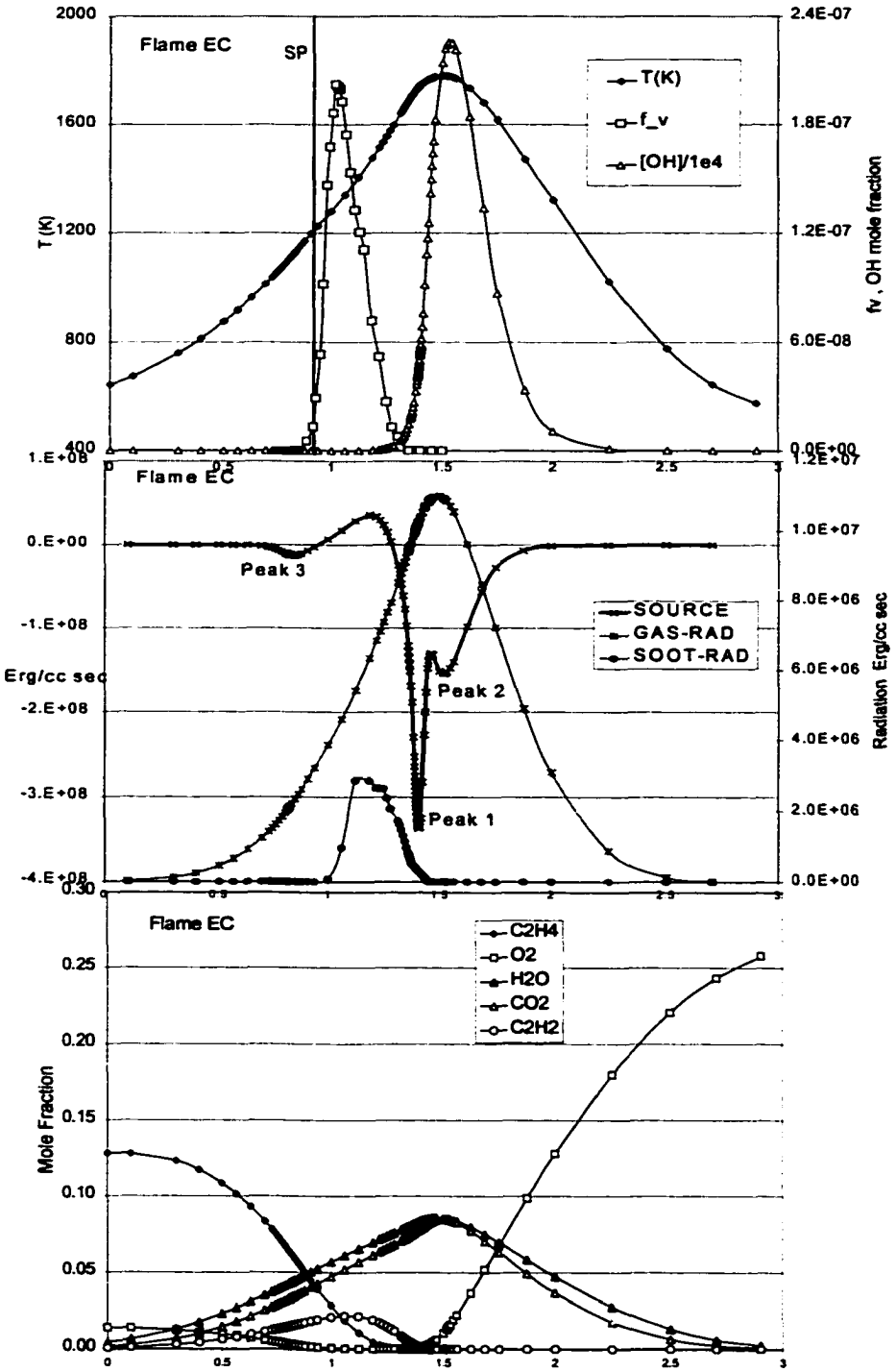

Fig A4.4 Distribution of (a) T, fv and OH (b) chemical energy release and radiation (c) major stable species in partially-premixed ethylene flame EC

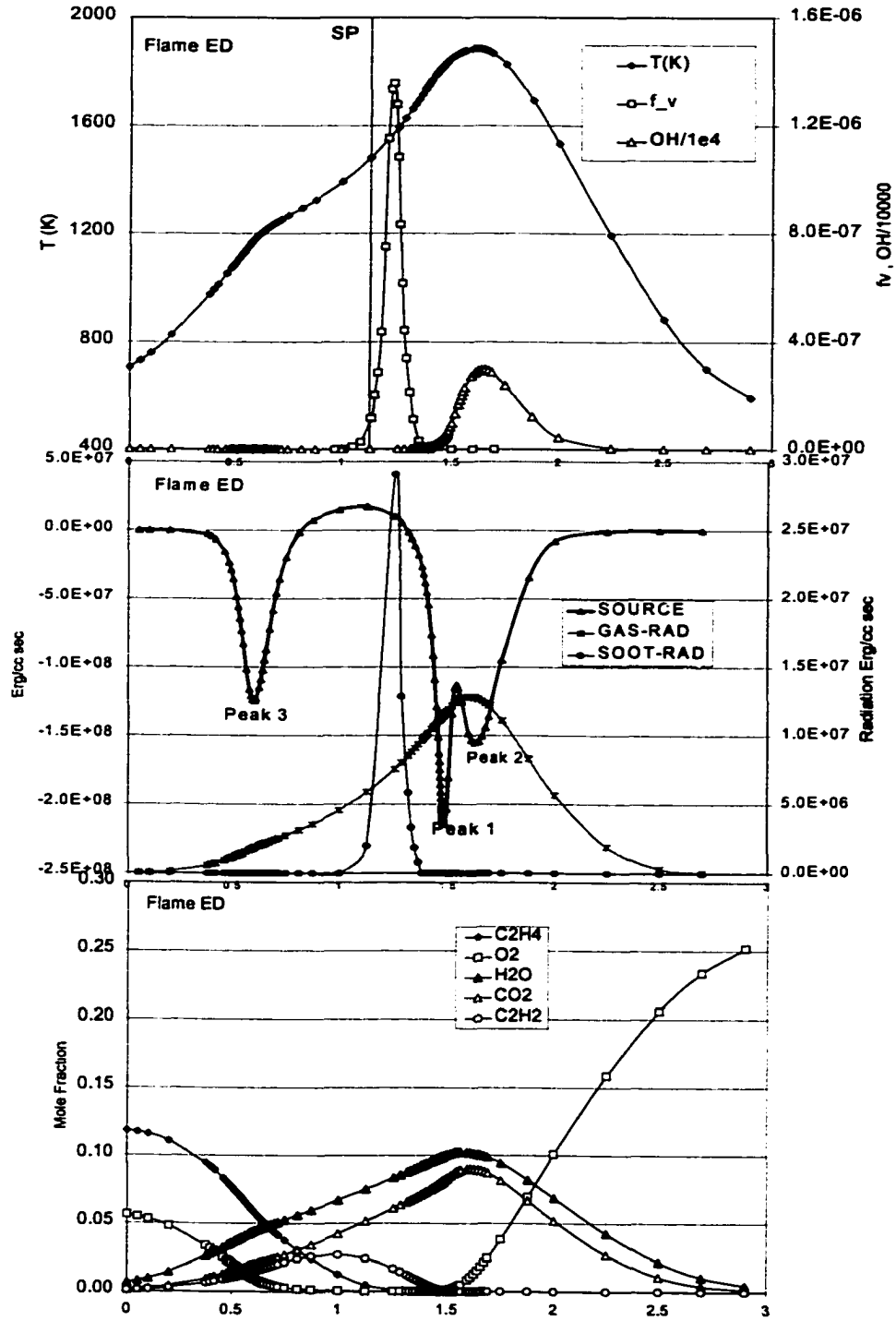

Fig A4.5 Distribution of (a) T, fv and OH (b) chemical energy release and radiation (c) major stable species in partially-premixed ethylene flame ED

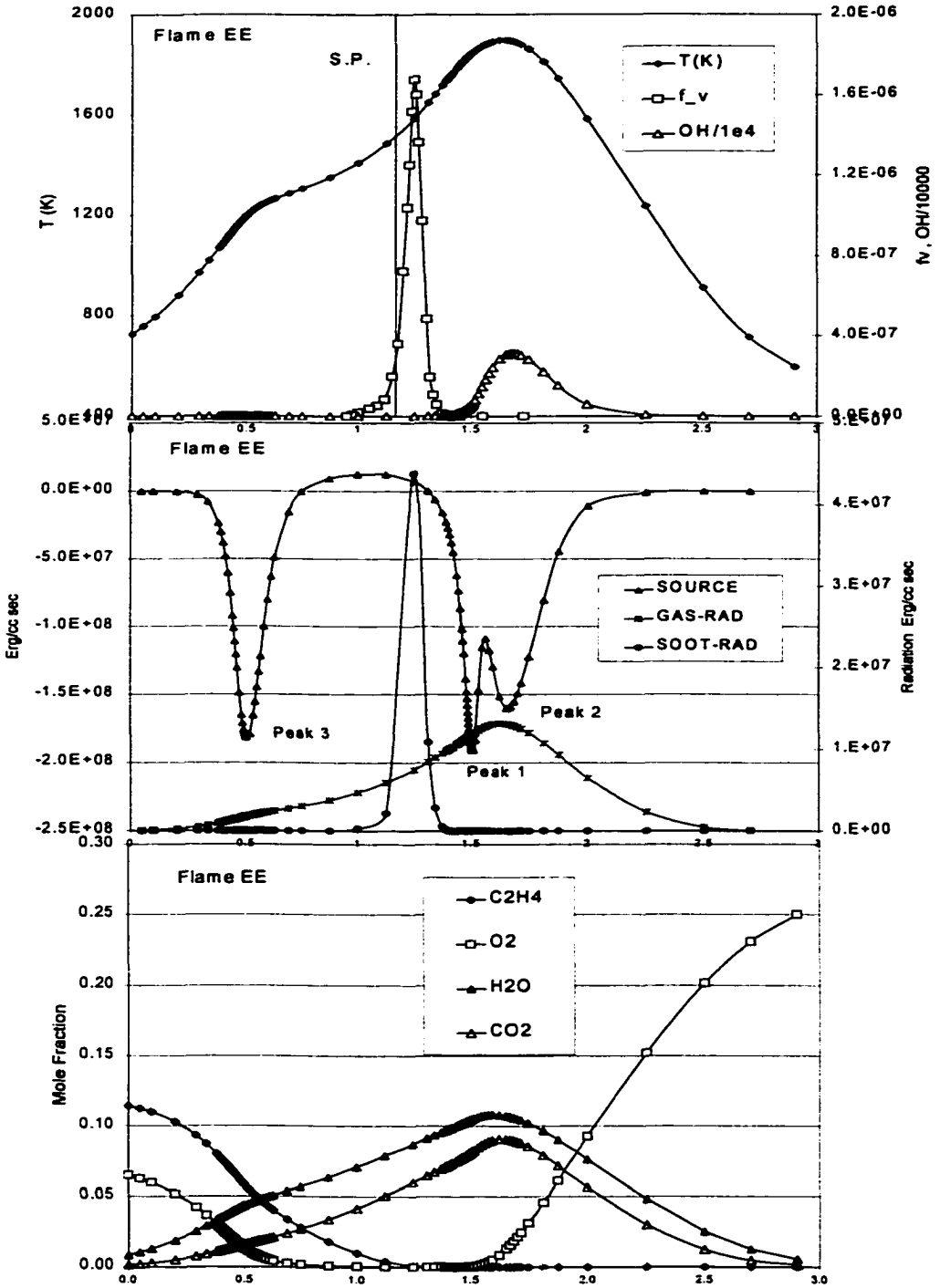

Fig A4.6 Distribution of (a) T, fv and OH (b) chemical energy release and radiation (c) major stable species in partially-premixed ethylene flame EE

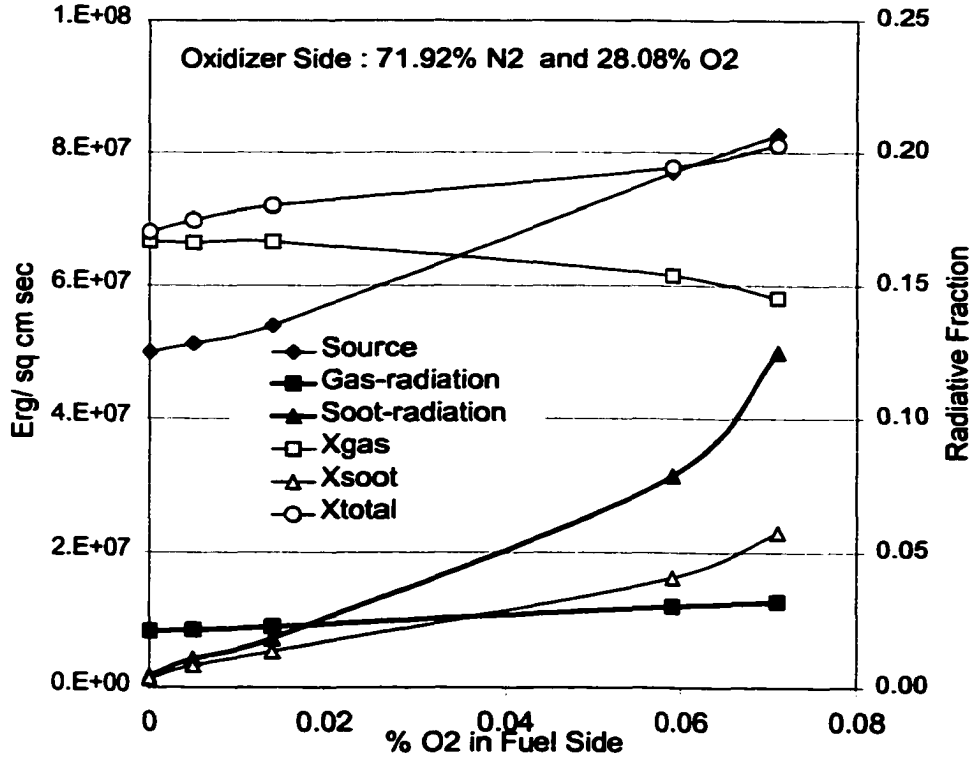

Fig A4.7 Trends for radiation and energy release

APPENDIX A5

Laser light extinction measurement setup for measurement of laser light extinction is shown in Fig. A4.1. 514.5nm Ar+ ion laser beam was collimated to 1mm diameter and focused to a 70 um diameter in the center of the burner using a 50 cm focal length lens. The extinction path length was confined to the central 5 cm region of the flame using two quartz tubes aligned concentric to the laser beam. The incident and the attenuated laser light intensities were collected using optical fibers mounted inside two integrating spheres (S1, S2) and measured using two Silicon (Hamamatsu S1336-5BK) photodiodes D1 and D2 as shown in Fig. A5.1. By using a precise positioning mechanism for the optical fiber, the intensity of the attenuated laser light falling on diode D2 could be adjusted to be equal to that of the incident laser light intensity falling on diode D1 in absence of any attenuating medium (assuming no attenuation by room air). Furthermore two potentiometers, R1 and R2, allowed minor adjustments to ensure that the outputs I1 and I2 of the two photodiodes were made equal with no attenuating medium between the two quartz tubes. The voltage signals I1 and I2 were detected using lock in detection using two SRS 510 lock in amplifiers. The lock in signal was obtained from a mechanical chopper operating at a frequency of 500Hz in the incident beam path. The signals I1 and I2 were grounded together. One of the lock in amplifiers was connected so that we could either measure signal I1 (typically ~ 40 mV, least count .01mV) or the difference I1-I2 on a more (least count .001 mV) sensitive scale.

The zero response (± 0.004 mV) was observed for the photodiodes with no light incident on them. A black cylindrical tube was placed around the photodiode and the fiber jacket to prevent stray room light from falling on the photodiode. To minimize the dark noise, the photodiode chip (2.5mm×2.5mm) was slightly larger than the optical fiber core (2mm diameter). The response of the two photodiodes I1 and I2 was found to be

linear with respect to each other with 99.9% confidence as shown in Fig. A5.2. Typical I1 and I2 signals were around 40-60 mV for laser power of 250mWatt. The photodiodes reached saturation for about 4mW of incident laser light according to the manufacturer. The sources of error, in addition to the instrument accuracy of measurement of I1 and I2-I1 using the lock in amplifiers, included noise in photodiode voltage, precision of the potentiometers R1 and R2 and the lock-in-amplifier noise. For typical value of I1~40mV uncertainty in I2/I1 was at least $\pm$ 0.1%.

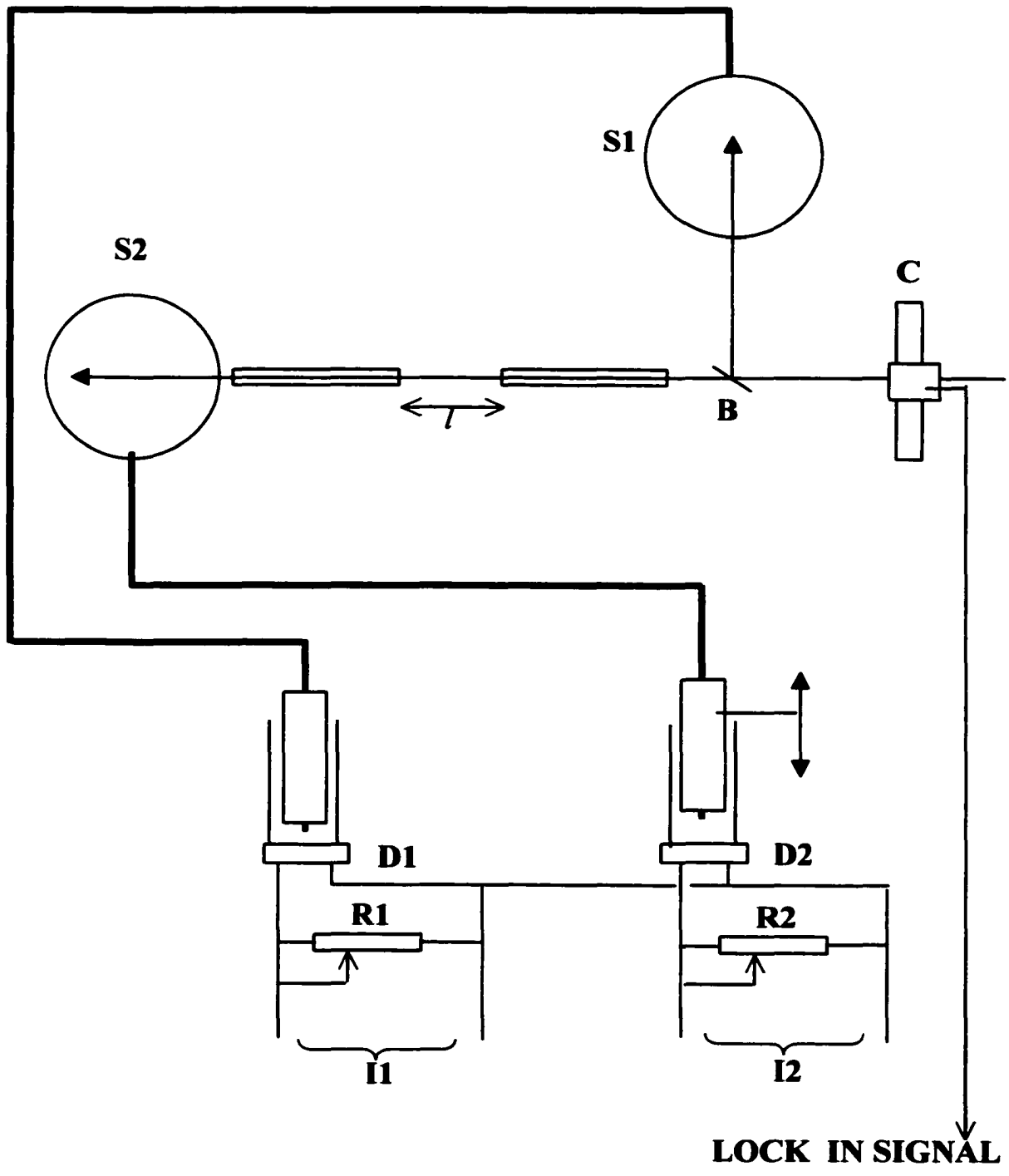

Fig. A5.1 Experimental Setup For Measurement of Laser Light Extinciton

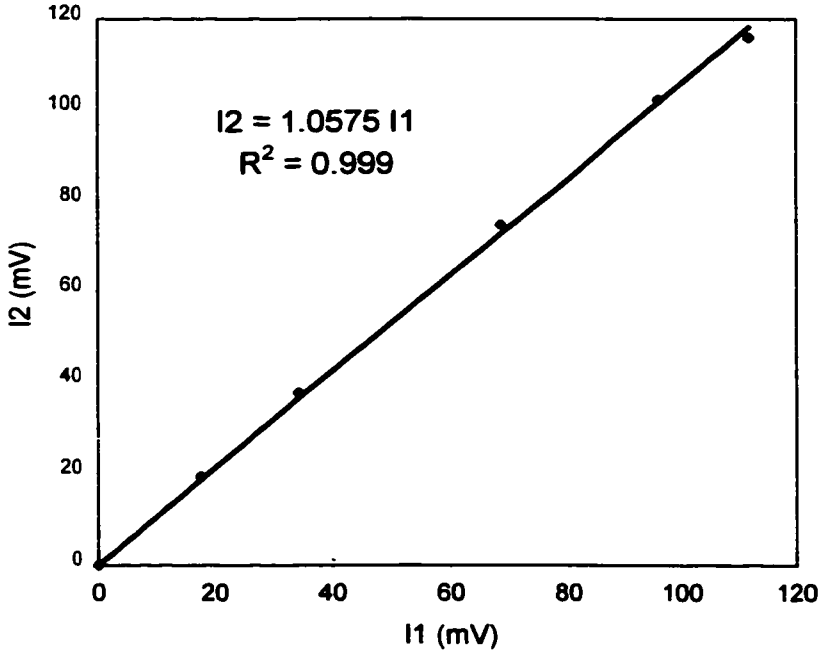

Fig A5.2 Linearity of the two photodiode signals

APPENDIX A6

Flame	Table	Page	Ref [41]
Blue-Ravi	3.1	21	
Surya 2	A1.1	183	
Surya 3	A1.1	183	
Blue			Blue
Flame 1.0	5.2	85	Flame 1
Flame 1.1	5.2	85	
Flame 1.2	5.2	85	
Flame 1.3	5.2	85	
Flame 1.4	5.2	85	
Flame 1.5	5.2	85	
Flame 4.0	5.3	86	Flame 4
Flame 4.1	5.3	86	
Flame 4.2	5.3	86	
Flame 4.3	5.3	86	
Flame A	5.4	117	
Flame A*	5.4	117	
Flame B	5.4	117	
Flame C	5.4	117	

Flame	Table	Page	Ref [41]
Flame D	5.4	117	
CH4 18%	7.2	158	
CH4 19%	7.2	158	
CH4 20%	7.2	158	
CH4 21%	7.2	158	
CH4 22%	7.2	158	
CH4 23%	7.2	158	
CH4 24%	7.2	158	
C_2H_4 11%	7.3	159	
C_2H_4 12%	7.3	159	
$C_2H_4$12.5%	7.3	159	
C_2H_4 13%	7.3	159	
C_2H_4 14%	7.3	159	
Flame EA	A4.1	208	
Flame EB	A4.1	208	
Flame EC	A4.1	208	
Flame ED	A4.1	208	
Flame EF	A4.1	208	

Table A6.1 A list of the flames studied

BIBLIOGRAPHY

25. Kim T.K., Alder B.J., Laurandau N.M., Gore J.P., Combust. Science and Technology, 110:361 (1995).
26. Gore J.P., Zhan N.J., Combustion and Flame, 105:414, 1996.
27. Lyle K.H., Tseng L.K., Gore J.P., Laurandeau N.M., Combustion and Flame, 116:627-639(1999).
28. Dupont V. and Williams A., Combustion and Flame, 114:103-118(1998).
29. Nishioka M., Nakagawa S., Ishikawa, Takeno T., Combustion and Flame, 98:127-139(1994).
30. Tanoff M.A., Smooke M.D., Osborne R.J., Thomas M.D., Pitz R.B., Twenty Sixth Symposium (International) on Combustion, The Combustion Institute, Pittsburgh, 1990, p 1121-1128.
31. Blevins R.G., Gore J.P., Combustion and Flame, 116:546-566(1999).
32. Ravikrishna R.B., Laurandeau N.M., Combustion and Flame, 122:474-482(2000).
33. Lutz A.E., Kee R.J., Grcar J.F., Rypley F.M., Sandia Lab Report, SAND96-8243(1997).
34. Carrier G.F., Fendell F.E. and Marble F.E., SIAM, Appl. Math., 28:2,(1975).
35. Kim H.K., Ph.D. Thesis, University of Michigan, Ann Arbor, U.S.A., (1998).
36. Von Karman, NACA Tech. Mem. 1092 (1921).
37. Abu-Romia, M.M., and Tien C.L., J. Heat Transfer, 11:321 (1967).
38. Grosshandler, W.L., Int. J. Heat Mass Transfer, 23: 1447 (1980)
39. Atreya A. and Agrawal S., Combust. Flame, 115:372 (1998)
40. Daguse T., Croonenbroek T., Rolon J.C., Darabiha N., Soufiani A., 106:271-287(1996).
41. Atreya A., Zhang C., Kim H.K., Suh J., Shamim T., 26th Symposium (International) on Combustion, The Combustion Institute, Pittsburgh, 1996, 2181.
42. Herding G., M.S. Thesis., Michigan State University, 1993.
43. Suh. J., Ph.D. Thesis, Univerisity of Michigan, 1997.
44. Lee K., Ph.D. Thesis, Michigan State University, 1991.
45. Mungekar H.P. and Atreya A., Proceedings of the 2nd Pacific Symposium on Flow Visualization and Image Processing,Paper 125, Honululu, May 16-19 (1999).
46. Ravikrishna R.V., Laurandeau N.M., Combustion and Flame, 122:474-482(2000).
47. Hahn W. and Wendt J.O.L., 18th International Symposium on Combustion, The Combustion Institute, Pittsburgh, 1981, p121-131.
48. Drake M.C. and Blint R.J., Combustion and Flame, 76:151-167, (1989).
49. Allen J.D., Combustion and Flame, 24:133-136, 1975.
50. Amin H., Combustion Science and Technology, Vol. 15, pp.31-40, 1977.
51. Jaasma D. and Borman G., Combustion Science and Technology, 1980, Vol. 23, pp 83-88.
52. Morio Hori, Combustion Science and Technology, 1980, Vol.23, pp. 131-135.
53. Morio Hori, 21st Symposium (International) on Combustion, The Combustion Institute, 1986, pp.1181-1188.
54. Scire J.J. Jr., Yetter R.A., Dryer F.L., Proceedings of the first joint meeting of the US sections of the Combustion Institute, Washington D.C., March 1999, p. 188.
55. http://www.me.berkeley.edu/gri_mech/
56. http://www.me.berkeley.edu/gri_mech/
57. Fristrom, R. M., Flame Structure, p.170-173, McGraw-Hill, New York, [1965].

58. Kent J.H., Combustion and Flame, Vol. 14, p279-282, (1970).
59. Ang. J.A., Pagni P.J., Mataga T.G., AIAA Journal, Vol. 26, No3, p323-329,(1988).
60. Heitor M.V. and Moreira A.L., Progr. Energ. Combust. Sci., Vol. 19, pp259-278,(1993).
61. Zhang C., Suh J., Atreya A., Proceedings of the Central States Section of the Combustion Institute, Mobil, AL, 1997, pp.343.
62. Omega Temperature Catalog, Vol H., (1998).
63. Siegel R. and Howel J.R., Thermal Radiation Heat Transfer, 2nd Edition, Hemisphere Publishing Corporation, New York, (1981).
64. Touloukian Y.S., Dewitt D.P.,Thermophysical Properties of Matter,Vol 8-9., Plenum Publishing Company,(1970).
65. Ohmi K., Yamamoto F., Uemura T., Coutanceau M., 3rd International Symposium on Fluid Control Measurement and Vizualization, FLUCOME-91, Aug 28-31, San Francisco, CA., pp435-442,(1991).
66. Dieke G.H. and Crosswhite H.M., The UV bands of OH, Quant Spectr Radiat Transfer, Vol. 2, pp. 97-199, Permagon, (1968).
67. Herzberg G., Spectra of diatomic molecules, 2nd Edition, pp 560-561, Van Nostrand Company, (1950).
68. Erickson W.D., Williams G.C., Hottel H.C., Combustion and Flame,18:127(1964).
69. Dalzell W.H., Williams G.C., Hottel H.C., Combustion and Flame, 14:161(1970).
70. Dobbins R.A. , Megaridis C.M., Applied Optics,Vol30, No30,pp4747,(1991).
71. Koylu U.O. ,Faeth G.M., Journal of Heat Transfer,115:409,(1993).
72. Krishnan S.S., Lin K.C., Wu J.S., Faeth G.M., ASME Winter Annual meeting, Dallas, TX,Nov16-21,1997.
73. di Statsio, J. Aerosol Science, Vol. 29, Suppl 1s, p1319, (1998).
74. Farias T.L., Koylu U.O., Carvalho M.G., Applied Optics, Vol. 35, No 33, p6560, (1996).
75. Gangopadhyay S., Elminyawi I., Sorenson C.M., Applied Optics, Vol. 30, No 33,p4859, (1991).
76. Koylu U.O., Combustion and Flame, 109:488,(1996).
77. Dobbins R.A., Santoro R.J., Semerjian H.G., The 23rd Symposium (International) on Combustion, The Combustion Institute, Pittsburgh, 1990, p1525.
78. Rosner and Koylu, In situ light scattering measurement of morphology of evolving flame synthesized nano aggregates, Applied Optics, 2686-2697(1999).
79. Mungekar H.P. and Atreya A., submitted,2000.
80. Barlow R.S., Flechtner G.J., Carter C.D., Chen J.Y., Combustion and Flame, Vol.120: 549-569, (2000).
81. Gore J.P., Viskanta R. and Lim J., Combustion and Flame, 121, p262-274,(2000).
82. Chung S.H., Kang K.T., Hwang J.Y., Lee W., Soot Zone Structure and Sooting Limit in Counter-Flow flames: Comparison of co-flow and counter-flow flames, Combustion and Flame, Vol. 109, 266-281, (1997).
83. Sick V., Hildebrand F., Lindsedt P., Quantitative Laser based measurements and detailed chemical kinetic modeling of NO concentrations in methane/air counter-

flow diffusion flames, The 27th Symposium (International) on Combustion, The Combustion Institute, (1998).
84. Mungekar H.P. and Atreya A., 1st Joint Meeting of the U.S. States of the Combustion Institute, Washington D.C., March, (1999).
85. Howard J.B and Pope C.J., Combined detailed gas phase kinetic modeling and soot aerosol dynamics, Technical Meeting of Western section of the Combustion Institute, (1996).
86. Frenklach M. and Wang H., Detailed modeling of soot nucleation and growth, The 23rd Symposium (International) on Combustion, The Combustion Institute, Pittsburgh, pp 1559-1466, (1990).
87. Mauss F., Schaffer T., Bockhorn H., Inception and growth of soot particles in dependence on the surrounding gas phase, Combustion and Flame, Vol 99: pp 697-705, (1994).
88. Lindtsedt P., Simplified Soot Nucleation and Surface Growth steps for non-premixed flames, in Soot Formaiton in Combustion, Bockhorn H., Editor, Springer Verlag, pp 417-439, (1994).
89. Hall R.J., Smooke M.D., Colket M.B., Predictions of soot dynamics in Opposed Jet Diffusion Flames, in Physical and Chemical Aspects of Combustion, Edited by Dryer F.L. and Sawyer R.F., Gordon and Breach Science Publishers, New York, pp. 191-230,(1997).
90. Krishnan S., Ph.D. Thesis, University of Michigan, (2000).
91. Miller J.H., The 23rd Symposium (International) on Combustion, The Combustion Institute, Pittsburgh, pp 91-98, (1990).
92. Harris S.J. and Wiener A.M., The 22nd Symposium (International) on Combustion, The Combustion Institute, Pittsburgh, pp 333, (1989).
93. Dobbins R.A., Fletcher R.A. and Chang H.C., Combustion and Flame, Vol. 115, pp 285-298, (1998).
94. Dobbins R.A., Fletcher R.A. and Schwartman A.F., Combustion Science and Technology, Vol 121., pp 103-121, (1996).
95. Randall L. Vander Wal, Combustion and Flame, Vol. 110, p281-284, (1997).
96. Du D.X., Axelbaum R.L. and Law C.K., The 20th Symposium (International) on Combustion, The Combustion Institute, Pittsburgh, pp 387, (1988).
97. Du D.X., Axelbaum R.L. and Law C.K., Soot Formation in Strained Diffusion Flames with Gaseous Additives, Combustion and Flame, Vol. 102, 11-20, (1995).
98. Du J. and Axelbaum R.L., The effect of flame strucuture on Soot particle inception in diffusion flames, Vol. 100, pp. 367-375, (1995).
99. Du D.X., Wang H., an Law C.K., Soot Formation in CounterFlow Ethylene Diffusion Flames from 1 to 2.5 Atmosphers, Combustion and Flame, Vol. 113, pp. 264-270, (1998).
100. Chung S.H., Kang K.T., Hwang J.Y., Lee W., Soot Zone Structure and Sooting Limit in Counter-Flow flames: Comparison of co-flow and counter-flow flames, Combustion and Flame, Vol. 109, 266-281, (1997)
101. Vincitore A.M. and Senkan S.M., Polyclyic Aromatic Hydrocarbon Formation in Opposed Flow Diffusion Flames of Ethane, Combustion and Flame, Vol 114., pp.259-266, (1998).